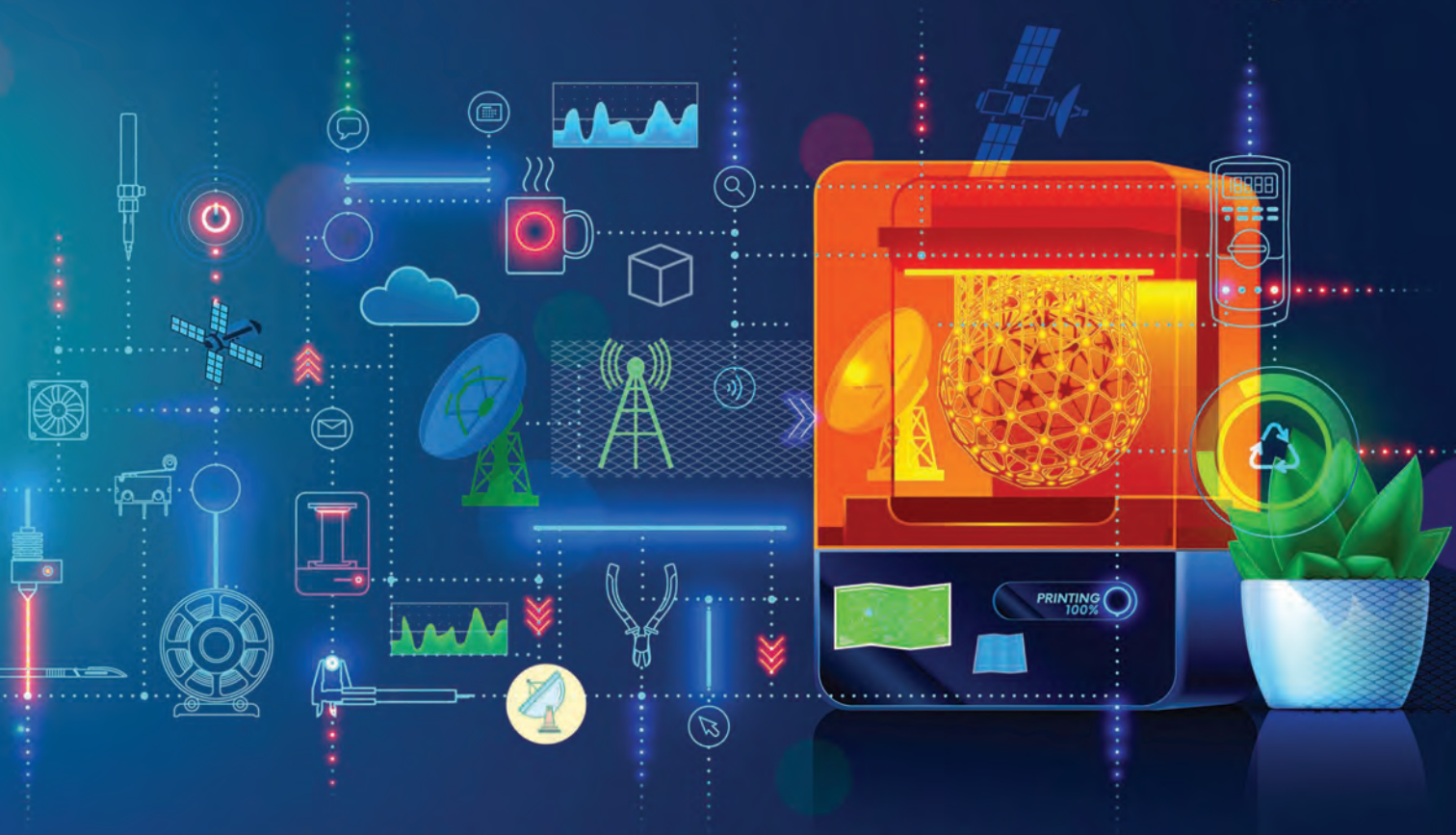


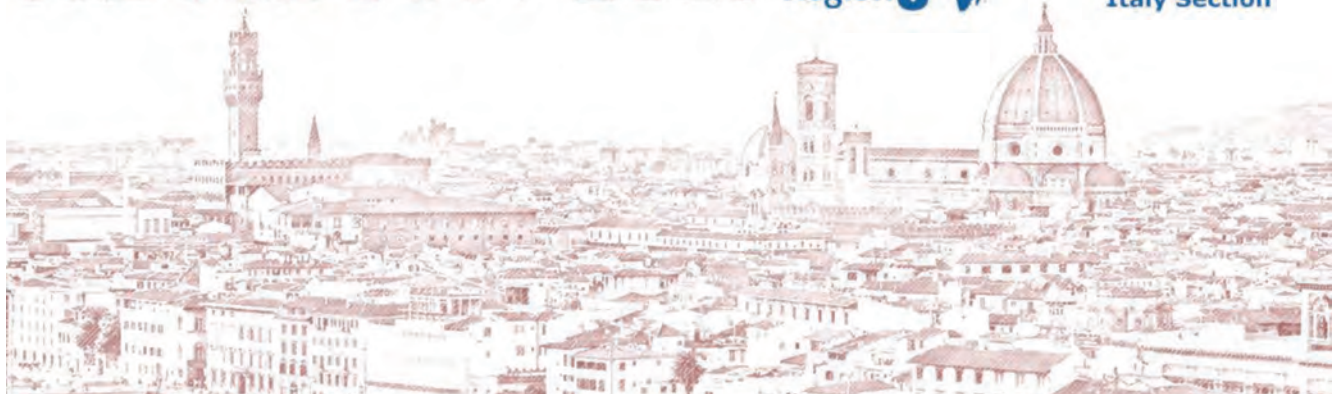
IEEE **Antennas & PROPAGATION** Magazine



3D PRINTING MATERIALS AND TECHNIQUES FOR RF TECHNOLOGIES

Latest Advances for Devices, Antennas, and Metamaterials





HISTELCON 2023

Florence, Italy - 7-9 September 2023

SCIENCE AND TECHNOLOGY OR TECHNOLOGY AND SCIENCE?

FIRST ANNOUNCEMENT AND CALL FOR PAPERS

HISTELCON is a flagship conference series of the IEEE Region 8 held every two years and is dedicated to any aspects of the history of electrical engineering, electronics, computing and their impact on social and economical development.

HISTELCON 2023 will be the eighth HISTELCON conference, coming back to Italy after the 2012 Pavia edition. It will be a hybrid event, held both live and online. The conference official language is English, and all presentations will be oral. The conference will be hosted in the magnificent city of Florence, Italy, in the *Antica Canonica di San Giovanni*, in Florence Cathedral Square.

CALL FOR PAPERS

In addition to the relations between **Technology and Science**, the conference is open to other topics, including:

- **Technology museums**
- **Computers and microprocessors**
- **Device and system vulnerability**
- **Foundational research and Big Science**
- **Measurement systems and units**
- **Big corporations**
- **Radio astronomy**
- **Humanistic studies and technology**

Save the date and join us in Florence!

Important dates

15 April 2023 – Paper Submission

20 May 2023 – Paper review notification

17 June 2023 – Final Camera-ready paper submission

28 June 2023 – Early bird registration expires

Papers can either be **one-page abstracts** or **two to four pages full papers**. Both will undergo the same review process with the same deadlines, but only full papers will be considered for publication in IEEE Xplore. To this aim, each accepted paper must be presented by a registered author. Not more than two papers can be presented by a single author. A charge applies to the second paper.

2023.ieee-histelcon.org
histelcon2023@ieeesezioneitalia.it

Organizers

Honorary Chair

Vincenzo Piuri, *Region 8 Director 2023-2024, University of Milan*

General Chairs

Massimo Guarneri, *IEEE History Activity Committee Italy Section chair, University of Padua*

Giuseppe Pelosi, *University of Florence*

Technical Program Chair

Stefano Selleri, *University of Florence*

Treasurer

Pisana Placidi, *University of Perugia*

Publication Chair

Monica Righini, *University of Florence*

Steering Committee

Martin Bastiaans, *Region 8 History Activities Chair, Eindhoven University of Technology*

Antonio Savini, *IEEE History Committee Chair and Italy Section LM Affinity Group Chair, University of Pavia*

Anthony C. Davies, *HISTELCON2019 Chair, Potters Bar, Herts, UK*

Victor Fouad Hanna, *1st HISTELCON Chair, University of Paris 6*

Gianfranco Chicco, *IEEE Italy Section chair, Politecnico di Torino*

Sergio Rapuano, *IEEE Italy Section past-chair, University of Sannio*

Tiziana Tambosso - *Region 8 Conference Coordination Committee Chair*

Donatella Lippi, *Fondazione Scienza e Tecnica*

Webmaster

Gianluca Mazzilli, *Athena Srl*



VOLUME 65 // NUMBER 3 // JUNE 2023

IEEE Antennas & PROPAGATION Magazine

IMAGE LICENSED BY INGRAM PUBLISHING

FEATURES

10 3D Printing Materials and Techniques for Antennas and Metamaterials

Thomas Whittaker, Shiyu Zhang, Alexander Powell, Chris J. Stevens, John (Yiannis) C. Vardaxoglou, and William Whittow

21 Reflectarrays and Metasurface Reflectors as Diffraction Gratings

Fu Liu, Do-Hoon Kwon, and Sergei Tretyakov

33 Enabling Spherical Beam Coverage for Millimeter-Wave Stationary and Mobile Applications

Junho Park, Ahmed Abdelmottaleb Omar, Jonghyun Kim, Jaehyun Choi, Beakjun Seong, Jongwoo Lee, and Wonbin Hong

46 Understanding the Shielding Efficiency of a Faraday Grid Cage

Bernhard Jakoby, Roman Beigelbeck, and Thomas Voglhuber-Brunnmaier

57 5G/Millimeter-Wave Rectenna Systems for Radio-Frequency Energy Harvesting/Wireless Power Transmission Applications

Daasari Surender, Md. Ahsan Halimi, Taimoor Khan, Fazal A. Talukdar, Nasimuddin, and Sembiam R. Rengarajan

77 An Accordion-Folding Series-Fed Patch Array With Finite Thickness

Matthew W. Nichols, Alfredo Gonzalez, Elias A. Alwan, and John L. Volakis



ON THE COVER

This issue of *IEEE Antennas and Propagation Magazine* includes a special memoriam in honor of the magazine's founding EIC Ross Stone. It also includes six diverse feature articles.

MAIN IMAGE—©SHUTTERSTOCK.COM/ANDREY SUSLOV,
IMAGE LICENSED BY INGRAM PUBLISHING FOR ICONS

Digital Object Identifier 10.1109/MAP.2023.3273071



MISSION STATEMENT:

IEEE Antennas and Propagation Magazine publishes feature articles and columns that describe engineering activities within its scope, taking place in industry, government, and universities. All feature articles are subject to peer review. Emphasis is placed on providing the reader with a general understanding of either a particular subject or of the technical challenges being addressed by various organizations as well as their capabilities to cope with these challenges. Review, tutorial, and historical articles are welcome.

DEPARTMENTS

4 EDITOR'S COMMENTS

Remembering the Founding Editor of IEEE Antennas and Propagation Magazine

8 PRESIDENT'S MESSAGE

To IEEE Antennas and Propagation Society Members

83 MEETINGS & SYMPOSIA

84 COURSES

86 BIOELECTROMAGNETICS

A Survey of On-Body Antenna Arrays: Future Improvements, New Designs, and Lessons Learned

97 TURNSTILE

The Annual Quiz

98 WOMEN IN ENGINEERING

Game of Tenures

102 YOUNG PROFESSIONALS

Innovation, a Skewed Balance Between Old and New—Lessons From My Journey to Compressive Antenna Arrays

107 AP-S COMMITTEES & ACTIVITIES

IEEE Antenna Measurements Committee Events

109 IN MEMORIAM

Remembering Ross Stone

118 HIDDEN WORD

IEEE ANTENNAS AND PROPAGATION MAGAZINE EDITORIAL BOARD

Editor-in-Chief

Francesco P. Andriulli
Politecnico di Torino, Italy
apm-eic@ieee.org

Abdulkadir Yuce

Nanyang Technological University,
Singapore
acyucel@ntu.edu.sg

Measurements Corner

Debatosh Guha
Institute of Radio Physics & Electronics, India
dguha@ieee.org

Editorial Assistant

Christina Tang-Bernas
University of Southern California,
California, USA
tangbern@usc.edu

Columns and Departments

Bioelectromagnetics

Asimina Kiourtis
The Ohio State University, Ohio, USA
kiourtis.1@osu.edu

Meetings & Symposia

Short Courses

Raymond Wasky
John Hopkins University, Maryland, USA
raymond.wasky@huapl.edu

Stand on Standards

Vikass Monebhurrun
CentraleSupélec, France
vikass.monebhurrun@supelec.fr

Turnstile

Rajeev Bansal
University of Connecticut, USA
rajeev@engr.uconn.edu

Women in Engineering

Francesca Vipiana
Polytechnic University of Turin, Italy
francesca.vipiana@polito.it

Young Professionals

C.J. Reddy
Altair Engineering, Inc., Virginia, USA
cjreddy@ieee.org

Past Editors-in-Chief

Ross Stone
Founding Editor-in-Chief
Stoneware Limited, California, USA
r.stone@ieee.org

Mahta Moghadam

University of Southern California,
California, USA
mahta@usc.edu

IEEE Periodicals

Magazines Department

445 Hoes Lane, Piscataway, NJ 08854 USA

Pilar Etuk,
Journals Production Manager

Katie Sullivan,
Senior Manager, Journals Production

Janet Duder, *Senior Art Director*

Gail A. Schnitzer,
Associate Art Director

Theresa L. Smith, *Production Coordinator*

Mark David, *Director, Business
Development—Media & Advertising*

Tel: +1 732 465 6473

Fax: +1 732 981 1855

m.david@ieee.org

Felicia Spagnoli, *Advertising
Production Manager*

Peter M. Tuohy, *Production Director*

Kevin Lisankie, *Editorial Services Director*

Dawn M. Melley, *Senior Director,
Publishing Operations*

Ruiji He

Beijing Jiaotong University, China
ruiji.he@bjtu.edu.cn

Yejun He

Shenzhen University, China
yjhe@szu.edu.cn

Wonbin Hong

Pohang University of Science and
Technology, South Korea
whong@postech.ac.kr

Mengmeng Li

Nanjing University of Science and
Technology, China
limengmeng@njust.edu.cn

Adrien Merlini

IMT Atlantique, France
adrien.merlini@imt-atlantique.fr

Paolo Rocca

University of Trento, Italy
paolo.rocca@unitn.it

Felix Vega

Directed Energy Research Center
Technology Innovation Institute
Abu Dhabi, United Arab Emirates
felix.vega@ieee.org

Hao Xin

University of Arizona, Arizona, USA
hxin@email.arizona.edu

Electromagnetic Perspectives

Christophe Caloz
KU Leuven, Belgium
christophe.caloz@kuleuven.be

EM Programmer's Notebook

Matthys Botha
Stellenbosch University, South Africa
mmbbotha@sun.ac.za

From the Screen of Stone

Ross Stone
Stoneware Limited, California, USA
r.stone@ieee.org

Hidden Word

Fred Gardiol
fred.gardiol@hispeed.ch

Historically Speaking

Trevor Bird
Antengenuity, Australia
tsbird@optusnet.com.au

Industry Activities

Rod Waterhouse
Octane Wireless, Maryland, USA
rwaterhouse@octanewireless.com

IEEE prohibits discrimination, harassment, and bullying.

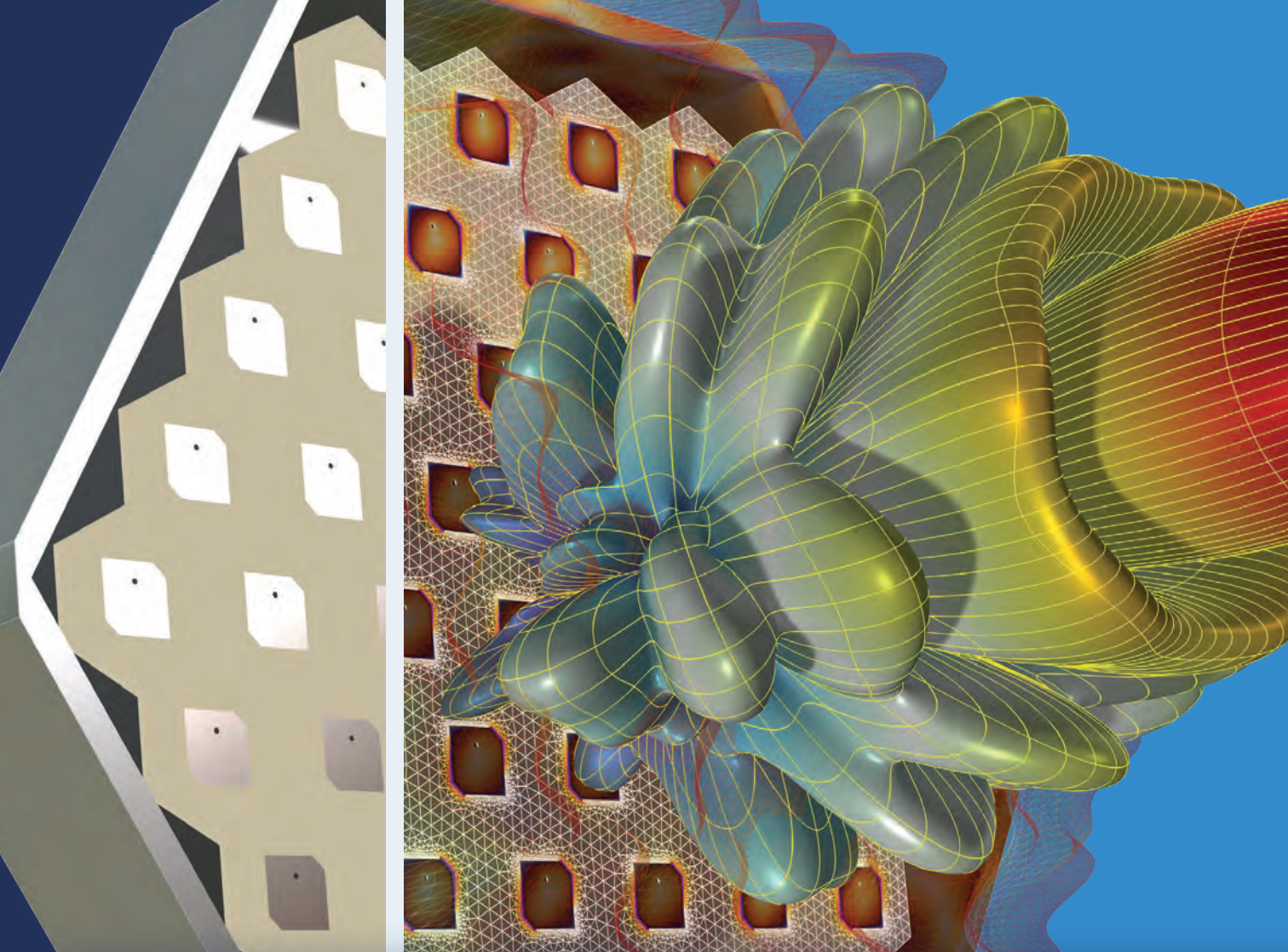
For more information, visit <http://www.ieee.org/web/aboutus/whatis/policies/p9-26.html>.

Address editorial correspondence to the Editor-in-Chief Francesco P. Andriulli, Dept. Electronics and Telecommunications, Politecnico di Torino, Corso Duca degli Abruzzi 24 10129, Turin, Italy; email: apm-eic@ieee.org.

General information for contributors: Contributions to *IEEE Antennas and Propagation Magazine* are accepted through ScholarOne Manuscripts at <https://mc.manuscriptcentral.com/apm-ieee>. Contributors are encouraged to contact the magazine editor-in-chief before submitting their articles to inquire whether their prospective submission is within the scope of the magazine. Article formatting requirements vary based on the type of article. The authors are asked to consult <http://ieeauthcenter.ieee.org/> and <https://www.ieeepubs.org/publications/ieee-antennas-and-propagation-magazine> for general instructions. Manuscripts should be in English. The editor-in-chief reserves the right to accept, reject, and/or edit any and all material submitted. Submission of material will be interpreted as assignment and release of copyright and any and all other rights as if the standard IEEE copyright and US Export Control Compliance Forms had been signed by the copyright owner. All material associated with contributions may be discarded after the issue containing the contribution goes to press, unless otherwise requested. The nominal deadline for material not requiring peer review or extensive editing is 120 days prior to the start of the month of publication. Contact the editor-in-chief if you have timely material that cannot make this deadline. All feature articles are subject to full peer review per IEEE policy. There is a limit of ten double-column printed pages for all articles. All contributions to

departments are reviewed by the associate editor(s) for that department, with additional peer review as deemed necessary by the associate editor. Conference reports should be no more than two pages and contain no more than five figures.

IEEE Antennas and Propagation Magazine (ISSN1045 9243) is published bimonthly by The Institute of Electrical and Electronics Engineers, Inc. Headquarters: 3 Park Avenue, 17th Floor, New York, NY 10016-5997, U.S.A. +1 212 419 7900. Responsibility for the contents rests upon the authors and not upon the IEEE, the Society, or its members. The magazine is a membership benefit of the IEEE Antennas and Propagation Society, and subscriptions are US\$6.00 per member per year (included in Society fee). Replacement copies for members are available for US\$20 (one copy only). Nonmembers can purchase individual copies for US\$135. Nonmember subscription prices are available on request. Copyright and Reprint Permissions: Abstracting is permitted with credit to the source. Libraries are permitted to photocopy beyond the limits of the U.S. Copyright law for private use of patrons: 1) those post-1977 articles that carry a code at the bottom of the first page, provided the per-copy fee is paid through the Copyright Clearance Center, 222 Rosewood Drive, Danvers, MA 01970, U.S.A.; and 2) pre-1977 articles without fee. For other copying, reprint, or republication permission, write to: Copyrights and Permissions Department, IEEE Service Center, 445 Hoes Lane, Piscataway NJ 08854 U.S.A. Copyright © 2023 by The Institute of Electrical and Electronics Engineers, Inc. All rights reserved. Periodicals postage paid at New York, NY, and at additional mailing offices. Postmaster: Send address changes to IEEE Antennas and Propagation Magazine, IEEE, 445 Hoes Lane, Piscataway, NJ 08854 U.S.A. Canadian GST #125634188. Printed in U.S.A.



Take the Lead in RF Design

with COMSOL Multiphysics®

Multiphysics simulation is expanding the scope of RF analysis to higher frequencies and data rates. Accurate models of microwave, mmWave, and photonic designs are obtained by accounting for coupled physics effects, material property variation, and geometry deformation. Ultimately, this helps you more quickly see how a design will perform in the real world.

» comsol.com/feature/rf-innovation



Francesco Andriulli

Remembering the Founding Editor of *IEEE Antennas and Propagation Magazine*

The editors of *IEEE Antennas and Propagation Magazine* with the entire editorial board mourn the passing of Ross Stone, our journal's founding editor, who left us on 29 March 2023. Our thoughts and prayers are with him, and we extend our deepest condolences to his dear ones, especially to his wife Sue and his daughter Michele. An "In Memoriam" column to honor Ross can be found in this issue [A1]. The "In Memoriam" column also contains thoughts, memories, and farewell messages that the magazine and our Society's president have received in these past days. Further messages received after the closure of this issue for publication will be published in the future together with further initiatives to honor Ross Stone's memory and legacy.

This issue of the magazine, the journal Ross has served and loved for so many years, is dedicated to his memory.

IN THIS ISSUE

The first contribution of this issue is a review by Whittaker et al. [A2] dealing with materials for 3D printing for engineering antennas and metamaterials. The article starts with a comprehensive review of the different material properties where both characterization for permittivity and losses are reported.

The "In Memoriam" column also contains thoughts, memories, and farewell messages that the magazine and our Society's president have received in these past days.

The work then moves to the treatment of the printing of metallic structures, again reviewing what can be done with the state of the art. Finally, different practical examples are reviewed, always with a rich bibliographic analysis that will prove quite useful for the reader. The article by Liu et al. [A3] is a tutorial on reflectarray and metasurface reflectors. The article opens with the treatment of active arrays discussing periodicity and current optimality, and then it moves to the treatment of reflectarrays and metamirrors, providing an in-depth bibliographic analysis on the topic. The article by Park et al. [A4] proposes a new class of antenna topology aiming at obtaining a near-spherical beam steering coverage for millimeter-wave frequencies. After a rich bibliographic analysis of the state of the art, the article presents the new design strategy focusing on specific scenarios and characterizing the

outcomes numerically. The article closes by reporting a prototyping session complemented by a rich campaign of measurements. The article by Jakoby et al. [A5] deals with the efficiency of a grid Faraday cage. The authors use a Fourier approach analyzing a circular 2D model of a cage. After an introduction that reviews previous relevant works, the article

dives into its main analysis obtaining, via Fourier techniques, the expression for the field in the presence of the cage as a function of all relevant electrical and structural parameters. The results are then discussed, and the limitations of the shielding are assessed in the different areas of interest. The article by Surender et al. [A6] reviews recent advances in rectenna technologies at 5G frequencies. After a general introduction, the article starts analyzing the main aspects of energy harvesting and wireless power transfer in 5G communications. Finally, the article by Nichols et al. [A7] deals with a new design concept combining antenna arrays with the possibility of physical reconfigurability to optimize occupation with controlled performance. The article starts with a general review of application scenarios. Then the main design idea is presented. The article then presents a campaign of both numerical and experimental tests

ORDER OF MAGNITUDE AHEAD



*Fast and easy creation
of EM scenarios*

released!

New:

Scenario Project:

- Assembly of component projects, merged into a single scenario project, by a set of Manipulations commands

Voxel Editor:

- Uses various Voxel formats to create WIPL-D projects with human phantoms

General Integral Equation Solver:

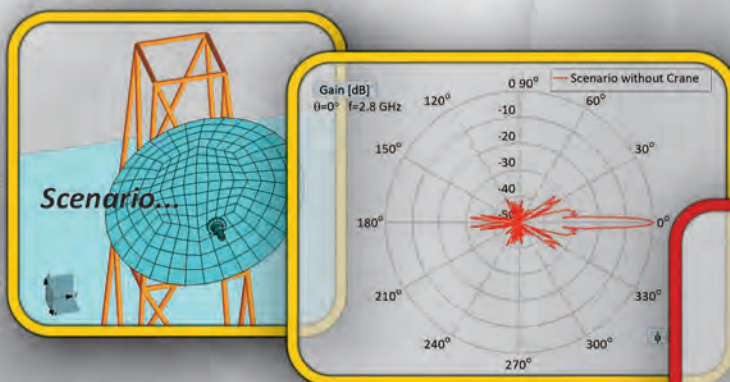
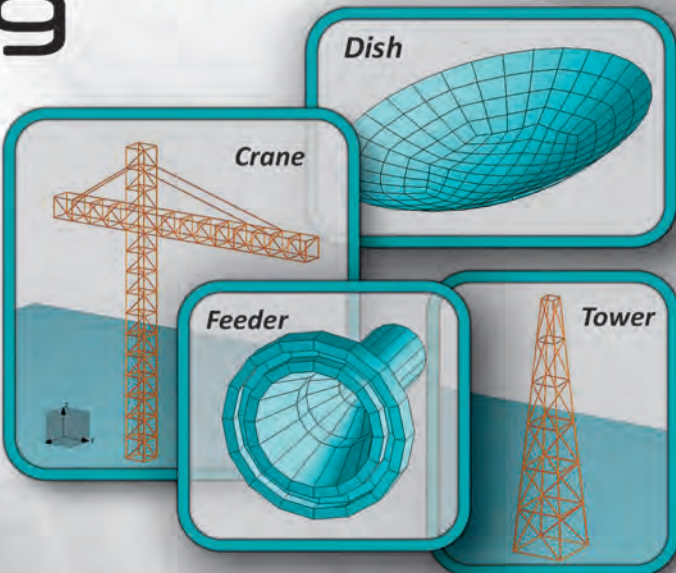
- Handles arbitrary Green's function (Example: antennas above real ground)

Medical MicroWave Imaging (MMWI) toolkit

- Detection of stroke position, size and shape in a simulated MMWI scenario

Periodic Boundary Condition (PBC):

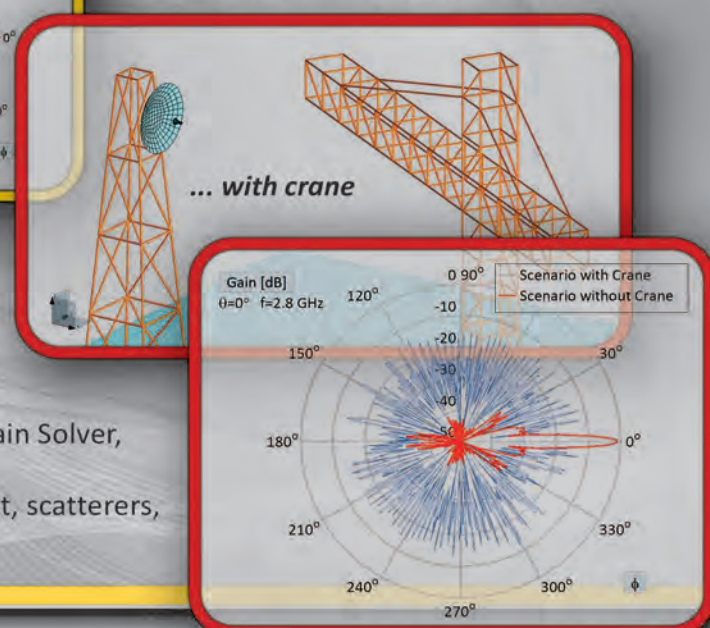
- Expanded to include antennas
- Max size of PBC cell enlarged up to 10λ
- Simulation accelerated up to 10 times



- Domain Decomposition Solver:
- Extended size (2000- λ aircraft with monopole)
 - Accuracy: increased up to 10 times
 - Analysis time: reduced up to 3 times

Graph Viewer:

- Using a math tool for post-processing the simulation results
- Customization of grid settings



Features:

- Full 3D EM simulation in frequency domain
- Metallic, dielectric and magnetic materials
- Lumped elements and distributed loadings
- Add-ons: GPU Solver, Optimizer, Time Domain Solver, Circuit Solver (Microwave) and 2D Solver
- Applications: antenna design and placement, scatterers, microwave circuits and waveguides, EMC ...



Do you like what you're reading?
Your feedback is important.
Let us know—send the editor-in-chief an e-mail!



validating the approach and showing its performance and impact.

APPENDIX: RELATED ARTICLES

- [A1] F. Andriulli and S. Maci, "Remembering Ross Stone," *IEEE Antennas Propag. Mag.*, vol. 65, no. 3, pp. 109–116, Jun. 2023, doi: 10.1109/MAP2023.3269213.
- [A2] T. Whittaker, S. Zhang, A. Powell, C. J. Stevens, J. C. Vardaxoglou, and W. Whittow, "3D printing materials and techniques for antennas and metamaterials: A survey of the latest advances," *IEEE Antennas Propag. Mag.*, vol. 65, no. 3, pp. 10–20, Jun. 2023, doi: 10.1109/MAP2022.3229298.
- [A3] F. Liu, D.-H. Kwon, and S. Tretyakov, "Reflectarrays and meta-surface reflectors as diffraction gratings: A tutorial," *IEEE Antennas Propag. Mag.*, vol. 65, no. 3, pp. 21–32, Jun. 2023, doi: 10.1109/MAP2023.3236278.
- [A4] J. Park et al., "Enabling spherical beam coverage for millimeter-wave stationary and mobile applications: A stackable patch antenna," *IEEE Antennas Propag. Mag.*, vol. 65, no. 3, pp. 33–45, Jun. 2023, doi: 10.1109/MAP.2022.3208797.
- [A5] B. Jakoby, R. Beigelbeck, and T. Voglhuber-Brunnmaier, "Understanding the shielding efficiency of a faraday grid cage: A spectral domain approach," *IEEE Antennas Propag. Mag.*, vol. 65, no. 3, pp. 46–56, Jun. 2023, doi: 10.1109/MAP.2022.3229287.
- [A6] D. Surender, M. A. Halimi, T. Khan, F. A. Talukdar, Nasimuddin, and S. R. Rengarajan, "5G/millimeter-wave rectenna systems for radio-frequency energy harvesting/wireless power transmission applications: An overview," *IEEE Antennas Propag. Mag.*, vol. 65, no. 3, pp. 57–76, Jun. 2023, doi: 10.1109/MAP.2022.3208794.
- [A7] M. W. Nichols, A. Gonzalez, E. A. Alwan, and J. L. Volakis, "An accordion-folding series-fed patch array with finite thickness: A folding technique for CubeSat arrays," *IEEE Antennas Propag. Mag.*, vol. 65, no. 3, pp. 77–82, Jun. 2023, doi: 10.1109/MAP.2022.3229295.

Antenna & Electromagnetics Laboratory
1948 - 2023
Celebrating 75 Years of Innovation
University of Illinois, Urbana, IL - September 8-10, 2023

Join Us!

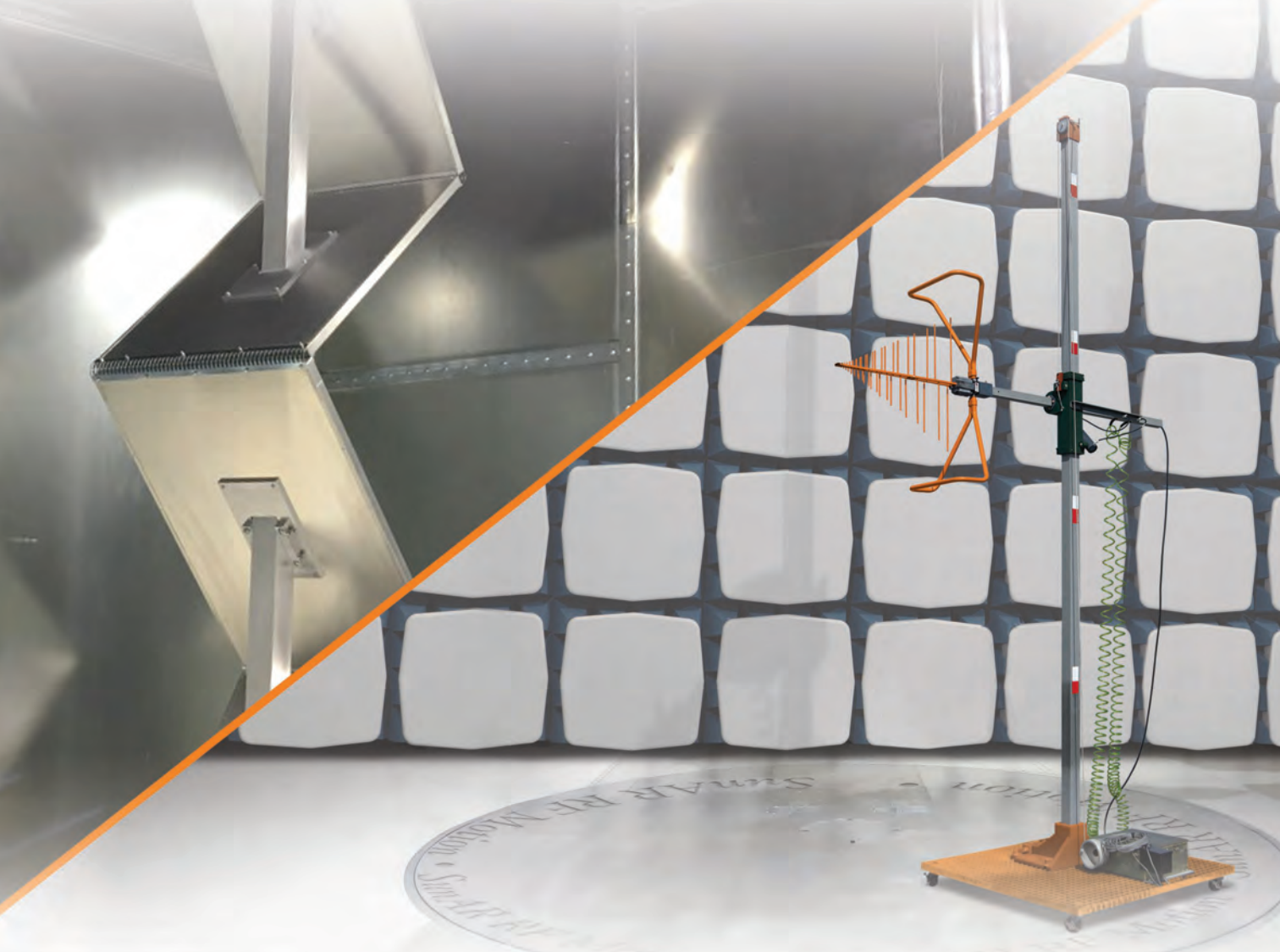
The University of Illinois Antenna and Electromagnetics Laboratory will be celebrating its 75th anniversary with a Reunion happening from Friday, September 8 to Sunday, September 10, 2023.

The EM Lab has a rich history of cutting edge, innovative, and revolutionary technological contributions that have helped shape the computer, communication, and electronic industries as well as academic research in many disciplines. Alumni and friends of the labs will meet throughout the three-day weekend to share a lifetime of memories, professional and personal experiences through seminars, meetings and social events. We hope that you will join us to remember and reflect on the many changes that have occurred, both personal and professional. Scheduled events include tours and visits, a symposium, a banquet, and entertainment.

For more information and updates, please visit the website at emlab.illinois.edu/reunion

Conveniently, the Reunion leads into the 48th Annual Antenna Applications Symposium (AAS), held at Allerton Park, Monticello, IL, from Monday, September 11-Wednesday, September 13, 2023. For more information on the AAS, including the program and keynote speakers, please visit the website at <https://publish.illinois.edu/antenna-applications-symposium/>

RF Testing Equipment That's Built to Last



SunAR RF Motion products give you the competitive edge with the long-lasting durability that AR products are known for. The SunAR product line includes:

- Antennas
 - Wireless & EMC testing
 - Distributed antenna systems (DAS)
- System controllers
- Turntables
- Reverberation chamber stirrers
- Antenna masts / positioners / stands

Many SunAR products can be customized to your specifications.

To learn more about customization options for masts, positioners, stirrers, and turntables, visit www.arworld.us/sunarrfmotion or call us at 215-723-8181.

The logo for AR, consisting of the letters "ar" in a stylized, lowercase font with a registered trademark symbol.

sunar rf motion

Other **ar** divisions: **rf/microwave instrumentation** • **modular rf** • **ar europe**



Stefano Maci

To IEEE Antennas and Propagation Society Members

It is my deep honor and pleasure to serve as the 2023 president of the IEEE Antennas and Propagation Society (AP-S). During the first few months of the year, several important discussions and decisions have been taken by the Society. What we can do to serve our members was a primary topic of discussion at the AdCom meeting held in Dubai on 25 February 2023. The proposal by Branislav Notaros, president-elect, and myself to lower the registration fee for student members of AP-S to US\$1 has been approved by the AdCom. This will allow our Society to attract many more student members in the near future. The balance of the Society for 2022 is extremely positive with a surplus mainly due to publications, paper downloading, and conference revenues. In 2022, we have had significant investments in new initiatives, mainly addressed to students and early-stage researchers, like the AP-S Fellowship (48 students awarded), Student Travel Grants (34 students awarded), and Undergraduate Summer Research Scholarship (20 students awarded). These initiatives are in addition to the several already existing successful programs to support students, including the C.J. Reddy Travel Grant.

New conferences have been sponsored by AP-S, sometimes cospon-

sored with our sister Society, the IEEE Microwave Theory and Technology Society (MTT-S). This is the case with two new conferences, the Microwave and Antennas and Propagation Conference (MAPCON) and International Microwave and Antenna Symposium (IMAS). The first MAPCON was held before the end of the last year in Bangalore, India, and will be repeated on 11–15 December 2023 in Ahmedabad, India. The first conference has been a great success with more than 460 papers and 800 attendees from 20 different countries. I would like to thank Puneet Kumar Mishra and Yahya Antar for the kind invitation to give a plenary lecture and the presentation of the Society. The other new cosponsored conference I had the pleasure to attend was IMAS, held in Cairo on 5 February 2023. Thanks to Hany Hammad for the invitation. The conference was also a success, with about 250 attendees. I will attend other exciting events before the end of the summer. The first will be the IEEE RADIO international conference, organized by Vikass Monebhurrum, in Balaclava, Mauritius, Africa, from 1 to 4 May 2023. The second is IMS 2023, the flagship conference of MTT-S, on next 11–16 June in San Diego, CA, USA. Attending IMS on behalf of AP-S is truly a pleasure because it gives me the opportunity to meet MTT-S members who I may not otherwise meet and to exchange information on future and

present joint initiatives, like the Joint Distinguished Lecture Program that MTT-S and AP-S recently started. I would like to thank Nuno Carvalho, IEEE MTT-S president, for inviting me to the MTT-S AdCom meeting in San Diego and for exchanging ideas on the common interests of the two Societies. I have reciprocated the invitation, asking him to attend our next AdCom meeting in Portland. The preparation of our flagship conference in Portland is proceeding well. This year, we got about 1,500 paper submissions, in line with the results obtained in 2021 and 2022, a bit less than the pre-COVID numbers. I would like to thank Jamesina Simpson and Reyhan Baktur (general cochairs) for the exceptional organization they are managing and Andy Chrysler, Karl Warneck, and Christos Christodoulou (Technical Program cochairs), for arranging a formidable technical program.

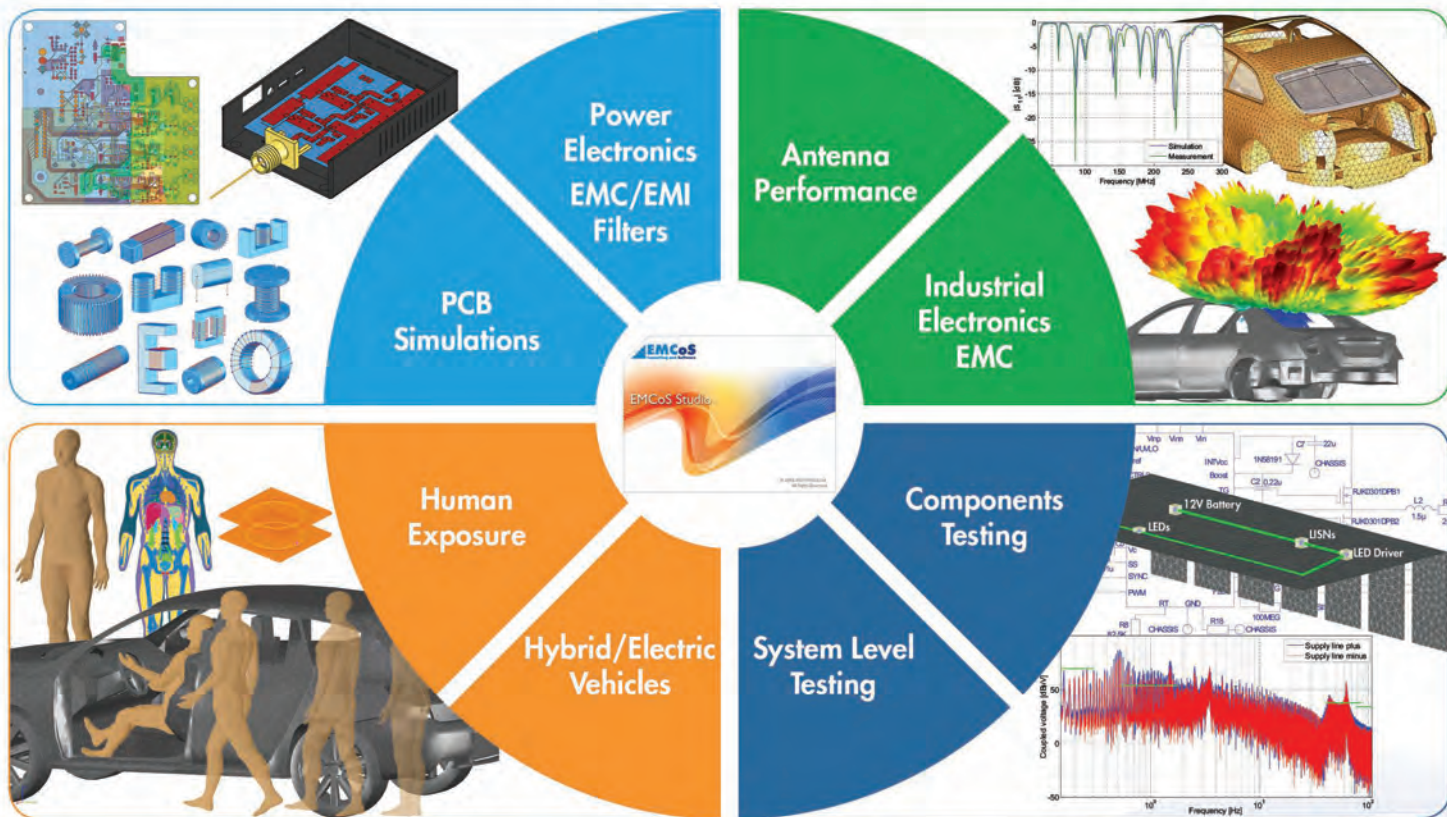
I wish to conclude this column by saying that in November of this year, we will have the review of the Society by the IEEE TAB, a review that occurs every five years. Branislav Notaros and I are working on collecting the rich documentation that will show the perfect shape of our Society! We will do our best to request timely coordination efforts from our AP-S committees.

Best regards.



EMCoS Studio

One software product for multiple solutions!



www.emcos.com
E-mail: info@emcos.com

EMCoS
Consulting and Software

Thomas Whittaker^{ID}, Shiyu Zhang^{ID}, Alexander Powell^{ID},
Chris J. Stevens^{ID}, John (Yiannis) C. Vardaxoglou^{ID},
and William Whittow^{ID}

3D Printing Materials and Techniques for Antennas and Metamaterials

A survey of the latest advances.

This is a review article of the latest advances in 3D printing for enabling new materials and new geometries for radio-frequency (RF) devices, antennas, and metamaterials.

The article discusses the achievable material properties and various optimized applications that are achievable by creating new shapes in either dielectric or metal. This article demonstrates what is currently possible with additive manufacturing

and the current limitations. Various additively manufactured RF devices are reviewed.

INTRODUCTION

This article is a review of the latest advances concerning 3D printing for RF, antennas, and metamaterials applications. For many years, RF engineers have been improving performance largely via changing the 2D shape of the metallization enabled, in part, by the recent advances in optimization via simulations. Electromagnetic (EM) performance and manufacturability

Digital Object Identifier 10.1109/MAP2022.3229298
Date of current version: 23 December 2022



IMAGE LICENSED BY INGRAM PUBLISHING

have always been the major concerns when proposing novel RF designs. In recent years, numerous researchers have demonstrated the EM advantages of 3D engineered EM materials and structures. However, many proposed ideas were not attractive in practice, due to the challenges in manufacturing. In recent decades, antennas and metamaterials fabrication have been dominated by mature subtractive manufacturing methods, such as etching and machining. They are specialized in creating 2D and exterior shapes, but the ability of engineering the internal structures is limited. Thanks to the additive manufacturing process, 3D printing has several advantages that include the ability to fabricate complex internal structures that enable bespoke dielectric properties; the ability to vary and grade the relative permittivity in two and even three axes; the ability to create cheaper, more efficient, and lightweight devices; and the ability to fabricate in 3D. Challenges include the resolution and surface roughness that becomes apparent at higher frequencies, the repeatability from laboratory to laboratory, the capability to 3D print dielectrics and low-loss conductors in the same process step, and the manufacturing challenges of scaling to large volumes. The growth in this area is demonstrated by there being 23 IEEE journal papers related to 3D-printed antennas in the five years between 2012 and 2016 and 211 IEEE journal papers between 2017 and 2021. This article reviews the state of the art in this area. The “Materials and Dielectric Properties” section discusses the achievable material properties and the additive manufacturing processes. The “Comparison of 3D Printing Techniques for RF Applications” section provides a comparison of the different 3D printing methods suitable for different RF applications. The “RF Components Printed With Plastics” section addresses new applications for new 3D-printed dielectric geometries that includes lenses, reflectarrays (RAs), polarizers, and impedance matching devices. The “3D-Printed Ceramic Components” section looks at additively manufactured ceramic components that exhibit low conductive and dielectric losses. The “Metalized Waveguides and Horn Antennas” and “Metaparticles for Isotropic Multimode Microwave Scattering” sections consider metallizing 3D-printed shapes to either enable new complex structures, such as scatterers, or minimize the cost and weight of devices.

MATERIALS AND DIELECTRIC PROPERTIES

FUSED FILAMENT FABRICATION

The most common materials used in fused filament fabrication (FFF) are acrylonitrile butadiene styrene (ABS) and polylactic acid (PLA). These are easy to print using basic off-the-shelf printers. The filaments are designed for their physical properties rather than their EM properties. ABS has a relative permittivity, ϵ_r , of ~2.69 and a loss tangent, $\tan \delta$, of ~0.012, while PLA has an ϵ_r of ~2.7 and a $\tan \delta$ of ~0.008 measured at 1 MHz [1]. The dielectric properties were measured with a range of techniques over the frequency range of 2–60 GHz: ABS had an ϵ_r of ~2.45 and a $\tan \delta$ of ~0.005, and PLA had an ϵ_r of ~2.55 and

a $\tan \delta$ of ~0.009 [2]. There are also lower-loss thermoplastics available with similar ϵ_r properties, such as high-impact polystyrene (HIPS), with an ϵ_r of ~2.49 and a $\tan \delta$ of ~8.53 \times 10^{-4} ; polypropylene (PP), with an ϵ_r of ~2.03 and a $\tan \delta$ of ~1.45 \times 10^{-4} ; and cyclo olefin copolymer (COC), with an ϵ_r of ~2.24 and a $\tan \delta$ of ~2.17 \times 10^{-4} , which makes these materials attractive for RF applications. The dielectric properties of a range of different 3D-printable materials as a function of processing temperature and the ϵ_r versus the $\tan \delta$ can be found in [3].

As a general rule with 3D-printed dielectrics, it is important to measure the dielectric properties of test printed samples before fabricating a more complex design, as changes to the printer and its settings can affect the ϵ_r and $\tan \delta$ [4]. It is impossible to achieve a 100% dense part, as air voids always exist between the extruded layers of filament. Changing the printer/printing parameters, such as the nozzle width, extrusion speed, material overlap, layer height and temperatures of the nozzle and testbed, can affect the number of air pockets introduced into the final print, which inevitably affects the realized ϵ_r and $\tan \delta$ values. It is recommended to print a range of samples while varying the printing parameters and measure their physical density and dielectric properties to find the optimum settings for your machine to achieve maximally dense parts and the highest effective permittivity. Structural and EM anisotropy is another aspect that may need to be considered due to the nonisotropic way the filament is extruded. Typically, filament is extruded in parallel lines with alternating layers between a 0 and 90° rotation, which tends to lead to different properties for the axes parallel and perpendicular to the print direction. Depending upon the application, this may need to be factored into the design.

3D-printable filaments are now being developed for their dielectric properties. These are typically manufactured by mixing high-permittivity ceramic additives, such as barium titanate powder, with thermoplastics and extruding them into filaments [5], [6]. They can exhibit an increased ϵ_r but often have higher losses and are more challenging to print. With a higher ceramic content, the filament becomes more brittle, and there is an increased likelihood of nozzle blockages occurring. A ceramic infill is required in a nanoparticulate form for the high ceramic loading to improve the printability and prevent extrusion blockage. Similarly, commercial filaments are available from PREPERM, with an ϵ_r of ~2.9, 4.4, 5.8, 7.6, 9.6, 11.9 and a $\tan \delta$ of ~0.004 at ~2 GHz. Optimizing the printer's settings for maximally dense parts is especially important for these ceramic-loaded filaments since any introduced air pockets will have a greater impact upon the realized ϵ_r value of the print [4]. The challenges to achieve a good quality print, especially for complicated geometries, increase as the ϵ_r increases, as the filaments are designed for their ϵ_r [4]. The dielectric properties and loss tangent values of a range of thermoplastics are plotted in Figure 1.



VAT POLYMERIZATION

The vat polymerization methods of additive manufacturing involve a light source selectively curing photocurable resin in a tank. Since the parts are effectively drawn with light, parts with fine details are possible, though the photocurable resins used often have high loss tangent values. Resin-based photocurable polymer materials for stereolithography were characterized over the frequency range of 0.2–1.4 THz by using time domain spectroscopy; the ϵ_r was ~2.8, and the $\tan \delta$ was ~0.08 [7]. Ceramic-loaded resins are available with higher permittivity and lower loss tangent values achievable; the part can also be fired afterward to burn off the resin and sinter the remaining ceramic powder [8]. Extra consideration of internal voids is needed for vat polymerization since drain holes need to be placed to clear them. Multimaterial prints are difficult to achieve with vat polymerization since multiple vats and intermediate washing stations are required, which increases greatly the complexity and cost of the process. The dielectric properties and loss tangent values of clear and ceramic-loaded resin (after firing) are plotted in Figure 1.

POWDER BED FUSION

The powder bed fusion (PBF) processes involve incrementally filling a tank with a polymer/ceramic/metal powder and using a heat source (typically a laser) to melt the top powder layer to form the part. Once finished, the part is suspended in the unmelted powder in the tank. These machines are several orders of magnitude more expensive than desktop dielectric 3D printers and are also expensive to run and maintain. Porosity

and surface roughness are potential issues of PBF methods, and an understanding of your printing parameters and material is required to minimize these issues [9], [10]. Sand/bead blasting and tumbling are potential postprocessing options available, which could also be used to polish surfaces of these prints and reduce losses. One great advantage with this method is that parts can be printed directly in ceramic and metal, which allows the use of higher-permittivity/lower-loss dielectrics (compared to polymers) and conductors with lower resistivity (compared to conductive inks).

3D PRINTING WITH CERAMICS SLURRIES

Using specialist material processing techniques, it is possible to process and 3D print high-permittivity, low-loss ceramics. One such process is direct ink writing (DIW), which involves extruding viscous ceramic slurries in a similar manner to FFF. The extruded part (known as a *green body*) then undergoes a drying process before it is sintered. With DIW, it has been shown that processing materials with an ϵ_r of ~35 and a $\tan \delta$ of <0.0001 can be achieved [11]. This process can also print with metal slurries alongside ceramics [12], [13], though the thermal expansion coefficients of the two materials need to be matched; otherwise, the green body will warp or crack during sintering. Out of the processes mentioned in this review, ceramics printed with DIW generally deliver the lowest-loss, highest-permittivity materials, with the capability of processing metals close to their bulk conductivity value in the same printed part. The dielectric properties and loss tangent values of a range of low- and high-sintering-temperature ceramics are included in Figure 1.

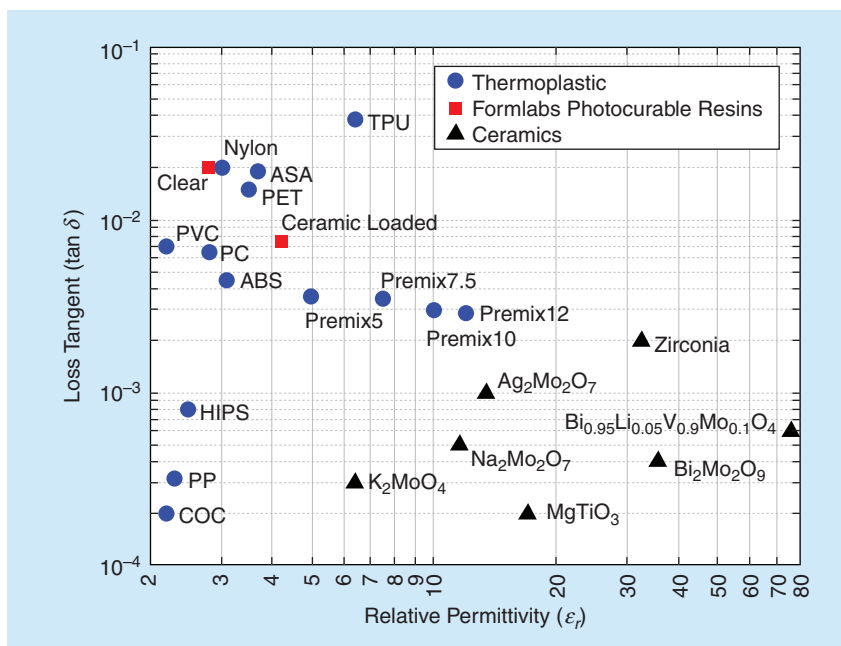


FIGURE 1. The dielectric constant and loss tangent values of various thermoplastics, resins, and ceramic dielectric materials: acrylic styrene acrylonitrile (ASA), ABS, COC, HIPS, polycarbonate (PC), polyethylene terephthalate (PET), polyvinyl chloride (PVC), PP, and thermoplastic polyurethane (TPU). The data were collected from academic literature and split-post dielectric resonator measurements at Loughborough University.

3D PRINTING WITH CONDUCTIVE MATERIALS

Achieving metallized parts can be tricky. Often, the part is printed in a dielectric material first, and metallization is achieved afterward by coating the required regions with a conductive ink/paint [14], [15] or by manually adding copper tape. Large areas of copper tape are easy to add and have good conductivity, while conductive inks/paints tend to have conductivity values lower than that of bulk metals but can be applied to complicated geometries. Since the 3D-printed parts are only for supporting the outer conductive surface, the core structure can be printed using high-resolution printing techniques, such as stereolithography and selective laser sintering (SLS)/melting, to achieve high geometry accuracy and good surface roughness. Surface polishing processes can be applied to the printed parts, such as sand/bead blasting and tumbling,

to further improve the surface roughness that is particularly important for high-frequency applications. These methods are great for research and proving concepts but not necessarily suitable for repeatable and robust mass manufacturing.

An alternative to metalizing the 3D dielectric is to print the structure directly in a metal, which removes one processing step. A conducting commercial FFF-compatible filament, Electrifi, is available, which can be printed as with conventional filaments. The stated conductivity is $\sigma \sim 1.67 \times 10^4$ S/m [1]; however, achieving this value can be challenging in practice. This relatively low conductivity is likely to lead to high losses in antennas; however, the filament could be effective as a shielding material. Electrifi has been used to 3D print RFID tags; ridges in the substrate were introduced to enable some miniaturization, but the read range was reduced from 8 m, with a copper tag, to 2 m, with Electrifi [16]. Electroplating the surface can improve the conductivity by >100 times [17].

An innovative method to create embedded 3D conducting structures was to introduce air channels with an inlet and an exit hole [3] in the 3D-printed structure. These channels were then filled afterward with Field's metal, which has a melting temperature of 65 °C. This method is often compatible with FFF-printed thermoplastic parts, which often have glass transition temperatures at ~100 °C. By using a fine 0.2-mm nozzle, repeatable printing of 0.4-mm channels could be achieved that did not leak. 3D resonant metamaterials were designed in this way [3].

PBF techniques allow the direct printing of metal components; however, surface roughness is a potential issue, which can increase loss. This technique was used to create waveguides and power dividers [18], a lightweight and cost-effective panel antenna in the millimeter waveband [19], a 3D beam scanning leaky wave antenna array at 30 GHz [20], and a wideband circularly polarized (CP) waveguide array antenna consisting of four antipodally ridged elements and a compact feeding network [21]. The example in [19] showed a comparison between a computer numerical control (CNC)-machined antenna and a SLS-printed antenna; on average, the SLS-printed antenna was 11% and 13% less efficient in the K- and Ka-bands, respectively, largely owing to increased surface roughness. The reader should note that accumulated losses associated with physical joins in conventionally manufactured parts (e.g., waveguide flange joins) could be greater than the surface roughness losses of 3D-printed parts since these parts can be printed in one go without the need for

joins. The example also found that the CNC-machined antenna had consistently lower dimensional errors compared to the design than the SLS-printed antenna. These factors illustrate that 3D printing is not a direct replacement for conventional manufacturing techniques, and often, the desired part needs to be optimized for the 3D printing method. As shown in [22], where different 3D printing methods were used to fabricate 3D Hilbert fractal antennas, each method has a tradeoff among cost, weight, physical robustness, and EM performance.

ARTIFICIAL DIELECTRICS

It is well known that if two dielectric materials are mixed, then the mixture forms an artificial dielectric, where the effective properties are likely to be between the two properties of the constituent materials. This holds true as long as the inclusion is much smaller than a wavelength ($l < \lambda/10$) [23]. Subresonant metallic inclusions can also be mixed with a dielectric host material, which will increase the effective permittivity but also reduce the effective permeability. Manufacturing artificial dielectrics is time-consuming to do via conventional manufacturing, but 3D printing naturally lends itself to creating these internal geometries, and the software typically requests a “volume infill percentage” setting for the print. Artificial dielectrics are a simple way of varying the EM material properties across the structure by using only one or two constituent materials [24]. An example of this is a flat graded-index (GRIN) lens, where the dielectric constant was varied across its volume [25]. The choice of infill pattern will also influence the EM performance and may lead to an anisotropic ϵ_r in two axes.

COMPARISON OF 3D PRINTING TECHNIQUES FOR RF APPLICATIONS

Table 1 summarizes the pros and cons of selective 3D printing techniques that have been applied for RF applications. The maximum print volume used to be one of the key factors in choosing the printing technique, but this was negated with the development of new bespoke machines with large build volumes. In addition, large geometries can also be split into multiple small parts to be printed separately [26]. Some of the polymer-based materials can benefit from using compatible solvents to join the bonding surfaces together without leaving extra materials after evaporation and curing. For instance, acetone (propanone) can be used for dissolving ABS material, and

TABLE 1. THE COMPARISON OF DIFFERENT ADDITIVE MANUFACTURING METHODS.

Technique	Resolution (Low, Medium, and High)	Option of Customized Materials	Multimaterial Printing	Metal Printing	Postprocessing
FFF	L to M	Many	Yes	Yes	No
Vat polymerization (e.g., digital light processing, stereolithography, and so on)	Medium to high	Few	No	No	Yes
PBF (SLS and selective laser melting)	Medium to high	Almost none	No	Yes	Yes
DIW	Low to medium	Few	Yes	Yes	Yes
Material jetting (e.g., PolyJet)	Medium to high	Almost none	Yes	No	Yes

D-limonene can be used for HIPS. Figure 2 shows a 3D-printed dielectric transmitarray (TA) that is composed of five parts. The TA was printed using ABS-based materials, and acetone was used for bonding. The bonding surface does not affect the TA performance but provides good mechanical strength.

FFF and DIW allow multimaterial printing using customized RF-graded materials. This is the major advantage of these two techniques even though they do not provide the high resolution of their counterparts. Although FFF and DIW cannot directly print metal as the PBF, they support printing conductive materials, which are equivalent to metal in RF applications. The conductive materials are usually made into paste so that they can be extruded using a nozzle. The extrusion process can be easily integrated into the multimaterial FFF processes. Figure 3(a) demonstrates the process of printing a metacapacitor by using a hybrid FFF printing method [28]. The conductive meta-atoms are printed using silver-based paste and can be fully sealed inside the thermoplastic material. The entire printing process is finished in a single step. Most conductive pastes require curing

to achieve their highest conductivity. In recent years, fast-curing and curing-free conductive pastes have become available. The viscosity of the conductive paste can be increased, so the paste layers can be stacked up with a good vertical wall definition. Figure 3(b) illustrates the printing of superdirective dimers of coupled self-resonant split-ring resonators. The increased height of the split-ring resonators was printed using a curing-free silver-based paste to allow stand-alone tall conductive walls.

Despite not supporting multimaterial printing, vat polymerization and PBF usually offer high-resolution printing, so the surface roughness is visibility finer compared with the FFF-printed surface [shown in Figure 4(a)]. This makes them more popular in high-millimeter-wave and subterahertz applications when compared with FFF. Another advantage of vat polymerization and PBF is being able to print complex overhanging structures. The unfused powder and uncured liquid of the support structures and can be easily removed in postprocessing. Figure 4(b) details an interlaced metamaterial mesh structure that was printed using SLS.

RF COMPONENTS PRINTED WITH PLASTICS

3D-PRINTED LENSES

Dielectric lenses are well-known techniques to alter wavefronts and increase gain. The simplest dielectric lenses are hemispherical in shape and made from homogeneous dielectrics. 3D-printed examples at different frequencies include samples at 10.7 [31], 60 [32], and 120 GHz [33]. At these high frequencies, care needs to be taken, and accurate machines need to be used, or the finished product may have limited accuracy. It was found that a fabrication error of ± 0.127 mm in the lens design led to a phase error of 1.63° at 13.4 GHz [34]. Clearly, these errors will become more significant at higher frequencies. The same paper discusses how the use of geometrical optics can alter the focal point to adjust for misprinted lenses [34].

The same performance can be achieved by varying the local relative permittivity instead of the shape; these are called *GRIN lenses*, as presented in Figure 5. The GRIN lens is composed of a series of concentric rings, where the highest relative permittivity is at the center and the lowest value is at the outer ring [25]. The thickness of the lens is defined by the focal length and maximum relative permittivity of the material. Ideally, the lens should have a smooth variation in the effective permittivity, analogous to the curvature of the hemispherical homogeneous lens. In practice, this is difficult to print, and it has been found that having six rings of varying permittivity is sufficient to emulate a smooth variation and achieve a similar gain to the smooth transition. The design is frequency independent but in practice is limited by the resolution of the printer since air voids that are introduced into the outer rings to lower the effective permittivity will have

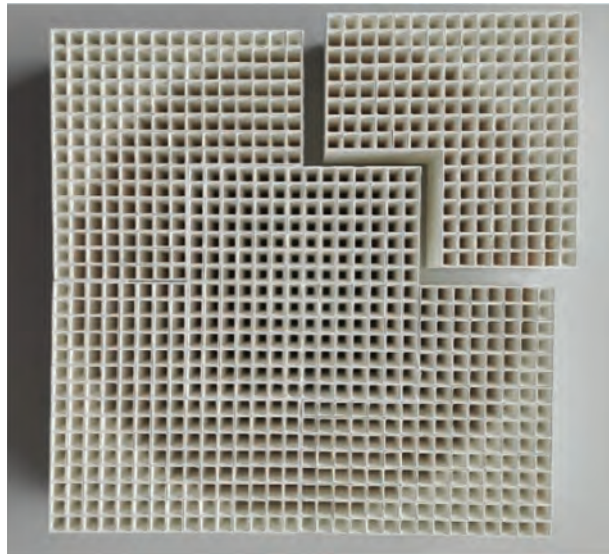


FIGURE 2. A 3D-printed perforated dielectric transmitarray (TA) with total dimensions of $180 \times 180 \times 32$ mm. The entire TA was printed in five parts using PREPERM ABS4.4 and then bonded using acetone. For more information, see [27].

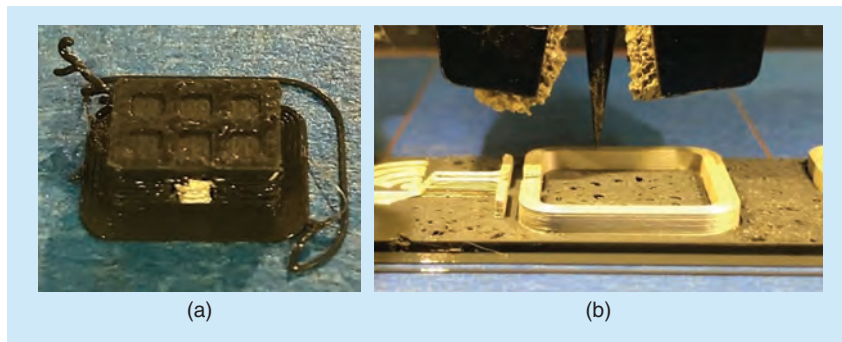


FIGURE 3. Melted thermoplastics and an air-curable silver ink. (a) A 3D metacapacitor before the meta-atoms are printed. (b) Superdirective dimers of coupled self-resonant split-ring resonators. For more information, see [28] and [29].

an inherit resonant frequency. The thickness of the lens can be reduced by starting with a higher relative permittivity of the host material and adding subresonant metallic inclusions to increase the effective permittivity of the artificial dielectric [25]. The losses of the dielectric material do not have a significant impact on the achieved gain of the lens. It is worth noting that using ϵ_r materials may affect the effectiveness of the lens, due to increased reflections as waves transition from air to the lens. A quarter-wavelength matching layer could be used here to improve the impedance mismatch, though this implementation would be frequency limited. GRIN lenses have been placed inside horn antennas to increase the gain [35]. Similarly, the gain of a horn antenna was increased by designing a higher ϵ_r in the middle and an ϵ_r close to air (by minimizing the volume fraction of the 3D-printed filament) at the edges of the circular horn antenna [36]. Integrating lenses into the antenna structure is an attractive use since the required focal length normally increases the size of the antenna system. In a related area, horn antennas have been filled with 3D-printed materials for biomedical applications. The aim was not to increase the gain but to match the impedance of the antenna to the human body to minimize reflections at the interface between air and body [37], [38], [39].

Another common alternative lens configuration is the Fresnel lens, where grooved concentric rings shape the wavefront of the illuminating beam; these lens designs are thinner and lighter than hemispherical lenses. 3D printing also provides the option of varying the local shape and local effective permittivity to make a hybrid lens, which further increases the gain of the lens [40]. By printing a block with two different relative permittivity values, where the ϵ_r varies locally, it is possible to engineer lenses with advanced capability. For example, a bifocal lens was designed, 3D printed, and measured, where the incident wave was directed in two different directions at two different frequencies [41]. The complex internal geometry was composed of two different dielectric materials that were topologically optimized, which could not have been achieved using conventional manufacturing techniques.

Conventionally, we use lenses to increase the gain of the antenna system. However, it is possible to design lenses that increase the beamwidth and hence reduce the maximum gain. An example of this used a 3D-printed lens to increase the 3-dB axial ratio beamwidth from 82 to 162° of a CP antenna [42]. This lens functioned over a wide bandwidth. Using a lens to increase the gain of the antenna is attractive, but often, the system

architecture requires the ability to steer the beam. This is achieved by changing the feeding position relative to the lens. The most common examples of lenses used to achieve beam steering are Luneburg lenses (LLs) [43], [44], [45], [46]. 3D printing allows the lens to be tailor-made by using dual materials and varied local ϵ_r increases. A spherical LL was converted into an ellipsoidal shape via transformation optics to increase the lens' aperture efficiency [44]. By carefully designing the shape and varying the local ϵ_r by using the 3D printing degrees of freedom, it was possible to minimize the size requirements and number of feeds required [44].

POLARIZATION CONVERTERS

Efficient polarizers can be produced by 3D printing anisotropic structures; for example, a dielectric slab with rectangular slots of air orientated at 45° to the electric fields can convert a linearly polarized beam into a CP beam [48]. The performance is wideband, and the limiting factor is when the width of the slots/dielectric strips approaches a wavelength. 3D printing also facilitates the combination of polarizer functionality with a lens design to create a single device [49], [50]. In [50], the functionality of Wollaston and Rochon prisms was integrated into 3D-printed lenses to generate and separate left- and right-handed CP beams at 30 GHz. The required phase change was introduced by changing the physical geometry of the unit cells.

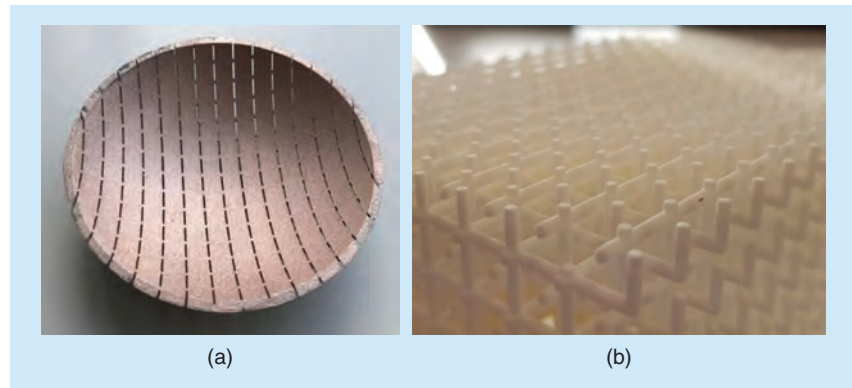


FIGURE 4. (a) A conductive coated conformal frequency-selective surface (FSS). The FSS was printed using stereolithography to achieve a lower surface roughness. (b) 3D-printed interlaced metamaterial meshes using SLS. For more information, see [15] and [30].

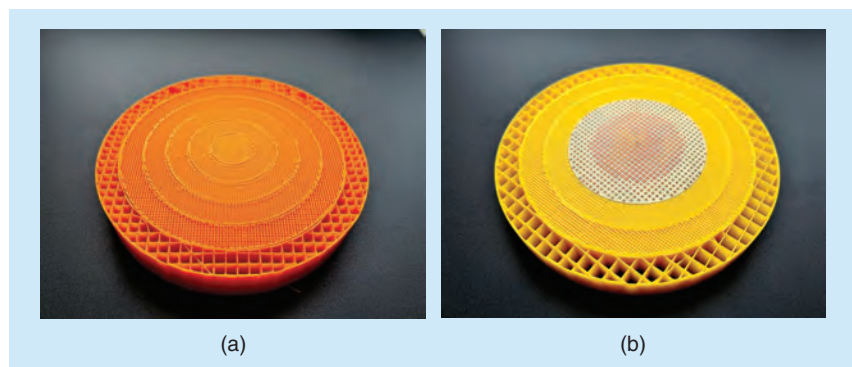


FIGURE 5. Two variations of a GRIN lens, where the dielectric properties are varied across the lens' radii. (a) A purely dielectric GRIN lens printed from ABS. (b) A GRIN lens printed from ABS with an added artificial dielectric disk providing an increased dielectric constant in the center. For more information, see [25] and [47].

Anisotropy has also been shown to create circular polarization when placed in the cavity of a Fabry-Pérot resonator antenna [51]. The 3D-printed metamaterial facilitated independent control of the axial ratio and directivity by controlling the phase difference in the standing waves of the two orthogonal electric field components inside the cavity. This paper also allowed the user to choose between linear polarization and circular polarization by mechanically rotating the metamaterial with respect to the antenna [51].

RAs

RAs are often popular in satellite applications, given their low-cost, low-profile, and high-gain characteristics. Typically, RAs are constructed from circuit board substrates and consist of an array of metallic resonators backed by a ground plane. A horn is often used to feed the RA and is offset from the center so as to not interfere with the reflection. However, narrow bandwidths and ohmic/surface wave losses are associated with the metallic elements; to avoid this, dielectric resonators have been explored [52], [53], [54], [55]. With 3D printing, low-profile 3D RAs can be realized.

The first reported FFF 3D-printed RA provided a high gain (20–28 dBi) over a wide bandwidth (26–34 GHz) [52]; see Figure 6(a). The 3D-printed structure contained 625 unit cells over the 12 × 12-cm surface. A phase response from 0 to 360° was achieved by varying the width of each dielectric element; therefore, the required phase distribution map can be converted into the CAD model to print. Similarly, unit cells with two orthogonal cuboids can also be used to convert a linearly polarized wave into a CP wave [53]; see Figure 6(b). By exploiting the extra degree of freedom, the width and height of both orthogonal cuboids were varied to change the orthogonal characteristics of the unit cells. This took extensive optimization via simulations and patient printing to create the delicate vertical architectures. Similar concepts have been used to generate four orbital angular momentum (OAM) modes at 30 GHz [54]. OAM is a growing research area, where multiple OAM modes can be carried in the same channel without interference, which can potentially increase channel capacity.

So far, the examples given all require a conductive ground plane to provide reflection, which suffers from ohmic losses.

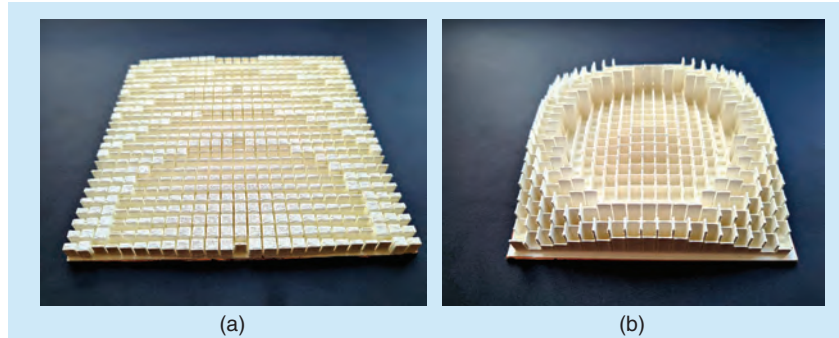


FIGURE 6. RAs that were 3D printed from thermoplastic filaments, with (a) a thermoplastic ϵ_r value of 4.4, where the effective permittivity of each unit cell was varied by changing the inclusion width, and (b) a thermoplastic ϵ_r value of 7.4, where the effective permittivity of the unit cells was varied by changing the inclusion height. For more information, see [52] and [53].

Using a dielectric mirror, an all-dielectric RA was 3D printed [55]. Layers of dielectric slabs separated by air gaps were used to create a dielectric mirror with bandgaps in the V- and K-bands. As the frequency increases, the reflections at each interface interfere with one another and can cause total reflections. Outside the bandgap, the structure is transparent to EM waves. The PLA and air thicknesses were 1.5 and 3 mm at 18–27 GHz and 0.8 and 1 mm at 40–75 GHz. By using multiple layers, a dual-band device was 3D printed [55].

DIELECTRIC RESONATOR ANTENNAS

Dielectric resonator antennas (DRAs) typically require materials with relative permittivity values on the order of 10–20. With new developments in thermoplastic–ceramic composite filaments for RF applications, 3D printing DRAs is possible. The efficiency of DRAs is highly dependent on the loss tangents of the materials. DRAs typically have homogenous structures that are simple geometric shapes. This is partly due to limitations of conventional manufacturing techniques. 3D printing may not be the optimal manufacturing route for DRAs, but it can provide a quick fabrication route, with extra degrees of freedom in terms of the shape and including heterogeneous properties. The bandwidth-versus-the-maximum-gain tradeoff has been analyzed via hundreds of simulations in [56].

3D printing was used to print a DRA that was composed of series of rings, with the highest ϵ_r at the center. The ϵ_r values were 10, 8.25, four, and 2.5 and were all 3D printed from one material by varying the local volume fraction of air. This design combined the transverse magnetic (TM) modes (TM01 δ , TM02 δ , and TM03 δ) to create a wide impedance bandwidth. Changing the 3D-printed infill fraction was also used to create a DRA with two effective dielectric regions. It was found that by increasing the air volume fraction in certain locations and including a metal cap to compensate for the frequency shift, the weight of the DRA could be reduced by 22% [57].

3D PRINTED CERAMIC COMPONENTS

3D printing ceramics involves expensive equipment (which includes the 3D printer and a furnace) and expert knowledge in materials. For these reasons, it is easier (and often quicker) to produce components with thermoplastics and resins. However, processing ceramics opens the possibility of higher-permittivity and lower-loss materials, higher temperature and power handling capabilities of the printed parts, and the potential for printing metal pastes.

A relatively easy method of manufacturing ceramic parts is the vat polymerization method with a preformulated ceramic-loaded resin. The resulting structure can then undergo rebinding and sintering to remove the resin and fuse the ceramic powder together.

Published examples include an LL manufactured from MgTiO_3 [58], an anisotropic CP DRA [59], and a dielectric CP helical antenna manufactured from zirconia [60].

Through process such as DIW, ceramics and metals can be printed together in the same component; however, this is a growing research area that faces considerable challenges of material compatibility and component warping due to unmatched thermal expansion coefficients. Current works demonstrate the potential of transmission lines and ring resonators printed on high-permittivity ceramics [13] in addition to miniaturized patch antennas by fully embedding the resonating patch in the ceramic [12]; an example is given in Figure 7.

METALIZED WAVEGUIDES AND HORN ANTENNAS

There have been many papers in recent years that have used 3D printing of dielectrics that are then electro- or electroless plated to form metal devices for RF applications. These are often waveguides and horn antennas, and the aim is to replicate the behavior of the fully metal version with a reduced manufacturing time and weight. The latter has particular relevance for the aviation and space industries [61]. There is a tradeoff in the optimal frequency of applications: at low frequencies, the metallization may not be thick enough to contain enough skin depths, whereas at higher frequencies, the surface roughness of the printed layers becomes a problem unless further postprocessing is implemented. The ease of manufacturing more complicated shapes allows the RF designer to imagine innovative designs that would be difficult with conventional subtractive techniques. Examples of these designs include a 3D helical antenna with nested tapered helices (2.4 and 5.4 GHz) [62], a cavity-backed slot antenna (4.8–7.5 GHz) [63], a coax-to-waveguide transition (8 GHz) [14], a 3D-printed Ku-band four-element steerable phased-array antenna with a fully integrated beam forming network [64], an ultrawideband Vivaldi antenna (10–15 GHz) taking advantage of its 3D shape to increase the bandwidth [65], a corrugated horn (11–13 GHz) [66], a K-band array antenna with waveguides that include water channels for cooling for high-power devices [67], a turnstile junction orthomode transducer for polarization separation in a waveguide (75–110 GHz) [68], and rectangular horn antennas, parabolic mirrors, and polarizers at 140–220 GHz [69].



FIGURE 7. A 3D-printed DIW metal–ceramic microstrip patch with silver and a high-permittivity, low-loss, and low-sintering-temperature ceramic ($\text{Ag}_2\text{Mo}_2\text{O}_7$). For more information, see [12].

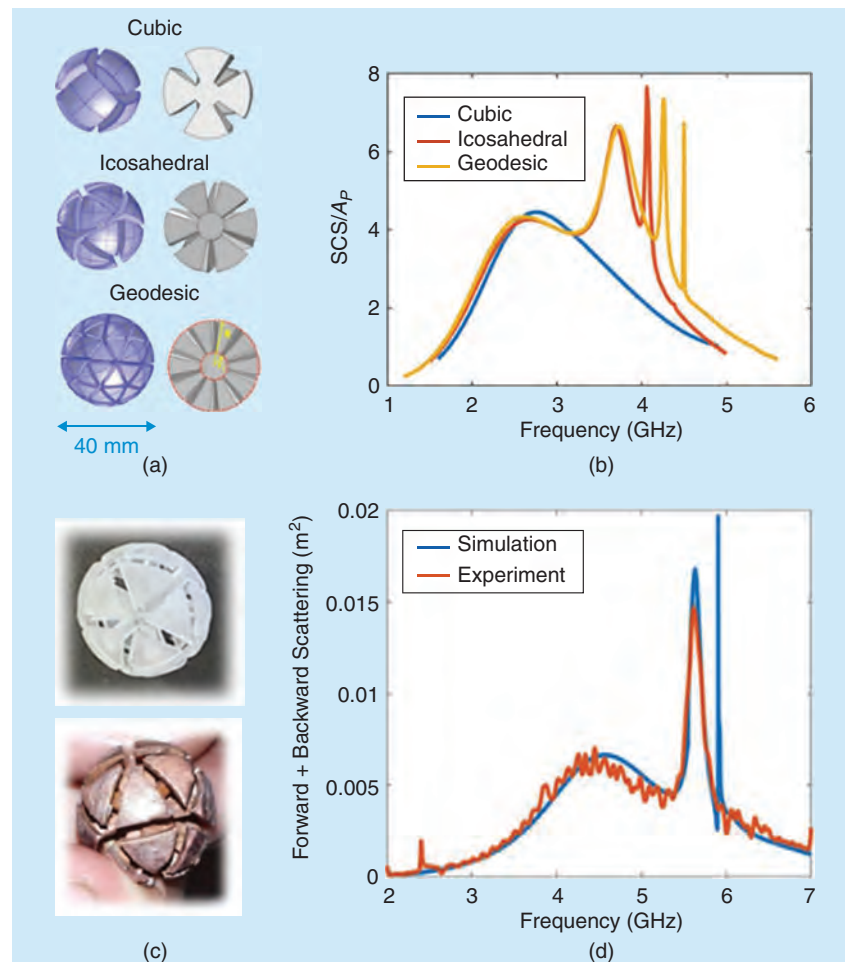


FIGURE 8. (a) The scattering cross section and electric near field of the first two modes of a metacube made from three crossed rods with square plates. (b) The scattering cross section and electric near field of the first two modes of a meta-icosahedron made from 10 crossed rods with triangular plates. (c) An experimental demonstration of scattering: the radar cross section of the particles measured in the forward and reverse directions compared with simulations on Comsol. Inset: 3D-printed samples of icosahedra electroplated in copper (some plates have been removed to reveal the interior structure). (d) The simulated scattering cross section of the meta-icosahedron in (b) and an equivalently sized spherical particle made of a Drude metal, with a plasma frequency determined by the rod-and-plate structure.

METAPARTICLES FOR ISOTROPIC MULTIMODE MICROWAVE SCATTERING

Control over the scattering behavior of EM waves is key for applications from antenna design [70], [71] to energy harvesting [72] to radar detection [73]. Subwavelength scatterers are an attractive means to achieve this due to their powerful scattering of radiation at their resonance condition and their small physical size. Metallic nanoparticles create a powerful scattering effect at optical frequencies by coupling free electrons oscillations at the surface of the metal with the electric field of incident radiation, an effect known as a *surface plasmon*. However, this behavior depends on electric field penetration into the particle since at microwave frequencies, metals are near-perfect electrical conductors, the fields are almost perfectly screened, and the powerful scattering due to surface plasmons cannot be excited.

It has been shown that the texturing of a metal surface can lead to the excitation of surface waves that mimic this plasmon behavior (“spoo” plasmons) [74], [75], [76], but these effects have been mostly limited to 2D metasurfaces and extrusions of 2D shapes. 3D metaparticles that can convincingly mimic this behavior have proved difficult to realize, and previous works attempting to reproduce these effects have been limited in both the functionality of their design and the performance of fabricated samples, due to available manufacturing methods [73], [77], [78], [79].

3D printing has enabled the scalable fabrication of complex metaparticles that can fully reproduce the powerful scattering of plasmonic nanoparticles at microwave frequencies. Spheres with a textured outer layer with symmetries based on the platonic solids [depicted in Figure 8(a)] are shown to powerfully scatter EM radiation in a manner comparable to that of metal nanoparticles at optical frequencies. The number of modes the particle can support is determined by the patterning of the particle outer layer, as shown in Figure 8(b), enabling control over the scattering power, bandwidth, and directionality (as higher-order resonances scatter more powerfully in the forward direction) simply by choosing the number and dimensions of grooves in identical metal spheres. Spheres with patterning corresponding to the highest-order platonic solid (the icosahedron) were 3D printed through vat polymerization (stereolithography) and then metalized via electroplating; both unplated and copper-plated metaparticles are presented in Figure 8(c). These particles can be shown to support three modes, which correspond to the dipole, quadrupole, and octupole plasmonic resonances. Experimental measurements of the forward and backward scattering of these particles in an anechoic chamber show excellent agreement with the simulations, as in Figure 8(d), and have applications in superdirective antennas and control over radar scattering.

CONCLUSIONS

3D printing of microwave components is a fast-growing research topic, as additive manufacturing provides many versatile methods of manufacturing components. 3D printing is ideal for low-midscale production of high-value components when conventional manufacturing techniques are not suitable. FFF is the most accessible method of 3D printing, as the machines

are relevantly inexpensive and there is a wide range of easily accessible materials. Other methods, such as vat polymerization and PBF, are capable of much finer resolutions but are not capable of multimaterial printing. Ceramic and metal printing are achievable with PBF and ceramic/metal powders and with DIW and ceramic slurries/metal pastes. Naturally, printing with ceramics and metals will lead to parts with lower dielectric and conductive losses; however, the manufacturing complexity increases since these parts often need to be fired/sintered in a second process. Additional information and links can be found in the supplementary information available at <https://www.doi.org/10.1109/MAP.2022.3229298>.

ACKNOWLEDGMENT

This work was supported by Engineering and Physical Sciences Research Council grants “Synthesizing 3D Metamaterials for Radio-Frequency, Microwave, and Terahertz Applications” (EP/N010493/1) and “Anisotropic Microwave/Terahertz Metamaterials for Satellite Applications” (EP/S030301/1). This article has supplementary information, provided by the authors, available at <https://www.doi.org/10.1109/MAP.2022.3229298>.



AUTHOR INFORMATION

Thomas Whittaker (t.whittaker@lboro.ac.uk) is a research associate with the Wolfson School of Mechanical, Electrical, and Manufacturing Engineering, Loughborough University, Loughborough LE11 3TU U.K. His research interests include 3D-printed microwave components and circuits, material characterization, metasurfaces, satellite communications, and anisotropy.

Shiyu Zhang (s.zhang@lboro.ac.uk) is with the Wolfson School of Mechanical, Electrical, and Manufacturing Engineering, Loughborough University, Loughborough LE11 3TU U.K. His research interests include engineered metamaterials, metasurfaces, frequency-selective surfaces, antennas and radio-frequency circuit components, additive manufacturing, and wearable antennas.

Alexander Powell (a.w.powell@exeter.ac.uk) is a research fellow in the Department of Physics and Astronomy, University of Exeter, Exeter EX4 4PY U.K. His research interests include developing novel 3D scattering particles (meta-atoms), which have example use cases in superdirective antennas, lenses, and superscatterers.

Chris J. Stevens (chris.stevens@eng.ox.ac.uk) is a professor in the Department of Engineering Science, University of Oxford,

Oxford OX1 3PJ U.K. His research interests include ultrawideband communications, metamaterials, ultrafast nanoelectronics, high-speed electromagnetics, and magnetic metamaterials.

John (Yiannis) C. Vardaxoglou (j.c.vardaxoglou@lboro.ac.uk) is a professor in the Wolfson School of Mechanical, Electrical, and Manufacturing Engineering, Loughborough University, Loughborough LE11 3TU U.K, where he established the Wireless Communications Research Group. He has been awarded 20 research grants and published more than 400 journal and conference papers. He is a Fellow of IEEE.

William Whittow (w.g.whittow@lboro.ac.uk) is a professor of radio-frequency materials at Loughborough University, Loughborough LE11 3TU U.K, where he leads the Wireless Communications Research Group. He has the principal investigator on £14 million of research grants and authored more than 280 journal and conference papers. He is a Senior Member of IEEE.

REFERENCES

- [1] D. Helena, A. Ramos, T. Varum, and J. N. Matos, "Antenna design using modern additive manufacturing technology: A review," *IEEE Access*, vol. 8, pp. 177,064–177,083, Sep. 2020, doi: 10.1109/ACCESS.2020.3027383.
- [2] C.-K. Lee et al., "Evaluation of microwave characterization methods for additively manufactured materials," *Designs*, vol. 3, no. 4, Sep. 2019, Art. no. 47, doi: 10.3390/designs3040047.
- [3] C. J. Stevens, I. Spanos, A. Vallecchi, J. McGhee, and W. Whittow, "3D printing of functional metal and dielectric composite meta-atoms," *Small*, vol. 18, no. 10, pp. 1–9, Jan. 2022, doi: 10.1002/smll.202105368.
- [4] T. Goulas et al., "The impact of 3D printing process parameters on the dielectric properties of high permittivity composites," *Designs*, vol. 3, no. 4, Nov. 2019, Art. no. 50, doi: 10.3390/designs3040050.
- [5] P. S. Grant et al., "Manufacture of electrical and magnetic graded and anisotropic materials for novel manipulations of microwaves," *Philos. Trans. A*, vol. 373, no. 2049, Aug. 2015, Art. no. 20140353, doi: 10.1098/rsta.2014.0353.
- [6] F. Castles et al., "Microwave dielectric characterisation of 3D-printed BaTiO₃/ABS polymer composites," *Scientific Rep.*, vol. 6, no. 1, Mar. 2016, Art. no. 22714, doi: 10.1038/srep22714.
- [7] N. Duangrit et al., "Terahertz dielectric property characterization of photo-polymer for additive manufacturing," *IEEE Access*, vol. 7, pp. 12,339–12,347, Jan. 2019, doi: 10.1109/ACCESS.2019.2893196.
- [8] W. Nawrot and K. Malecha, "Additive manufacturing revolution in ceramic microsystems," *Microelectron. Int.*, vol. 37, no. 2, pp. 79–85, May 2020, doi: 10.1108/MI-11-2019-0073.
- [9] J. C. Snyder and K. A. Thole, "Understanding laser powder bed fusion surface roughness," *J. Manuf. Sci. Eng.*, vol. 142, no. 7, Jul. 2020, Art. no. 071003, doi: 10.1115/1.4046504.
- [10] O. A. Peverini et al., "Selective laser melting manufacturing of microwave waveguide devices," *Proc. IEEE*, vol. 105, no. 4, pp. 620–631, Apr. 2017, doi: 10.1109/JPROC.2016.2620148.
- [11] A. Goulas et al., "Microstructure and microwave dielectric properties of 3D printed low loss Bi₂Mo₂O₉ ceramics for LTCC applications," *Appl. Mater. Today*, vol. 21, Dec. 2020, Art. no. 100862, doi: 10.1016/j.apmt.2020.100862.
- [12] A. Goulas et al., "Additively manufactured ultra-low sintering temperature, low loss Ag₂Mo₂O₇ ceramic substrates," *J. Eur. Ceram. Soc.*, vol. 41, no. 1, pp. 394–401, Jan. 2021, doi: 10.1016/j.jeurceramsoc.2020.08.031.
- [13] R. Cheisari et al., "Multi-material additive manufacturing of low sintering temperature Bi₂Mo₂O₉ ceramics with Ag floating electrodes by selective laser burnout," *Virtual Phys. Prototyping*, vol. 15, no. 11, pp. 1–15, Jan. 2020, doi: 10.1080/17452759.2019.1708026.
- [14] C. Guo et al., "A 3-D printed \$E\$-plane waveguide magic-T using air-filled coax-to-waveguide transitions," *IEEE Trans. Microw. Theory Techn.*, vol. 67, no. 12, pp. 4984–4994, Dec. 2019, doi: 10.1109/TMTT.2019.2944355.
- [15] H. F. Álvarez et al., "3D conformal bandpass millimeter-wave frequency selective surface with improved fields of view," *Scientific Rep.*, vol. 11, no. 1, Dec. 2021, Art. no. 12846, doi: 10.1038/s41598-021-91218-y.
- [16] R. Colella, F. P. Chietera, F. Montagna, A. Greco, and L. Catarinucci, "Customizing 3D-printing for electromagnetics to design enhanced RFID antennas," *IEEE J. Radio Freq. Identif.*, vol. 4, no. 4, pp. 452–460, Dec. 2020, doi: 10.1109/jrfid.2020.3001043.
- [17] M. J. Kim et al., "One-step electrodeposition of copper on conductive 3D printed objects," *Additive Manuf.*, vol. 27, pp. 318–326, May 2019, doi: 10.1016/j.addma.2019.03.016.
- [18] F. Sun, Y. Li, L. Ge, and J. Wang, "Millimeter-wave magneto-electric dipole antenna array with a self-supporting geometry for time-saving metallic 3-D printing," *IEEE Trans. Antennas Propag.*, vol. 68, no. 12, pp. 7822–7832, Dec. 2020, doi: 10.1109/TAP.2020.3016158.
- [19] M. Ferrando-Rocher, J. I. Herranz-Herruzo, A. Valero-Nogueira, and B. Bernardo-Clemente, "Selective laser sintering manufacturing as a low cost alternative for flat-panel antennas in millimeter-wave bands," *IEEE Access*, vol. 9, pp. 45,721–45,729, Mar. 2021, doi: 10.1109/ACCESS.2021.3067637.
- [20] J. Cao, H. Wang, S. Tao, S. Mou, and Y. Guo, "Highly integrated beam scanning groove gap waveguide leaky wave antenna array," *IEEE Trans. Antennas Propag.*, vol. 69, no. 8, pp. 5112–5117, Aug. 2021, doi: 10.1109/TAP.2020.2995470.
- [21] J. Wu, C. Wang, and Y. Guo, "A wideband circularly polarized array antenna with compact and high-efficiency feeding network," *IEEE Trans. Antennas Propag.*, vol. 68, no. 1, pp. 62–69, Jan. 2020, doi: 10.1109/TAP.2019.2935093.
- [22] K. Johnson et al., "Digital manufacturing of pathologically-complex 3D printed antennas," *IEEE Access*, vol. 7, pp. 39,378–39,389, Mar. 2019, doi: 10.1109/ACCESS.2019.2906868.
- [23] L. Lewin, "The electrical constants of a material loaded with spherical particles," *Proc. Inst. Electr. Eng.*, vol. 94, no. 27, pp. 65–68, Jan. 1947, doi: 10.1049/ji-3-2.1947.0013.
- [24] S. Zhang, W. Whittow, and J. C. Vardaxoglou, "Additively manufactured artificial materials with metallic meta-atoms," *IET Microw., Antennas Propag.*, vol. 11, no. 14, pp. 1955–1961, Nov. 2017, doi: 10.1049/iet-map.2016.0952.
- [25] S. Zhang, R. K. Arya, W. G. Whittow, D. Cadman, R. Mittra, and J. C. Vardaxoglou, "Ultra-wideband flat metamaterial GRIN lenses assisted with additive manufacturing technique," *IEEE Trans. Antennas Propag.*, vol. 69, no. 7, pp. 3788–3799, July 2021, doi: 10.1109/TAP.2020.3044586.
- [26] Y. Rahmat-Samii, J. Budhu, R. E. Hodges, D. C. Hofmann, and D. Rufatto, "A novel 60-cm nonpherical 3-D printed voxelized lens antenna: Design, fabrication and measurement," in *Proc. IEEE Int. Symp. Antennas Propag. USNC-URSI Radio Sci. Meeting*, Jul. 2019, pp. 1699–1700, doi: 10.1109/APUSNCURSINRSM.2019.8889115.
- [27] A. Massaccesi, P. Pirinoli, and J. C. Vardaxoglou, "A multilayer unit-cell for perforated dielectric transmitarray antennas," in *Proc. IEEE Int. Symp. Antennas Propag. USNC-URSI Nat. Radio Sci. Meeting*, 2019, pp. 263–264, doi: 10.1109/APUSNCURSINRSM.2018.8605712.
- [28] T. W. Whittaker, W. G. Whittow, and J. C. Vardaxoglou, "Artificially engineered capacitors for discrete high-frequency electronic circuitry," *IEEE Trans. Microw. Theory Techn.*, vol. 68, no. 1, pp. 74–86, Jan. 2020, doi: 10.1109/TMTT.2019.2950224.
- [29] A. Vallecchi, A. Radkovskaya, L. Li, G. Faulkner, C. J. Stevens, and E. Shamona, "Superdirective dimers of coupled self-resonant split ring resonators: Analytical modelling and numerical and experimental validation," *Scientific Rep.*, vol. 10, no. 1, Dec. 2020, Art. no. 274, doi: 10.1038/s41598-019-56988-6.
- [30] A. W. Powell, R. C. Mitchell-Thomas, S. Zhang, D. A. Cadman, A. P. Hibbins, and J. R. Sambles, "Dark mode excitation in three-dimensional interlaced metallic meshes," *ACS Photon.*, vol. 8, no. 3, pp. 841–846, Mar. 2021, doi: 10.1021/acphotonics.0c01811.
- [31] T. Hayat, M. U. Afzal, A. Lalbakhsh, and K. P. Esselle, "3-D-printed phase-rectifying transparent superstrate for resonant-cavity antenna," *IEEE Antennas Wireless Propag. Lett.*, vol. 18, no. 7, pp. 1400–1404, Jul. 2019, doi: 10.1109/LAWP.2019.2917767.
- [32] A. Bisognin et al., "Ball grid array-module with integrated shaped lens for WiGig applications in eyewear devices," *IEEE Trans. Antennas Propag.*, vol. 64, no. 3, pp. 872–882, Mar. 2016, doi: 10.1109/TAP.2016.2517667.
- [33] S. Ooms and P. Reynaert, "A 120-CHz wireless link using 3D-printed lens with flexible dielectric fiber feed and 28-nm CMOS transceiver," *IEEE Solid-State Circuits Lett.*, vol. 3, no. 1, pp. 142–145, Jul. 2020, doi: 10.1109/LSSC.2020.3008224.
- [34] J. Budhu and Y. Rahmat-Samii, "3D-printed inhomogeneous dielectric lens antenna diagnostics: A tool for assessing lenses misprinted due to fabrication tolerances," *IEEE Antenna Propag. Mag.*, vol. 62, no. 4, pp. 49–61, Aug. 2020, doi: 10.1109/MAP.2019.2946566.
- [35] K. V. Hoel, M. Ignatenko, S. Kristoffersen, E. Lier, and D. S. Filipovic, "3-D printed monolithic GRIN dielectric-loaded double-ridged horn antennas," *IEEE Trans. Antennas Propag.*, vol. 68, no. 1, pp. 533–539, Jan. 2020, doi: 10.1109/TAP.2019.2938563.
- [36] S. Zhang, D. Cadman, and J. C. Vardaxoglou, "Additively manufactured profiled conical horn antenna with dielectric loading," *IEEE Antennas Wireless Propag. Lett.*, vol. 17, no. 11, pp. 2128–2132, Nov. 2018, doi: 10.1109/LAWP.2018.2871029.
- [37] S. Rashid et al., "3-D printed UWB microwave bodyscope for biomedical measurements," *IEEE Antennas Wireless Propag. Lett.*, vol. 18, no. 4, pp. 626–630, Apr. 2019, doi: 10.1109/LAWP.2019.2899591.

- [38] S. Sarjogian, Y. Alfadhl, X. Chen, and C. G. Parini, "A 3-D-printed high-dielectric materials-filled pyramidal double-ridged horn antenna for abdominal fat measurement system," *IEEE Trans. Antennas Propag.*, vol. 69, no. 1, pp. 64–73, Jan. 2021, doi: 10.1109/TAP.2020.3008653.
- [39] S. Sarjogian, M. H. Sagor, Y. Alfadhl, and X. Chen, "A 3D-printed high-dielectric filled elliptical double-ridged horn antenna for biomedical monitoring applications," *IEEE Access*, vol. 7, pp. 94,977–94,985, Jul. 2019, doi: 10.1109/ACCESS.2019.2928629.
- [40] S. Zhang, P. Liu, and W. Whittow, "Design and fabrication of 3-D-printed high-gain broadband Fresnel zone lens using hybrid groove-perforation method for millimeter-wave applications," *IEEE Antennas Wireless Propag. Lett.*, vol. 21, no. 1, pp. 34–38, Jan. 2022, doi: 10.1109/LAWP.2021.3116459.
- [41] B. Vial, T. Whittaker, S. Zhang, W. G. Whittow, and Y. Hao, "Optimization and experimental validation of a bi-focal lens in the microwave domain," *AIP Adv.*, vol. 12, no. 2, Feb. 2022, Art. no. 025103, doi: 10.1063/5.0074062.
- [42] C. Mu, S. Fang, H. Liu, Z. Wang, and S. Fu, "3-D-printed dielectric lens with cone-shaped cavity for axial ratio beamwidth enhancement of circularly polarized patch antenna," *IEEE Access*, vol. 7, pp. 105,062–105,071, Jul. 2019, doi: 10.1109/ACCESS.2019.2931938.
- [43] Y. Li, L. Ge, M. Chen, Z. Zhang, Z. Li, and J. Wang, "Multibeam 3-D-printed Luneburg lens fed by magnetoelectric dipole antennas for millimeter-wave MIMO applications," *IEEE Trans. Antennas Propag.*, vol. 67, no. 5, pp. 2923–2933, May 2019, doi: 10.1109/TAP.2019.2899013.
- [44] C. Wang, Y. Xia, G. Guo, M. Nasir, and Q. Zhu, "Ellipsoidal Luneburg lens binary array for wide-angle scanning," *IEEE Trans. Antennas Propag.*, vol. 68, no. 7, pp. 5702–5707, Jul. 2020, doi: 10.1109/TAP.2020.2969875.
- [45] C. Wang, J. Wu, and Y.-X. Guo, "A 3-D-printed wideband circularly polarized parallel-plate Luneburg lens antenna," *IEEE Trans. Antennas Propag.*, vol. 68, no. 6, pp. 4944–4949, Jun. 2020, doi: 10.1109/TAP.2019.2955222.
- [46] K. Liu, C. Zhao, S. W. Qu, Y. Chen, J. Hu, and S. Yang, "A 3-D-printed multi-beam spherical lens antenna with ultrawide-angle coverage," *IEEE Antennas Wireless Propag. Lett.*, vol. 20, no. 3, pp. 411–415, Mar. 2021, doi: 10.1109/LAWP.2021.3054042.
- [47] S. Zhang, R. K. Arya, S. Pandey, Y. Vardaxoglou, W. Whittow, and R. Mittra, "3D-printed planar graded index lenses," *IET Microw., Antennas Propag.*, vol. 10, no. 13, pp. 1411–1419, Oct. 2016, doi: 10.1049/iet-map.2016.0013.
- [48] Q.-Y. Guo, Q. W. Lin, and H. Wong, "A high gain millimeter-wave circularly polarized Fabry-Pérot antenna using PRS-integrated polarizer," *IEEE Trans. Antennas Propag.*, vol. 69, no. 2, pp. 1179–1183, Feb. 2021, doi: 10.1109/TAP.2020.3001110.
- [49] G.-B. Wu, Y.-S. Zeng, K. F. Chan, S.-W. Qu, and C. H. Chan, "3-D printed circularly-polarized lens antenna operating at terahertz frequencies," in *Proc. URSI Int. Symp. Electromagn. Theory (EMTS)*, 2019, vol. 67, no. 7, pp. 4429–4437, doi: 10.23919/URSI-EMTS.2019.8931543.
- [50] J. Zhu et al., "3-D printed planar dielectric linear-to-circular polarization conversion and beam-shaping lenses using coding polarizer," *IEEE Trans. Antennas Propag.*, vol. 68, no. 6, pp. 4332–4343, Jun. 2020, doi: 10.1109/TAP.2020.2972625.
- [51] F. Wu and K. M. Luk, "Circular polarization and reconfigurable of Fabry-Pérot resonator antenna through metamaterial-loaded cavity," *IEEE Trans. Antennas Propag.*, vol. 67, no. 4, pp. 2196–2208, Apr. 2019, doi: 10.1109/TAP.2019.2893213.
- [52] S. Zhang, "Three-dimensional printed millimetre wave dielectric resonator reflectarray," *IET Microw., Antennas Propag.*, vol. 11, no. 14, pp. 2005–2009, Nov. 2017, doi: 10.1049/iet-map.2017.0278.
- [53] Q. Cheng et al., "Dual circularly polarized 3-D printed broadband dielectric reflectarray with a linearly polarized feed," *IEEE Trans. Antennas Propag.*, vol. 70, no. 7, pp. 5393–5403, Jul. 2022, doi: 10.1109/TAP.2022.3142735.
- [54] B. Li, P. F. Jing, L. Q. Sun, K. W. Leung, and X. Lv, "3D printed OAM reflectarray using half-wavelength rectangular dielectric element," *IEEE Access*, vol. 8, pp. 142,892–142,899, Aug. 2020, doi: 10.1109/ACCESS.2020.3013678.
- [55] J. Zhu, Y. Yang, D. McGloin, S. Liao, and Q. Xue, "3-D printed all-dielectric dual-band broadband reflectarray with a large frequency ratio," *IEEE Trans. Antennas Propag.*, vol. 69, no. 10, pp. 7035–7040, Oct. 2021, doi: 10.1109/TAP.2021.3076528.
- [56] E. B. Whiting, S. D. Campbell, G. Mackertich-Sengerdy, and D. H. Werner, "Dielectric resonator antenna geometry-dependent performance tradeoffs," *IEEE Open J. Antennas Propag.*, vol. 2, pp. 14–21, 2021, doi: 10.1109/ojap.2020.3037826.
- [57] M. Cuevas, F. Pizarro, A. Leiva, G. Hermosilla, and D. Yunge, "Parametric study of a fully 3D-printed dielectric resonator antenna loaded with a metallic cap," *IEEE Access*, vol. 9, pp. 73,771–73,779, May 2021, doi: 10.1109/ACCESS.2021.3081068.
- [58] Y.-H. Lou, Y.-X. Zhu, G.-F. Fan, W. Lei, W.-Z. Lu, and X.-C. Wang, "Design of Ku-band flat Luneburg lens using ceramic 3-D printing," *IEEE Antennas Wireless Propag. Lett.*, vol. 20, no. 2, pp. 234–238, Feb. 2021, doi: 10.1109/LAWP.2020.3046489.
- [59] C. D. Morales, C. Morlaas, A. Chabory, R. Pascaud, M. Grzeskowiak, and G. Mazingue, "3D-printed ceramics with engineered anisotropy for dielectric resonator antenna applications," *Electron. Lett.*, vol. 57, no. 18, pp. 679–681, Aug. 2021, doi: 10.1049/el2.12234.
- [60] S. Wang et al., "Radar cross-section reduction of helical antenna by replacing metal with 3-D printed zirconia ceramic," *IEEE Antennas Wireless Propag. Lett.*, vol. 19, no. 2, pp. 350–354, Feb. 2020, doi: 10.1109/LAWP.2019.2962524.
- [61] K. Glatre, L. Hildebrand, E. Charbonneau, J. Perrin, and E. Amyotte, "Paving the way for higher-volume cost-effective space antennas: Designing for manufacturing, assembly, integration, and test," *IEEE Antennas Propag. Mag.*, vol. 61, no. 5, pp. 47–53, Oct. 2019, doi: 10.1109/MAP.2019.2932313.
- [62] Y. Tawk, "A dynamic dual tapered 3-D printed nested helical antenna," *IEEE Trans. Antennas Propag.*, vol. 68, no. 2, pp. 697–702, Feb. 2020, doi: 10.1109/TAP.2019.2943427.
- [63] M. Amjadi and K. Sarabandi, "Ultra-wideband, compact, and high-gain two-port antenna system for full-duplex applications," *IEEE Trans. Antennas Propag.*, vol. 69, no. 11, pp. 7173–7182, Nov. 2021, doi: 10.1109/TAP.2021.3072626.
- [64] S. Shin et al., "Polymer-based 3-D printed Ku-band steerable phased-array antenna subsystem," *IEEE Access*, vol. 7, pp. 10,6662–10,6673, Aug. 2019, doi: 10.1109/ACCESS.2019.2932431.
- [65] V. Gjokaj, J. Papapolymerou, J. D. Albrecht, B. Wright, and P. Chahal, "A compact receive module in 3-D printed Vivaldi antenna," *IEEE Trans. Compon., Packag. Manuf. Technol.*, vol. 10, no. 2, pp. 343–346, Feb. 2020, doi: 10.1109/TCMT.2019.2961345.
- [66] L. Wu, H. Chu, D. Cao, S. Peng, and Y. Guo, "3-D printed antenna subsystem with dual-polarization and its test in system level for radiometer applications," *IEEE Access*, vol. 8, pp. 127,856–127,865, Jul. 2020, doi: 10.1109/ACCESS.2020.3008727.
- [67] B. Zhang et al., "A metallic 3-D printed airborne high-power handling magneto-electric dipole array with cooling channels," *IEEE Trans. Antennas Propag.*, vol. 67, no. 12, pp. 7368–7378, Dec. 2019, doi: 10.1109/TAP.2019.2935085.
- [68] J. Shen and D. S. Ricketts, "Compact W-band 'Swan Neck' turnstile junction orthomode transducer implemented by 3-D printing," *IEEE Trans. Microw. Theory Techn.*, vol. 68, no. 8, pp. 3408–3417, Aug. 2020, doi: 10.1109/TMTT.2020.2992065.
- [69] S.-H. Shin, X. Shang, N. M. Ridder, and S. Lucyszyn, "Polymer-based 3-D printed 140–220 GHz low-cost quasi-optical components and integrated subsystem assembly," *IEEE Access*, vol. 9, pp. 28,020–28,038, Feb. 2021, doi: 10.1109/ACCESS.2021.3057606.
- [70] A. E. Krasnok, C. R. Simovski, P. A. Belov, and Y. S. Kivshar, "Superdirective dielectric nanoantennas," *Nanoscale*, vol. 6, no. 13, pp. 7354–7361, Jul. 2014, doi: 10.1039/c4nr01231c.
- [71] A. E. Krasnok, A. E. Miroshnichenko, P. A. Belov, and Y. S. Kivshar, "Huygens optical elements and Yagi-Uda nanoantennas based on dielectric nanoparticles," *JETP Lett.*, vol. 94, no. 8, pp. 593–598, Dec. 2011, doi: 10.1134/S0021364011200070.
- [72] Y. Zhai et al., "Scalable-manufactured randomized glass-polymer hybrid metamaterial for daytime radiative cooling," *Science*, vol. 355, no. 6329, pp. 1062–1066, Mar. 2017, doi: 10.1126/science.aai7899.
- [73] A. W. Powell et al., "Strong, omnidirectional radar backscatter from subwavelength, 3D printed metacubes," *IET Microw., Antennas Propag.*, vol. 14, no. 14, pp. 1862–1868, Nov. 2020, doi: 10.1049/iet-map.2020.0178.
- [74] J. B. Pendry, L. Martin-Moreno, and F. J. Garcia-Vidal, "Mimicking surface plasmons with structured surfaces," *Science*, vol. 305, no. 5685, pp. 847–848, Aug. 2004, doi: 10.1126/science.1098999.
- [75] M. J. Lockyear, A. P. Hibbins, and J. R. Sambles, "Microwave surface-plasmon-like modes on thin metamaterials," *Phys. Rev. Lett.*, vol. 102, no. 7, Feb. 2009, Art. no. 073901, doi: 10.1103/PhysRevLett.102.073901.
- [76] A. Pors, E. Moreno, L. Martin-Moreno, J. B. Pendry, and F. J. Garcia-Vidal, "Localized spoof plasmons arise while texturing closed surfaces," *Phys. Rev. Lett.*, vol. 108, no. 22, May 2012, Art. no. 223905, doi: 10.1103/PhysRevLett.108.223905.
- [77] D. Muha, M. Mlakar, S. Hrabar, and D. Zaluški, "Practical realization of isotropic RF replica of plasmonic sphere," in *Proc. 6th Eur. Conf. Antennas Propag. (EuCAP)*, 2012, pp. 2706–2709, doi: 10.1109/EUCAP.2012.6206495.
- [78] D. Muha, M. Mlakar, S. Hrabar, D. Zaluški, and M. Martinis, "Analysis of magnetic response of circular arrangement of RF replicas of isotropic plasmonic spheres," in *Proc. 20th Int. Conf. Appl. Electromagn. Commun.*, 2010, pp. 1–4.
- [79] S. Hrabar, Z. Eres, and H. Kumric, "Spherical resonators acting as RF replicas of plasmonic nanospheres," in *Proc. IEEE Antennas Propag. Soc. AP-S Int. Symp.*, 2007, pp. 4340–4343, doi: 10.1109/APS.2007.4396502.



Reflectarrays and Metasurface Reflectors as Diffraction Gratings

A tutorial.

Reconfigurable reflectors have significant potential in future telecommunication systems, and approaches to the design and realization of full and tunable reflection control are now actively studied. Reflectarrays, being the classical approach to realize scanning reflectors, are based on the phased-array theory (the so-called generalized reflection law) and physical optics approximation of the reflection response. To overcome the limitations of the reflectarray technology, researchers actively study inhomogeneous metasurfaces, using the theory of diffraction gratings. To make these devices tunable and fully realize their potential, it is necessary to unify the two approaches and study reconfigurable reflectors from a unified point of view. Here, we offer a tutorial on reflectarrays and metasurface reflectors, explaining their common fundamental properties that stem from the diffraction theory. This tutorial is suitable for graduate and postgraduate students and hopefully will help to develop deeper understanding of both phased arrays and diffraction gratings.



Digital Object Identifier 10.1109/MAP.2023.3236278
Date of current version: 7 February 2023

INTRODUCTION

During the past few years, many research groups have been studying the possible use of reconfigurable intelligent surfaces (RISs) in future wireless communication systems [1], [2], [3], [4], [5], [6], [7], [8], [9], [10]. The main functionality of these RISs is to reflect incident waves (coming from a specified direction or directions) into desired directions.

Basically, this is the same function as usually realized by reflectarray antennas. Most commonly, reflectarrays are used as flat or conformal equivalents of parabolic reflectors, while RISs are usually designed to reflect plane waves, but this is not a principal difference. Such RISs are equivalent to focusing reflectors with an infinite focal distance.

Realizations of anomalously reflecting metasurfaces are usually designed as phase gradient reflectors, which are made of reactive impedance boundaries with a linearly varying phase of the local reflection coefficient. However, recent research has shown that such realizations have a fundamentally limited efficiency, which degrades when the desired performance significantly deviates from that of uniform mirrors.

IMAGE LICENSED BY INGRAM PUBLISHING

and retroreflectors [11], [12], [13], [14], [15]. This degradation is attributed to the excitation of parasitic propagating modes that scatter part of the incident power in unwanted directions. Actually, similar effects are known also for reflectarrays, which function well only if the reflected rays do not have to be tilted much. When the deflection angle is large (i.e., elements are close to the reflectarray edge), the specular reflection is not controlled and considered wasted, lowering the efficiency [16, Sec. 4.1.4]. The physical reason behind a deteriorating reflection efficiency with an increasing deflection angle is the wave impedance mismatch between the incident and deflected plane waves. Recognized first in perfect anomalously refracting metasurfaces [13], [15], [17], this wave impedance mismatch for efficiency reduction is analogous to the angle-dependent scan impedance mismatch in phased arrays. While it can be tolerated for conventional applications of reflectarrays, for the envisaged use of anomalous reflectors as RISs, this limitation can significantly compromise usability. Indeed, most usage scenarios of RISs assume that the reflected waves can be sent in any direction.

Recently, it was shown that advanced metasurfaces can control reflection theoretically perfectly, without any spurious scattering (except that caused by manufacturing imperfections and dissipation losses), e.g., [14], [15], [18], [19], [20], [21], and [22]. Different design approaches have been developed (we summarize and discuss them in the “Reflectarrays and Metamirrors” section). Interestingly, all of them are based on the theory of diffraction gratings and do not use the conventional design methods and topologies that have been developed for phased arrays and reflectarray antennas.

For the proper understanding and further development of devices for full and efficient control of wave reflection, it appears that it is necessary to analyze the basic principle of inhomogeneous reflectors, looking at both metasurfaces (realized with subwavelength structures) and reflectarrays (formed by repeating antenna elements at half-wavelength intervals) from a unified point of view. While these two techniques are different, they have fundamental similarities: both can be considered diffraction gratings. In this basic tutorial article, from the diffraction grating theory, we explain the fundamental principles behind any device that creates plane waves propagating in a certain direction. In the final section, we summarize and classify the currently known methods to design and realize anomalous reflectors and discuss current research challenges.

ACTIVE ARRAYS

In the design of reflectarrays and reflecting metasurfaces, the main challenge is to ensure that the proper currents on the

In the design of reflectarrays and reflecting metasurfaces, the main challenge is to ensure that the proper currents on the reflector are excited to create the desired reflected fields.

reflector are excited to create the desired reflected fields. However, first, one needs to know what current distribution is necessary to be realized. To this end, we discuss active arrays [23], assuming that we can fix any desirable current distribution over a planar surface. Our goal is to determine what current distribution we should set to create the desired propagating waves. Here, it is enough to consider sheets of electric surface currents. Then, we are able to properly determine the needed current profile over the reflector by using this simple model, although these

sheets create waves on both sides (a ground plane or a complementary sheet of magnetic surface current can be introduced to realize one-side excitation).

For simplicity, we consider infinite arrays, and our desired reflected modes are plane waves. For infinite arrays, the most common design goal is to ensure that in the regions far enough from the array, where all the evanescent fields can be neglected, there is only one plane wave propagating in the desired direction, corresponding to a delta function array factor. For finite arrays, this goal is equivalent to the radiation pattern having only one main beam in the desired direction, without any grating lobes. In this sense, conclusions made for infinite arrays will hold also for finite arrays.

THE PERIOD OF THE RADIATING CURRENT DISTRIBUTION FOR A GIVEN RADIATION DIRECTION

Let us suppose that the reflected field that we want to create in the far zone is a set of propagating plane waves. We assume that this desired set of plane waves varies along the planar radiating surface (the coordinate x) as a periodic function. This means that the tangential wavenumbers (along x) of all radiated harmonics are in rational relations. The very important special case is when only one obliquely propagating plane wave is launched in angle θ (referenced to the surface normal) with tangential wavenumber $k_t = k_0 \sin \theta$, where $k_0 = 2\pi/\lambda$ is the free space wavenumber and λ is the wavelength. Then, the x -dependence of this field $e^{-jk_t x}$ is a periodic function, with period $D = \lambda / \sin \theta$. The case of launching aperiodically distributed fields can be, in principle, treated as a limiting case of the infinite period. Later, we also discuss possibilities to launch a single plane wave with aperiodic current distributions.

It is clear that the required current distribution should be in a phase synchronism with all the desired free space modes. Assuming that the radiating current distribution is periodic, with period D , it can be expanded into spatial Fourier series with tangential wavenumbers:

$$k_{tn} = \frac{2\pi n}{D}, \quad n = 0, \pm 1, \pm 2, \dots \quad (1)$$

In general, we should select the period D so that the tangential wavenumbers of all desired plane waves will be found among this set of numbers (for some values of index n). Let us consider the special case of launching only one plane wave at a certain angle θ . In this case, it is enough to properly set only one Fourier harmonic of the current. The tangential wavenumber of the desired plane wave is

$$k_t = k_0 \sin \theta = \frac{2\pi}{\lambda} \sin \theta. \quad (2)$$

We need to select D so that at least one harmonic of the current distribution is in phase with the desired radiated wave. Comparing (1) and (2), the condition reads $n/D = \sin \theta/\lambda$; that is, $D = n\lambda/\sin \theta$. Since we want to send the energy in only one direction, it is reasonable to choose n as small as possible (that is, D as small as possible) to minimize the number of diffraction maxima or “open channels” (the directions where the array can radiate). Here, $n = 0$ is not a valid solution since in that case, $k_t = 0$, so we select $n = 1$, which gives

$$D = \frac{\lambda}{\sin \theta}. \quad (3)$$

In this case, the period of the radiating current is equal to the period of variations of the fields in the plane wave that we want to create. Obviously, this is an expected result.

Very importantly, we note that the array period D is greater than or equal to λ for any angle θ . The limit $D \rightarrow \lambda$ corresponds to $\theta \rightarrow \pi/2$, that is, to the endfire array. For small angles (radiation directions close to the normal), the period is very large. As a specific numerical example, we consider arrays that create a single plane wave in the $\theta = 70^\circ$ direction, for which $D \approx 1.0642\lambda$.

We have noted that it is desirable to select as small a period D as possible. More specifically, for a given period D , all harmonics whose tangential wavenumber k_m satisfies the inequality $|k_m| = 2\pi |n|/D < k_0 = 2\pi/\lambda$ are propagating modes. This corresponds to

$$|n| < \frac{D}{\lambda}. \quad (4)$$

In our example case of $\theta = 70^\circ$, we have $|n| < 1.0642$. This means that if we set any periodic current on the antenna (using active sources) with this period, the radiation in the far zone can go only to 0° , 70° , and -70° directions (corresponding to $n = 0, 1$, and -1 , respectively). All higher-order harmonics are evanescent. Note, however, that for scanning in other directions, the situation can be very different since we may need a rather large D compared with λ .

We see that from the diffraction theory point of view, any periodic antenna array that radiates in any direction except the normal direction is a diffraction grating because its period D is larger than the wavelength, and it radiates into an $n \neq 0$ spatial harmonic.

THE OPTIMAL CURRENT DISTRIBUTION

We see that any periodic reflectarray (radiating current distribution) can reflect (radiate) in more than one direction

because $D > \lambda$; see (4). The next task is to set such a current distribution so that the waves in all the unwanted directions have zero amplitude.

Let us denote the current distribution as $J(x)$, where x is the coordinate along the antenna array plane. In our example of exciting a single plane wave, the tangential fields of the desired plane wave mode vary as $e^{-jk_0x \sin \theta}$. As discussed in the preceding, the current distribution on the antenna should be a periodic function with the same period, $D = \lambda/\sin \theta$. But what specific function with this period should we select? An appropriate current distribution can be found by using the theory of waveguide excitation, e.g., [24, Sec. 4.12]. The fields excited in a waveguide by a given distribution of external currents are found as an expansion over the waveguide eigenmodes. In our case, the waveguide is free space, and its modes are plane waves that can, in general, propagate at any angle θ . The amplitudes of excited plane wave modes are proportional to the excitation integrals (integrals of the current distribution and complex conjugate of the desired radiated field distribution, [24, eq. 4.108]). It is enough to integrate over one period.

Continuing discussing the specific example of launching a single plane wave along the $\theta = 70^\circ$ direction, where the period $D \approx 1.0642\lambda$, in fact, allows three propagating plane wave modes, the current distribution $J(x)$ should be such that

$$\int_0^D J(x) e^{jk_0x \sin \theta} dx \rightarrow \text{maximum} \quad (5)$$

$$\int_0^D J(x) e^{-jk_0x \sin \theta} dx = 0, \quad \int_0^D J(x) dx = 0. \quad (6)$$

These are the coupling integrals for all three allowed propagating modes with the selected period of the array. These conditions ensure that the current distribution effectively launches the desired wave and that it is orthogonal to all the other existing propagating harmonics. Importantly, we do not impose any restrictions on the amplitudes of evanescent fields in the vicinity of the array, as the goal is to create the desired field in the far zone. However, note that in reflectarray and metasurface realizations, evanescent modes are to be controlled to optimize far-zone fields, and we briefly discuss this in the “Reflectarrays and Metamirrors” section.

Clearly, there are many possible solutions of $J(x)$ satisfying (5) and (6). The simplest and most obvious one is the current with a constant amplitude and linear phase gradient. For example, selecting $J(x) = Ae^{-jk_0x \sin \theta}$ (A is the complex amplitude), we maximize the integral in (5) because the product of the two exponentials is just unity. The integrals in (6) are zero because of double/single variations over the period. This is why the current does not radiate into -70° and normal directions.

Let us consider another case with a small tilt angle, say, $\theta = 5^\circ$. We use the same simple theory and first select the period such that the array radiates the plane wave along this direction. Now the appropriate period is $D = \lambda/\sin \theta \approx 11.47\lambda$. The plane wave Fourier harmonics will propagate when $|n| < D/\lambda = 11.47$; see (4). Thus, our desired direction corresponds to $n = 1$, but there are 22 more directions (11 on the left, 10 on the right side from the normal, and the normal direction)

where the waves can also propagate. The current distribution should be such that

$$\int_0^D J(x) e^{jk_0 x \sin \theta} dx \rightarrow \text{maximum} \quad (7)$$

$$\int_0^D J(x) e^{jn k_0 x \sin \theta} dx = 0, \quad n = 0, -1, \pm 2, \pm 3, \dots \quad (8)$$

The current distribution with the ideal linear phase gradient $J(x) = Ae^{-jk_0 x \sin \theta}$ clearly satisfies all these relations. For approximate (e.g., step-wise) settings, finding solutions for (7) and (8) is a nontrivial task. On the other hand, for small angles, the required linear phase variation is smooth, and the coupling to other propagating harmonics is weak. Thus, reasonably smooth discretization of the linear phase current creates nearly perfect single-wave fields in the far zone.

REALIZATION WITH SMALL RADIATING ELEMENTS (LINEAR PHASE GRADIENT)

Next, we discuss the principle of diffraction grating (metagrating) realizations [18], [25], [26], [27], [28]. Instead of a continuous current distribution, the diffraction grating realizations excite the desired plane wave, with just a few small radiating elements placed in each period. To understand how it works, we assume that the current distribution over the antenna plane is a set of a few delta function sources. That is, we consider an array of small radiators with an isotropic element pattern.

Let us try to reach the goal for radiation in $\theta = 70^\circ$ by using only two such small active radiators per period, with arbitrary selected positions $x = a$ and b . The current distribution function

becomes $J(x) = A\delta(x - a) + B\delta(x - b)$, where A and B are the complex amplitudes of the two point sources (line sources in the 2D scenario). Substituting this current distribution into (6), we get only a trivial solution $A = B = 0$.

This means that we need at least three elements per period. Let us assume

$$J(x) = A\delta(x) + B\delta\left(x - \frac{D}{3}\right) + C\delta\left(x - \frac{2D}{3}\right) \quad (9)$$

and substitute it for (6); we get

$$B = -A(1 + e^{j\frac{2\pi}{3}}) = Ae^{-j\frac{2\pi}{3}}, \quad C = -(A + B) = Ae^{j\frac{2\pi}{3}} \quad (10)$$

to ensure that there is no radiation in the normal and -70° directions. We see that in this equal spacing configuration, the three line sources have the same amplitude and a linear phase drop (a total of 2π over one period). By substituting this solution into (5), we find that the result is $3A$ (nonzero), meaning that in the far zone, there is a perfect plane wave in the desired direction. The positions of the small radiators can be varied, adding degrees of freedom in design. Here, we note that a recent paper [29] studied the excitation of plane waves by arrays of line currents. In that paper, excitation conditions are also imposed on evanescent modes, resulting in the conclusion that only continuous current distributions with a linear phase gradient can launch a single plane wave.

The preceding results are verified with numerical simulations, as presented in Figure 1. When the three line sources (2D point sources in the figure) are assigned according to (9) and (10), with $A = 1 \text{ mA}$, indeed, there is a perfect plane wave generated in the desired direction θ that is larger than the critical

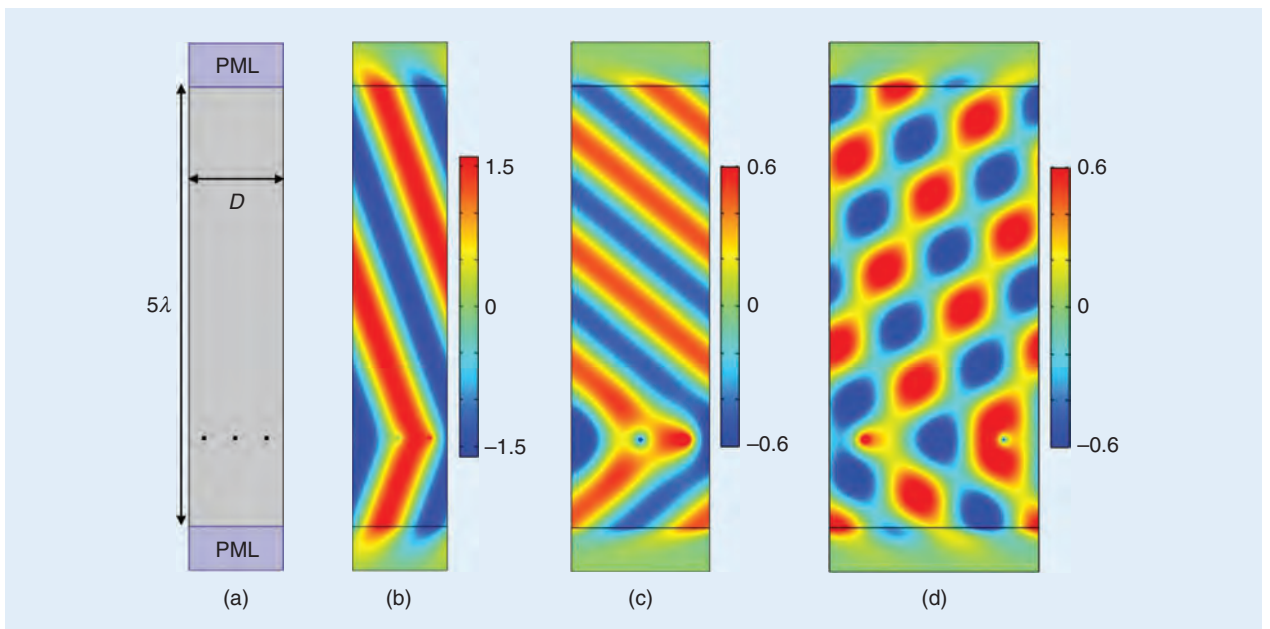


FIGURE 1. The radiation from three discrete radiators, with the current distribution given by (9) and (10). Note that the supercell shown here has a lateral shift along the x -axis. (a) The simulation setup, where the currents are flowing in the out-of-screen direction. (b)–(d) The scattered electric field patterns for angles $\theta = 70^\circ$, 40° , and 25° , respectively. PML: perfectly matched layer.

angle 30° in Figure 1(b) and (c). The critical angles correspond to $D/\lambda \in \mathbb{N}$ ($\theta = 30^\circ$ gives $D/\lambda = 2$), which opens up more propagating modes. However, when $\theta \leq 30^\circ$, the scattered field is not a single plane wave, as more channels are open, as demonstrated in Figure 1(d). The working angles $\theta > 30^\circ$ correspond to $|n| < D/\lambda < 2$, which means that three point sources are enough for generating perfect plane waves when only three modes $|n| < 2$ are propagating modes.

For the case of many propagating modes, the design complicates. For the preceding example of radiation in the direction of $\theta = 5^\circ$, we need to satisfy a system of 23 equations. However, we can use a simple approach based on (9) and (10). Similarly, for N discrete sources that are evenly distributed over D , we can assume that the current distribution follows

$$J(N, x) = \sum_{m=0}^{N-1} A e^{-j2\pi \frac{m}{N}} \delta\left(x - \frac{Dm}{N}\right) \quad (11)$$

i.e., with the same amplitude and a linear phase drop of 2π over D . Associated with a uniform linear array of isotropic radiators with a linear phase, the radiation pattern of the source current (11) corresponds to the array factor in array theory [30]. Then, the radiation will be perfect if we select enough discrete points N , ensuring that integration in (8) satisfies the orthogonality conditions for all n that correspond to unwanted propagating channels. In general, if the periodicity allows propagation of $2m+1$ plane waves, one needs $m+2$ discrete sources to excite only one of these plane waves. This is also true for equally spaced segments, and it can be concluded from Table 1 in the next section.

REALIZATION WITH RADIATING SEGMENTS (LINEAR PHASE GRADIENT)

In actual realizations of antenna arrays, for example, using patch antennas, the radiating currents are not point sources; rather, they are small radiating elements. To analyze this case, we consider the discretization of the current distribution into segments. In each segment, the current is uniform, while for different segments, currents have different phases, still following the linear

phase profile in the step-wise fashion. In this case, we can write the current distribution as

$$J(N, x) = A e^{j\Phi(N, x)}, \quad \text{with } \Phi(N, x) = -2\pi \frac{\text{Floor}\left(\frac{xN}{D}\right)}{N} - \delta\phi \quad (12)$$

where A is the complex amplitude, N is the segment number in each period D , $\Phi(N, x)$ is the phase function corresponding to the discretized phase profile, $\delta\phi$ is a phase shift factor, and the function $\text{Floor}(x)$ gives the greatest integer smaller than or equal to the argument x .

With such a segmented current distribution, we can calculate the integral in (8), and the results are listed in Table 1 for $A = 1$ and $\delta\phi = 0$. The value will indicate whether there is a plane wave propagating to each port n . As one can see, when $N = 3$, the integration is nonzero for ports $n = -5, -2, 1, 4$, and 7, meaning that if these ports correspond to propagating modes (depending on angle θ), there will be plane waves propagating to those ports. As the number of segments N increases, more ports are suppressed, corresponding to zero integrals, and only the port $n = 1$ is excited. Indeed, as N increases, the segmented current distribution is closer to the analytical uniform one with a linear phase. We further note that a change of $\delta\phi$ in (12) does not change the integration results at all, meaning that the phase can be arbitrarily shifted.

Actually, the point sources and uniform current segments may be replaced by suitable array elements, say, with currents of square shape or cosine shape. We check whether the radiation remains perfect for the same element number per period. Instead of (9) or (12), we assume

$$J(x) = AF(x) + BF\left(x - \frac{D}{3}\right) + CF\left(x - 2\frac{D}{3}\right) \quad (13)$$

where $F(x)$ is the normalized current distribution function at each array element and A, B , and C are the complex amplitudes of the currents at the array elements. The radiation pattern of one array element with the current distribution $F(x)$ is the element pattern. For example, we can assume a square shape or a sine shape

TABLE 1. THE ABSOLUTE VALUE OF INTEGRALS (8) FOR THE CURRENT DISTRIBUTION (12), WITH PORT NUMBER n AND SEGMENT NUMBER N .

N	n														
	-7	-6	-5	-4	-3	-2	-1	0	1	2	3	4	5	6	7
2	0.09D	0	0.13D	0	0.21D	0	0.64D	0	0.64D	0	0.21D	0	0.13D	0	0.09D
3	0	0	0.16D	0	0	0.42D	0	0	0.83D	0	0	0.21D	0	0	0.12D
4	0.13D	0	0	0	0.3D	0	0	0	0.91D	0	0	0	0.18D	0	0
5	0	0	0	0.24D	0	0	0	0	0.94D	0	0	0	0	0.16D	0
6	0	0	0.2D	0	0	0	0	0	0.96D	0	0	0	0	0	0.14D
7	0	0.17D	0	0	0	0	0	0	0.97D	0	0	0	0	0	0
8	0.14D	0	0	0	0	0	0	0	0.97D	0	0	0	0	0	0
9	0	0	0	0	0	0	0	0	0.98D	0	0	0	0	0	0

$$F(x) = \begin{cases} 1 & \text{if } 0 < x < w \\ 0 & \text{otherwise} \end{cases}, \quad F(x) = \begin{cases} \sin(\pi x/w) & \text{if } 0 < x < w \\ 0 & \text{otherwise} \end{cases} \quad (14)$$

where w is the width of the array element and is smaller than $D/3$. Then, following the same approach as before, i.e., solving (6) with the current in (13) and (14), we find that the condition for radiation only to the desired angle ($n = 1$) is when the complex amplitudes are $B = Ae^{-j2\pi/3}$ and $C = Ae^{j2\pi/3}$, which are independent of w . We note that this solution is exactly the same as the solution (10) for point source realization in the “Realization With Small Radiating Elements (Linear Phase Gradient)” section, clearly indicating that the point sources and uniform current sections can be replaced by other suitable radiating elements. This agrees with the principle of pattern multiplication in arrays [30]. The limitation is that the element pattern of these elements should not have a null in the desired direction of radiation.

GENERAL PERIODIC CURRENT DISTRIBUTIONS (METAGRATINGS)

It is important to note that the radiating elements of periodic arrays do not have to be equally spaced, and the phase shifts between the elements do not have to follow the linear phase advance law. Indeed, instead of (9), let us assume

$$J(x) = A\delta(x) + B\delta(x - a) + C\delta(x - b) \quad (15)$$

where $0 < a$ and $b < D$. By substituting it into (6) to eliminate the wave radiation in the normal and $-\theta$ directions ($n = 0$ and $n = -1$), we find that the solution of B and C , in terms of A , reads

$$B = A \frac{\sin\left(\frac{\pi b}{D}\right)}{\sin\left[\frac{\pi(b-a)}{D}\right]} e^{-j(\pi - \pi a/D)}, \quad C = A \frac{\sin\left(\frac{\pi a}{D}\right)}{\sin\left[\frac{\pi(b-a)}{D}\right]} e^{j\pi b}. \quad (16)$$

It is clear that when the radiating elements are not equally spaced, the required phase distribution does not follow the linear phase gradient law. In addition, the amplitudes of the currents are also changed. For example, when we set $a = D/6$ and $b = 2D/3$, as in Figure 2(a), the required complex amplitudes of the second and third sources read $B = (-3/4 - j\sqrt{3}/4)A$ and $C = (-1/4 + j\sqrt{3}/4)A$, and with this setting, we can still get the desired single-wave radiation, as illustrated in Figure 2(a).

If we set $b = 2a$ in (16), we find the required complex amplitudes as $B = 2A \cos(\pi a/D) e^{-j(\pi - \pi a/D)}$ and $C = Ae^{j2\pi a/D}$. If we further make a much smaller than D so that the three sources are clustered, the phase quickly varies among the three sources; i.e., the first and third sources have small phases of zero and $2\pi a/D$ ($a \ll D$), while the middle source has a phase that is close to $-\pi$. Moreover, the amplitude of the middle source is close to two, while the amplitudes of the other two are one. As examples, in Figure 2(b) and (c), we perform two sets of simulations, with $b = 2a = D/4$ and $b = 2a = D/10$, respectively. The results show that these clustered sources can still generate the desired radiation without any unwanted scatterings. Anomalous reflectors based on periodic arrays of a few small scatterers in each period are often called *metagratings* [18].

We note that it is straightforward to analyze similarly the case of small tilt angles with more discrete point sources. Obviously, the realization of such fast variations of the reflection

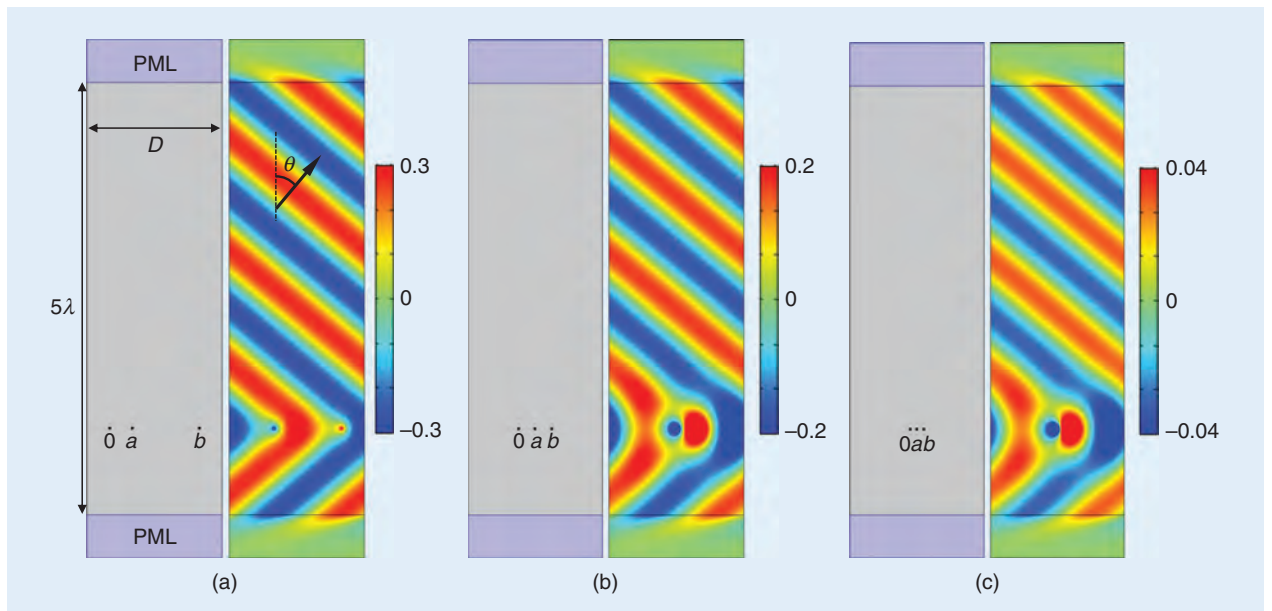


FIGURE 2. The radiation from $N = 3$ discrete current sources that are arbitrarily positioned in one period (with a lateral shift along x). Each subfigure shows the simulation setup and radiated electric field pattern for $\theta = 40^\circ$. The assumed values are (a) $a = D/6$ and $b = 2D/3$, (b) $b = 2a = D/4$, and (c) $b = 2a = D/10$. The complex amplitudes B and C are obtained from (16), with $A = 1\text{mA}$.

phase in reflectarrays is challenging. Thus, for the case when many plane waves can propagate, it is preferred to use equal spacing and a linear phase gradient.

In fact, these conclusions hold true not only for small point-like radiating elements but also for arrays of radiating segments. For example, if we assume the current distribution function as

$$J(x) = AF(x) + BF(x-a) + CF(x-b) \quad (17)$$

similar to (15) for the point sources, the required amplitudes are also found to be given by (16) and independent of the segment width w . For infinite arrays, the performance should not depend on the current distribution function and element pattern if the amplitudes A , B , and C are set properly and the element pattern has no null in the desired radiation direction.

The assumption of a real-valued function $F(x)$ corresponds to the case of small resonant antennas as array elements. This is the case when the current distribution over a unit element is a standing wave, and the current phase is uniform over the unit cell. Also, arrays of slots in metal sheets can be modeled in this way. However, it is possible to assume that the current distribution is a complex-valued function, and the conclusions will not change.

It is obvious that these models assume that the current distribution over each array element is fixed and independent from the excitation of this element and all the other elements in the array. In the case of reflectarrays and metasurfaces, this is equivalent to the assumption that the distribution of near fields in the vicinity of the array does not depend on the incidence angle.

To give a clear overview of the different models of the diffraction grating approach, in Figure 3, we summarize the different current distribution functions discussed in the preceding. As we can see in Figure 3(a) and (b), the equally spaced

element realizations all have the linear phase profile, while for the nonequally spaced element design, the phase is not a linear 2π phase dropping over the period, and the amplitude is not a constant in Figure 3(c).

DIFFRACTION GRATING APPROACH VERSUS PHASED-ARRAY APPROACH

In the preceding theory, we started from stating that current distributions for launching a single plane wave in a desired direction should be periodic functions, with the period related to the period of the radiated plane wave. One reason for that assumption is that the excitation current and desired field must be in a phase synchronism. The other reason is that by fixing the period as defined by the desired reflection angle or angles, one makes sure that the reflector can create a plane wave exactly in the desired direction. The design goal is then to properly distribute the reflected power among the allowed “open channels,” minimizing scattering into all directions except the desired one. From the practical point of view, the design of periodic structures reduces to the design of only one period, which is a great simplification.

However, the current distribution does not have to be a periodic function. Conditions (5) and (6) as well as (7) and (8) can be considered conditions on the spatial Fourier transforms of the current distributions if we assume that $J(x)$ is not necessarily periodic and extend the integration over the whole x -axis. Actually, Floquet periodic functions of the form

$$J(x) = \sum_{m=-\infty}^{\infty} A_m e^{-j(k_0 \sin \theta + \frac{2\pi m}{d})x} \quad (18)$$

can satisfy the required conditions for launching only one plane wave in the θ direction. Formula (18) corresponds to an ideal current profile $e^{-jk_0 x \sin \theta}$ that is modulated by an arbitrary

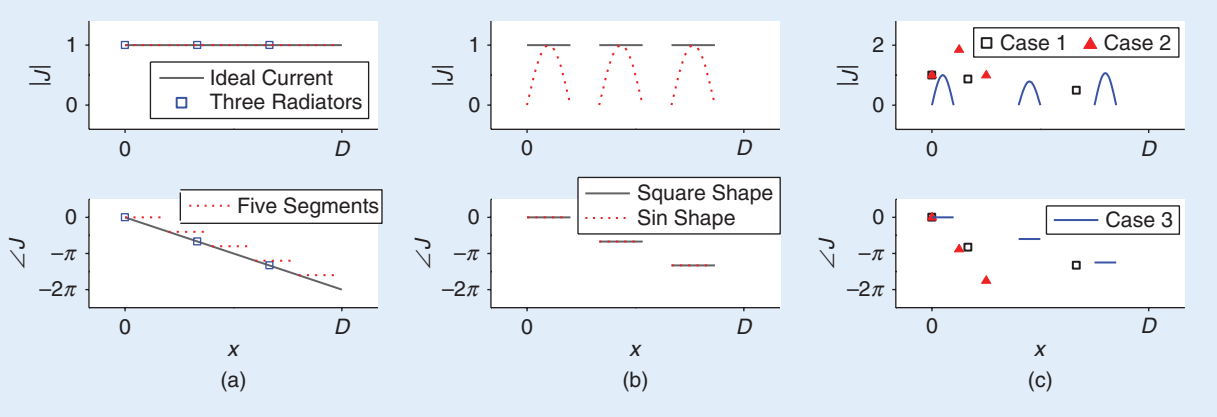


FIGURE 3. The required current distribution functions (amplitude and phase) for the diffraction grating approach. (a) The ideal current $J(x) = Ae^{-jk_0 x \sin \theta}$ in the “The Optimal Current Distribution” section, the required currents for three radiators is given in (9) and (10) for Figure 1 [or, equivalently, (11), with $N = 3$] in the “Realization With Small Radiating Elements (Linear Phase Gradient)” section, and that for five segments with the current in (12), with $N = 5$ and $\delta\phi = 0$ in the “Realization With Radiating Segments (Linear Phase Gradient)” section. (b) Currents with the form of (13) and (14), with patches showing the square shape and sine shape $F(x)$. (c) The nonequally spaced element realizations in the “General Periodic Current Distributions (Metagratings)” section, using (15)–(17). Cases 1 and 2 correspond to the ones in Figure 2(a) and (b). Case 3 is the “patch” realization in (17), with the sine shape current in (14) and $a = 2D/5$, $b = 3D/4$, and $w = D/10$. Here, $A = 1$ is used in all figures.

periodic function $F(x)$ with period d : $J(x) = F(x)e^{-jk_0x\sin\theta}$. Expanding $F(x)$ into a Fourier series, we arrive at (18). Really, the $m=0$ term is the ideal current profile $e^{-jk_0x\sin\theta}$ (the uniform amplitude and linear phase gradient) that launches a single plane wave in the θ direction. Indeed, this function is obviously orthogonal to all other plane waves as eigenmodes of free space because

$$\int_{-\infty}^{\infty} e^{-jk_0x\sin\theta} e^{jk_0x\sin\theta'} dx = 0 \quad \text{for all } \theta' \neq \theta. \quad (19)$$

Thus, if we ensure that all other members of the series (18) have this property, currents of the form (18) will excite only one propagating plane wave. To ensure this property, we demand that $|k_0\sin\theta + 2\pi m/d| > k_0$ for all $m \neq 0$. In this case, the tangential components of the wave vectors of all harmonics with $m \neq 0$ are larger than $k_0\sin\theta'$ for all θ' , and the orthogonality condition (19) is satisfied. It is convenient to rewrite this condition as

$$\left| \sin\theta + \frac{\lambda}{d}m \right| > 1. \quad (20)$$

Then, the condition for the required repeating period d of the current elements can be analyzed. For $\theta \rightarrow 0$, the condition is satisfied if $d < \lambda$ (the most “dangerous” term is, obviously, the term $m = -1$). For $\theta \rightarrow \pi/2$, the condition is true if $d < \lambda/2$. That is why for scanning phased arrays, the period d is conventionally chosen to be equal to $\lambda/2$: this choice ensures that for any scan angle, no parasitic diffraction lobes will be created for infinite scanning phased arrays.

The case when the current distribution is not a periodic function is equivalent to the limit case when the period is infinity. As we see, when the period approaches infinity, although there are infinitely many allowed plane

wave propagation directions, it is possible to excite only one propagating plane wave by properly phasing the currents at the phased-array elements.

If the radiation direction is fixed to angle θ and no scan is required, by choosing $m = -1$ in (20), the period d of the general periodic structure can be set for that specific angle as

$$d < \lambda/(1 + \sin\theta). \quad (21)$$

This is recognized as the condition for avoiding grating lobes in arrays [30]. For instance, for our example of $\theta = 70^\circ$, we need $d < 0.5155\lambda$. This is also verified from the results of Figure 1:

- For the minimum required radiators $N = 3$ in each supercell, the critical angle is $\theta = 30^\circ$, which gives the critical supercell period $D = \lambda/\sin\theta = 2\lambda$. This requires that the critical distance between radiators is $d = D/3 = 2\lambda/3$, which is consistent with (21), for general periodic structures. For angles greater than this critical angle, (21) is always valid.
- For $N = 5$, the critical angle is $\theta = 14.48^\circ$, which gives the critical supercell period $D = \lambda/\sin\theta = 4\lambda$. Thus, the critical distance is $d = D/5 = 4\lambda/5$, which is consistent with (21).

The periodic “modulation function” $F(x)$ can be a complex-valued function. An important special case is the form $f(x')e^{jk_0x'\sin\theta}$, defined in the region $-d/2 < x' < d/2$. Periodically repeating this modulation, we have the current in the M th period (where $x = Md + x'$) as

$$\begin{aligned} J(x) &= F(x)e^{-jk_0x\sin\theta} = f(x')e^{jk_0(x-Md)\sin\theta}e^{-jk_0x\sin\theta} \\ &= f(x')e^{-jMd\cos\theta}. \end{aligned} \quad (22)$$

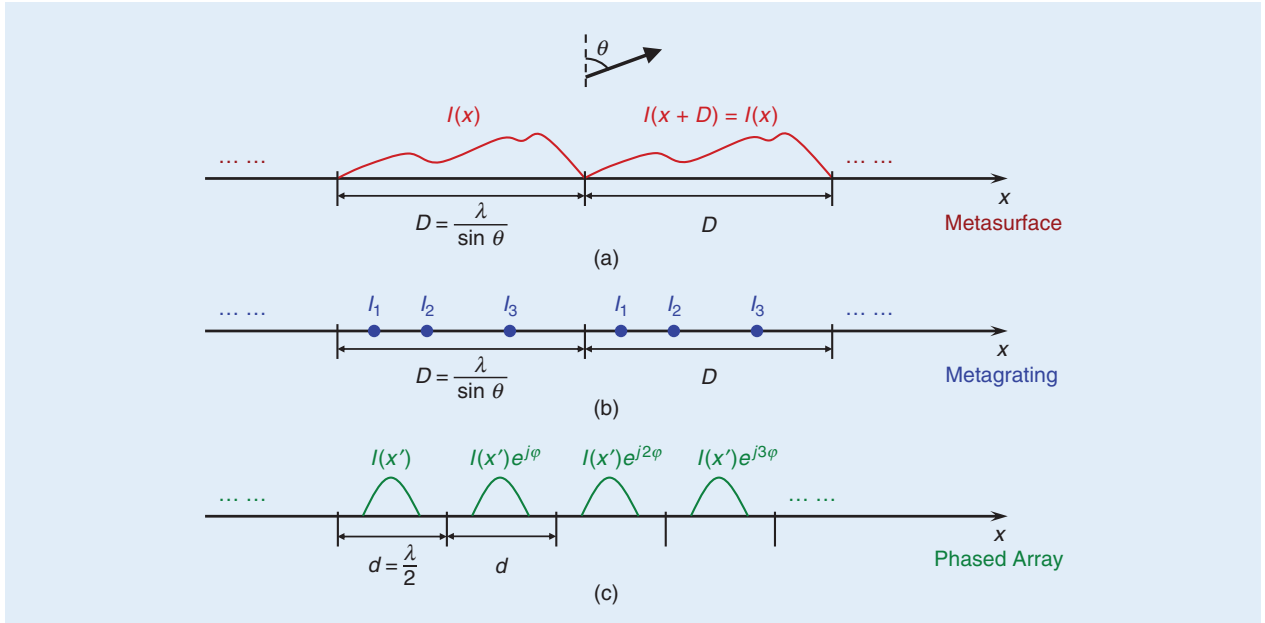


FIGURE 4. The (a) metasurface design approach (effectively continuous periodic current distribution), (b) metagrating design approach (a few small scatterers in each period), and (c) phased-array design approach (in general, aperiodic current distribution).

This is the phased-array design approach. The structure is formed by an array of unit cells with size d (the array elements). The unit cells have the same current distribution function $f(x')$, but the phase of their current linearly varies from cell to cell. The continuous linear phase profile is replaced by a discrete one. The most common assumption is the real-valued function $f(x')$, which corresponds to arrays of, e.g., resonant dipoles, resonant patches, and horn antennas.

We see that the phased-array approach is quite different from the conventional approach to the design of diffraction gratings and metasurfaces for reflection control. Here, we start from fixing the unit cell size d , usually at $d = \lambda/2$. Assuming the same current distribution function over each unit cell (usually the resonant mode of an antenna array element), we adjust the phases of the unit cells to create constructive interference in the desired direction.

Figure 4 illustrates and compares these two approaches. Figure 4(a) and (b) correspond to the diffraction grating approach for designing anomalous reflectors. In this case, we select a proper period $D = \lambda/\sin\theta$ and then find a suitable current distribution (the solution is not unique). For the case of the discretized point radiators in Figure 4(b), for launching the wave to 70° , where we have three propagating Floquet modes, we need three discrete sources in each period.

In Figure 4(c), which describes the phased-array approach, we have an array of identical “patches” spaced by $\lambda/2$. We assume that all the elements have the same amplitude pattern (a cosine shape is shown) and that the phase is uniform over each unit cell. Then, we feed this array with a linearly varying phase source so that the phases vary from unit to unit as

$$\Phi(n) = k_0 x(n) \sin\theta = \frac{2\pi}{\lambda} n \frac{\lambda}{2} \sin\theta = \pi n \sin\theta \quad (23)$$

with n being the unit index, as shown in the figure. Importantly, we note that this current distribution is, in general, not a periodic function. The periodicity condition reads

$$n\pi \sin\theta = 2\pi m \quad (24)$$

where m is the number of unit cells that will have the same phase as cell number zero. Obviously, this condition can be satisfied only if $\sin\theta$ is a rational number.

Figure 5 gives an example of the active phased array for generating radiation toward $\theta = 70^\circ$. Due to the nonperiodicity of the current distribution, we consider a finite phased array made of $N = 40$ “patches” with width $w = \lambda/4$ and spacing $d = \lambda/2$. The current of this finite phased array is set to follow (22), with $f(x')$ being a cosine shape [the inset of Figure 5(a)]. It indeed radiates in the desired direction, as shown by the electric field pattern in Figure 5(b) and the normalized far field (the black solid curve) in Figure 5(c). Due to the finiteness of the array, there are side lobes but no other main beams. When increasing the radiating aperture size by adding more “patches,” the pattern tends to a delta function. This is illustrated by the red dashed curve in Figure 5(c) for $N = 100$.

If we choose the element spacing in the phased array equal to $D/3 = (1/3)\lambda/\sin\theta$, the phase array becomes periodic, and it is equivalent to the diffraction grating picture for $\theta > 30^\circ$. Hence, for active arrays, the difference between diffraction grating and phased-array approaches is of a practical nature in essence. In diffraction gratings, a periodic physical configuration stipulated by the incidence and reflection angles is chosen so that the design domain is reduced to a single supercell. In phased arrays, the cell size (i.e., the element spacing) is determined a priori (usually $\lambda/2$) based on the required beam scanning capability. The functionality of creating one propagating wave is performed by element excitations following a spatially linear phase profile.

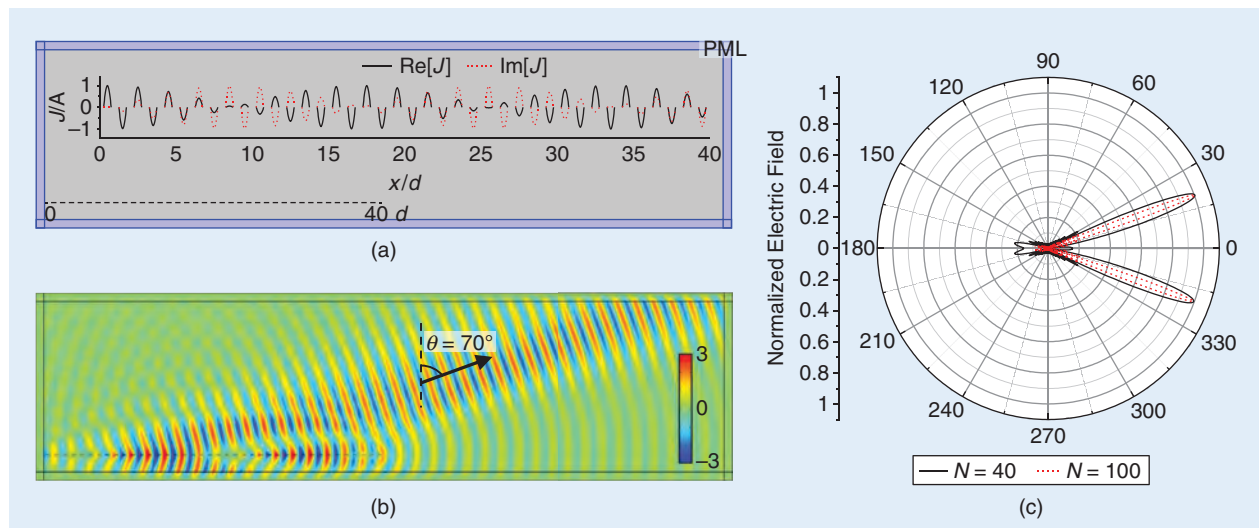


FIGURE 5. The radiation from a finite phased array consisting of $N = 40$ “patches,” with $w = \lambda/4$ and $d = \lambda/2$. (a) The simulation setup. The inset shows the current distribution. (b) The simulated electric field pattern for the $N = 40$ phased array. (c) The normalized far field (electric field). The black solid (red dashed) line corresponds to the phased array consisting of $N = 40$ ($N = 100$) “patches.”

The fundamental difference between the two design approaches is in realizing scanning capability. For diffraction gratings, the period of the array should be adjusted for each desired reflection angle, which, in practice, requires enough small subwavelength unit cells. For phased arrays, the period is fixed, which, in principle, allows the use of $\lambda/2$ -sized unit cells. In this case, the required current distribution over the plane is, in general, aperiodic. This issue does not create practical problems for active phased arrays, which are all of a transmitting type. However, the realization of the required linear phase profile for wide-angle scanning by adjusting the reactive bulk loads of passive reflectarray antenna elements is rather difficult.

Let us stress that there is a very important simplifying assumption in the root of the phased-array antenna theory. Namely, it is assumed that the current distribution over one array element does not depend on the currents on the other elements. The current density on the first element can be written as $I_0 f(x)$, where $f(x) = 0$ at $x < 0$, with $x > d$, and I_0 is the current amplitude fixed by external sources. Only under this assumption, the current of the M th element is $I_M f(x - Md)$, where f is the same function. This assumption is an approximation. It holds very well for active resonant antenna elements (when the current distribution is approximately fixed by the resonant mode) and arrays of horn antennas (where the current, or aperture field, is very close to the fundamental mode of the horn). We stress that the current amplitudes I_M depend on external voltages applied to all elements. By knowing the impedance matrix of the array, we can always find such voltages to realize the desired distribution of current amplitudes over the antenna plane.

Finally, let us discuss the role of diffraction grating theory in understanding phased arrays. Although the current and field distribution over a reflectarray aperture is not periodic, the array is “geometrically periodic,” as it is formed by identical antennas separated by a $\lambda/2$ distance. Moreover, the current distribution is Floquet periodic, defined by a periodic modulation function $F(x)$. Another aspect is that an array without periodicity of loads and induced current can be treated as a periodic array with an infinite period ($D = \infty$). In this case, there are infinitely many propagating “Floquet harmonics” of the diffraction gratings theory. Generally speaking, the diffraction grating method has limited applicability; however, some general conclusions remain valid.

REFLECTARRAYS AND METAMIRRORS

In contrast to active antenna arrays, where each antenna element is fed by an external controllable source, currents on elements of reflectarrays and metasurfaces are excited by incident

In diffraction gratings, a periodic physical configuration stipulated by the incidence and reflection angles is chosen so that the design domain is reduced to a single supercell.

waves (and fields scattered from all other array elements). The usual design aim is to synthesize the induced current distribution $J(x)$ to create a constant amplitude linear phase profile. However, unlike in the active phased-array case, we do not have full control over the magnitude and phase of $J(x)$ by using a passive surface subject for the illumination of incident waves. The coupling of array elements and interference of incident and reflected waves need to be carefully taken into account.

Let us first consider the design approach based on the diffraction grating theory. That is, we fix the array period as defined by the incidence angle and desired reflection direction and then design a surface to perform the required operation. In the following discussion, we consider the same example functionality as in the examples in the preceding: the reflection of a normally incident plane wave into a plane wave in an arbitrary direction. We can consider two cases:

- 1) If we specify the scattered field as a single plane wave, for example, tilted at 70° , and calculate the required surface impedance Z_s of the reflector, an alternately active/lossy surface results [11], [13]. This is not desirable or even possible from the realization perspective.
- 2) If we specify the periodic surface reactance to give a local reflection coefficient profile with a unit magnitude and linear phase gradient, passivity is guaranteed. However, the reflected field ends up including parasitic propagating waves. In our example, reflected power also goes into the -70 and 0° directions, e.g., [14]. Other (and more than two) parasitic scattering directions open up for other combinations of the incidence and anomalous reflection angles.

Neither case is satisfactory. Researchers work on finding other solutions that use only passive (as small a dissipation as possible) array elements. The only possibility is to allow the excitation of other field modes beside the only plane wave in the desired direction. If all these other modes are evanescent Floquet harmonics, they do not propagate into the far zone, and the perfect performance of the device is not compromised. There can be several ways to approach this task:

- 1) Model the reflector as a boundary defined by its surface (input) impedance. Allowing the excitation of surface-bound modes, design the surface impedance so that only the desired reflected propagating mode exists, enforcing $\text{Re}[Z_s(x)] = 0$ as an additional condition. Finding $Z_s(x)$ for creating only one propagating plane wave is simple, but guaranteeing passivity is not straightforward. This approach has been used, for example, in [19] and [22]. Importantly, actual realizations of the optimized surface impedance still require the locally periodic approximation, possibly leading to performance degradation. For this reason, the method developed in [10]

- imposes an additional condition of slow variation of the surface impedance, which can make the approximate design of surface topology more accurate.
- 2) Start from a certain topology (usually a patterned metal sheet on a grounded dielectric substrate) and optimize the evanescent fields so that the effective sheet impedance of the thin patterned metal layer is lossless at every point. This is the approach used in [21] and [31] for scalar metasurfaces and [32] for tensor metasurfaces. In this approach, the impedance model is used only for a single patterned sheet, not for the whole metasurface structure. In addition, the locally periodic approximation is also used in this method but only for the design of the reactive sheet instead of the whole metasurface body.
 - 3) Considering arrays of thin metal strips on a grounded substrate and using the periodic Green's function for a grounded dielectric substrate, find the loading impedances of the strips analytically. Translate the required loading element into a gap capacitor, as is done, e.g., in [27] and [28]. This approach is a variation of the metagrating design method. This way, it is possible to treat anomalous transmission as well as reflection [33].
 - 4) Design the current distribution so that only the desired plane wave is created by direct optimization of the metasurface structure (not relying on sheet/surface impedance boundary conditions and not requiring reactive input impedance at any surface except the ground plane). Passivity is guaranteed by microscopically considering passive inclusions, but creating only one plane wave is not as easy as in 1). This approach is used in [14] and [34].
 - 5) Find a surface where the input impedance is purely reactive for the desired set of waves, and design the local surface reactance $X_s(x)$ [20], [35]. This is the power flow-conformal solution, which does not need optimizations of the spatial dispersion properties of the reflector.

Let us next discuss the design approach based on the phased-array theory. That is, we fix the unit cell size, usually to $\lambda/2$. We position geometrically identical passive antenna elements in each cell and find such loads connected to the elements so that the induced current distribution has the required linear phase profile [with a periodic modulation, as in (22)].

Under the simplifying assumption that the current distribution over each antenna element is the same for any incident field distribution and any loads connected to all the elements, we can use the impedance matrix method to find the load impedances for realizing the desired phase distribution. Unfortunately, we run into the same problem as in the diffraction grating design: these loads have active/lossy behavior [35]. Thus, one needs to impose an additional constraint on the load impedances (zero real parts) and design some optimization procedure for finding reactive loads that approximate the required amplitude and current distribution in the best possible way. Basically, we end up with the same problem of engineering near fields so that the power is properly channeled from “virtually lossy” to “virtually active” antenna elements (engineering spatial dispersion). It is not clear if just one control element per $\lambda/2$ will be enough

to reach the goal, and we may need to use subwavelength elements, similar to the metasurface scenario.

The main difficulty in the phased-array (reflectarray) approach is that the array of antennas (including the loads) is no longer a periodic structure. This makes the number of ports for connecting load impedances infinite, and all the loads are, in general, different. In contrast, the periodic metasurface approach requires the design and optimization of only one period, and usually only a few parameters need to be optimized. We stress that this is not a problem in a conventional practical phased-array antenna in either transmission or receiving mode because it corresponds to a transmissive device. A transmissive device does not have the interference problem between the incident and scattered waves, which is the reason for the active/lossy nature of the required surface impedance of an ideal boundary anomalously performing reflection.

CONCLUSIONS

In recent literature on metasurfaces for the control of reflected waves, there have been many publications on the suggested use of reconfigurable anomalous reflectors for the engineering and optimization of the propagation environment. The vast majority of these works are based on the locally periodic approximation of the array response. That is, a locally defined reflection coefficient is used for calculating the reflected fields, and it is assumed that the fields can be somehow controlled by changing the parameters of the unit cell at each position. This is the conventional reflectarray antenna design assumption. It is known that this local design gives acceptable performance for moderate tilt angles (moderate deviations from the reflection law for uniform mirrors). However, for envisaged applications, it is required that beams can be directed in any desired direction, which needs more advanced designs. The majority of the current research in this field uses variations of periodic metasurfaces (diffraction grating design methods). Here, impressive results have been achieved in designing and realizing anomalous reflectors for fixed sets of incidence and reflection angles. The main problem is the realization of electrical reconfigurability: in this design approach, the period of the array is defined by the incidence and reflection angles, which demands the change of the array period by adjusting the tunable components of small unit cells.

On the other hand, the phased-array approach uses a set of periodically arranged antennas, and the geometrical period is fixed for all scan angles. However, the distribution of controllable loads is not periodic in this case, which requires the global optimization of the whole array for each scan angle. Moreover, it is not known if the optimization of loads of a conventional $\lambda/2$ -spaced array can lead to acceptable performance for the requirement of an extremely wide scan angle range. Approaches for optimizing the reactive loads of reflectarray antennas can be found, e.g., in [35] and [36], but it appears that more research on this design approach is needed.

ACKNOWLEDGMENT

This work was supported, in part, by the National Natural Science Foundation of China, under grant 12274339, the

European Integrated Training Network Meta Wireless and the U.S. Army Research Office, under grant W911NF-19-2-0244. Fu Liu also acknowledges financial support from Xi'an Jiaotong University and Shaanxi Province, China.

AUTHOR INFORMATION

Fu Liu (fu.liu@xjtu.edu.cn) is with the School of Electronic Science and Engineering, Faculty of Electronic and Information Engineering, Xi'an Jiaotong University, Xi'an 710049, China. His research interests include complex artificial electromagnetic materials (metamaterials and metasurfaces), transformation optics, and wireless power transfer. He is a Member of IEEE.

Do-Hoon Kwon (dhkwon@umass.edu) is with the Department of Electrical and Computer Engineering, University of Massachusetts Amherst, Amherst, MA 01003 USA. His research interests include antenna and array bandwidth properties, microwave metamaterials and metasurfaces, and cloaking. He is a Senior Member of IEEE.

Sergei Tretyakov (sergei.tretyakov@aalto.fi) is with the Department of Electronics and Nanoengineering, Aalto University, 02150 Espoo, Finland. His research interests include electromagnetic field theory, complex media electromagnetics, metamaterials, and microwave engineering. He is a Fellow of IEEE.

REFERENCES

- [1] C. Liaskos, S. Nie, A. Tsoliaridou, A. Pitsillides, S. Ioannidis, and I. Akyildiz, "A new wireless communication paradigm through software-controlled metasurfaces," *IEEE Commun. Mag.*, vol. 56, no. 9, pp. 162–169, Sep. 2018, doi: 10.1109/MCOM.2018.1700659.
- [2] M. Di Renzo et al., "Smart radio environments empowered by reconfigurable meta-surfaces: An idea whose time has come," *EURASIP J. Wireless Commun. Netw.*, vol. 2019, no. 1, pp. 1–20, May 2019, doi: 10.1186/s13638-019-1438-9.
- [3] E. Basar, M. Di Renzo, J. De Rosny, M. Debbah, M.-S. Alouini, and R. Zhang, "Wireless communications through reconfigurable intelligent surfaces," *IEEE Access*, vol. 7, pp. 116,753–116,773, Aug. 2019, doi: 10.1109/ACCESS.2019.2935192.
- [4] W. Tang et al., "The future of wireless? Subject editor spotlight on programmable metasurfaces," *IET Electron. Lett.*, vol. 55, no. 7, pp. 360–361, Apr. 2019, doi: 10.1049/el.2019.0471.
- [5] Q. Wu and R. Zhang, "Towards smart and reconfigurable environment: Intelligent reflecting surface aided wireless network," *IEEE Commun. Mag.*, vol. 58, no. 1, pp. 106–112, Jan. 2020, doi: 10.1109/MCOM.001.1900107.
- [6] Ö. Özdogan, E. Björnson, and E. G. Larsson, "Intelligent reflecting surfaces: Physics, propagation, and pathloss modeling," *IEEE Wireless Commun. Lett.*, vol. 9, no. 5, pp. 581–585, May 2020, doi: 10.1109/LWC.2019.2960779.
- [7] C. Huang, A. Zappone, G. C. Alexandropoulos, M. Debbah, and C. Yuen, "Reconfigurable intelligent surfaces for energy efficiency in wireless communication," *IEEE Trans. Wireless Commun.*, vol. 18, no. 8, pp. 4157–4170, Aug. 2019, doi: 10.1109/TWC.2019.2922609.
- [8] Q. Wu and R. Zhang, "Intelligent reflecting surface enhanced wireless network via joint active and passive beamforming," *IEEE Trans. Wireless Commun.*, vol. 18, no. 11, pp. 5394–5409, Nov. 2019, doi: 10.1109/TWC.2019.2936025.
- [9] M. Di Renzo et al., "Smart radio environments empowered by reconfigurable intelligent surfaces: How it works, state of research, and the road ahead," *IEEE J. Sel. Areas Commun.*, vol. 38, no. 11, pp. 2450–2525, Nov. 2020, doi: 10.1109/J SAC.2020.3007211.
- [10] M. Di Renzo, F. H. Danufane, and S. Tretyakov, "Communication models for reconfigurable intelligent surfaces: From surface electromagnetics to wireless networks optimization," *Proc. IEEE*, vol. 110, no. 9, pp. 1164–1209, Aug. 2022, doi: 10.1109/JPROC.2022.3195536.
- [11] N. M. Estakhri and A. Alù, "Wave-front transformation with gradient metasurfaces," *Phys. Rev. X*, vol. 6, no. 4, Oct. 2016, Art. no. 041008.
- [12] A. Epstein and G. V. Eleftheriades, "Synthesis of passive lossless metasurfaces using auxiliary fields for reflectionless beam splitting and perfect reflection," *Phys. Rev. Lett.*, vol. 117, no. 25, Dec. 2016, Art. no. 256103, doi: 10.1103/PhysRevLett.117.256103.
- [13] V. S. Asadchy, M. Albooyeh, S. N. Tsvetkova, A. Díaz-Rubio, Y. Ra'di, and S. Tretyakov, "Perfect control of reflection and refraction using spatially dispersive metasurfaces," *Phys. Rev. B*, vol. 94, no. 7, Aug. 2016, Art. no. 075142, doi: 10.1103/PhysRevB.94.075142.
- [14] A. Díaz-Rubio, V. Asadchy, A. Elsakka, and S. Tretyakov, "From the generalized reflection law to the realization of perfect anomalous reflectors," *Sci. Adv.*, vol. 3, no. 8, Aug. 2017, Art. no. e1602714, doi: 10.1126/sciadv.1602714.
- [15] V. S. Asadchy, A. Wickberg, A. Díaz-Rubio, and M. Wegener, "Eliminating scattering loss in anomalously reflecting optical metasurfaces," *ACS Photon.*, vol. 4, no. 5, pp. 1264–1270, Apr. 2017, doi: 10.1021/acspophotonics.7b00213.
- [16] J. Huang and J. A. Encinar, *Reflectarray Antennas*. Hoboken, NJ, USA: Wiley, 2008.
- [17] J. P. S. Wong, A. Epstein, and G. V. Eleftheriades, "Reflectionless wide-angle refracting metasurfaces," *IEEE Antennas Wireless Propag. Lett.*, vol. 15, pp. 1293–1296, 2016, doi: 10.1109/LAWP.2015.2505629.
- [18] Y. Ra'di, D. L. Soumas, and A. Alù, "Metagratings: Beyond the limits of graded metasurfaces for wave front control," *Phys. Rev. Lett.*, vol. 119, no. 6, 2018, Art. no. 067404, doi: 10.1103/PhysRevLett.119.067404.
- [19] D.-H. Kwon, "Lossless scalar metasurfaces for anomalous reflection based on efficient surface field optimization," *IEEE Antennas Wireless Propag. Lett.*, vol. 17, no. 7, pp. 1149–1152, Jul. 2018, doi: 10.1109/LAWP.2018.2836299.
- [20] A. Díaz-Rubio, J. Li, C. Shen, S. Cummer, and S. Tretyakov, "Power flow-conformal metamirrors for engineering wave reflections," *Sci. Adv.*, vol. 5, no. 2, Feb. 2019, Art. no. eaau7288, doi: 10.1126/sciadv.aau7288.
- [21] X. Wang, A. Díaz-Rubio, and S. A. Tretyakov, "Independent control of multiple channels in metasurface devices," *Phys. Rev. Appl.*, vol. 14, no. 2, Aug. 2020, Art. no. 024089, doi: 10.1103/PhysRevApplied.14.024089.
- [22] J. Budhu and A. Grbic, "Perfectly reflecting metasurface reflectarrays: Mutual coupling modeling between unique elements through homogenization," *IEEE Trans. Antennas Propag.*, vol. 69, no. 1, pp. 122–134, Jan. 2021, doi: 10.1109/TAP.2020.3001450.
- [23] R. J. Mailloux, *Phased Array Antenna Handbook*, 3rd ed. Norwood, MA, USA: Artech House, 2017.
- [24] R. E. Collin, *Foundations for Microwave Engineering*. New York, NY, USA: IEEE Press, 2001.
- [25] V. Popov, F. Boust, and S. N. Burokur, "Controlling diffraction patterns with metagratings," *Phys. Rev. Appl.*, vol. 10, no. 1, May 2018, Art. no. 011002, doi: 10.1103/PhysRevApplied.10.011002.
- [26] A. Epstein and O. Rabinovich, "Unveiling the properties of metagratings via a detailed analytical model for synthesis and analysis," *Phys. Rev. Appl.*, vol. 8, no. 5, Aug. 2017, Art. no. 054037, doi: 10.1103/PhysRevApplied.8.054037.
- [27] O. Rabinovich and A. Epstein, "Analytical design of printed circuit board (PCB) metagratings for perfect anomalous reflection," *IEEE Trans. Antennas Propag.*, vol. 66, no. 8, pp. 4086–4095, Aug. 2018, doi: 10.1109/TAP.2018.2836379.
- [28] O. Rabinovich, I. Kaplan, J. Reis, and A. Epstein, "Experimental demonstration and in-depth investigation of analytically designed anomalous reflection metagratings," *Phys. Rev. B*, vol. 99, no. 12, Mar. 2019, Art. no. 125101, doi: 10.1103/PhysRevB.99.125101.
- [29] T. B. Hansen, "Array of line sources that produces preselected plane waves," *Wave Mot.*, vol. 106, no. 20, Jun. 2021, Art. no. 102791, doi: 10.1016/j.wavemoti.2021.102791.
- [30] C. A. Balanis, *Antenna Theory: Analysis and Design*, 4th ed. Hoboken, NJ, USA: Wiley, 2016.
- [31] D.-H. Kwon, "Planar metasurface design for wide-angle refraction using interface field optimization," *IEEE Antennas Wireless Propag. Lett.*, vol. 20, no. 4, pp. 428–432, Apr. 2021, doi: 10.1109/LAWP.2021.3050194.
- [32] C. Yepes, M. Faenzi, S. Maci, and E. Martini, "Perfect non-specular reflection with polarization control by using a locally passive metasurface sheet on a grounded dielectric slab," *Appl. Phys. Lett.*, vol. 118, no. 23, Jun. 2021, Art. no. 231601, doi: 10.1063/5.0048970.
- [33] O. Rabinovich and A. Epstein, "Arbitrary diffraction engineering with multilayered multielement metagratings," *IEEE Trans. Antennas Propag.*, vol. 68, no. 3, pp. 1553–1568, Mar. 2020, doi: 10.1109/TAP.2019.2950813.
- [34] A. M. H. Wong and G. V. Eleftheriades, "Perfect anomalous reflection with a bipartite Huygens' metasurface," *Phys. Rev. X*, vol. 8, no. 1, Feb. 2018, Art. no. 011036, doi: 10.1103/PhysRevX.8.011036.
- [35] O. Tereshin, V. Sedov, and A. Chaplin, *Synthesis of Antennas on Wave-Delay Structures (in Russian)*. Moscow, Russia: Syaz, 1980.
- [36] G. Xu, V. G. Ataloglu, S. V. Hum, and G. V. Eleftheriades, "Extreme beam-forming with impedance metasurfaces featuring embedded sources and auxiliary surface wave optimization," *IEEE Access*, vol. 10, pp. 28,760–28,684, Mar. 2022, doi: 10.1109/ACCESS.2022.3157291.



Enabling Spherical Beam Coverage for Millimeter-Wave Stationary and Mobile Applications

A stackable patch antenna.

IMAGE LICENSED BY INGRAM PUBLISHING

Junho Park , Ahmed Abdelmottaleb Omar ,
Jonghyun Kim , Jaehyun Choi , Beakjun Seong ,
Jongwoo Lee, and Wonbin Hong 

The limited beam-scanning angles of planar phased arrays are one of the most critical challenges for millimeter-wave (mm-wave) wireless communication systems. This article proposes a new class of antenna topology, denoted as a *stackable patch antenna (SPA)*, that achieves near-spherical beam-steering coverage for mm-wave applications. The proposed SPA consists of two identical rectangular patch antenna elements. By separately controlling the magnitude and phase of the excitation ports, the proposed antenna can radiate in multiple directions that are normal or parallel to the patch elements. In addition, the proposed structure has the advantage of enabling end-fire radiation when the structure is encompassed by the full metallic frame of a device. This is accomplished without any deformation or modification of the metal frame.

As an example of a mm-wave device, the metal frame of a user device is modeled and fabricated. Near-isotropic

beamforming coverage is achieved by placing two SPA packages diagonally at each opposing corner of the mobile devices, resulting in maximizing the cumulative distribution function (CDF) specified by the 3rd Generation Partnership Project (3GPP) for proof-of-concept purposes. The measured beam-scanning performances in the normal and parallel directions to the patch are $\pm 43^\circ$ (peak gain: 8.4 dBi) and $\pm 33^\circ$ (peak gain: 5.1 dBi), respectively. No distinctive nulls in the end-fire direction exist despite the presence of the metallic frame. The feasibility of the SPA is further verified in indoor stationary scenarios. The access point (AP) based on the SPA improves the received power CDF corresponding to the lower percentile range by more than 3 dB compared to the reference scenario incorporating five APs with transceivers.

INTRODUCTION

Beamforming antenna technology is imperative to combat the large propagation loss at the mm-wave spectrum, for example, in user equipment (UE) attempts to connect to APs [1]. To

compensate for the narrow analog beamwidth of mm-wave, beam steering can be used to enable a wider angular coverage for mm-wave wireless devices. Naturally, the integration of phased-array antennas and improvement of beam coverage have been extensively studied and presented for mm-wave stationary and mobile applications.

Recently, an advanced packaging strategy integrated a multiple mm-wave beamforming antenna-in-package (AiP) within UE to mitigate hand blockage effects and maximize the beam coverage. In [2], two mm-wave AiP modules are conformally arranged along the top and bottom bezel area of a cellular device to maximize the beam-steering angles in the end-fire direction (in the direction parallel to the plane containing the antenna elements). The corner and the lateral area of the UE can be utilized to incorporate end-fire antennas [3], [4], [5], [6], [7], [8], [9], [10], [11]. The planar folded slot antennas [8] with a height profile of less than $1/9 \lambda_0$ are proposed for a multilayer substrate within UE. The horizontal metal strip line-coupled dipoles and vertical magnetoelectric monopoles are complementally integrated to achieve an end-fire radiation with dual polarization [10]. In [11], the vertically polarized electric dipole is formed to generate end-fire beams and fit at the edge of UE. In addition, the phased arrays can be integrated inside the back cover of cellular devices to enable broadside beamforming and mitigate the antenna placement restrictions due to the real estate issues within UE [12].

However, most of the solutions have not taken into account the metallic frame of the UE [8], [13], [14], [15], [17], [18], [19]. The metal frame of a wireless device is important for its mechanical stability, and it also functions as a protective frame of the device. However, from the vantage point of the antenna, the metal frame functions as an obstacle for the end-fire radiation mode. When the metal frame is placed in front of conventional end-fire antennas, the radiation patterns are severely distorted and reflected. This becomes extremely problematic for mm-wave beamforming antennas since the antenna beam direction becomes out of sync with the corresponding beamforming algorithm. The end-fire radiation plays an important role in stabilizing the communication link [20].

Various solutions have been studied to overcome the blockage of metallic frames in mm-wave mobile devices. One solution [21], [22] is to etch mm-wave slot arrays directly on the metal frame. The three-element phased array can be integrated into a UE by forming a $20 \times 3.5\text{-mm}^2$ window in the metal frame [23]. In [24], a $25 \times 10 \times 6\text{-mm}$ aperture is cut into the metal frame to place a mm-wave module. In [25], numerous longitudinal slots are cut out of the metal frame to utilize it as an electromagnetic coupling structure so that horizontally polarized bow tie arrays can radiate through the frame with enhanced beam-steering gain. Similarly, two rows of grooves

From the vantage point of the antenna, the metal frame functions as an obstacle for the end-fire radiation mode.

filled with dielectric material were formed on the frame to overcome the main beam blockage [26]. However, these solutions require modification of the metal frame, which increases the complexity of the fabrication of the metal frame and reduces its mechanical strength. In addition, the integration of phased-array antennas within the metallic frame can cause an undesirable short circuiting effect, which significantly degrades the performance of the sub-6-GHz antennas [27].

The wide-beam lens and antenna designs for mm-wave stationary applications have received great interest. A gradient index lens is presented to overcome the effective aperture size reduction caused by beam steering, which is an intrinsic property of all types of planar arrays [28]. The fabricated prototype demonstrates a maximum gain of 21.2 dBi and a wide scanning range up to $\pm 58^\circ$ within a 3.1-dB scan loss. In [29], a dipole-based antenna topology including a substrate-integrated cavity is proposed for wide-angle beam-scanning applications in the H-plane. The experimental results show that the proposed antenna achieves solutions with a wide beamwidth of more than 180° and a wide beam-scanning ability up to 65° , with a low scanning loss of 3.7 dB and a low sidelobe level of -15 dB. However, most studies have not taken into account the compatibility with current beamforming phased-array AiP architectures and scalability for implementing spherical beamforming antenna systems for both stationary and mobile applications.

Setting the challenges surrounding the metal frame aside, achieving a spherical beam-steering antenna for mm-wave mobile and stationary applications remains one of the most critical challenges within the wireless community at present. This article proposes a new class of antenna topology, denoted as the SPA, that achieves near-spherical beam-steering coverage for mm-wave applications. As illustrated in Figure 1, the SPA concept can be applied to two stacked compact AiPs within mobile applications, contributing to the enhancement of spherical beam coverage, which fundamentally eliminates the need for any deformation of the metal frame. In addition, the stationary application (e.g., fixed wireless infrastructure) can incorporate the SPA-based AP, which not only improves the beam coverage but also reduces the number of APs as well as the cost of installing APs.

SPA FOR SPHERICAL BEAM COVERAGE

CONCEPTUAL DESIGN

The SPA element consists of two identical microstrip patch antennas, which operate at the fundamental TM_{01} mode. A single microstrip element using a low-temperature cofired ceramic (LTCC) process is devised as an example and illustrated in Figure 2(a). The multilayer printed circuit board fabrication process may be utilized as well. The LTCC package

contains 10 stacked layers, and each layer features a thickness of 100 μm with relative permittivity $\epsilon_r = 5.9$ and loss tangent $\tan \delta = 0.002$. Silver metal layers feature a thickness of 10 μm . The diameters of the vias and capture pads are 100 μm and 150 μm , respectively. The patch is excited by a vertical probe, which is protruding through the ground plane. Strip-line topology is employed to guide the electromagnetic wave from the feeding port to the patch. The strip line is guided by electrical walls created by vias to reduce the coupling effect with other elements when forming the array configuration. The resonant frequency of the patch is realized by controlling the length of the patch (l_p) and is designed to operate at 28 GHz for exemplification. The impedance of the strip line is determined by the width of the line (l_f) and the height of the substrate (h_f). Two identical patches are arranged symmetrically with a separation distance (d_s) in the z -direction, as shown in Figure 2(b).

Two important parameters affect the radiation characteristics of the SPA: one is the relative permittivity of the substrate, and the other is the separation distance (d_s). The relative permittivity of the LTCC ($\epsilon_r = 5.9$) is sufficient for the fringing fields to be concentrated in the substrate at the radiating edges [30]. Moreover, the thickness of commercially available recent mobile devices is typically fewer than 10 mm, resulting in an electrically small separation distance (d_s). For clarity, in this article, the far-field radiation directions of the SPA are defined and classified into the broadside radiation ($\pm z$) and the end-fire radiation/out-of-phase mode ($\pm x$ and $\pm z$), and the operating frequency is 28 GHz.

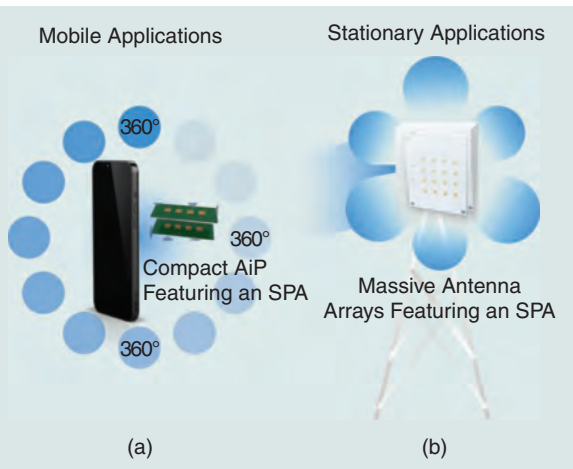


FIGURE 1. The SPA concept for the realization of spherical beam coverage of mm-wave mobile and stationary applications. (a) A 1×4 phased array SPA is integrated within a present-day mobile device featuring a metal frame to enable end-fire radiation, which can significantly contribute to achieving spherical coverage of the mobile device. (b) The SPA concept is applied to stationary applications featuring a large-scale phased array of more than 16 antenna elements. The APs consisting of the 4×4 phased arrays with SPA technology efficiently improve the beam coverage, which is explained in the “Feasibility of the Spa in Indoor Stationary Scenarios” section.

OPERATING PRINCIPLE

A 1×4 phased array SPA is illustrated in Figure 2(c). The separation between the antenna elements is 5 mm ($0.47 \lambda_0$ at 28 GHz), which is smaller than a half wavelength to avoid grating lobes during beam scanning. The proposed antenna can achieve various radiation patterns by adjusting the magnitude and phase of the signal applied at each port. Figure 3(a) and (b) shows the simulated 3D radiation plot of the simple 1×4 patch array when the top/bottom four ports are activated with in-phase excitation. These broadside radiation modes are defined as the top broadside and bottom broadside modes, respectively.

When activating all ports and when a phase difference of 180° is applied between the top and bottom patch elements, end-fire radiation is accomplished, and the simulated 3D radiation

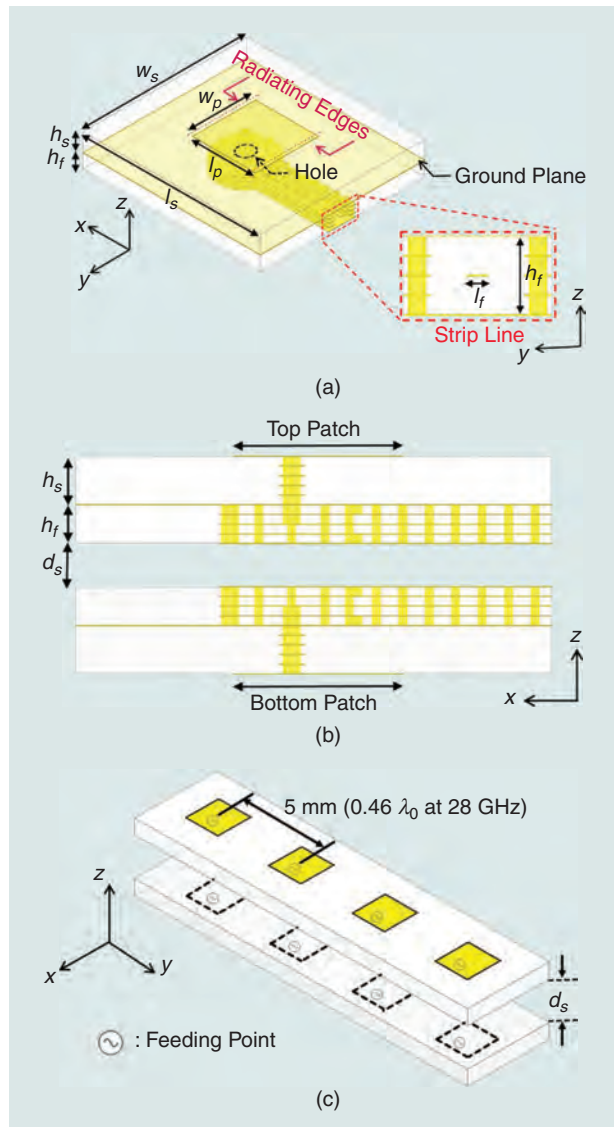


FIGURE 2. (a) The single microstrip element. (b) A cross section of the SPA concept. (c) The basic structure of the SPA array ($w_s = 5 \text{ mm}$, $w_p = 1.92 \text{ mm}$, $l_s = 5.4 \text{ mm}$, $l_p = 1.92 \text{ mm}$, $h_s = 0.54 \text{ mm}$, $h_f = 0.43 \text{ mm}$, $l_f = 0.12 \text{ mm}$, and $d_s = 4.9 \text{ mm}$).

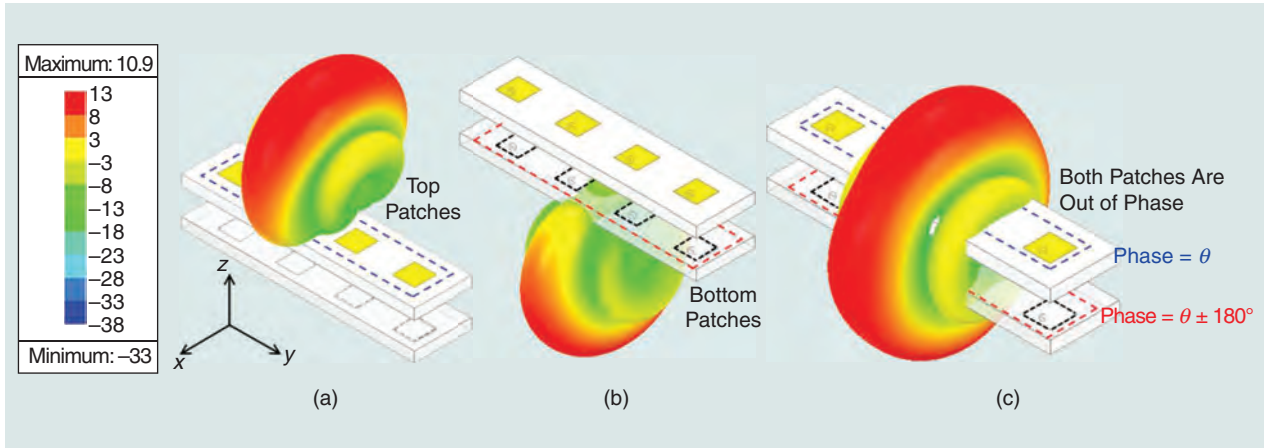


FIGURE 3. Simulated 3D radiation patterns of the (a) top broadside mode, (b) bottom broadside mode, and (c) out-of-phase mode.

plot is shown in Figure 3(c). Although the phase difference between the top and bottom patches is 180° , bidirectional broadside radiation can be achieved. This is due to the fact that the ground planes between the patch elements prevent electric currents that are out of phase from being mutually canceled. In addition, the phase difference of the fringing fields at the radiating edges is near zero, resulting in vertically polarized (z -axis) end-fire radiation (please refer to [19, Figure 3]). This radiation mode is defined as the out-of-phase mode/end-fire radiation. The maximum realized gain shown in Figure 3(a) and (b) is 10.9 dBi in the $+z$ -and $-z$ -directions, respectively, while the maximum realized gain in Figure 3(c) is 8 dBi in the $\pm z$ -direction. The intensity of the electric currents induced on the patches is identical in all modes. However, there is a gain difference between the broadside and out-of-phase modes in the broadside direction. This is attributed to the out-of-phase mode, in which a fraction of the fringing fields contributes to radiation in the end-fire direction instead

of the broadside direction, resulting in a relatively reduced realized gain compared to the broadside mode.

It is worth mentioning that each antenna can be designed independently, regardless of the presence of the antenna on the opposite layer because the two patch antennas on the top and bottom layers are electrically isolated through the ground plane. The input impedance (Z_{in}) at the center of the patch is ideally zero so that the coaxial feeding point is offset along the x -axis at the center for 50Ω impedance matching. Consequently, the fringing field at the radiating edges in the $+x$ -axis direction, which is near the feeding point, is stronger than the $-x$ -axis. Logically, it is advantageous to place the feeding point of the patch in the $+x$ -direction. The realized gains of the out-of-phase mode in the $+x$ - and $-x$ -axes are 6.3 and 3 dBi, respectively.

PARAMETRIC STUDY

A parametric study regarding the effect of d_s is conducted to further examine the SPA concept for metal frame devices. To study the effect of the separation distance of an SPA, d_s is varied from 0 to 7.5 mm. The separation distance has an influence on the radiation pattern in the out-of-phase mode, as shown in Figure 4. When d_s equals 0 mm, the most ideal dimension of the SPA, an omnidirectional radiation pattern can be achieved in the E-plane ($x-z$ -plane). As d_s increases, the omnidirectional radiation pattern in the E-plane is deformed. The fringing fields from the top and bottom patches are vertically polarized, which are considered as two vertically polarized element arrays separated by distance d_s [16]. Considering that the thickness of present-day mobile devices ranges from approximately 7 (0.65 λ_0) to 8 mm (0.74 λ_0), the configured distance between the patch elements remains within the realistic and practical range.

INTEGRATION WITH THE METAL FRAME

EFFECT OF THE METAL FRAME

To compare the radiation characteristic of the SPA in free space with the metal frame-integrated situation, an antenna

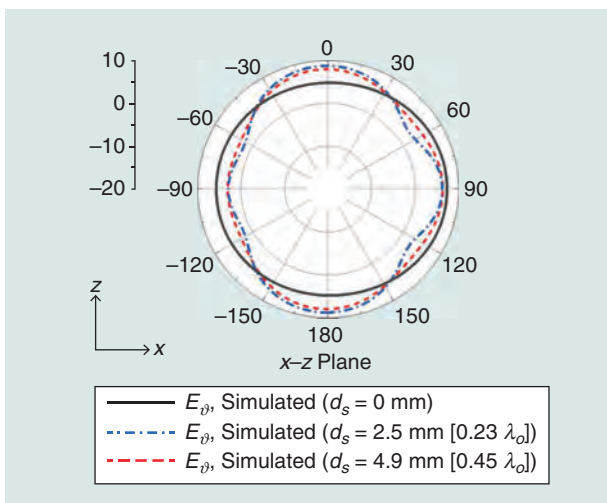


FIGURE 4. The variation of the radiation pattern in the E-plane in the out-of-phase mode according to the separation distance (d_s).

package is designed, as shown in Figure 5(a). To enhance the spherical coverage, four patch elements are arranged along the y -axis (SPA 1) to achieve end-fire radiation along the x -axis, and the other four elements are arranged along with the x -axis (SPA 2) to achieve end-fire radiation along the y -axis. The metal frame is designed to be $74 \times 149 \times 7.6$ mm in size, emulating the real-life chassis of present-day user devices. The antenna package is symmetrically duplicated in the z -axis to establish the SPA configuration and integrated with the metal frame, as illustrated in Figure 5(b).

The simulated E-field distribution of the SPA in the out-of-phase mode without the metal frame is plotted in Figure 6(a). As mentioned earlier, the fringing fields induced by patches at the top and bottom are summed in the end-fire direction, resulting in vertically polarized end-fire radiation. Figure 6(b) shows the E-field distribution in the end-fire direction when the metal frame is included. As the fringing field propagates along the x -axis, it encounters the metal frame. However, the

SPA can generate the radiation in the end-fire direction without any deformation of the metal frame by synthesizing the fringing field beyond the metal frame.

EFFECT OF THE METAL FRAME'S WIDTH AND ITS DISTANCE FROM THE ANTENNA ARRAY

The radiation property of the proposed SPA is studied according to the distance between the antenna array and the metal frame (df) as well as the width of the metal frame (wf), as illustrated in Figure 7. The values of the realized gain in Figure 7(b) and (c) are extracted at the end-fire direction in the end-fire mode. It can be seen from the realized gain in Figure 7(b) that, as the distance between the metal frame and the antenna “ df ” increases, the realized gain in the end-fire direction increases. This is attributed to an increment in fringing fields as the ground plane in front of the antenna increased. A distance of 1.7 mm is chosen as a reasonable distance. A smaller distance may be selected on the cost of realized gain in the end-fire direction.

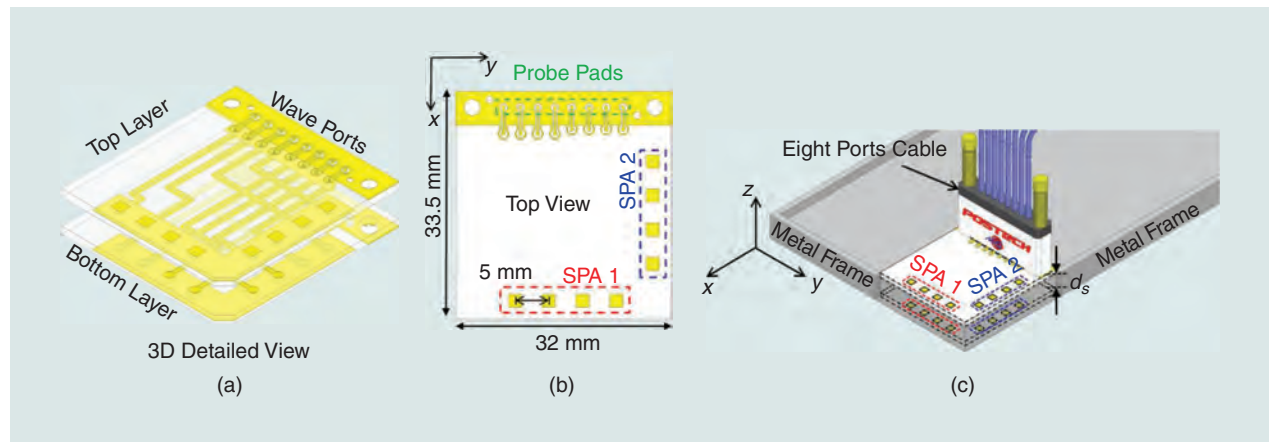


FIGURE 5. Illustration of (a) 3-D view of the proposed SPA package. (b) The top view of the proposed SPA package. (c) The SPA packages integrated into metal frame. (Some part of the metal frame and 8 ports cable on the bottom side are removed for a clear view, $d_s = 4.9$ mm.)

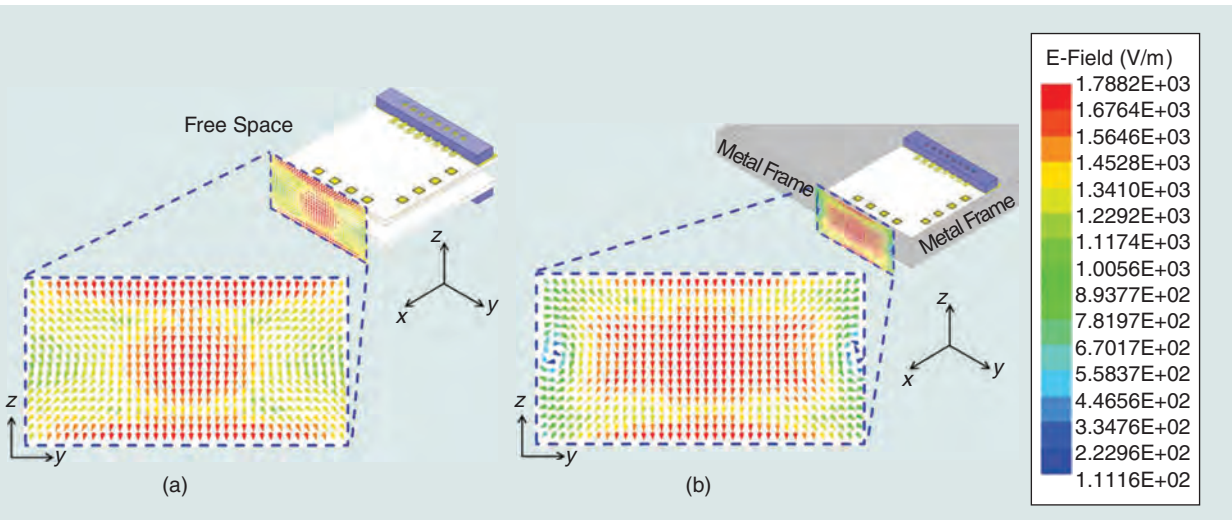


FIGURE 6. The simulated E-field distribution of the SPA under the (a) free space condition and (b) metal frame integrated condition.

Regarding the width of the metal frame, it is confirmed from Figure 7(c) that the realized gain of the proposed array is proportional to w_f . This is mainly attributed to the thickened metal frame improving the coupling intensity between fringing fields from the SPA. In addition, the beam shape, not shown here, is well maintained regardless of the width of the metal frame. Although a thick metal frame can improve the realized gain of the proposed SPA mode, a thin metal frame design is preferred in present-day mm-wave devices. It is worth mentioning that the \pm broadside realized gain almost does not change in both simulations.

EFFECTIVE ISOTROPIC RADIATED POWER OF AN SPA INTEGRATED IN METAL FRAME USER DEVICES

Conventional planar antenna arrays inherently exhibit a quasi-hemisphere spatial coverage. Therefore, isotropic spherical coverage cannot be achieved even if two planar antenna arrays are placed on the front and back sides of the device. Moreover, conventional broadside antenna arrays cannot achieve radiation in the forward direction of the metal frame, i.e., the $\pm x$ - and $\pm y$ -axes. A quasi-isotropic spherical coverage can be achieved by using the SPA concept and placing two SPA modules on diagonally opposing sides/edges of a mobile

By arranging the SPA packages as in configuration 3, it is possible to meet both quasi-isotropic spherical coverage and the 3GPP specification.

device, as shown in Figure 8(a). One of the two antenna modules can be activated using the antenna diversity method. It is worth mentioning that L-shaped metal blockages are employed behind antenna arrays to mimic the effect of the main board and battery of the mm-wave device.

To evaluate the effect of the SPA on spherical beamforming coverage, the total beam-scanning patterns and CDF of the effective isotropic radiated power

(EIRP) distribution with three array topologies are extracted and presented in Figure 8(b) and (c), respectively. First, in configurations 1 and 2, a single SPA module is placed at the corner of the mobile device. The y -oriented 1×4 SPA array is activated in configuration 1, while the x - and y -oriented 1×4 SPA arrays are activated in configuration 2. To enhance the spherical beamforming coverage, an additional SPA module is placed diagonally, as shown in configuration 3. Configuration 3 can achieve an isotropic spherical coverage by controlling the magnitude (on/off) and phase of each port in a switched diversity manner. Twenty-one beams are used per each SPA module to calculate the total beam-scanning patterns and CDF of the EIRP distribution. The total beam-scanning patterns of each configuration are simulated and select the highest realized gain at every

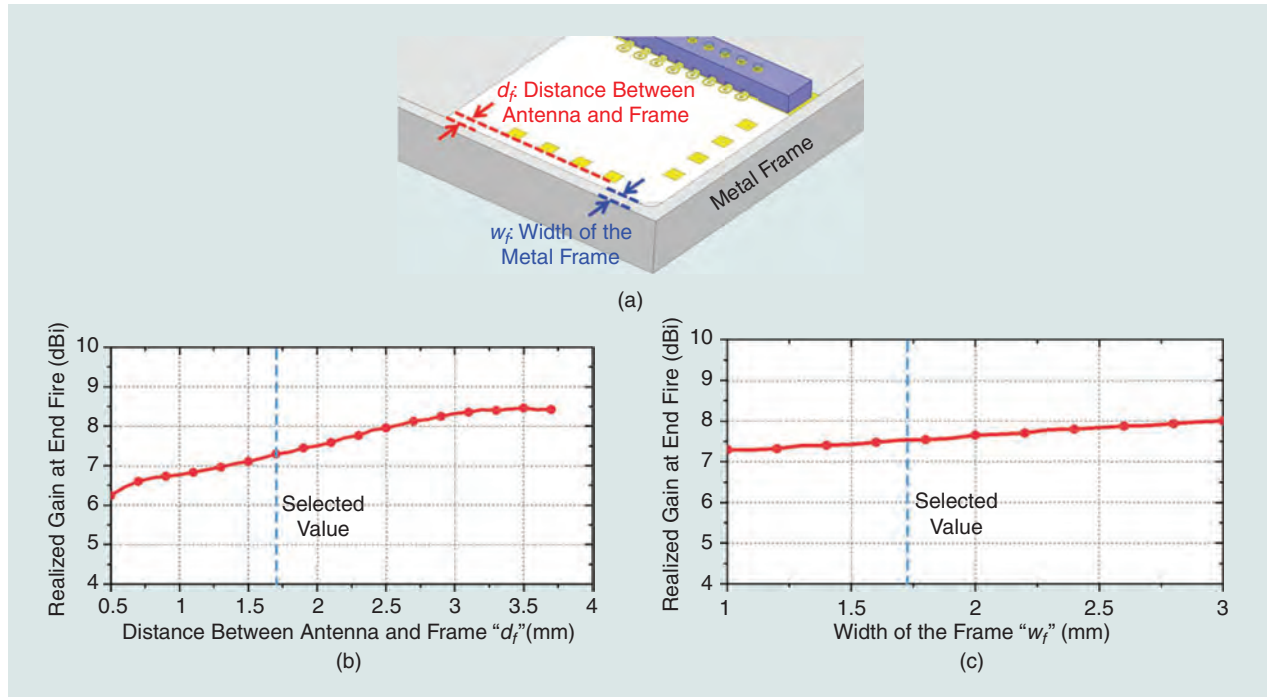


FIGURE 7. The simulated effect of two parameters on the end-fire realized gain. (a) The simulation model. (b) The effect of changing the distance between the antenna array and the metal frame. (c) The effect of changing the width of the metal frame.

spherical angular point (φ, θ) . Then EIRP (φ, θ) is calculated as follows:

$$\text{EIRP}(\varphi, \theta) = \text{Realized gain } (\varphi, \theta) + P_{\text{out}} \quad (1)$$

P_{out} is the total radio-frequency integrated circuit (RFIC) output power to each antenna port, and then the EIRP (φ, θ) is normalized to be 22.4 dBm as specified by 3GPP regarding the UE minimum peak EIRP for power

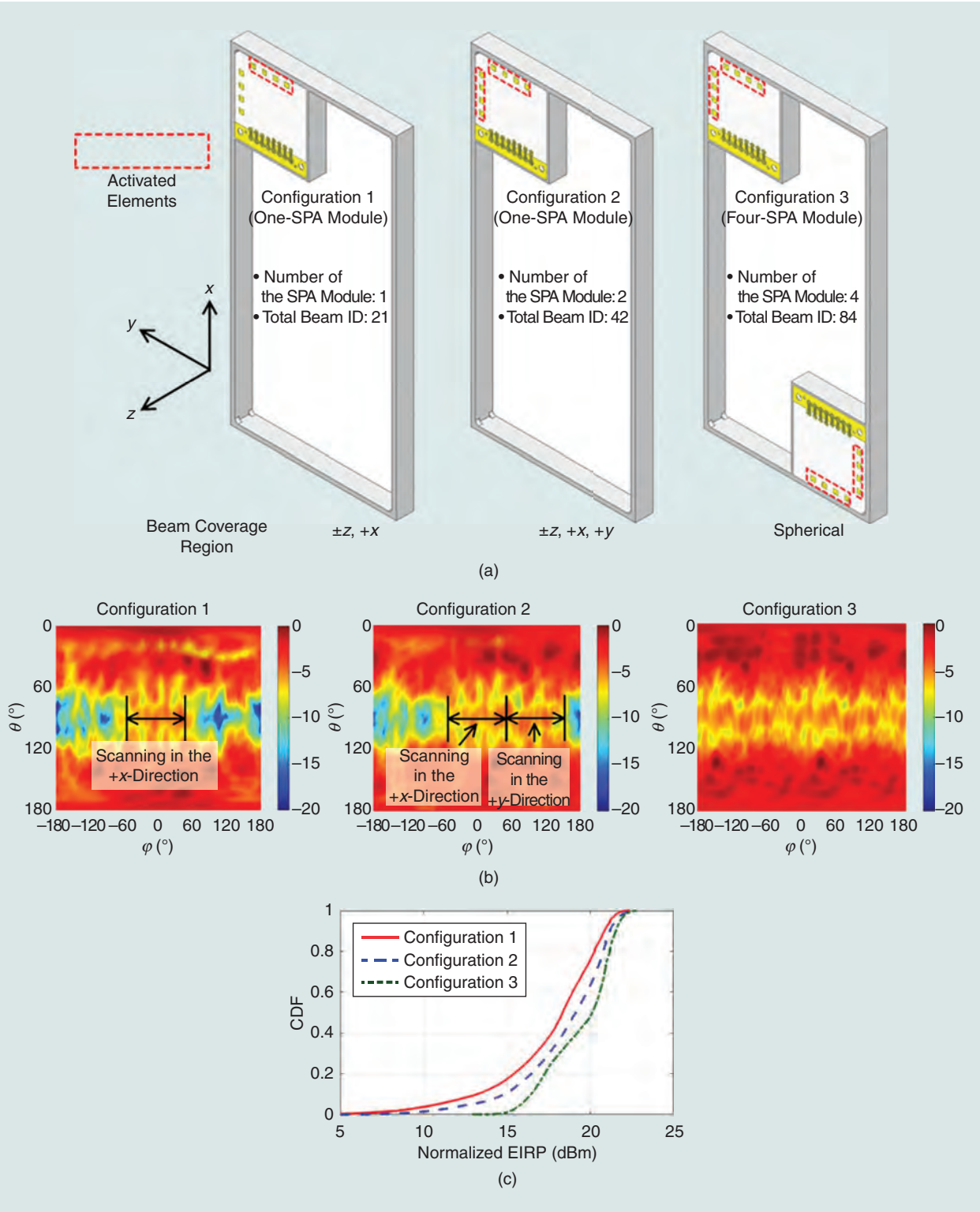


FIGURE 8. Quasi-isotropic spherical coverage. (a) Three SPA configurations. (b) The total beam-scanning patterns. (c) The CDF of the EIRP distribution.

class 3. Therefore, the peak EIRP values are aligned through three curves. These simulated CDF curves are shown graphically in Figure 8(c). The difference in the CDF curve between configurations 1 and 2 results from the absence or presence of radiation in the $+y$ -axis. This can be further examined in Figure 8(b) to quantify the difference in the beam coverage region between configurations 1 and 2. When comparing CDF curves of configurations 2 and 3, configuration 3 is clearly improved, which is attributed to the existence of beam coverage in the $-x$ - and $-y$ -directions, also illustrated in Figure 8(b). This ascertains the fact that higher spherical coverage is realized through configuration 3 compared to configuration 2.

From the perspective of the 3GPP specification, configuration 1 requires at least 4.9 dBm of accepted output power (P_{out}) to meet the 11.2-dBm value at $CDF = 50\%$ [see Figure 8(c)]. Given the fact that the recently released output power of the 5G RFIC specification is from 10 to 16 dBm, configuration 1 satisfies the requirement of the EIRP at both $CDF = 100\%$ and 50% , which are specified in 3GPP. Therefore, by arranging the SPA packages as in configuration 3, it is possible to meet both quasi-isotropic spherical coverage and the 3GPP specification.

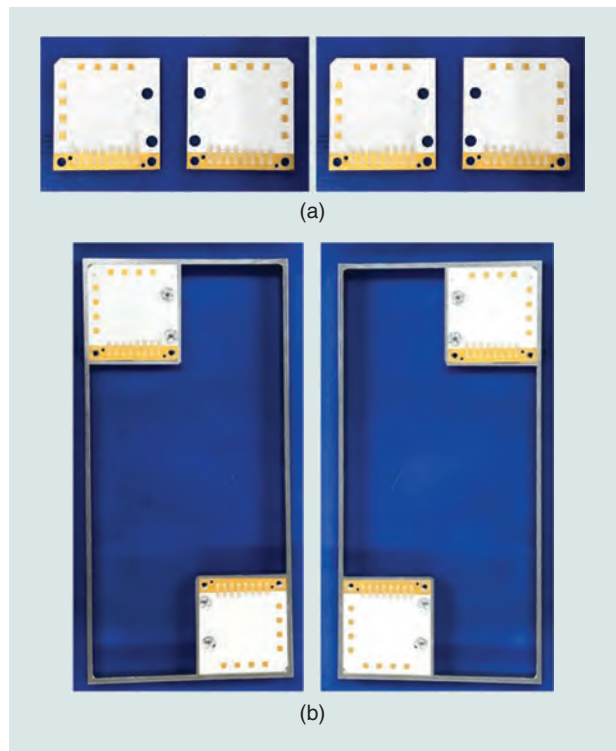


FIGURE 9. Photographs of the (a) fabricated SPA packages and (b) front and backside views of the SPA with a metal frame.

It should be noted that an SPA can be integrated into mobile devices in a planar manner without distorting the metal frame and achieve near-equal spherical coverage as well.

PROTOTYPE AND MEASUREMENT

FABRICATION

A prototype of the SPA package is fabricated using an LTCC processing technique as shown in Figure 9(a). A metal frame made of aluminum is shown in Figure 9(b). A series of plastic pillars are used to fix the SPA packages to the fabricated metal frame. Simulations indicate that these pillars have a minimal effect on the antenna topology.

EXPERIMENTAL RESULTS

The S-parameters are measured using an N5247A Keysight PNA-X. The input reflection coefficients of the eight ports are illustrated in Figure 10. GGB Industries picoprobe ground-signal-ground (GSG) wafer probe tips featuring 500- μ m pitch are used to contact GSG pads [see Figure 5(a)]. Simulation results confirm the interelement isolation of more than 16 dB at 26.5–29.5 GHz. The discrepancy between the simulated and measured results is due to the fabrication error of the LTCC process and the deviation in substrate material properties.

The far-field radiation patterns of the fabricated SPA packages with metal frames are measured using an anechoic far-field chamber at Pohang University of Science and Technology, Pohang, Republic of Korea. The measurement setups for both the broadside and end-fire modes are shown in Figure 11. The beamforming capabilities of the SPA are accessed using a mm-wave RF reference board consisting of 16 RF channels. Two eight-port multi-coaxial cables are utilized to excite the 16 ports of the SPA packages. However, the magnitude and phase can be scaled in 0.5-dB and 5° steps, respectively, by controlling the GUI through the Ethernet interface. Therefore, it is possible to calibrate the power and phase before measuring the radiation patterns. All measurements were made in the environment where antennas are integrated into the fabricated metal frame.

The measured and simulated radiation patterns of SPA 1 and SPA 2 [see Figure 5(b)] in the E-plane at 28 GHz are illustrated in Figures 12(a) and (b) and 13(a) and (b), respectively. They were measured from -90° to 90° due to the limitation of the anechoic far-field chamber environment. The radiation patterns of broadside mode on the opposite side are not presented due to the symmetric configuration. The radiation pattern of the broadside mode of SPA 1 is slightly distorted due to blockage and scattering caused by adjacent cables. It is ascertained that a good correlation between the simulated and measured radiation patterns is achieved.

The beam-steering performances of SPA 1 are illustrated in Figure 11(c)–(e). The measured peak gains of the antenna array in broadside mode and out-of-phase mode are 8.4 and

4.98 dBi, respectively. Similarly, the beam-steering performances of SPA 2 are illustrated in Figure 13(c)–(e). The measured peak gains in broadside mode and out-of-phase mode are 8.3 and 5.1 dBi, respectively. It is worth mentioning that the simulated antenna efficiency of the SPA features more than 70%, including the insertion loss of the RF connector at 28 GHz. Table 1 summarizes the performance comparison with recently reported 5G mobile antennas, taking into account the metal frame. It should be noted that an SPA can be integrated into mobile devices in a planar manner without distorting the metal frame and achieve near-equal spherical coverage as well.

FEASIBILITY OF THE SPA IN INDOOR STATIONARY SCENARIOS

Two indoor propagation scenarios are verified through a 3D ray shoot-and-bound (SBR) simulation at a center frequency of 28 GHz to estimate the beam coverage of the large-scale AiP featuring an SPA, as shown in Figure 14. The length and width of the hallway are 600 and 150 m, respectively, and the ceiling height is 4.7 m. The entire hallway is constructed of concrete material with a thickness of 30 cm. The four-element phased array with 8-dBi gain is used as a receiver above ground to collect data.

In the reference scenario [Figure 14(a)], five APs consisting of 4×4 phased arrays are deployed at 100-m intervals on

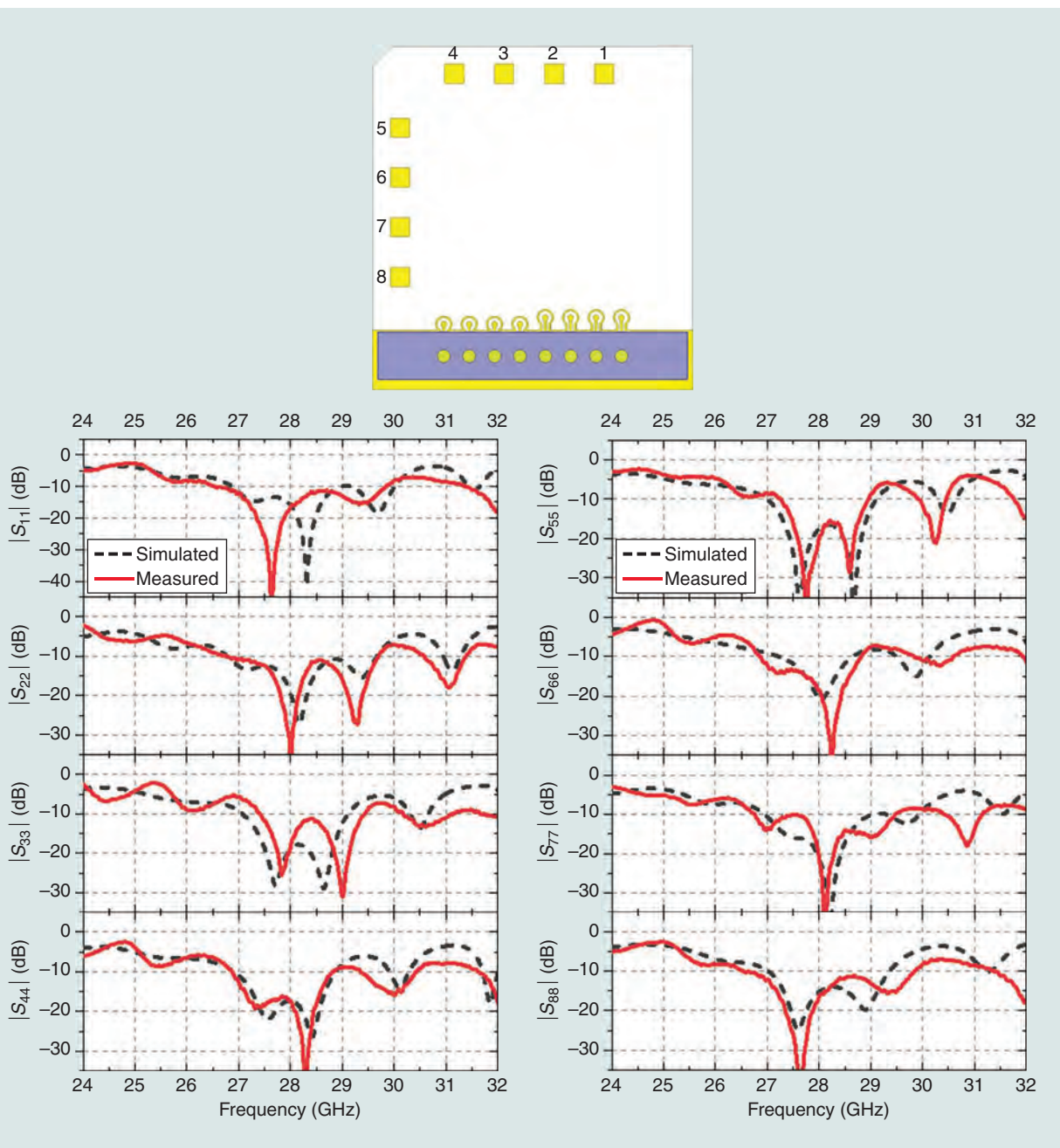


FIGURE 10. The simulated and measured reflection coefficients.

the ceiling. In the proposed scenario, three APs consisting of 4×4 phased arrays with SPA technology are deployed at intervals of 150 m on the ceiling. Each AP operates as a transmitter to which a total transmit power of 30 dBm is applied. The UE,

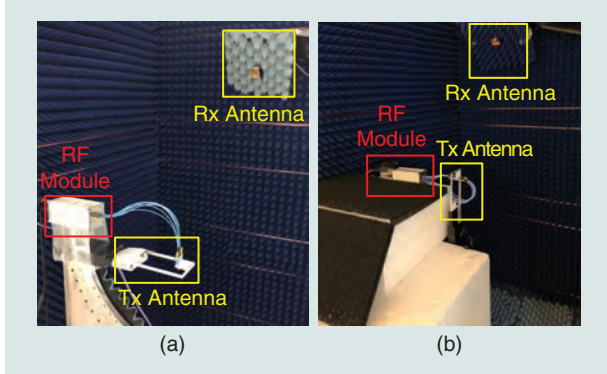


FIGURE 11. The measurement setup of the proposed SPA with a metal frame: the (a) broadside mode and (b) out-of-phase mode. Rx: receiver; Tx: transmitter.

which steers the directional beam toward the ceiling direction, moves from the start point to the endpoint at a linear interval of 5 m to accurately collect the received power data. Since interferences from neighboring APs are not considered, the results from each AP and UE are extracted separately and overlapped. It is confirmed from Figures 15 and 16 that, despite using only three ceiling-type APs, an AiP with an SPA improves the received power CDF corresponding to the lower percentile range by more than 3 dB compared to the reference scenario including 5 APs.

CONCLUSIONS

A concept of an SPA has been devised for mm-wave mobile and stationary applications for the first time. It has been verified that the proposed structure has the advantage of relieving the recently arising main beam blockage issue without requiring deformation of the metal frame. The isotropic coverage has been accomplished by placing two SPA packages diagonally at two corners of a mobile device as an example. This concept is exemplified at 28 GHz for a proof of concept and is ascertained

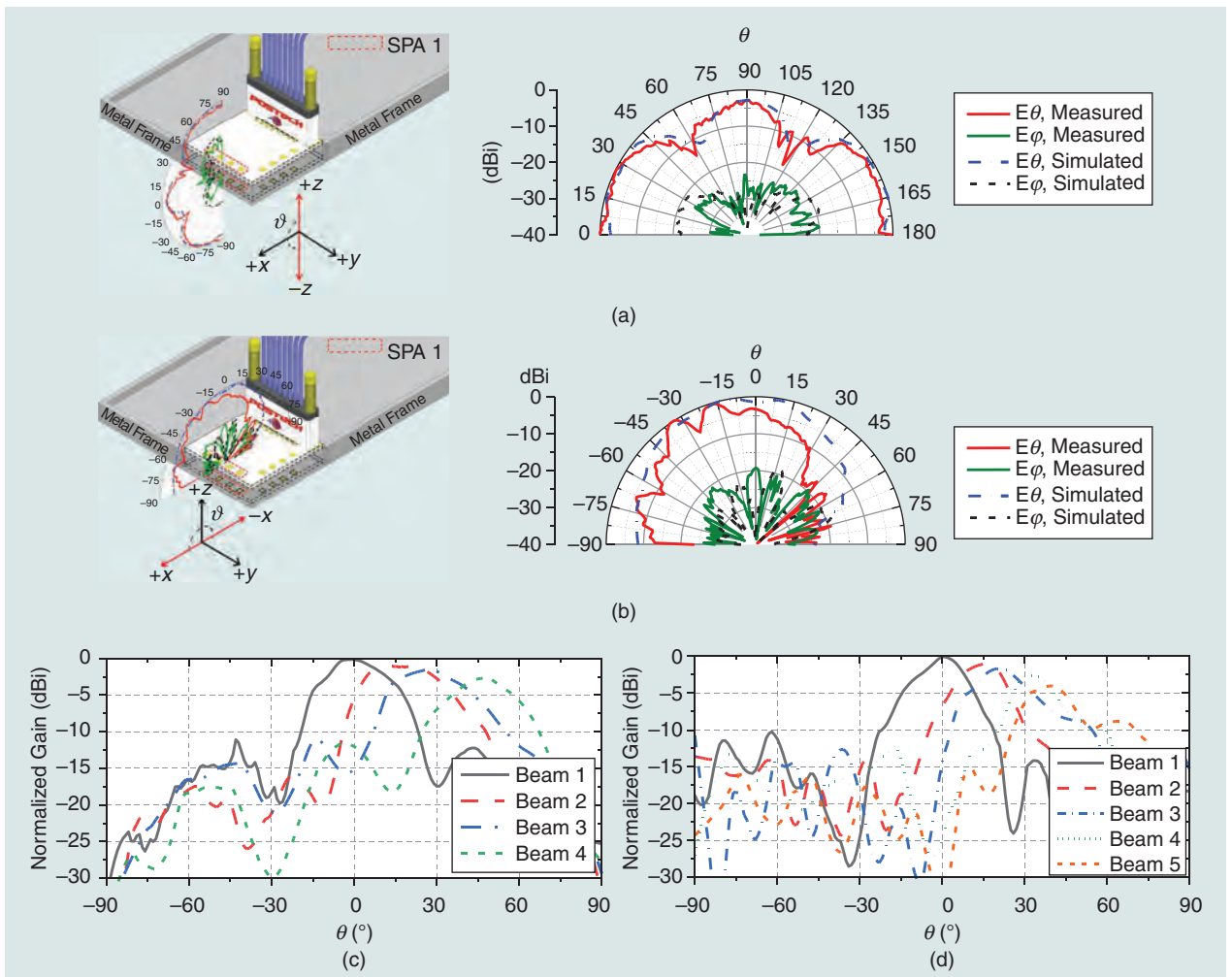


FIGURE 12. The measured and simulated normalized far-field radiation patterns of SPA 1 in the E-plane in the (a) out-of-phase mode and (b) top broadside mode as well as the measured normalized far-field beamforming pattern in the H-plane in the (c) broadside mode and (d) out-of-phase mode.

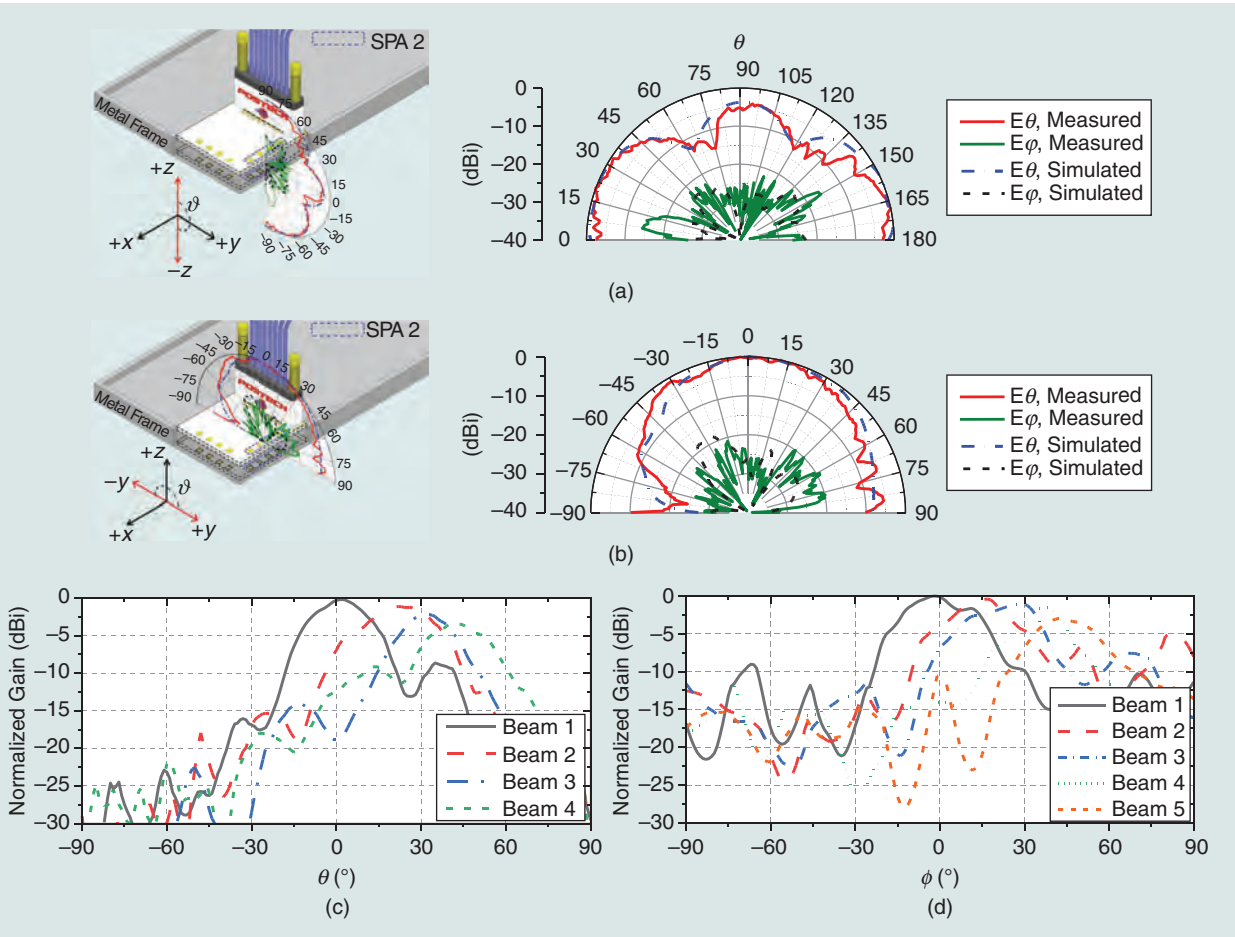


FIGURE 13. The measured and simulated normalized far-field radiation patterns of SPA 2 in the E-plane in the (a) out-of-phase mode and (b) top broadside mode as well as the measured normalized far-field beamforming pattern in the H-plane in the (c) broadside mode and (d) out-of-phase mode.

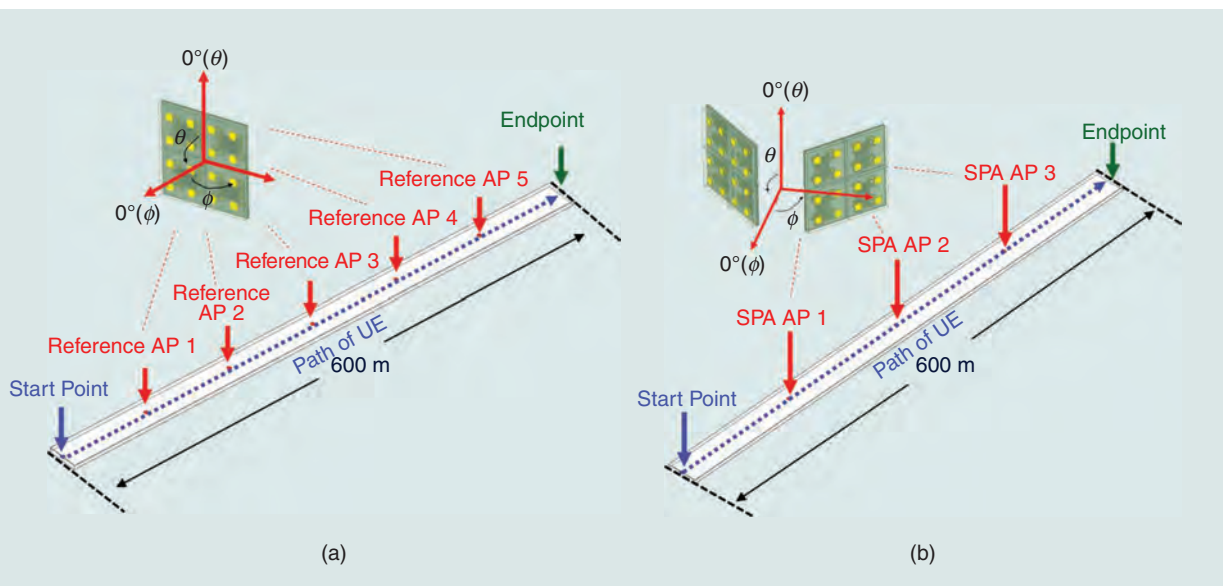


FIGURE 14. The mm-wave indoor link deployment. (a) The 4×4 AiPs are deployed at an interval of 100 m on the ceiling. (b) The 4×4 AiPs featuring an SPA are deployed at an interval of 150 m on the ceiling.

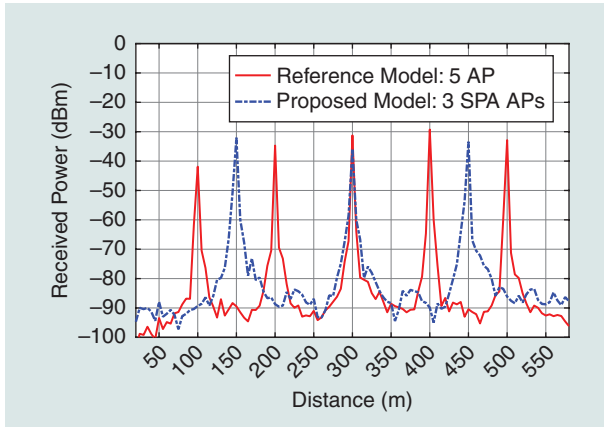


FIGURE 15. The received power versus UE distance from the starting point in two indoor link deployments.

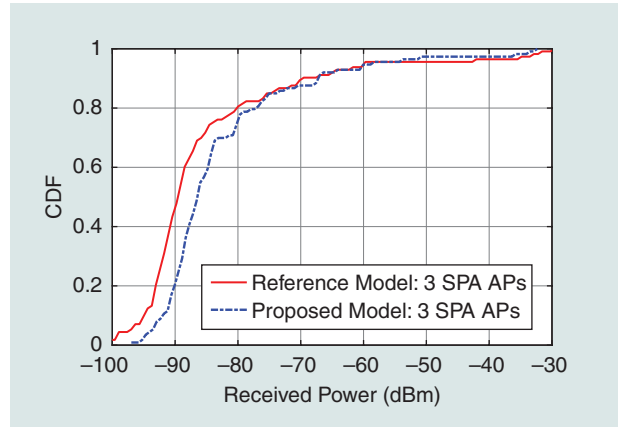


FIGURE 16. The CDF of the received power in two indoor link deployments.

TABLE 1. A COMPARISON WITH THE MM-WAVE ANTENNAS INTEGRATED INTO 5G METAL FRAME MOBILE DEVICES.

Reference	[13]	[14]	[15]	[8]	This Work
Topology	Two 1×8 cavity-backed slot array	1×4 Vivaldi array	1×4 bow tie array	1×4 Vivaldi array	Diagonally placed SPA packages
Pattern	End fire	End fire	End fire	End fire	Switchable End fire/broadside
Bandwidth (GHz)	27.5–30	25–30	22–28.4	25.3–27.5	27–28.5
Deformation of the metal frame	Yes	Yes	Yes	Yes	No
Beam coverage region (axis)	$\pm y$	$+x$	$+x$	$+x$	Spherical ($\pm x, y$, and z)

to satisfy the CDF benchmark in accordance with the 3GPP standards. The measured maximum realized gains in the broadside and end-fire directions are 8.4 and 5.1 dBi, respectively. The measured beam-steering performances in the broadside and end-fire directions are $\pm 43^\circ$ and $\pm 33^\circ$, respectively. The system-level SBR simulation demonstrates that AiP modules with the SPA significantly enhance the spherical coverage CDF of fixed ceiling-type APs by more than 3 dB in lower percentile ranges with fewer transceivers. These results prove that the proposed SPA technology efficiently improves the spherical beamforming coverage in both mobile and stationary scenarios.

ACKNOWLEDGMENT

Junho Park and Ahmed Abdelmottaleb Omar equally contributed to this work. This work was supported in part by Institute of Information and Communications Technology Planning and Evaluation grants funded by the Korea government (MSIT) (2020-0-00858, 2018-0-00823) and in part by the Material Component Technology Development Program funded by the Ministry of Trade, Industry, and Energy (Korea) (20010540).

AUTHOR INFORMATION

Junho Park (jaypark@kreemo.io) is the head of Research and Development Team at KREEMO Inc., Seoul 06682, South Korea. His research interests include millimeter-wave phased-array antennas and radio-frequency front-end designs for 5G/beyond 5G communication systems. He is a Member of IEEE.

Ahmed Abdelmottaleb Omar (ahmed.omar.1@kfupm.edu.sa) is an assistant professor at the King Fahd University of Petroleum and Minerals, Dhahran 34464, Saudi Arabia. His research interests include the analysis and design of frequency selective surface; microwave absorbers; and compact, wideband, and millimeter-wave 5G antennas. He is a Member of IEEE.

Jonghyun Kim (jonghyunkim@postech.ac.kr) is an engineer with the System Large-Scale Integration Division at Samsung Electronics, Hwaseong 18448, South Korea. His research interests include radio-frequency and analog circuits.

Jaehyun Choi (jaehyunchoi@postech.ac.kr) is a professional engineer with the Antenna-in-Package Department at LG Innotek Co. Ltd., Seoul 07796, South Korea. His research

interests include multiphysics-based antennas, the circuit design of microwave/millimeter-wave, and radar in autonomous vehicles.

Beakjun Seong (bjseong@kreemo.io) is an engineer with the Research and Development Team at KREEMO Inc., Seoul 06682, South Korea. His research interests include design and verification for millimeter-wave antennas and radio-frequency modules.

Jongwoo Lee (jwlee30@kreemo.io) was a vice president of the Sales and Marketing Team at KREEMO Inc., Seoul 06682, South Korea. His research interests include millimeter-wave antennas and Internet of Things systems.

Wonbin Hong (whong@postech.ac.kr) is the Muenjae Distinguished Professor with the Department of Electrical Engineering, Pohang University of Science and Technology, Pohang 37673, South Korea. He is also with Kreemo Inc., Seoul 06682, South Korea. His research interests include applied electromagnetics and wireless circuits. He is a Senior Member of IEEE.

REFERENCES

- [1] W. Roh et al., "Millimeter-wave beamforming as an enabling technology for 5G cellular communications: Theoretical feasibility and prototype results," *IEEE Commun. Mag.*, vol. 52, no. 2, pp. 106–113, Feb. 2014, doi: 10.1109/MCOM.2014.6736750.
- [2] W. Hong, K. Baek, Y. Lee, Y. Kim, and S. Ko, "Study and prototyping of practically large-scale mmWave antenna systems for 5G cellular devices," *IEEE Commun. Mag.*, vol. 52, no. 9, pp. 63–69, Sep. 2014, doi: 10.1109/MCOM.2014.6894454.
- [3] Y.-W. Hsu, T.-C. Huang, H.-S. Lin, and Y.-C. Lin, "Dual-polarized quasi Yagi-Uda antennas with Endfire radiation for millimeter-wave MIMO terminals," *IEEE Trans. Antennas Propag.*, vol. 65, no. 12, pp. 6282–6289, Dec. 2017, doi: 10.1109/TAP.2017.2734238.
- [4] H. Li, Y. Li, L. Chang, W. Sun, X. Qin, and H. Wang, "Wideband dual-polarized Endfire antenna array with overlapped apertures and small clearance for 5G millimeter-wave applications," *IEEE Trans. Antennas Propag.*, vol. 69, no. 2, pp. 815–824, Feb. 2021, doi: 10.1109/TAP.2020.3016512.
- [5] O. Jo, J.-J. Kim, J. Yoon, D. Choi, and W. Hong, "Exploitation of dual-polarization diversity for 5G millimeter-wave MIMO beamforming systems," *IEEE Trans. Antennas Propag.*, vol. 65, no. 12, pp. 6646–6655, Dec. 2017, doi: 10.1109/TAP.2017.2761979.
- [6] A. Li, K.-M. Luk, and Y. Li, "A dual linearly polarized end-fire antenna array for the 5G applications," *IEEE Access*, vol. 6, pp. 78,276–78,285, Dec. 2018, doi: 10.1109/ACCESS.2018.2884946.
- [7] J. Zhang, K. Zhao, L. Wang, S. Zhang, and G. F. Pedersen, "Dual-polarized phased array with end-fire radiation for 5G handset applications," *IEEE Trans. Antennas Propag.*, vol. 68, no. 4, pp. 3277–3282, Apr. 2020, doi: 10.1109/TAP.2019.2937584.
- [8] J. Park, H. Seong, Y. N. Whang, and W. Hong, "Energy-efficient 5G phased arrays incorporating vertically polarized Endfire planar folded slot antenna for mmWave mobile terminals," *IEEE Trans. Antennas Propag.*, vol. 68, no. 1, pp. 230–241, Jan. 2020, doi: 10.1109/TAP.2019.2930100.
- [9] A. Li and K. Luk, "Single-layer wideband end-fire dual-polarized antenna array for device-to-device communication in 5G wireless systems," *IEEE Trans. Veh. Technol.*, vol. 69, no. 5, pp. 5142–5150, May 2020, doi: 10.1109/TVT.2020.2979636.
- [10] H.-T. Chou, S.-J. Chou, J. D. S. Deng, C.-H. Chang, and Z.-D. Yan, "LTCC-based antenna-in-package array for 5G user equipment with dual-polarized Endfire radiations at millimeter-wave frequencies," *IEEE Trans. Antennas Propag.*, vol. 70, no. 4, pp. 3076–3081, Apr. 2022, doi: 10.1109/TAP.2021.3118819.
- [11] W. El-Halwagy, R. Mirzavand, J. Melzer, M. Hossain, and P. Mousavi, "Investigation of wideband substrate-integrated vertically-polarized electric dipole antenna and arrays for mm-Wave 5G mobile devices," *IEEE Access*, vol. 6, pp. 2145–2157, 2018, doi: 10.1109/ACCESS.2017.2782083.
- [12] S. Shakib, J. Dunworth, V. Aparin, and K. Entesari, "mmWave CMOS power amplifiers for 5G cellular communication," *IEEE Commun. Mag.*, vol. 57, no. 1, pp. 98–105, Jan. 2019, doi: 10.1109/MCOM.2018.1701378.
- [13] W. Li, W. Chung, and K. Wong, "Highly-integrated dual-band mmWave antenna array for 5G mobile phone application," in *Proc. 14th Eur. Conf. Antennas Propag. (EUCAP)*, 2020, pp. 1–5, doi: 10.23919/EuCAP48036.2020.9135212.
- [14] R. Rodríguez-Cano, S. Zhang, and G. F. Pedersen, "Beam-steerable multi-band mm-wave bow-tie antenna array for mobile terminals," in *Proc. 14th Eur. Conf. Antennas Propag. (EUCAP)*, 2018, pp. 1–4, doi: 10.1049/cp.2018.0418.
- [15] S. Zhang, I. Syrytsin, and G. F. Pedersen, "Compact beam-steerable antenna array with two passive parasitic elements for 5G mobile terminals at 28 GHz," *IEEE Trans. Antennas Propag.*, vol. 66, no. 10, pp. 5193–5203, Oct. 2018, doi: 10.1109/TAP.2018.2854167.
- [16] C. A. Balanis, *Antenna Theory and Design*, 3rd ed. New York, NY, USA: Wiley, 2005.
- [17] S. Zhang, X. Chen, I. Syrytsin, and G. F. Pedersen, "A planar switchable 3-D-coverage phased array antenna and its user effects for 28-GHz mobile terminal applications," *IEEE Trans. Antennas Propag.*, vol. 65, no. 12, pp. 6413–6421, Dec. 2017, doi: 10.1109/TAP.2017.2681463.
- [18] I. Syrytsin, S. Zhang, G. F. Pedersen, and A. S. Morris, "Compact quad-mode planar phased array with wideband for 5G mobile terminals," *IEEE Trans. Antennas Propag.*, vol. 66, no. 9, pp. 4648–4657, Sep. 2018, doi: 10.1109/TAP.2018.2842303.
- [19] I. Syrytsin, S. Zhang, G. F. Pedersen, K. Zhao, T. Bolin, and Z. Ying, "Statistical investigation of the user effects on mobile terminal antennas for 5G applications," *IEEE Trans. Antennas Propag.*, vol. 65, no. 12, pp. 6596–6605, Dec. 2017, doi: 10.1109/TAP.2017.2681701.
- [20] W. Hong, K.-H. Baek, and S. Ko, "Millimeter-wave 5G antennas for smartphones: Overview and experimental demonstration," *IEEE Trans. Antennas Propag.*, vol. 65, no. 12, pp. 6250–6261, Dec. 2017, doi: 10.1109/TAP.2017.2740963.
- [21] J. Bang and J. Choi, "A SAR reduced mm-Wave beam-steerable array antenna with dual-mode operation for fully metal-covered 5G cellular handsets," *IEEE Antennas Wireless Propag. Lett.*, vol. 17, no. 6, pp. 1118–1122, Jun. 2018, doi: 10.1109/LAWP.2018.2836196.
- [22] B. Yu, K. Yang, C. Sim, and G. Yang, "A novel 28 GHz beam steering array for 5G mobile device with metallic casing application," *IEEE Trans. Antennas Propag.*, vol. 66, no. 1, pp. 462–466, Jan. 2018, doi: 10.1109/TAP.2017.2772084.
- [23] R. Montoya Moreno, J. Ala-Laurinaho, A. Khrapkov, J. Ilvonen, and V. Viikari, "Dual-polarized mm-Wave Endfire antenna for mobile devices," *IEEE Trans. Antennas Propag.*, vol. 68, no. 8, pp. 5924–5934, Aug. 2020, doi: 10.1109/TAP.2020.2989556.
- [24] J. Kurvinen, H. Kähkönen, A. Lehtovuori, J. Ala-Laurinaho, and V. Viikari, "Co-designed mm-Wave and LTE handset antennas," *IEEE Trans. Antennas Propag.*, vol. 67, no. 3, pp. 1545–1553, Mar. 2019, doi: 10.1109/TAP.2018.2888823.
- [25] R. Rodriguez-Cano, S. Zhang, K. Zhao, and G. F. Pedersen, "mm-Wave beam-steerable Endfire array embedded in a slotted metal-frame LTE antenna," *IEEE Trans. Antennas Propag.*, vol. 68, no. 5, pp. 3685–3694, May 2020, doi: 10.1109/TAP.2020.2963915.
- [26] R. Rodriguez-Cano, K. Zhao, S. Zhang, and G. F. Pedersen, "Handset frame blockage reduction of 5G mm-Wave phased arrays using hard surface inspired structure," *IEEE Trans. Veh. Technol.*, vol. 69, no. 8, pp. 8132–8139, Aug. 2020, doi: 10.1109/TVT.2020.2996360.
- [27] J. Kurvinen et al., "Capacitively-loaded feed line to improve mm-Wave and Sub-6 GHz antenna co-existence," *IEEE Access*, vol. 8, pp. 139,680–139,690, Jul. 2020, doi: 10.1109/ACCESS.2020.3012773.
- [28] Z. Qu, S. Qu, Z. Zhang, S. Yang, and C. H. Chan, "Wide-angle scanning lens fed by small-scale antenna array for 5G in millimeter-wave band," *IEEE Trans. Antennas Propag.*, vol. 68, no. 5, pp. 3635–3643, May 2020, doi: 10.1109/TAP.2020.2967086.
- [29] C. Mao, M. Khalily, P. Xiao, L. Zhang, and R. Tafazolli, "High-gain phased array antenna with Endfire radiation for 26 GHz wide-beam-scanning applications," *IEEE Trans. Antennas Propag.*, vol. 69, no. 5, pp. 3015–3020, May 2021, doi: 10.1109/TAP.2020.3028181.
- [30] J. Kim, J. Park, A. A. Omar, and W. Hong, "A symmetrically stacked planar antenna concept exhibiting quasi-isotropic radiation coverage," *IEEE Antennas Wireless Propag. Lett.*, vol. 19, no. 8, pp. 1390–1394, Aug. 2020, doi: 10.1109/LAWP.2020.3003011.





Bernhard Jakoby^{ID}, Roman Beigelbeck, and
Thomas Voglhuber-Brunnmaier^{ID}

Understanding the Shielding Efficiency of a Faraday Grid Cage

A spectral domain approach.

The static shielding properties of Faraday wire cages are intuitive as for a small mesh size, the effect on the field can be expected to approach that of an ideal Faraday cage, i.e., a closed conductive surface. However, as it has been recently pointed out, the shielding efficiency is somewhat worse than one might expect and does not particularly conform to the simple approximation of an exponentially decaying field, as it is, e.g., described in *The Feynman Lectures on Physics*. In the present contribution, we use the case of a circular 2D wire cage to illustrate how the residual field inside such a cage can be visualized in terms of a spatial spectral consideration of the induced charge. It is shown how the residual field in the cage's center is related to a single Fourier coefficient of this spectral expansion, and that the approximation of the induced charge as a sampled version of the induced charge of a

corresponding ideal Faraday cage yields useful approximations for the residual fields close to the cage boundary. The latter also turn out to justify the exponential decay approximation, at least in this region.

INTRODUCTION

The first description of the screening of electric (and in particular, electrostatic) fields by metallic, or more generally, conductive, cages is generally attributed to Faraday's observations, as reported in his seminal monograph [1]. Today, Faraday cages and their effect can be considered common knowledge, being taught in schools and known to the common public, particularly in connection with protection from lightning strikes, as illustrated by demonstrations in science museums or the protective effect of sitting in a car during a thunderstorm. In 2016, Rajeev Bansal reported in *IEEE Antennas and Propagation Magazine*'s "Turnstile" column [2] that Chapman et al. investigated the shielding

Digital Object Identifier 10.1109/MAP.2022.3229287
Date of current version: 5 January 2023

This work is licensed under a Creative Commons Attribution-NonCommercial-NoDerivatives 4.0 License. For more information, see <https://creativecommons.org/licenses/by-nc-nd/4.0/>

efficiency of Faraday cages composed of grids devising and using rigorous methods, finding that the shielding is not as powerful as may be intuitively expected [3]. For a 2D circular cage, an external line charge in a distance d from the center of the cage creates a remaining field in the center of the cage, which is found to be approximately proportional to $\log(r/r_0)/nd$, where r/r_0 denotes the radius of the wires the cage is made of (normalized to some reference value r_0), and n is the number of wires forming the 2D cage. They also pointed out that apparently, the shielding efficiency before had scarcely been analyzed in a rigorous mathematical manner; at least such an analysis cannot be found in common textbooks or accessible journals, which was the stimulus for their own work. In particular, an (approximately) exponential decay of the fields inside the cage, which is commonly assumed, was proven wrong. As an example, for such a simplified treatment, *The Feynman Lectures on Physics* [4] are cited stating the origin of the flawed treatment is that “Feynman considers equal charges rather than equal potentials” on the wires. Later in this article, we discuss the context of Feynman’s treatment, illustrating that Feynman’s conclusions can indeed be justified for large or infinitely extended wire grids as has also been pointed out by other authors [5].

The original analysis provided in [3] considered the electrostatic case, which was later extended to the dynamic case [6], where in both cases the devised concept of homogenized boundary conditions was successfully employed. In particular, it is confirmed that the static case can be a useful approximation if the wavelength is large compared to the spacing of the grid (unless spurious resonances are excited in the cage). It is also pointed out that the treatment of lightning and sparking involves complex nonlinear effects such as ionization, which is also not covered by an electrostatic approach. The interested reader seeking a thorough treatment of the problem is particularly referred to these works.

In this contribution, we do not aim at such a rigorous analysis but rather at developing an illustrative view on the problem by utilizing a tool well-known to electrical engineers, i.e., Fourier analysis.

As in [3], for the sake of simplicity, we consider the case of a circular cage in two dimensions and treat the purely electrostatic

case. This consideration, to a certain extent, also particularly applies to the dynamic cases where the wavelengths involved are much larger than the spacing of the considered grid. For the sake of completeness, we also note that shielding of static and quasi-static magnetic fields is a different (and quite challenging) topic, see, e.g., [7].

In the following, we first introduce a mathematical description of the problem, where the field is described in terms of a Fourier series expansion of the induced charges. We particularly consider the residual field in the center of the cage and close to the cage boundary, where the approximate assumption that the charges in the grid wires represent a sampled version of the charge induced in an ideal (closed) Faraday cage is particularly useful. These considerations are illustrated by means of an example.

STATEMENT OF THE PROBLEM AND SPECTRAL CONSIDERATIONS

We consider 2D electrostatics in free space, i.e., in 3D space everything is considered uniformly extended to infinity with respect to one spatial dimension, say z , such that we can simplify the 3D equations by setting $\partial/\partial z = 0$. In the following, we use polar coordinates with radial and angular coordinates r and α , respectively, where the coordinate center is located in the center of the cage. Figure 1 shows a Faraday cage composed of $N = 12$ circular conductive wires with diameters (widths) w that are uniformly distributed on a circle $r = R$, i.e., with radius R . In the general case, the wires shall be considered located at angles $\alpha_n = n2\pi/N$ with $n = 0 \dots N - 1$. We consider the important case of thin wires, referring to the assumption that the diameter w of each wire is significantly smaller than the spacing between them and the dimension of the cage, which essentially means that $w \ll 2\pi R/N$. As in [3], we consider the field generated by a 2D point charge (which is a line charge in 3D) located in a distance d from the cage’s center and lying on the x -axis as excitation in our problem. Even though we consider static fields, in this article we use the term *incident field*, commonly used in electromagnetic scattering, to address this field contribution.

In electrostatics, the electric field is conservative and the field vector \mathbf{E} can be expressed as the negative gradient of the

electric potential φ , i.e., $\mathbf{E} = -\nabla\varphi$. In charge-free regions, such as the region within the cage, the potential φ fulfills Laplace's equation $\Delta\varphi = 0$. When using polar coordinates, the potential can be written as a function $\varphi(r, \alpha)$ and will be 2π -periodic in α such that it can be expanded in a Fourier series with respect to α : (Note that two types of indices are used in this article. Whenever an index refers to a spectral Fourier component, we use the letter k , whereas n is used as the index for the cage wires $n = 0 \dots N - 1$.)

$$\begin{aligned}\varphi(r, \alpha) &= \sum_{k=-\infty}^{+\infty} \tilde{\varphi}_k(r) \exp(jk\alpha) \\ &= \frac{\tilde{\varphi}_{c,0}}{2} + \sum_{k=1}^{\infty} (\tilde{\varphi}_{c,k}(r) \cos(k\alpha) + \tilde{\varphi}_{s,k}(r) \sin(k\alpha)).\end{aligned}\quad (1)$$

Here the imaginary unit is denoted by $j = \sqrt{-1}$. The r -dependent Fourier coefficient $\tilde{\varphi}_n(r)$ is thereby given by

$$\tilde{\varphi}_k(r) = \frac{1}{2\pi} \int_0^{2\pi} \varphi(r, \alpha) \exp(-jk\alpha) d\alpha \quad (2)$$

which is related to the coefficients of the alternative sine and cosine representations by

$$\begin{aligned}\tilde{\varphi}_{c,k} &= \tilde{\varphi}_k + \tilde{\varphi}_{-k} \quad (\text{for } k \geq 0) \\ \tilde{\varphi}_{s,k} &= j(\tilde{\varphi}_k - \tilde{\varphi}_{-k}) \quad (\text{for } k \geq 1).\end{aligned}\quad (3)$$

Inserting the expansion (1) into Laplace's equation $\Delta\varphi = 0$ in polar coordinates leads to a simple general solution for the r -dependent Fourier coefficients $\tilde{\varphi}_k(r)$, or alternatively, $\tilde{\varphi}_{c,k}(r)$ and $\tilde{\varphi}_{s,k}(r)$, which, inside the cage, yields an r -dependence proportional to $r^{|k|}$ [see “Supplement A” of the supplementary material (available at 10.1109/MAP.2022.3229287), where the case $k = 0$ is also discussed]. Each spectral coefficient corresponds to a particular contribution to the total field.

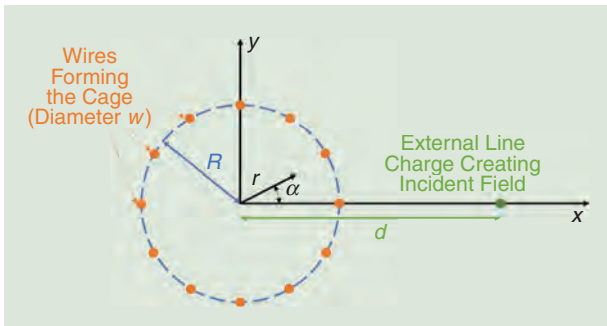


FIGURE 1. A 2D circular wire cage and a line charge in some distance d , serving as a source for the external field to be screened.

In the following, we first introduce a mathematical description of the problem, where the field is described in terms of a Fourier series expansion of the induced charges.

This already gives a clue as to what we need to identify in the remaining field in the cage's center. Close to the center, i.e., for vanishing r , out of all the terms proportional to $r^{|k|}$, the asymptotically dominant one will be proportional to r , i.e., the one for $k = \pm 1$. Thus, the associated spectral coefficients essentially determine the remaining field close to the center.

Close to the cage, i.e., when r approaches R , the situation is not as clear and depends on amplitude distribution of the individual spectral coefficients.

The remaining fields close to the cage boundary as well as those close to the center can serve as particular measures for the screening efficiency of the cage. As outlined in the next section, considering the field in the cage's center is in line with the conclusions made in [3], whereas the fields just behind the wire grid happen to support Feynman's conclusion [4] to a certain extent, as is further discussed.

To discuss all of this, we move on to look into the utilization of the Fourier series expansion in a bit more detail.

THE FIELD INSIDE THE CAGE

The field remaining inside the cage can be represented as a superposition of the incident field and the field generated by the induced charges on the wires of the cage, which ideally cancel out the former as well as possible. To determine the residual field, the first step is to solve for the induced charges, and there are a variety of analytical and numerical as well as approximate methods to obtain these. Later in this section, we show some simple approaches for illustrational purposes but will not particularly stress this point as there are many suitable ways for calculating electrostatic fields, which are extensively discussed in the literature. For the treated circular Faraday cage, we particularly refer to [3], which provides a more profound insight into these topics.

For the present, let us assume that the charge distribution in the cage wires is already known, and we consider how the residual field can be obtained. The charge distribution on each wire is located at the wire's surface and, in general, is not uniformly distributed across the surface. This is in contrast to the simple case of a single isolated charged wire with a circular cross section where the surface charge would be uniformly distributed. In this case, the field generated outside of the wire by these surface charges is identical to that of an equivalent line charge located at the wire's center (replacing the wire). This is a consequence of the equivalence principle of electrostatics (see, e.g., [8]). Similarly, even though in our case the charge on a particular wire's surface will not be uniformly distributed, in distances sufficiently large compared to the wire's diameter w , the field originating from the charges on a particular wire will approach that of an equivalent

line charge q_n (for wire number n) placed instead of the wire at its center location at the angle $\alpha_n = n2\pi/N$, which can be used to approximately evaluate the field within the cage.

These equivalent line charges, which are located at positions $r = R$ and $\alpha_n = n2\pi/N$ (with $n = 0 \dots N - 1$), can, in turn, be conceptually described in terms of a surface charge distribution $\sigma(\alpha)$ located at the circle (cylinder in 3D) $r = R$

$$\sigma(\alpha) = \frac{1}{R} \sum_{n=0}^{N-1} q_n \delta\left(\alpha - n \frac{2\pi}{N}\right) \quad (4)$$

using Dirac delta functions $\delta(\alpha)$ to represent the line charges, where q_n are the associated line charge densities. The factor $1/R$ maintains proper scaling, i.e., integrating the surface charge density around the entire circumference yields the sum of the line charges:

$$\int_0^{2\pi} \sigma(\alpha) R d\alpha = \sum_{n=0}^{N-1} q_n. \quad (5)$$

This representation nicely connects to the case of the ideal Faraday cage, where a distributed surface charge distribution on the circle $r = R$ is obtained. As this surface charge exactly compensates the incident field inside the circle, it can also be used to represent the incident field in terms of an equivalent charge distribution, which is simply equal to the negative ideal surface charge density.

As discussed in “Supplement A” of the supplementary material (available at 10.1109/MAP.2022.3229287), a Fourier series representation allows for a convenient and simple representation of fields and charges. Also, the surface charge representing the equivalent line charges from (4) can be expanded into a Fourier series yielding

$$\tilde{\sigma}_k = \frac{1}{2\pi R} \sum_{n=0}^{N-1} q_n \exp\left(-jn k \frac{2\pi}{N}\right) \quad (6)$$

as Fourier series coefficients, which are periodic in the discrete variable k . One period, e.g., from $k = 0$ to $k = N - 1$, corresponds to the spectral representation of the discrete Fourier transform (DFT), which can be efficiently computed using the fast Fourier transform (FFT) algorithm. (Note that a periodic but continuous function corresponds to a discrete spectrum, as described by the Fourier series. A periodic and discrete function corresponds to a periodic and discrete spectrum, as described by the DFT. The FFT is a numerically efficient way to calculate the DFT, which is why these terms are sometimes used alternately.) Although the spatial charge distribution in terms of line charge is discrete, the fields generated by these line charges are, of course, continuous, and

For the present, let us assume that the charge distribution in the cage wires is already known, and we consider how the residual field can be obtained.

to calculate their spectral representation we stick to the classical Fourier series.

In the following, we consider that the external field exciting the cage is provided by a line charge in a distance d from the cage’s center, as shown in Figure 1, which yields symmetric fields and charges with respect to α . In doing so, the real-valued representation of the Fourier series (1) is particularly handy as the coefficients of the sine terms vanish, e.g., $\tilde{\phi}_{s,k} = 0$ for the potential.

Also, using the resulting cosine series, we have to deal with only positive spectral indices k , which eases the notation in the following considerations, yet they similarly apply to asymmetric cases. For this special case, the Fourier cosine coefficients, e.g., of the surface charge density, are related to the general coefficients by

$$\tilde{\sigma}_{c,k} = 2\tilde{\sigma}_k = 2\tilde{\sigma}_{-k} \quad (k \geq 0). \quad (7)$$

Under these assumptions, analogous to (1), we therefore have

$$\sigma(r, \alpha) = \frac{\tilde{\sigma}_{c,0}}{2} + \sum_{k=1}^{\infty} \tilde{\sigma}_{c,k}(r) \cos(k\alpha). \quad (8)$$

The zeroth-order coefficient $\tilde{\sigma}_{c,0}$ corresponds to the total charge of the cage, which has to vanish in the case of electrostatic induction because the wires are connected and initially uncharged. When calculating the charges numerically, a nonvanishing, zeroth-order coefficient can thus be an indicator of inaccuracies. As outlined in “Supplement A” of supplementary material (available at 10.1109/MAP.2022.3229287), the potential ϕ_s due to the charges on the wire can be similarly expanded in a Fourier series with respect to α . (Note that the subscript “ s ” stands for “scattered,” indicating that this field is related to the induced charges as opposed to the “incident” field generated by the exciting charge.)

As a result, a simple solution ansatz for the r -dependent coefficients is obtained, i.e.,

$$\begin{aligned} \tilde{\phi}_{s,c,k}(r) &= A_k r^k && \text{inside the cage } (r < R), \text{ and} \\ \tilde{\phi}_{s,c,k}(r) &= B_k r^{-k} && \text{outside of the cage } (r > R) \end{aligned} \quad (9)$$

with yet-to-be-determined coefficients A_k and B_k . By virtue of the orthogonality of the expansion functions in the Fourier series (cosine functions in the present case), the spatial domain interface conditions across sheets of surface charge translate into corresponding conditions for every spectral component. In particular, by virtue of Gauss’s law, the surface-normal component of the electric displacement (in free space $\epsilon_0 \mathbf{E}$) experiences a jump when passing through a sheet

carrying a surface charge, which yields the following condition for the spectral coefficients of potential and charge at the surface $r = R$:

$$\frac{\partial \tilde{\varphi}_{s,c,k}(r)}{\partial r} \Big|_{r=R+} - \frac{\partial \tilde{\varphi}_{s,c,k}(r)}{\partial r} \Big|_{r=R-} = \frac{\tilde{\sigma}_{c,k}}{\epsilon_0}. \quad (10)$$

Together with continuity of the potential at $r = R$, i.e.,

$$\tilde{\varphi}_{s,c,k} \Big|_{r=R+} = \tilde{\varphi}_{s,c,k} \Big|_{r=R-} \quad (11)$$

one can solve for the coefficients A_k and B_k , and the following solution of the Fourier coefficient for the potential inside the cage is obtained:

$$\tilde{\varphi}_{s,c,k}(r) = \left(\frac{r}{R}\right)^k \frac{R}{2k\epsilon_0} \tilde{\sigma}_{c,k} \quad (12)$$

and therefore, by inserting these coefficients in the Fourier cosine series expansion, we obtain the desired representation of the field in terms of the generating charges

$$\varphi_s(r, \alpha) = \sum_{k=1}^{\infty} \left(\frac{r}{R}\right)^k \frac{R}{2k\epsilon_0} \tilde{\sigma}_{c,k} \cos(k\alpha). \quad (13)$$

It is particularly useful that this approach can not only be used to represent the field generated by the induced charges (the “scattered” fields) but also the incident field. As the charge density σ_{id} induced in an ideal circular Faraday cage exactly cancels out the incident field inside the cage and as σ_{id} represents a distribution of surface charges on the surface $r = R$, the incident field can be expressed in terms of these charges and their Fourier series coefficients. “Supplement B” of the supplementary material (available at 10.1109/MAP.2022.3229287) summarizes some fundamental properties for the ideal circular Faraday cage and also provides a closed-form expression for Fourier coefficients of the induced surface charge density $\tilde{\sigma}_{id,l,n}$ for the special case when the incident field stems from a line charge, as depicted in Figure 1 [see (28)].

HOW WELL DOES IT SHIELD?

The answer to this question depends on the criterion used to evaluate it. It is near at hand to start with considering the field at the center of the cage as it can be expected that the remaining field will be smaller close to the center. But what can also be of interest is how fast the field decreases right behind the screen when moving toward the center. Let us have a look at these cases.

CENTER OF THE CAGE

The electric field at the center of the cage ($r = 0$) can be fully characterized in terms of its radial component [note that at $r = 0$, we have the following simple relation between the polar components of the electric field $E_r(0, \alpha) = E_\alpha(0, \alpha - \pi/2)$, and thus, all the information is contained in one of these components]:

$$E_r \Big|_{r=0} = -\frac{\partial \varphi}{\partial r} = -\frac{\partial \varphi_s}{\partial r} - E_{inc,r}. \quad (14)$$

Here, φ_s denotes the electric potential generated by the induced charges on the wire cage, and $E_{inc,r}$ denotes the r component of the electric field generated by external charges, i.e., the line charge at $x = d$ (and $y = 0$) in our example. $E_{inc,r}$ is given simply by the field of a line charge in distance d and readily obtained as

$$E_{inc,r} = \frac{-q_{inc} \cos \alpha}{2\pi\epsilon_0 d}. \quad (15)$$

Utilizing the Fourier series expansion (13) for the scattered field, the derivative with respect to r can be taken for every element of the series (representing a power series with respect to r), and upon setting $r = 0$, we are left with a single nonzero element of the series, i.e., $k = 1$, yielding for the total field

$$E_r(0, \alpha) = -\frac{\tilde{\sigma}_{c,1}}{2\epsilon_0} \cos \alpha - \frac{q_{inc}}{2\pi\epsilon_0 d} \cos \alpha. \quad (16)$$

So the remaining field in the center is essentially determined by the first-order Fourier series coefficient $\tilde{\sigma}_{c,1}$ of the induced charge distribution! This equation is exact, i.e., not an approximation, and holds for an arbitrary charge distribution along the circle $r = R$; it also holds for the continuous charge distribution induced in an ideal Faraday cage, which is considered in “Supplement B” of the supplementary material available at 10.1109/MAP.2022.3229287. As can be seen in (28), the corresponding Fourier coefficient for $k = 1$ indeed exactly cancels the incident field as it should be as the charges induced in the ideal cage cancel the incident field everywhere inside the cage ($r < R$). [Note that (28) in “Supplement B” of the supplementary material (available at 10.1109/MAP.2022.3229287) provides the two-sided Fourier coefficient, which has to be multiplied by two to obtain the corresponding coefficient of the cosine series.]

CLOSE TO THE CAGE BOUNDARY

Again, we can use the spectral Fourier representation for the induced charges to establish the residual field. At first sight, it is near at hand to assume that the induced charges in the wire cage will closely resemble a “sampled” version of the continuous charge distribution of the ideal Faraday cage $\sigma_{id}(\alpha)$ [see “Supplement B” of the supplementary material (available at 10.1109/MAP.2022.3229287)]. Indeed, as illustrated in this section and in the example, this turns out to be a useful approximation close to the cage boundary, however, its accuracy deteriorates when the residual fields in the cage’s center (i.e., for $r \ll R$) are calculated. Figure 2 illustrates the idea of sampling and the resulting spectra. The continuous charge distribution (upper-left plot), which, by definition, is periodic in α , corresponds to a spectrum of discrete Fourier coefficients. The charge distribution can be “sampled,” yielding a set of N line charges uniformly distributed at angles $\alpha_n = n2\pi/N$ around the circumference $r = R$. In the sampled version, the strength of each line charge is proportional to the value of the continuous charge distribution sampled at the location of the respective line charge, i.e., at the

corresponding angle α_n (lower-left plot). As it is well known from the spectral analysis of sampled signals (see, e.g., [9]), the spectrum, i.e., the Fourier coefficients representing this arrangement of line charges, is given by a periodic repetition of the coefficients associated with the sampled (continuous) function. The coefficients contained within one spectral period can also be obtained by applying an FFT to the original charge coefficients.

The line charge densities q_n associated with the sampled version in (4) are given by

$$q_n \approx \frac{2\pi R}{N} \sigma_{\text{id}}\left(n \frac{2\pi}{N}\right). \quad (17)$$

The factor $2\pi R/N$ represents the length of one of N equally sized segments of the circle and relates the surface charge density at the sampling location to an associated (approximate) line charge density. Obviously, for sufficiently large N , the compensating field generated by such a distribution of line charges can be expected to come arbitrarily close to the continuous charge distribution on the ideal Faraday cage, and also, the sampled version cancels out the incident field fairly well. However, particularly for small N , the sampled ideal charge distribution does not represent the actually induced charges very accurately, as also pointed out in [3]. Thus, the actually induced charge distribution on the wires tends to compensate the incident external field not as well as it would be possible, in principle, for an arrangement of line charges. Yet, on second thought, the physical requirement determining the charge distribution among the wires is not the cancellation of the incident field inside the cage but the boundary condition of a constant potential at the wire surfaces, which obviously represents a different requirement.

Still, approximation of the sampled ideal charge distribution provides some very valuable insights and turns out to be useful, particularly when considering fields close to the cage boundary,

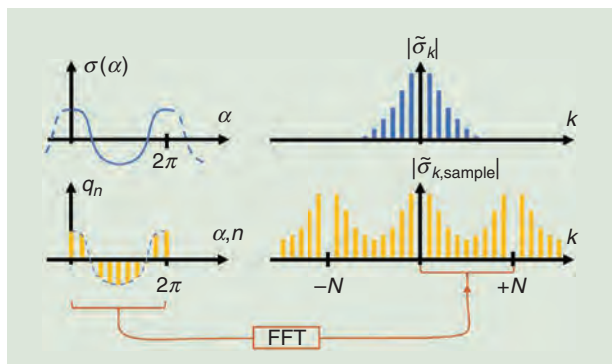


FIGURE 2. Spectra (Fourier series coefficients) of continuous and sampled charge distribution. The spectrum associated with the sampled distribution is a periodic repetition of the original one.

But what can also be of interest is how fast the field decreases right behind the screen when moving toward the center.

as illustrated further in this section. Considering the corresponding discrete charge distribution as given in (17) according to the spectral properties of sampled signals (see, e.g., [9]), the resulting Fourier coefficients are

$$\tilde{\sigma}_k \approx \sum_{m=-\infty}^{+\infty} \tilde{\sigma}_{\text{id},k-mN} \quad (18)$$

i.e., the spectrum for the sampled version is given by the sum of the

periodically repeated spectra of the underlying continuous function σ_{id} with a period N , as presented in Figure 3. Note that here we use the complex Fourier series (rather than the cosine series), which allows for representing the impact of sampling in a simpler fashion.

The spectrum is now not only discrete but also periodic and, as mentioned previously, the coefficients within one period ($n = 0 \dots N - 1$) can be efficiently obtained using the FFT algorithm, taking the FFT of the discrete charges q_n in spatial domain. Depending on the width of the ideal charge distribution's spectrum $\tilde{\sigma}_{\text{id},k}$, the shifted spectra will, in general, overlap to a certain extent (see also the discussion later in this section).

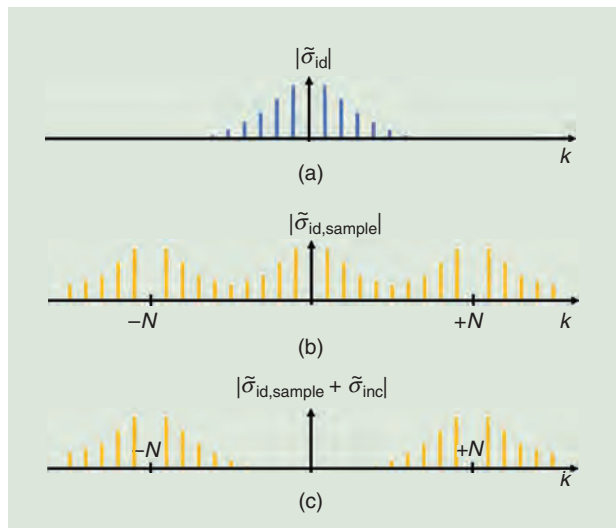


FIGURE 3. (a) The spectrum of the charge distribution induced in the ideal Faraday cage, (b) the sampled ideal distribution, which may serve as an, albeit coarse, approximation of the actually induced charges, and (c) the spectral sum of the sampled distribution plus the equivalent charge distribution $\tilde{\sigma}_{\text{inc}}$ generating the incident field inside the cage. Note that the Fourier coefficient for $k = 0$ vanishes due to the charge neutrality, i.e., the total charge on the cylinder vanishes. The spectrum of the sampled charge distribution is given in terms of a periodic repetition of the spectrum of the function being sampled. As can be seen, when adding the distributions $\tilde{\sigma}_{\text{id},sample}$ and $\tilde{\sigma}_{\text{inc}}$, the “baseband” contribution cancels out such that the residual field is entirely given in terms of the shifted spectra in this approximation.

If we now want to obtain the field generated by the induced charges, we employ (13). [We note that (13) refers to the Fourier cosine expansion; for symmetric situations, these are related to the complex series coefficients by (7).] Note that even though the charge spectrum is periodic, the spectrum of the potential is, in general, not periodic as the potential is a continuous function of α in spatial domain. At the same time, due to the intrinsic periodicity in spatial (α) domain, the spectrum remains discrete. Hence, the associated spectral coefficients of the potential for a given r are also not periodic, which is represented by the fact that the k th series coefficient in (13) features a factor $(r/R)^k/k$, which is obviously not periodic in k .

To represent the incident field inside the cage, we now use the previously mentioned fact that, inside the cage, the incident field can be represented simply as the field that would be created inside the cage by a fictitious charge distribution σ_{inc} on $r = R$, which is equal to the negative ideal charge distribution, i.e., $\sigma_{\text{inc}}(\alpha) = -\sigma_{\text{id}}(\alpha)$. This is the case as σ_{id} would exactly compensate for the incident field inside the cage.

If we now adopt our preliminary assumption that the induced charges on the wires are approximately equal to a sampled version of the ideal continuous distribution $\sigma_{\text{id}}(\alpha)$, the total field inside the cage is approximately related to an “effective” charge distribution whose spectrum is that of the periodically repeated spectrum of the ideal distribution (representing the sampled ideal charge distribution) as given by (18) but omitting the fundamental period $m = 0$, which is cancelled out by adding the negative ideal charge distribution $\sigma_{\text{inc}}(\alpha) = -\sigma_{\text{id}}(\alpha)$, which effectively cancels the “baseband” of the periodically repeated spectrum. This is illustrated in the bottom plot of Figure 3(c). Therefore, using the “sampling approximation,” the residual field is related to the entire spectrum of the sampled charge distribution, except for the “baseband” contribution ($k = 0$) in the series in (18).

This effective charge distribution $\tilde{\sigma}_k + \tilde{\sigma}_{\text{inc},k}$ can now be used to calculate the residual field using (13). As previously pointed out, this series for the potential inside the cage ($r < R$) features coefficients proportional $(r/R)^k/k$ which, close to the cage boundary $r = R$, essentially impose an additional decay, with $1/k$ for increasing k .

We now introduce a further approximation by assuming that the spectral width of the ideal charge distribution $\tilde{\sigma}_{\text{id},k}$ is small compared to the shift parameter N in (18). This also means that neighboring shifted spectra overlap only moderately (which is also assumed in Figures 3 and 4). This condition will often be fulfilled as a Faraday cage will typically feature a mesh width, within which the external field will only moderately change, which in a spectral domain translates into a narrow spectral width of $\tilde{\sigma}_{\text{id},k}$ compared to the number of samples N , which also means that the sampling is more “dense.” Consider now that apart from constant factors, the k th spectral coefficient of the potential is essentially given by the associated spectral coefficient of the charge times a k -dependent factor $(r/R)^k/k$, as given in (12). In our current consideration, the relevant charge spectrum (including an effective charge distribution accounting for the incident field) is approximately given the periodically repeated spectrum of the ideal charge distribution where the fundamental period around $k = 0$ is almost entirely canceled out (see Figure 4). The envelope associated with the factor $(r/R)^k/k$, which has to be applied to obtain the spectrum of the potential, is also indicated as a dashed line in Figure 4. The shifted charge spectra are centered around $k = mN$ with integer m . If the spectral widths of these shifted spectra are small, which means that they are essentially concentrated around $k = mN$, instead of the factor k -dependent factor $(r/R)^k/k$, we can use an approximately constant factor $(r/R)^{mN}/mN$ to be applied to each of these partial, shifted spectra. This in turn means that upon transformation back into spatial (α) domain,

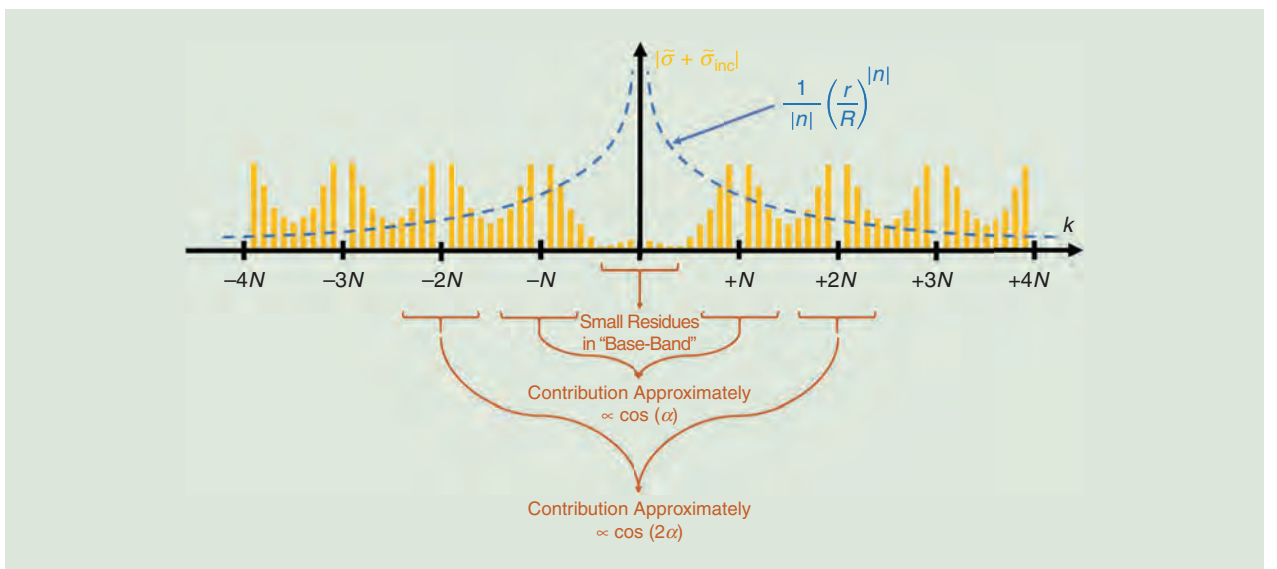


FIGURE 4. The spectrum of the actually induced charge distribution $\tilde{\sigma}$ plus the equivalent charge distribution $\tilde{\sigma}_{\text{inc}}$ representing the incident field. As the real induced charge distribution does not exactly correspond to the sampled ideal charge distribution (as considered in Figure 3), the “baseband” contribution is not entirely canceled out by $\tilde{\sigma}_{\text{inc}}$.

the m th partial spectrum (shifted by mN) is weighed with a constant factor $(r/R)^{mN}/mN$ and, using the Fourier shift theorem for the inverse transform, results in the ideal charge distribution $\sigma_{\text{id}}(\alpha)$ times an additional phase term $\exp(jmN\alpha)$, accounting for the spectral shift by mN . Combining the terms for $\pm m$, the phase terms yield a cosine function $\cos(mN\alpha)$ for each partial spectrum such that the entire spectrum is given by

$$\begin{aligned}\varphi(r, \alpha) &\approx \sigma_{\text{id}}(\alpha) \frac{R}{\epsilon_0} \sum_{m=1}^{\infty} \frac{\rho^{mN}}{mN} \cos(mN\alpha) \\ &= -\sigma_{\text{id}}(\alpha) \frac{R}{\epsilon_0} \frac{\ln[1 + \rho^{2N} - 2\rho^N \cos(N\alpha)]}{2N}\end{aligned}\quad (19)$$

where $\rho = r/R$ and \ln denotes the natural logarithm. Note that the series starts at $m = 1$ instead of zero, which accounts for the canceled baseband contribution. The closed-form solution for the series was obtained by considering a related geometric series for the complex variable $Z = \rho^N \exp(jN\alpha)$, where the original series can be represented as the real part of the indefinite integral of the geometric series for Z with respect to Z . This approximation is particularly appealing as it can be established for arbitrary incident fields as the ideal charge distribution $\sigma_{\text{id}}(\alpha)$ can be readily expressed in terms of the incident field at the cage boundary [see (26)]. The existence of this closed-form solution shall, however, not cloud the main point, i.e., that the residual field behind the cage boundary (and its decay), by virtue of considering the sampling approximation, can be directly related to the spectral repetitions of the ideal charge distribution.

A simpler, yet less accurate approximation is obtained by keeping only the first term of the series featuring the slowest decay for decreasing ρ , yielding

$$\varphi(r, \alpha) \approx \sigma_{\text{id}}(\alpha) \frac{R}{N\epsilon_0} \rho^N \cos(N\alpha). \quad (20)$$

The electric field components can be readily obtained from the potential by

$$E_r = -\frac{\partial \varphi}{\partial r} \quad (21)$$

and

$$E_\alpha = -\frac{1}{r} \frac{\partial \varphi}{\partial \alpha} \quad (22)$$

which shows that the field components show an r -dependence $r^{(N-1)}$. Note again that this approximation is particularly useful to describe the fields close to the screen, while it becomes particularly inaccurate when $r \rightarrow 0$, where it predicts that the field strength vanishes entirely.

As shown in the previous section, the field at the center is essentially determined by the first spectral coefficient of the induced charge [see (16)]. If the charges on the wires were actually sampled versions of the ideal continuous charge distribution, the field at the center would indeed almost completely vanish as the field generated by the “baseband” contributions of the periodically repeated charge spectrum, i.e., the term

associated with $m = 0$ in (18), is exactly canceled by the incident field. Referring to (16), for vanishing E_r at $r = 0$, the first Fourier coefficient of the induced charge density would have to be $\tilde{\sigma}_{c,1} = 2\tilde{\sigma}_1 = -q_{\text{inc}}/\pi d$. Referring to (28) in “Supplement B” of the supplemental material (available at 10.1109/MAP.2022.3229287), we find that this is exactly the first Fourier coefficient of the charge distribution of the ideal Faraday cage, i.e., $\tilde{\sigma}_{\text{id},1}$. Yet, the sampled ideal charge distribution would have additional, albeit small, contributions to $\tilde{\sigma}_1$, stemming from the shifted spectra, i.e., the terms associated with $m \neq 0$ in (18), which is why the field in the center would not exactly vanish, even if the sampled ideal charge distribution were induced in the cage wires. Hence, as discussed in the previous section, if one wants to know the remaining field in the center of the cage, the first spectral coefficient has to be determined exactly, which is not feasible with the sampling approximation, as will also be illustrated in the examples presented in the next section. When moving close to the cage boundary ($r \rightarrow R$), however, the contributions of the spectral “baseband” become less prominent. Therefore, the sampled ideal charge

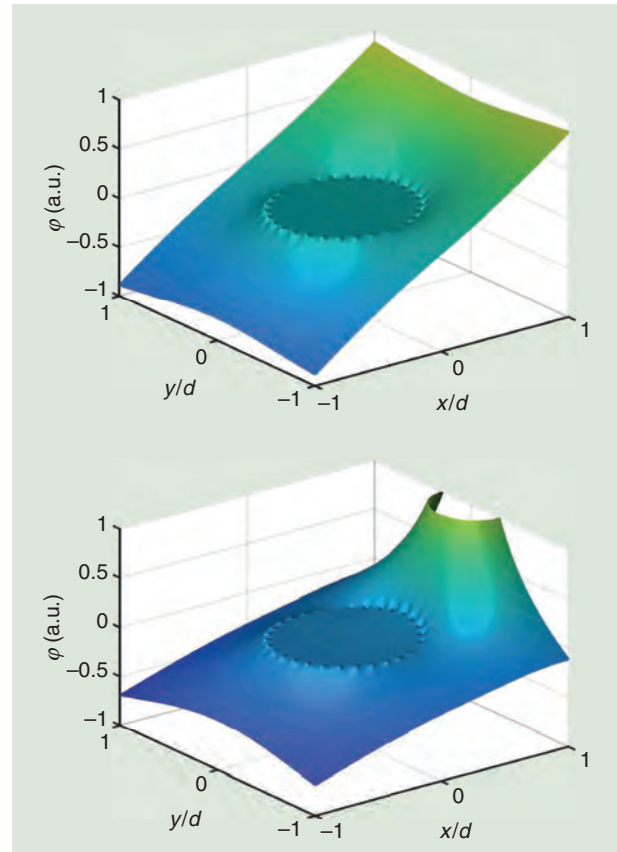


FIGURE 5. The electrostatic potential around a 2D circular wire cage ($N = 30$ wires) exposed 1) to a uniform electric field oriented in the $-x$ direction (the radius of the cage is 0.5 in used scaled units) and 2) to the field generated by a line charge at $x = d$, where the radius of the cage is $0.5 d$ and the diameter of the individual wires is $w = 0.01 d$. These results were obtained using a numerical simulation, as described in “Supplement C” of the supplementary material (available at 10.1109/MAP.2022.3229287). a.u.: arbitrary units.

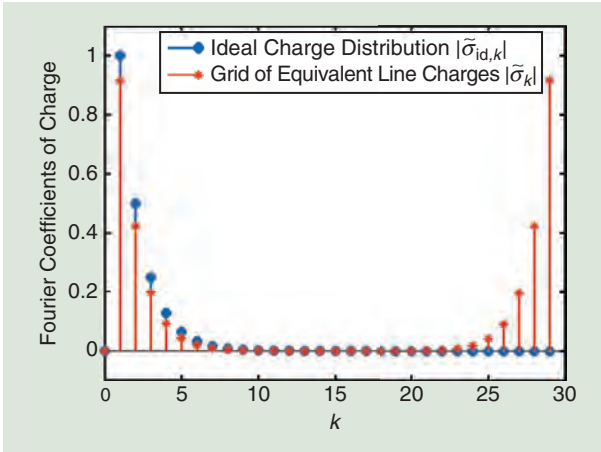


FIGURE 6. The Fourier coefficients $\tilde{\sigma}_k$ corresponding to the equivalent line charges (representing the charges on the cage wires) yield a periodic pattern of Fourier coefficients, which can be obtained using the FFT algorithm. The Fourier coefficients of the induced charge distribution $\tilde{\sigma}_{id,k}$ of the corresponding ideal Faraday cage (a conducting cylinder) are similar for low n . The coefficients $\tilde{\sigma}_k$ approximately correspond to a superposition of periodically repeated patterns of $\tilde{\sigma}_{id,n}$ as the induced charges on the wires are approximately equal to the sampled ideal charge distribution. (The coefficients are all real and negative; the plot shows their absolute value.)

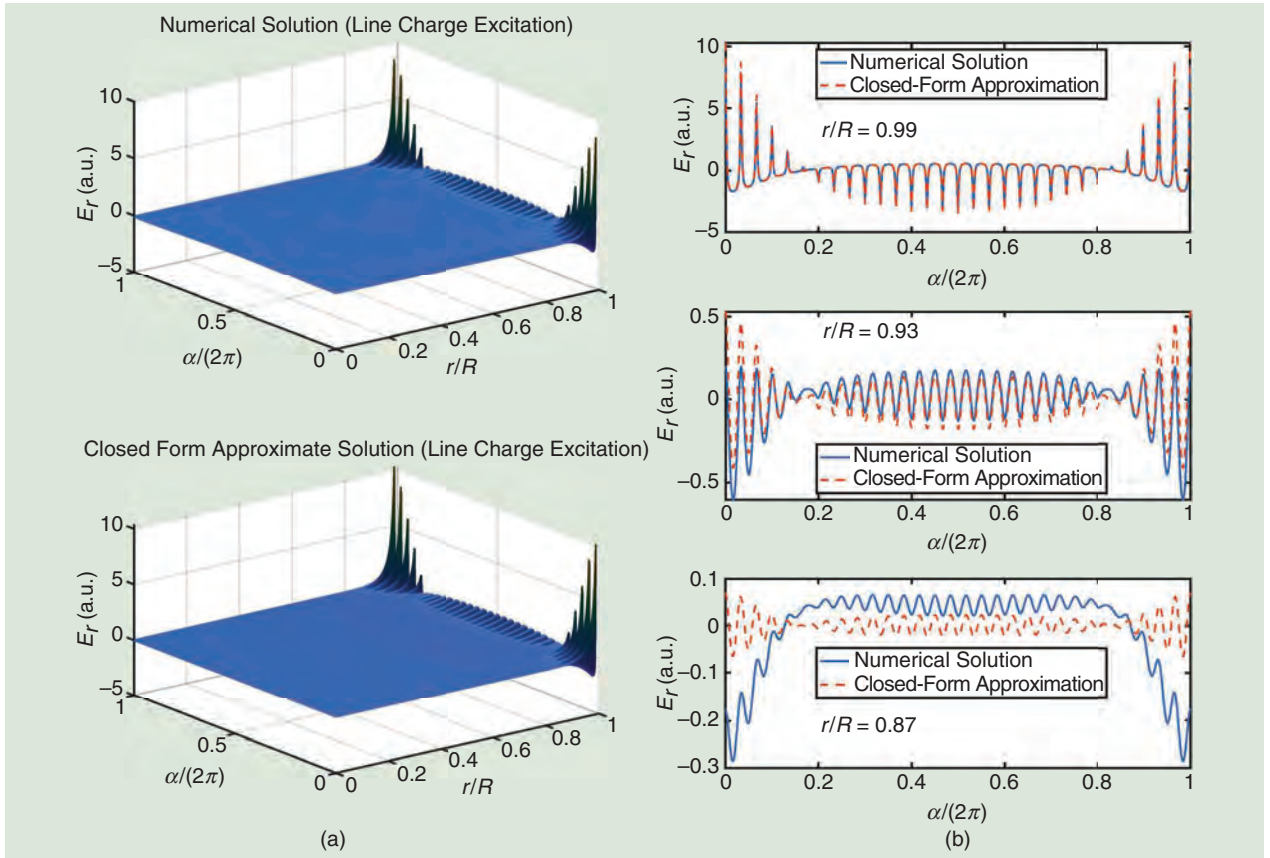


FIGURE 7. (a) The radial field component E_r inside the cage upon excitation by an external line charge versus the polar coordinates r and α and (b) versus α for different constant radii r . For the (a) plots, the upper plot gives the numerical solution and the lower plot the approximation according to (19).

approximation and others based thereon can at least qualitatively describe the field behavior. In particular, we can expect a dominating r -dependence $(r/R)^N$ for the potential, as shown in (20).

If we increase the cage size $R \rightarrow \infty$ but keep the distance (or arc length) between the wires, i.e., $a = 2\pi R/N$, constant, we can introduce a scaled-coordinate $\xi = (R - r)/a$, which, for increasing $\xi > 0$, leads from the cage boundary to the inside to the cage. The dominant dependence $(r/R)^N$ turns into $(1 - 2\pi\xi/N)^N$, which, in the limit $N \rightarrow \infty$, yields an exponential decay

$$\lim_{N \rightarrow \infty} \left(1 - \frac{2\pi\xi}{N}\right)^N = \exp(-2\pi\xi) \quad (23)$$

which corresponds to the statement given in *The Feynman Lectures on Physics* [4]. This means that Feynman's approximation is still valid for a large cage if the cage's wire spacing is small enough for the sampling approximation to be made.

Still, deep inside the cage, the approximation is not as good as there are substantial contributions from the remaining charges in the “baseband” present (see Figure 4), which are small but yield fields, which do not decay as strongly, as will also be illustrated by the examples in the next section. In “Supplement C” of the supplementary material (available at 10.1109/MAP.2022.3229287), relevance of the approximations made is briefly summarized.

EXAMPLES

In this section, we show the shielding efficiency and application of the different approximations presented for a simple example. As we are not so much interested in the shielding efficiency itself (which has been studied in the references given earlier) but rather demonstrate the degree of validity of the approximations, and particularly, the underlying consideration of periodically repeated spectra associated with the sampling approximation, we refrain from extended parameter studies. All the calculations were performed using scaled quantities, where the scaled line charge density $\hat{\rho}_l$ is related to the line charge density ρ_l by $\hat{\rho}_l = \rho_l / (2\pi\epsilon_0)$ with the vacuum permittivity ϵ_0 . For excitation by a single line charge, we set $\hat{\rho}_l$ to unity yielding associated units for the resulting fields (labeled as "a.u." in the plots).

In particular, we consider a cage consisting of $N = 30$ wires, which will be excited by the field of a positive line charge in a distance d from its center (see also Figure 1). Alternatively, we also briefly consider a uniform external field afterward. The radius of the wire cage amounts to $r = d/2$, and the diameter of the wires is $w = 0.01 d$. This means that the wire diameter amounts to roughly 10% of the spacing between the wires. The resulting potential landscape is shown in Figure 5 for the case of an external uniform field (oriented in a $-x$ direction) and for the field generated by the external line charge. In both cases, it can be seen that the potential inside the cage is fairly constant, corresponding to a vanishing electric field. Also, the location of the

Also, the location of the wires is clearly visible as they pin the potential to a constant value, i.e., the potential of the cage.

wires is clearly visible as they pin the potential to a constant value, i.e., the potential of the cage.

Solving for the charges on the wire, we compare the resulting Fourier coefficients of the equivalent line charge array with the Fourier coefficients of the induced continuous charge distribution in an ideal Faraday cage, which is shown in Figure 6. As discussed previously in this section, the coefficients $\tilde{\sigma}_k$ approximately represent a superposition of spectra of $\tilde{\sigma}_{id,k}$ shifted by $\pm mN$.

The field around the cage in terms of the potential illustrated in Figure 5 was obtained using the numerical method outlined in "Supplement C" of the supplementary material available at 10.1109/MAP.2022.3229287. In Figure 7, we show the corresponding radial field strength E_r according to the numerical solution and the approximate closed-form solution corresponding to (19). The field was obtained in polar (r, α) coordinates and is plotted in 3D surface plots using the polar coordinates as independent axes. The figure qualitatively suggests that the approximation is reasonable. To investigate this in more detail, we plot E_r versus α for three different r : $r = 0.99 R$, $r = 0.93 R$, and $r = 0.87 R$. It can be seen that accuracy of the approximation deteriorates quite quickly by increasing the distance $R - r$ from the cage boundary $r = R$, yet the magnitude of E_r also decreases rapidly (consider the y -axis scaling of the three plots) such that this relative error is not shown as clearly in the plot given in Figure 7, i.e., the absolute error is comparatively small everywhere.

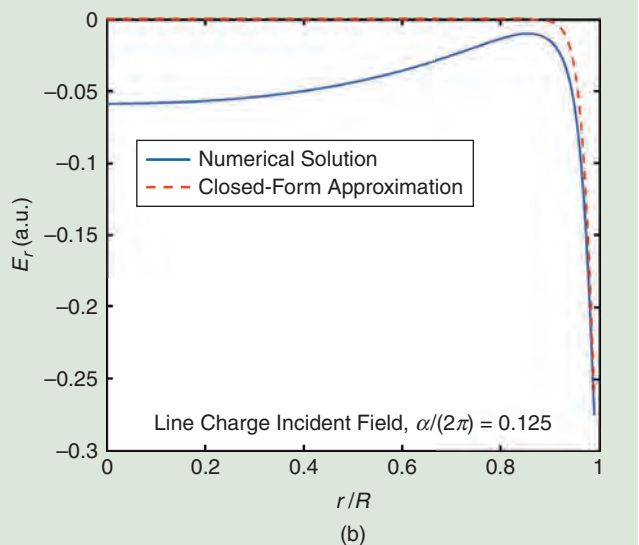
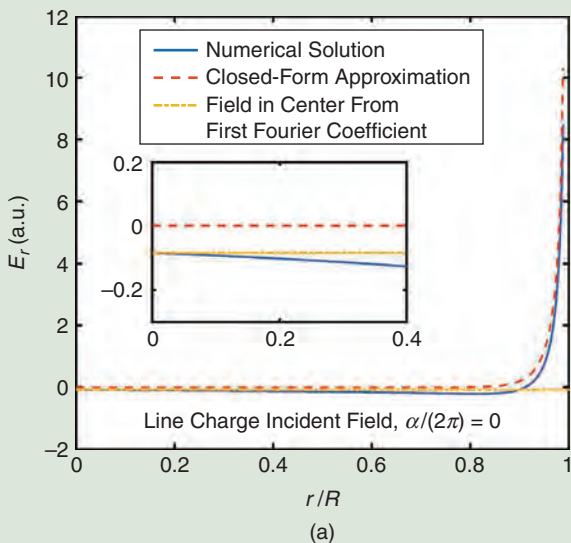


FIGURE 8. The radial field component E_r inside the cage upon excitation by an external line charge versus r for different constant angles α . These plots again represent cross sections through the ones given in Figure 7(a). The inset in (a) ($\alpha = 0$) shows a zoomed-in version illustrating the (limited) accuracy of the approximation close to the cage's center, showing the validity of the center field approximation (16) at the same time as indicated by the "Field in Center From First Fourier Coefficient."

This behavior can also be seen when plotting E_r versus r ; we did this for two fixed angles α : $\alpha = 0$ corresponding to the axis formed by the cage's center and exciting the line charge (where the strongest field E_r can be expected), and $\alpha = 0.125 \times (2\pi)$ corresponding to a 45° angle to this axis. In the first case, the approximation appears reasonable, but a closer inspection reveals that the residual E_r at the center of the cage ($r = 0$) is not reproduced; here the approximation yields a zero field. For $\alpha = 0.125 \times (2\pi)$, the approximation is qualitatively worse but again, the fields are much smaller in absolute value.

Figure 8 also depicts the characteristics for $\alpha = 0$, again with a magnified inset highlighting the behavior of small field strengths at the origin. The closed-form approximation approaches zero while the numerical result yields a small, yet nonzero, residual field. The dashed-dotted line indicates the field in the center according to (16), which corresponds to the first spectral coefficient. The numerical result asymptotically approaches this value for $r \rightarrow 0$. Note that this residual field is related to the difference of the two first ($k = 1$) spectral coefficients shown in Figure 6.

Figures 9–11 in “Supplement D” of the supplemental material (available at 10.1109/MAP.2022.3229287) show similar plots for the angular field component E_α conforming to the same observations. Note that $\alpha = 0$ was not selected as the scan line for the plot versus r as E_α vanishes along this line; instead, $\alpha = 0.017 \times (2\pi)$ was used, which corresponds to the radial line, which is approximately between the first two wires of the cage. Furthermore, Figures 12–17 in “Supplement D” of the supplemental material (available at 10.1109/MAP.2022.3229287) show corresponding plots for a uniform incident field.

CONCLUSIONS

The shielding efficiency of a circular Faraday cage with respect to arbitrary external (“incident”) electrostatic fields was considered as a 2D problem, demonstrating the application of a Fourier approach to represent the remaining field in the cage, where fields and charges were expanded into a Fourier series with respect to the angular coordinate. It turns out that the remaining field in the center of the cage is directly related to the first-order Fourier series coefficient of the charge distribution induced in the cage wires. A simple, approximate consideration where the induced field was expressed as a sampled version of the continuous charge distribution of an equivalent ideal Faraday cage (a conducting cylinder) showed that the field close to the cage boundaries can be expressed in terms of the shifted spectra that were a result of the sampling. Based on this consideration, a simple, closed-form approximation was established. The approach also explained to what extent the often-disputed claim that the field decays exponentially behind the boundary can be maintained.

ACKNOWLEDGMENT

Roman Beigelbeck is grateful for stimulating discussions with Andreas Kainz and other researchers involved in grant 3619S92411 from the German Federal Office for Radiation

Protection. This article has supplementary downloadable material available at 10.1109/MAP.2022.3229287.



AUTHOR INFORMATION

Bernhard Jakoby (bernhard.jakoby@jku.at) is a full professor with the Institute for Microelectronics and Microsensors at the Johannes Kepler University, A4040 Linz, Austria. He has worked in academic research in Belgium and the Netherlands as well as in the German automotive industry. He is a member of the Austrian Academy of Sciences and a Fellow of the IEEE.

Roman Beigelbeck (roman.beigelbeck@donau-uni.ac.at) is a senior scientist at the Department for Integrated Sensor Systems, the University for Continuing Education, A2700 Krems, Austria. He has (co)-authored more than 150 peer-reviewed papers. His current research comprises (semi)-analytical modeling techniques for sensing and thin-film characterization applications.

Thomas Voglhuber-Brunnmaier (thomas.voglhuber-brunnmaier@jku.at) is a senior researcher with the Institute for Microelectronics and Microsensors at the Johannes Kepler University Linz, A4040 Linz, Austria. Since 2008, he has been working on the modeling of microsensors for liquid property sensing.

REFERENCES

- [1] M. Faraday, *Experimental Researches in Electricity*, vol. 1. Redditch, U.K.: Read Books Ltd., 2016.
- [2] R. Bansal, “Shielded no more? [Turnstile],” *IEEE Antennas Propag. Mag.*, vol. 58, no. 4, pp. 88–89, Aug. 2016, doi: 10.1109/MAP.2016.2569409.
- [3] S. J. Chapman, D. P. Hewett, and L. N. Trefethen, “Mathematics of the Faraday cage,” *SIAM Rev.*, vol. 57, no. 3, pp. 398–417, Sep. 2015, doi: 10.1137/140984452.
- [4] R. Feynman, R. B. Leighton, and M. Sands, *The Feynman Lectures on Physics*, vol. 2. Reading, MA, USA: Addison-Wesley, 1964.
- [5] K. Subbarao and S. Mahajan, “Is Feynman’s analysis of electrostatic screening correct?” 2016, *arXiv:1609.05567*.
- [6] D. P. Hewett and I. J. Hewitt, “Homogenized boundary conditions and resonance effects in Faraday cages,” *Proc. Roy. Soc. A, Math., Phys. Eng. Sci.*, vol. 472, no. 2189, May 2016, Art. no. 20160062, doi: 10.1098/rspa.2016.0062.
- [7] T. Sumner, J. Pendlebury, and K. Smith, “Convectional magnetic shielding,” *J. Phys. D, Appl. Phys.*, vol. 20, no. 9, p. 1095, Sep. 1987, doi: 10.1088/0022-3727/20/9/001.
- [8] K. Simonyi, *Foundations of Electrical Engineering: Fields–Networks–Waves*. New York, NY, USA: Pergamon, 1963.
- [9] J. R. Barry, E. A. Lee, and D. G. Messerschmitt, *Digital Communication*. Berlin, Germany: Springer Science & Business Media, 2012.
- [10] M. Zahn, *Electromagnetic Field Theory: A Problem Solving Approach*. New York, NY, USA: Wiley, 1979.
- [11] I. S. Gradshteyn and I. M. Ryzhik, *Table of Integrals, Series, and Products*, 5th ed. San Diego, CA, USA: Academic, 1994.
- [12] R. E. Collin, *Antennas and Radiowave Propagation*. New York, NY, USA: McGraw-Hill, 1985.



5G/Millimeter-Wave Rectenna Systems for Radio-Frequency Energy Harvesting/Wireless Power Transmission Applications

An overview.

In this article, we present an overview of the 5G rectifying antenna and its primary elements for applications in millimeter-wave (mm-wave) energy harvesting (EH) and wireless power transmission (WPT). The wide spectrum available for 5G communication bands have attracted significant attention for extensive applications. The power received by the harvesting antenna relies on the size of the antenna. Hence, the realization of antenna and rectenna systems with good efficiency at 5G mm-wave is a challenge. This review article highlights the recent advances in 5G rectenna systems for different applications at the component and structure levels. The primary objectives of the article are 1) to



IMAGE LICENSED BY INGRAM PUBLISHING

explore the potential advances of mm-wave rectenna systems and the feasibility of their designs to attain desired characteristics and 2) to present a comparative assessment of performance parameters of existing rectenna systems.

INTRODUCTION

Demands for extremely high data rates, large network capacity, and flawless connectivity have increased globally as wireless technologies, such as 5G cellular systems, the Internet of things (IoT), and machine-to-machine, machine-to-human,

and human-to-machine communications, have advanced. 5G communication has been considered an appealing approach for meeting energy demands. The prime objective of 5G communication systems is to supply cellular consumers with higher data rates, lower power consumption, and better quality of services consistently. The frequency spectrum of 5G communication has been divided into several bands, including lower-band 5G (<1 GHz), midband 5G (3.1–6 GHz), and higher-band 5G (24.25–52.6 GHz) [1], [2], [3].

The rapid growth of the IoT and smart cities with increased data rates necessitates the deployment of millions of IoT devices with sensors. This could affect a large number of batteries that need to be charged and changed regularly. As a result, the design and implementation of autonomous self-powered systems, i.e., the unremitting IoT, is essential [4]. A radio-frequency (RF) EH technique is one potential means of achieving these goals. Researchers are now interested in the RFEH approach because of its unique features, such as maximum conversion efficiency and environmental independence, compared to other EH approaches. The rectenna is a specialized device designed exclusively for RFEH applications. The basic elements of the rectenna are the antenna and the rectifier [5]. The rectenna was investigated for WPT applications initially and also explored in RFEH applications [6]. The 5G/mm-wave bands are studied extensively in the outside atmosphere, due to increased energy demands. As a result, establishing 5G mm-wave rectenna systems for mm-wave EH/WPT applications is desirable.

Many review articles on rectennas for mm-wave EH/WPT applications have been reported in the literature; however, their scope has been limited [7], [8], [9], [10], [11]. Wagih et al. [7] have reviewed rectennas at mm-wave, including the higher band of 5G for mm-wave EH/WPT applications. Wagih et al. [8] have reviewed applications of rectennas in RFEH and WPT in view of antenna impedance bandwidth and radiation properties. Sleebi et al. [9] have reviewed the rectenna, its design challenges, and different rectifier topologies suitable for rectenna system design. Hassani et al. [10] have reviewed an RFEH approach for IoT systems. They highlighted the design requirements of RFEH for 5G systems and design constraints. Surender et al. [11] have reviewed various rectenna systems based on their frequencies of application. However, the reported review articles are not focused on rectenna systems operating at the frequency bands of current interest, such as 5G/mm-wave operating bands. To the best of the authors' knowledge, there is no publication addressing 5G/mm-wave rectennas for EH/WPT applications and their performance enhancement.

Researchers are now interested in the RFEH approach because of its unique features, such as maximum conversion efficiency and environmental independence.

EH/WPT ASPECTS IN 5G MM-WAVE COMMUNICATION

5G is frequently referred to as the Internet's enabler for everyone, everywhere, and everything. One of the technological goals of 5G is to increase cellular network capacity by a factor of 100 as compared to 4G (to generate a maximum data rate of >10 Gb/s) [12]. To meet the urgent demands for increased data rates and larger capacity, new spectrum usage techniques, including licensed, unlicensed, and shared spectra, are being researched. Sub-6-GHz (450 MHz–6 GHz) and mm-wave bands (24.25–52.6 GHz) spectrum are now assigned to 5G communication [13]. Sub-6-GHz bands are used to provide more coverage while maintaining reasonable data speeds. They can keep interoperability with 4G at the same time. The 5G standard's mm-wave bands are intended for ultrahigh-data-rate communication among devices in close proximity.

By 2025, it is expected that there will be over 35 billion linked devices, with over 20 billion of those being machine-to-machine configurations. As a result, one of the most significant tasks of 5G is to enable IoT communications with the ability to run the network independently for accessing services uninterrupted. On this front, EH is increasingly recognized as a promising solution. The eternal IoT with the design and execution of energy-independent self-powered systems is thus extremely desirable. mm-Wave EH and WPT are possible techniques to achieve these objectives. The mm-wave energy available in 5G wireless mobile bands (above 24 GHz) is a significant source of RF scavenging. This highlights the ability of 5G to construct a useful wireless power network or power grid.

RECTENNA DESCRIPTION

W.C. Brown first proposed the concept of the rectenna in the 1960s, intending to drive a model helicopter (Figure 1). WPT and helicopter technology have been successfully coupled to create a flying aircraft that is powered purely by a microwave beam [14], [15]. The significance of microwave-powered helicopter research goes far beyond its ability to give a new and practical capability in aerospace. The improved microwave energy-generating technology at superpower levels has enabled WPT over long distances for remote energization of objects and vehicles without the use of cables. WPT applications are explored in the fields of sensing, implantable devices, self-powered sensors, and so on. The rectenna is a device that helps to perform various applications of WPT.

Rectennas are composed of an antenna, an impedance matching network (IMN), a rectifier, and a dc pass filter, as illustrated in Figure 2. The amount of power input to the rectenna system may affect the overall rectenna system output.

The power input to the rectenna system can be increased by a suitable antenna, which is possible because of the high-gain, multiresonance, broadband resonance, and wide coverage characteristics of the antenna. A rectifier is one of the essential components of a rectenna system. The performance of the rectifier mainly relies on the selection of an appropriate diode and suitable rectifier topology. Schottky diodes are found suitable at RF power levels, due to their fast switching speed and low turn-on voltage. The diode is usually chosen based on the level of RF power input to the rectifier circuit and the operating frequency of the received RF energy. Generally used rectifier topologies are a half-wave rectifier (shunt/series), a voltage doubler rectifier (VDR), a full-wave bridge rectifier (FWR), and a Greinacher rectifier. The fundamental performance characteristics of the rectenna for both RFEH and WPT applications are presented in Table 1. Various design approaches to mm-wave EH/WPT systems for 5G applications are discussed in the following sections in detail.

RFEH/WPT SYSTEMS FOR SUB-6-GHZ BANDS

This section illustrates various approaches to RFEH/WPT systems to operate at 5G within the frequency

band of 0.5–6 GHz. The primary intention of any rectenna system is to harvest as much power from an ambient/dedicated source as possible and to increase the rectenna system output. Different classification-based strategies are explored in this part to suit the criteria of RFEH/WPT systems.

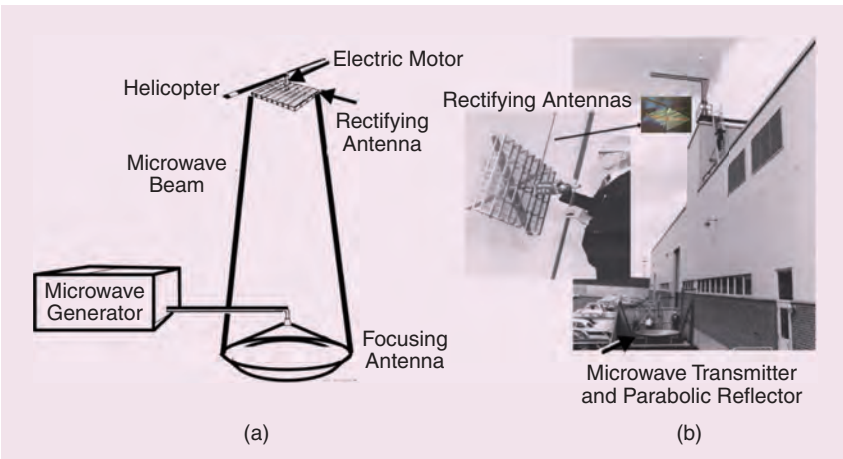


FIGURE 1. The wireless powered transmission experimental setup with a flying drone model by W.C. Brown. (a) The basic elements of a microwave-powered helicopter system [6]. (b) First WPT-aided flying drone experiment. [14].

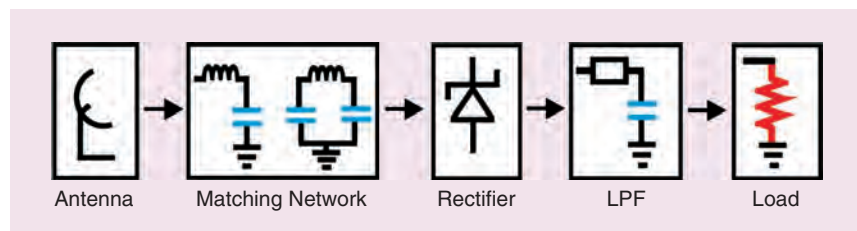


FIGURE 2. A rectenna system. LPF: low-pass filter.

TABLE 1. THE PERFORMANCE CHARACTERISTICS OF RECTENNA SYSTEMS.

Rectenna System for WPT	Rectenna System for RFEH
A dedicated source of energy is essential for a known channel.	Both ambient and dedicated sources of energy are utilized.
An antenna with directional radiation is desired.	An antenna with omnidirectional radiation is desired.
The rectenna can be designed at any of the operating frequencies.	The rectenna must be designed at specific frequencies that are available in most of the surrounding atmosphere.
Performance is independent of ambient energy density.	Performance relies on the density of energy in the ambient environment.
The available incident RF energy is predictable.	The availability of incident RF energy is unpredictable.
It is sensitive to polarization mismatch.	It is sensitive to polarization mismatch.
It is suitable to operate at single/ dual-band applications efficiently.	Ambient RFEH is associated with multiband harvesting; hence, it is suitable to operate in multiband applications.
A high-gain antenna is desired with the known channel of propagation.	A high-gain antenna is undesirable due to the unknown channel of propagation.
Circular polarization rectennas have been mainly proposed for WPT due to their relative immunity to being mispositioned.	All polarization rectennas are highly preferred due to multisource harvesting. Dual-polarized antennas are useful to receive most of the polarized waves from the surroundings.

ANTENNA CONFIGURATIONS

An irregular diamond shape of the radiator was adopted for multiresonance characteristics, including 5G [16]. A monopole antenna with a circular geometry and equally spaced rectangular strips has been investigated for reconfigurability at the operating band [17]. A modified E-shaped microstrip antenna [18], a fan-shaped structure with a coplanar waveguide (CPW) feed [19], and a slit-loaded bow tie antenna fed by a pair of microstrip lines [20] were employed for 5G RFEH applications. A notch included a slotted-ground plane [21] and a hexagonal slot embedded in a circular monopolar antenna [22], widening the operating range. A

To meet the urgent demands for increased data rates and larger capacity, new spectrum usage techniques, including licensed, unlicensed, and shared spectra, are being researched.

back-to-back approach to the patch helps achieve wide angular coverage [23] (see Figure 3).

RECTIFIER CONFIGURATIONS

A CMOS-based multistage rectifier with two different paths for low and high input power levels was designed for harvesting applications [24]. For designing a dual-band rectifier, a Greinacher rectifier topology was investigated in [25]. A shunt diode rectifier using a high-impedance microstrip line was designed in [26]. A dc feedback loop was created for enhancing the rectifier performance at low input

power levels and also to operate the rectifier efficiently across a wide range of input power levels (see Figure 4).

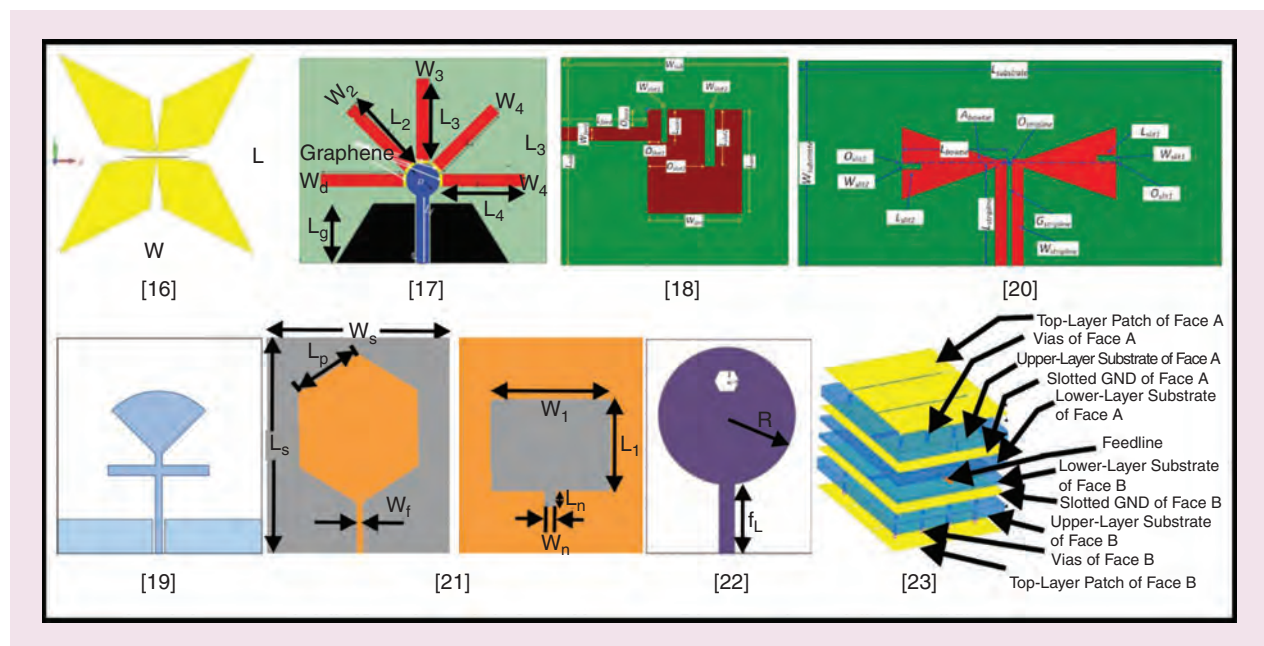


FIGURE 3. Antenna configurations for sub-6-GHz RFEH applications.

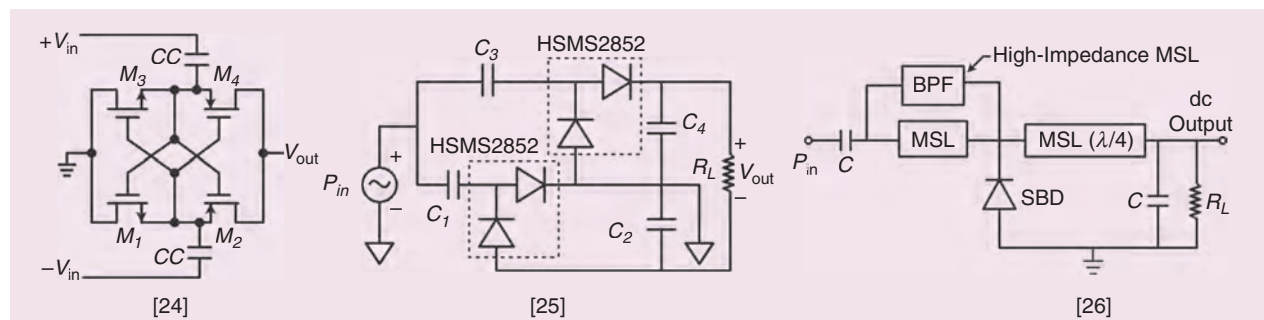


FIGURE 4. Rectifier topologies for sub-6-GHz RFEH applications. BPF: bandpass filter; MSL: microstrip line, SBD: shottky barrier diode.

RECTENNA CONFIGURATIONS

Rectenna performance was investigated with different combinations of rectifier array circuits, such as 1×1 , 2×2 , 4×4 , and 8×8 [27]. It is noticed that the number of elements in an antenna array affects the output voltage more than the efficiency, as shown in Figure 5. A rectenna using a modified E-shaped microstrip antenna and a two-stage voltage multiplier [28] as well as an optical rectenna system using a solar cell

antenna [29] were designed for IoT applications. A flexible keyhole shape of an antenna and a VDR were used in the rectenna design [30]. A rectifier consisting of two tapered lines connected at the core of the rectifier circuit enhanced the rectifier power conversion efficiency (PCE) and output voltage performance.

A CPW-fed circular patch antenna deposited on a transparent polyethylene terephthalate substrate for efficient operation in both indoor and outdoor conditions was designed in [31]. In [32], a dual-band rectenna was developed using an antenna with a slots-loaded ground plane and a series-connected rectifier circuit. A rectenna with a combination of a stub-loaded planar antenna and a half-wavelength shunt rectifier has been presented [33]. The length of the stubs controls the operating frequency of the antenna circuit. A spiral-slot antenna integrated into a diplexer and transponder circuitry was chosen for designing the rectenna [34].

The sub-6-GHz grid in 5G communication allows for ubiquitous exposure, but it runs into spectrum scarcity, making it difficult to sustain a considerable rise in the number of wireless appliances in 5G and beyond. There is growing interest in putting 5G mm-wave cells beneath existing sub-6-GHz cells to provide appropriate network capacity and widespread coverage. Due to its vast spectrum of resources at higher frequencies, mm-wave has been widely exploited for long-distance communication in terrestrial and satellite applications, resulting in extremely high data rates. Designing an EH/WPT system at the mm-wave 5G band is highly desirable due to its increased availability and its ability to design a harvesting system with a compact dimension (see Figures 6–8).

EH SYSTEMS FOR 5G MM-WAVE

This section discusses various design approaches to mm-wave EH systems for 5G mm-wave applications.

ANTENNA CONFIGURATIONS

A dual-patch antenna configuration [35], a two-leg Yagi antenna [36], and a pair of concentric ring slots [37], described in Figure 9, were investigated for mm-wave EH applications. A flexible mm-wave antenna is designed by

By 2025, it is expected that there will be over 35 billion linked devices, with over 20 billion of those being machine-to-machine configurations.

printing a triangular-shaped patch on a flexible field-effect transistor (FET) substrate [38]. A reconfigurable Y-shaped patch antenna [39] and an asymmetric antipodal Vivaldi antenna (AVA) [40] were developed for mm-wave EH applications. In [39], the reconfigurability is achieved by integrating two p-i-n diodes with the microstrip patch radiator. A flexible textile antenna integrated into an electromagnetic bandgap (EBG) structure was designed for on-body applications in [41].

RECTIFIER CONFIGURATIONS

In [42], a W-band zero-bias detector from Virginia Diodes was found suitable to operate efficiently up to a frequency of 81 GHz. A multi-IMN consisting of a T-section impedance transformer and a series shunt stub was investigated for tri-band rectifier design in [43] (see Figure 10).

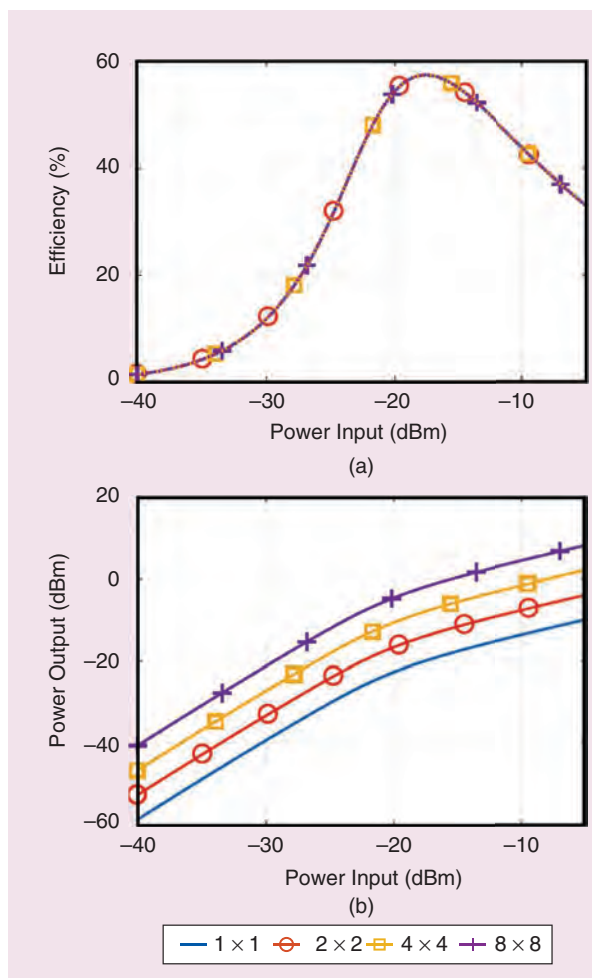


FIGURE 5. A performance comparison: (a) efficiency and (b) output power [27]. dBm: decibels referenced to 1 mw.

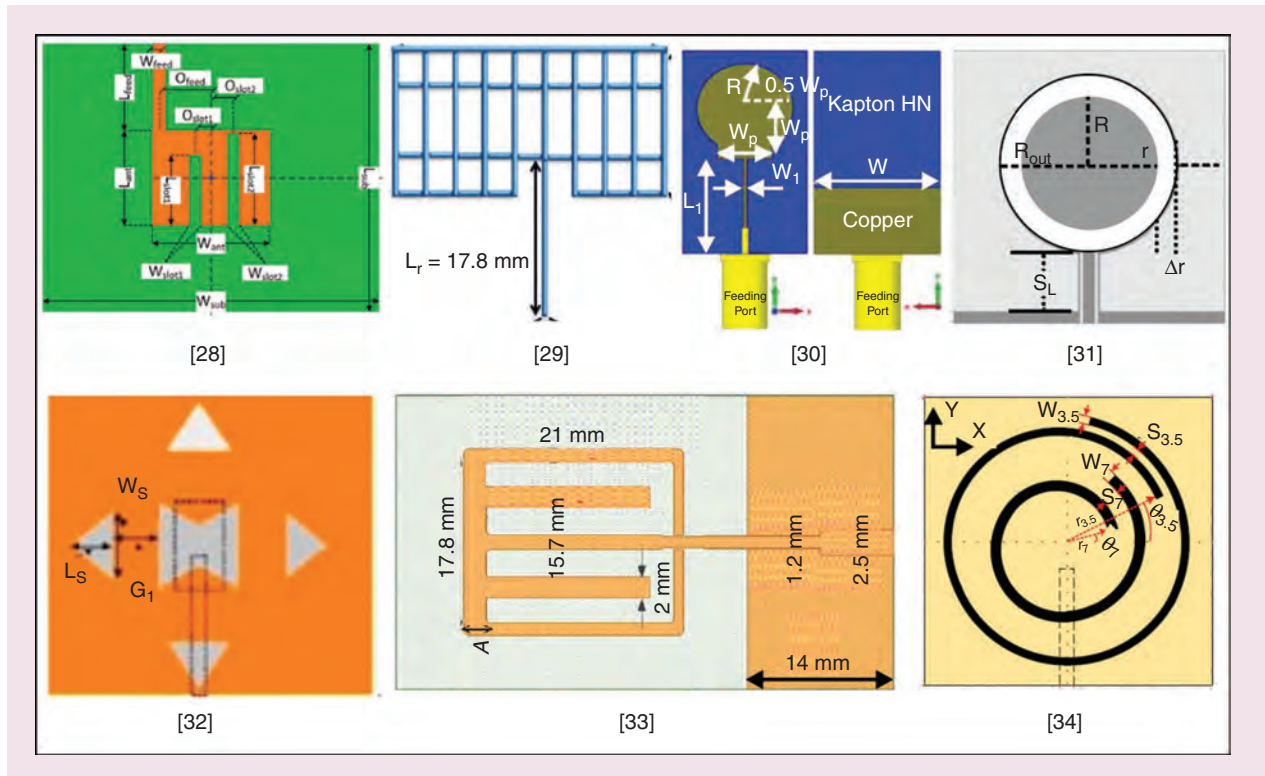


FIGURE 6. Rectenna designs for sub-6-GHz RFEH/WPT applications.

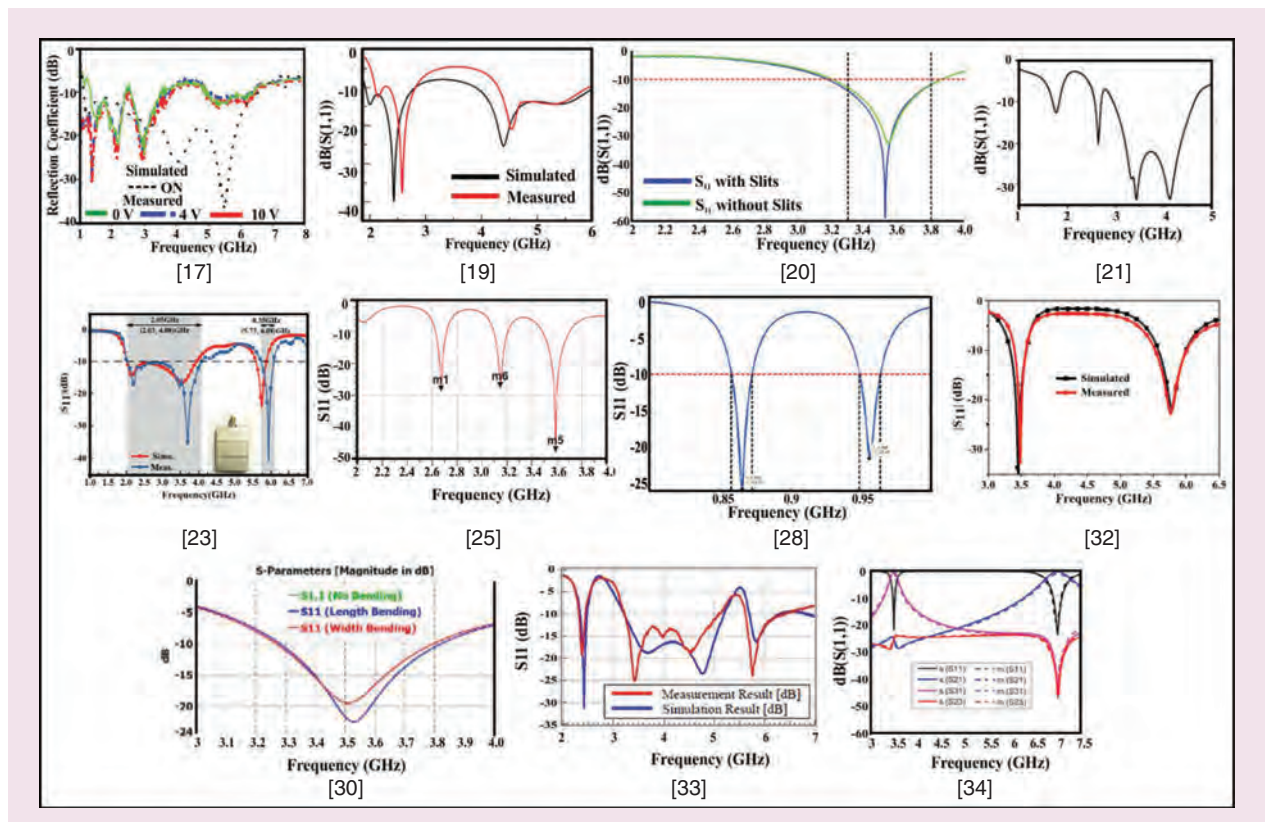


FIGURE 7. The $|S_{11}|$ plots of antenna configurations for sub-6-GHz RFEH/WPT applications.

RECTENNA CONFIGURATIONS

The performance of a receiving rectifying element (RRE) with different combinations of antenna array cells, such as quadrupoles, double dipoles, collinear wire, and mesh,

was investigated [44]. A better rectification efficiency performance of the RRE was achieved with double dipoles and quadrupoles. A mm-wave EH RFID tag was designed with CMOS technology in [45]. A monopole

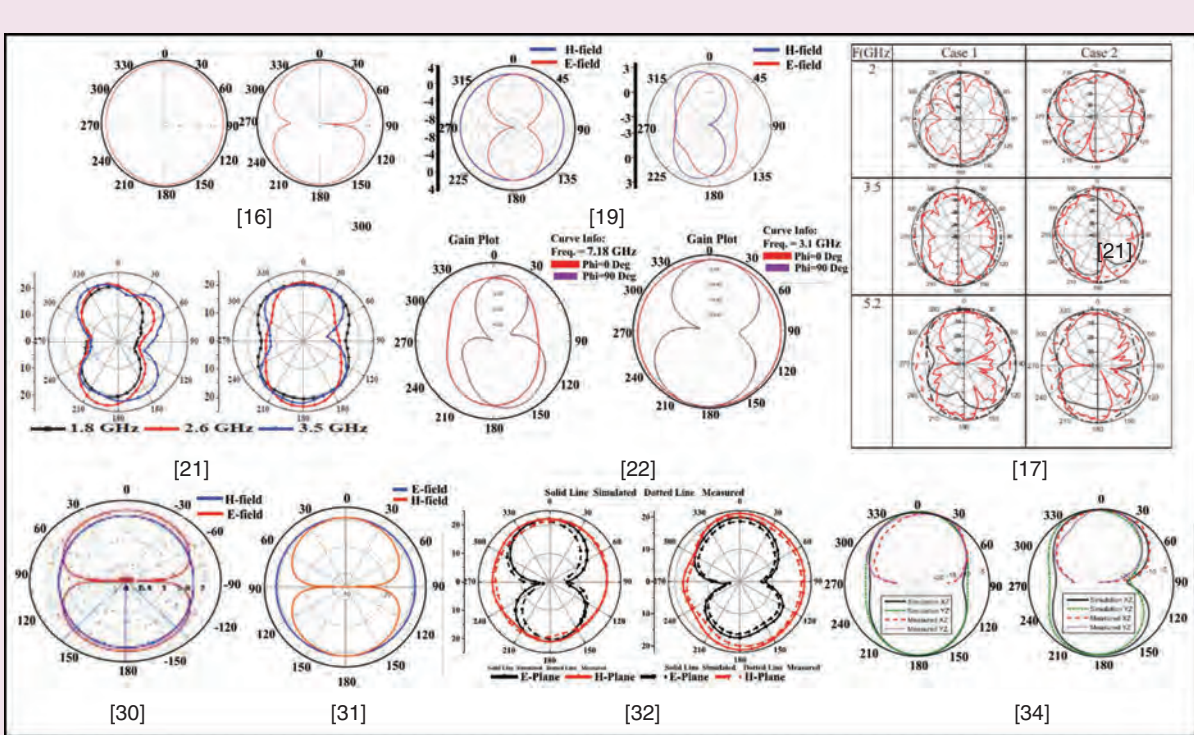


FIGURE 8. The radiational characteristics of antenna configurations for sub-6-GHz RFEH/WPT applications.

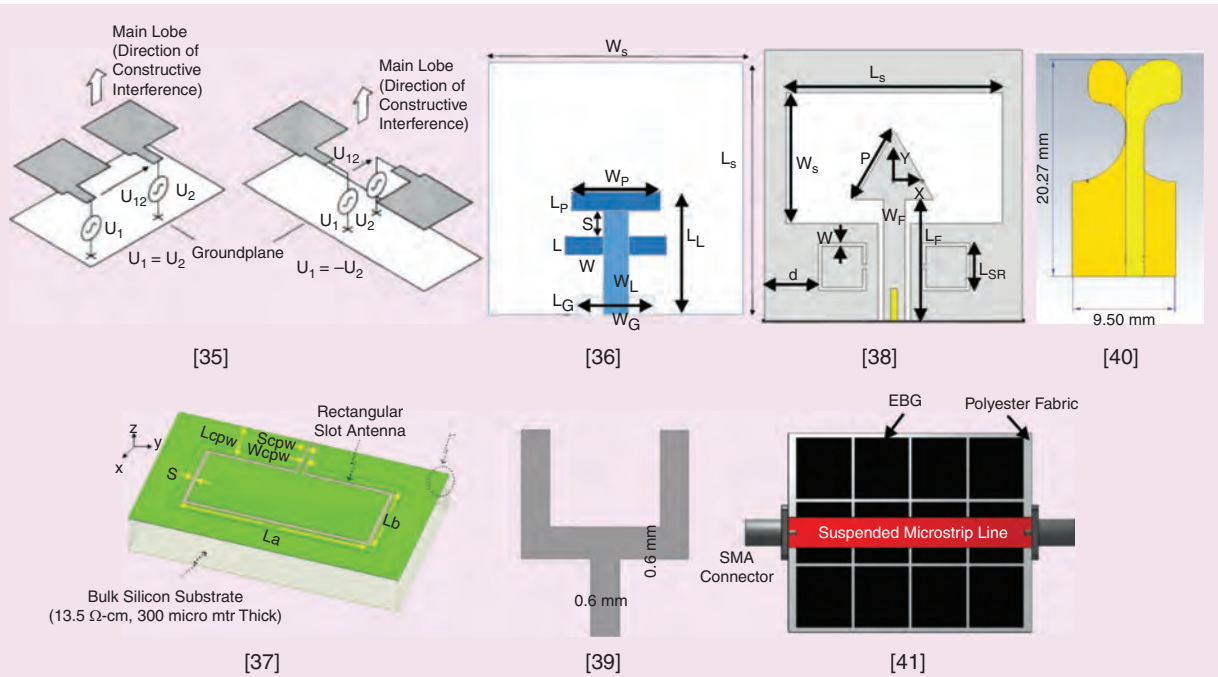


FIGURE 9. The antenna geometries for mm-wave EH applications.

antenna with a three-stage inductive peak rectifier in [46], a CMOS-based rectenna with a dipole antenna and a single-stage Dickson rectifier in [47], and an array of antenna elements in [48], [49], and [50] were investigated for rectenna system design. The array of antennas enhances the antenna gain, thereby increasing the harvested power. Enhanced rectifier performance in terms of PCE was observed using a metal–insulator–metal (MIM) diode at the V band [51]. A graphene FET (GFET)-based rectenna was implemented to increase the impedance bandwidth of the rectifier circuit [52], [53].

A compact harvesting system that is immune to the wireless link parameters and loading variations was designed for biomedical implants [54]. A packaged integrated harvester system operated at 26 GHz was designed to be embedded within 3D-printed multilayer flexible packaging structures [55]. A graphene self-switching diode-based rectenna was investigated experimentally for the first time using a patch antenna array [56]. The graphene diode is designed for the maximum possible nonlinearity in the current–voltage curve. A textile-based rectenna is implemented using an AVA and a VDR for wearable applications [57].

WPT SYSTEMS FOR 5G MM-WAVE APPLICATIONS

Several mm-wave rectenna configurations for WPT systems have been proposed in recent decades. This section delves into the advancements in rectenna design techniques that have occurred over time. These techniques lower transmission costs and design complexity, provide a high level of power utility, and allow for the installation of a battery management facility.

Improved microwave energy-generating technology at superpower levels has enabled WPT over long distances for remote energization of objects and vehicles without the use of cables.

ANTENNA CONFIGURATIONS

A coplanar stripline-fed folded dipole in [58], a lens-based antenna for low diffraction loss [59], and a dual-port electromagnetically coupled square patch array antenna in [60] were investigated for WPT applications. The array elements are rotated by 45° to reduce the mutual coupling among the elements. An array of antenna elements is used to achieve a high gain [61], [62]. A metasurface superstrate enhances the harvested power [63], while a metasurface array antenna exhibits a wide angular coverage [64]. A flexible textile antenna with an inset microstrip feed was designed for mm-wave WPT applications in [65]. A triple L-arms patch slotted antenna with a diamond-shaped ground was implemented for 5G applications [66].

RECTIFIER CONFIGURATIONS

A VDR circuit with microstrip technology was developed for WPT applications [67]. To enhance the rectifier PCE, a harmonic harvesting rectifier circuit was implemented using a $\lambda/4$ open circuit stub resonator [68]. Transmission line (TL)-based impedance transformers are used to match the real impedance of the antenna and rectifier circuits [69]. An integral form of a double compact microstrip resonant cell low-pass filter and a CPW feedline with CMOS technology have been developed to design a very small-sized rectenna [70]. A TL-based VDR was designed for dual-band characteristics at 28- and 38-GHz frequencies [71]. A CMOS technology-based rectifier was implemented for WPT applications at the W and Ka bands [72]. A performance comparison of the rectifier at two mm-wave frequencies is presented in Figures 11 and 12.

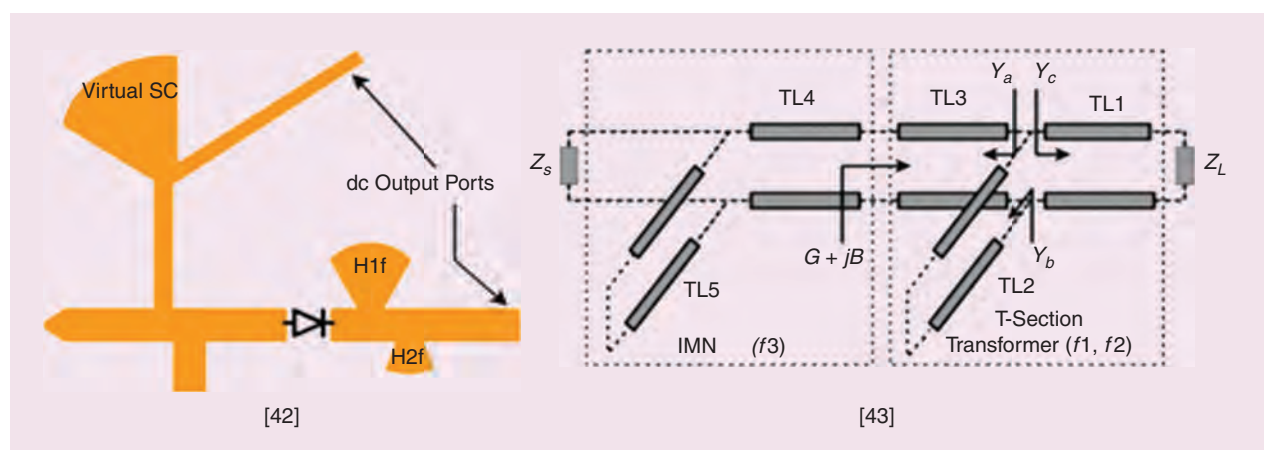


FIGURE 10. Rectifier configurations for mm-wave EH applications. TL: transmission line; Virtual SC: virtual short circuit.

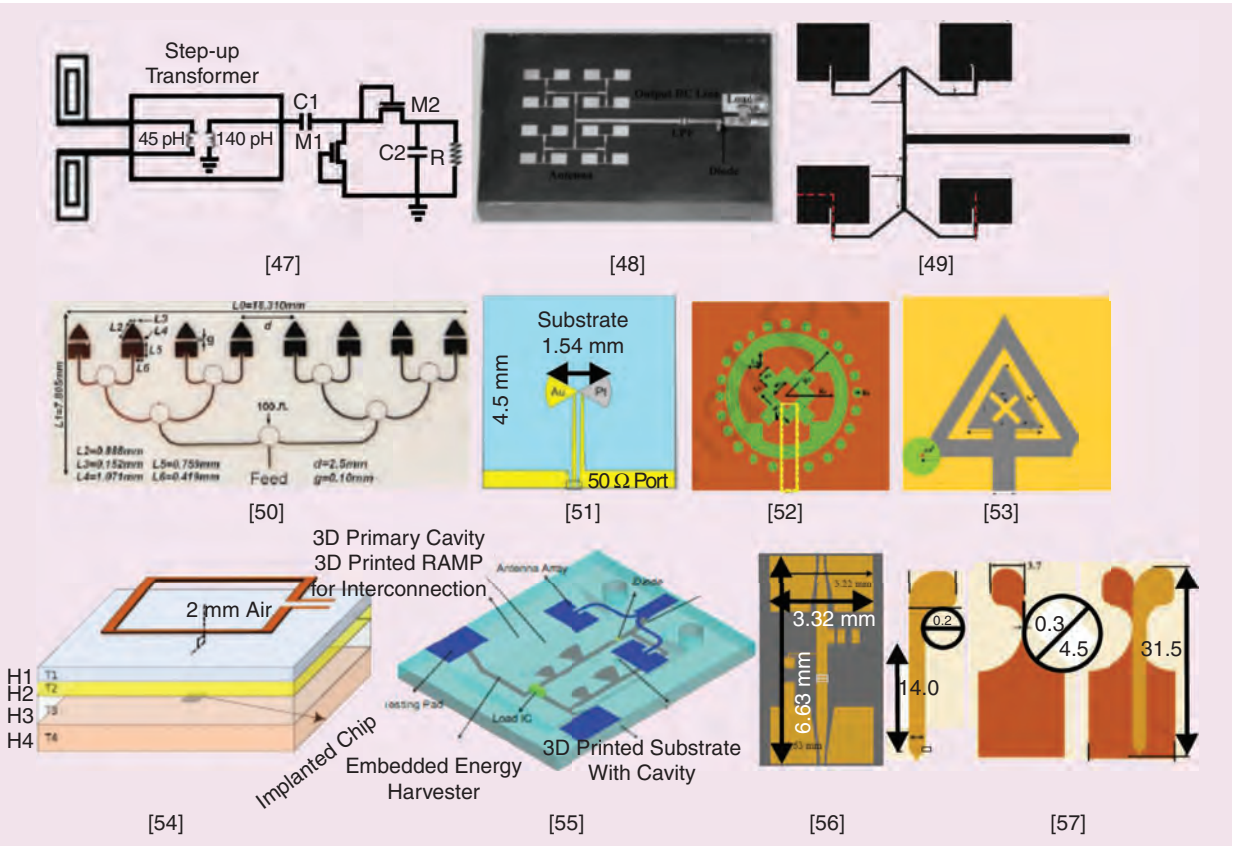


FIGURE 11. Antenna/rectifier configurations for mm-wave EH applications.

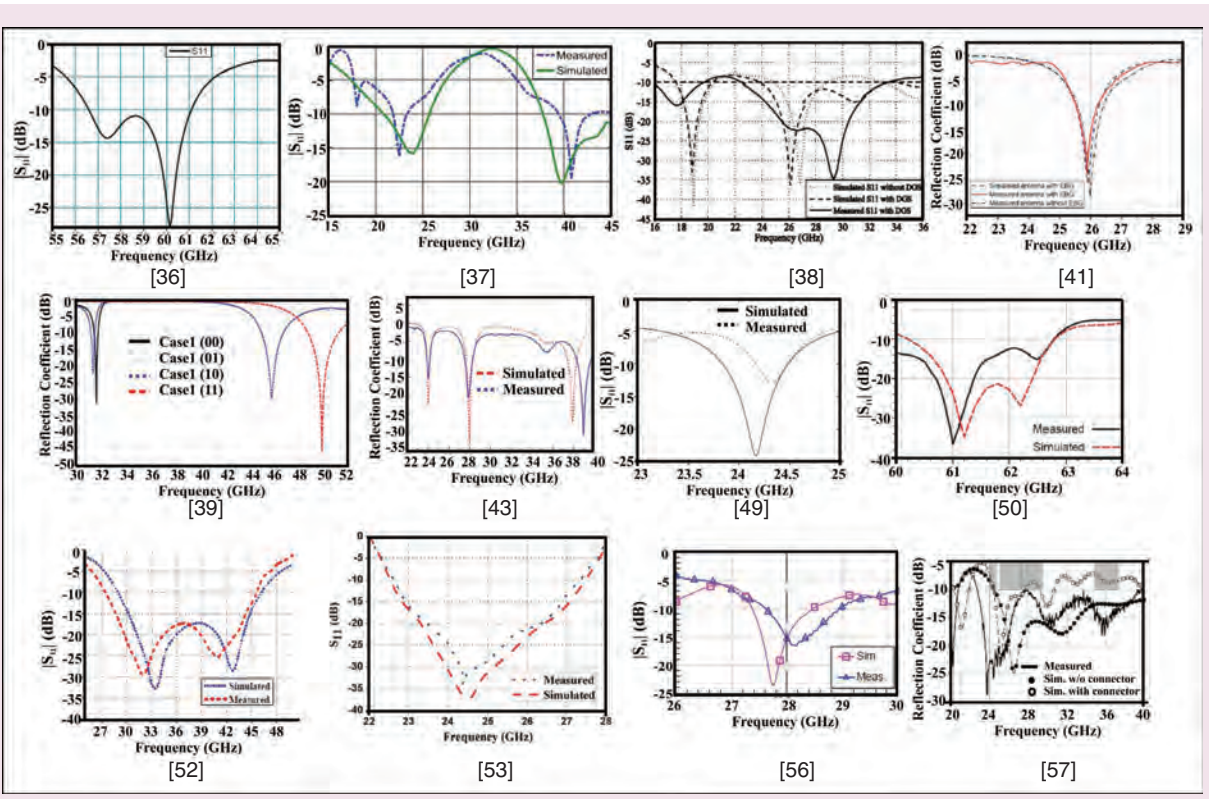


FIGURE 12. The $|S_{11}|$ plots of antenna configurations for mm-wave EH applications.

It has been shown that it is essential to improve the diode performance for enhancing the rectifier performance at sub-terahertz frequencies [73]. At the W band, the TL-based approach to the matching network shows low loss [74]. The tunnel diode-based rectifier exhibits better conversion efficiency over the Schottky diode-based

rectifier for input power levels of <1 dB referenced to 1 mW (dBm) [75], as illustrated in Figure 13(a). A hybrid form of technology involving a two-stage Dickson charge pump/voltage multiplier and gallium arsenide technology was found to be suitable for enhancing the rectifier performance [76] (see Figure 14).

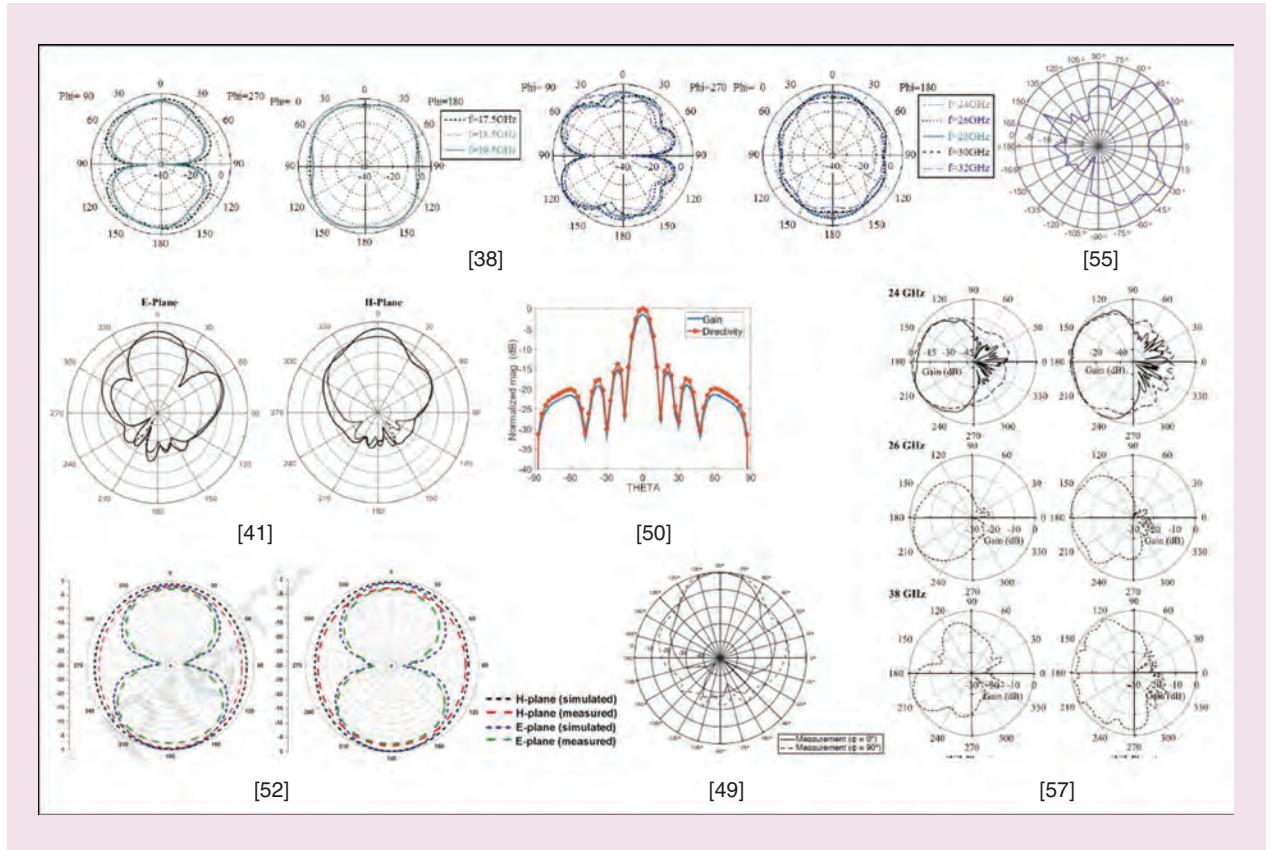


FIGURE 13. The radiational characteristics of antenna configurations for mm-wave EH applications.

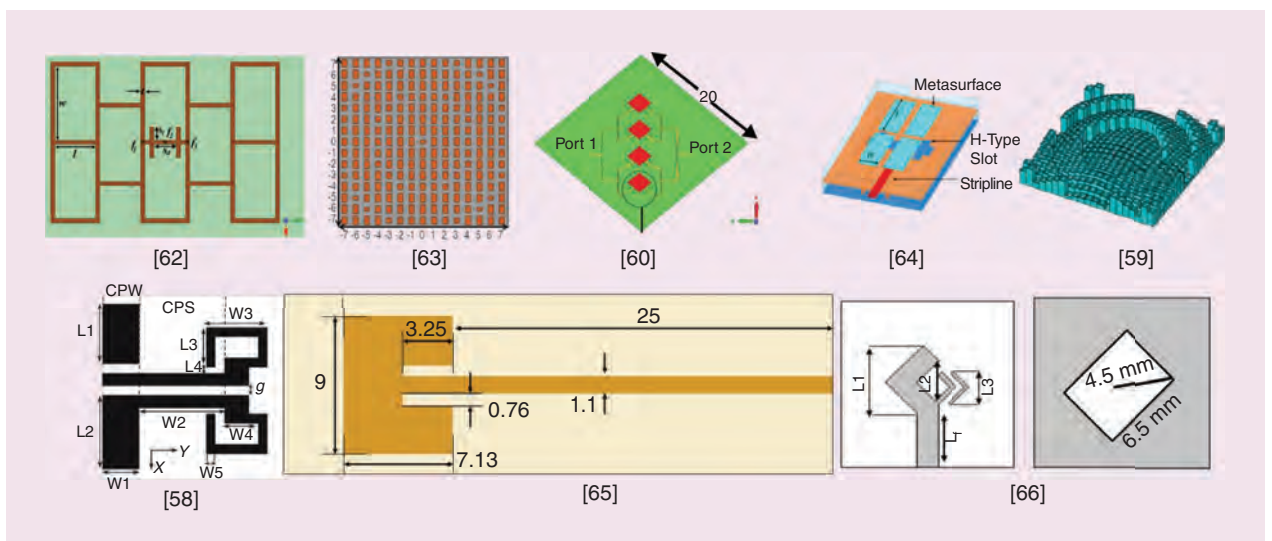


FIGURE 14. Antenna geometries for mm-wave WPT applications.

RECTENNA CONFIGURATIONS

The design and development of mm-wave rectennas and power beaming systems were presented in [77]. The diode characteristics at 2.45 and 35 GHz were investigated [78]. An array-based rectenna system exhibits better output voltage performance [79]. A full-wave rectifier-based rectenna with a tapered slot and finite-width ground CPW (FGCPW) TLs using CMOS technology was implemented in [80]. The FGCPW TLs help to reject harmonic components. An adjustable stub and a resonator included after the diode in a shunt topology increase the PCE [81]. Hatano et al. found that the rectenna with a class F load showed better performance than the conventional rectenna with a capacitive load and that the performance increases with an increase in the number of diodes, as revealed in Figure 13(b) [82].

A mm-wave rectifier circuit as a monolithic microwave integrated circuit was fabricated to reduce the rectifier dimension and also to increase the rectifier PCE [83]. A substrate integrated waveguide (SIW) technology of rectenna design reduces the losses [84]. An SIW cavity-backed antenna was integrated into a self-biased rectifier to create a rectenna [85]. The SIW cavity-backed antenna array enhances the gain and also achieves circular polarization (CP). A high-efficiency rectifier was designed using two output class F dc pass filters and a high-gain Fabry-Perot resonator antenna [86]. A rectenna with a grid type of antenna integrated into a complementary cross-coupled oscillator-like rectifier was designed [87]. A simple rectenna was implemented using a dipole antenna and a single diode element [88]. A rectenna using a microstrip patch antenna and a rectifier circuit was designed with microelectromechanical system technology [89]. A fin line transfer circuit was used in the design process for reducing losses. A 35-GHz rectenna was developed using a patch antenna fed by a coupling slot and MA4E1317 diode-based shunt rectifier circuit in [90] (see Figure 15).

A rectenna was implemented by a bow tie-shaped antenna coupled to a MIM diode [91]. A flexible rectenna system for a conformal surface was designed using a flexible cylindrical patch antenna array and a flexible rectifier circuit [92]. In [93], a slot-coupled patch antenna array with SIW cavity back feeding was used for enhanced gain with proper isolation among the elements (see Figures 16 and 17). The performance of rectennas was analyzed for two rectifier topologies using two different diodes at 24 GHz [94]. A performance comparison of two rectenna arrays is investigated in [95], as revealed in Figure 18. A transparent optical rectenna was investigated for the first time for harvesting purposes [96]. A rectenna was designed

To direct the radiated energy from the base station antenna array to the end user while overcoming increasing path losses, beam steering antennas will be required.

using a tapered slot antenna and a CMOS switching rectifier to increase the antenna gain, radiation efficiency, and PCE [97]. A similar output performance to that presented in Figure 18 was observed with the increased number of rectenna array elements [98]. The rectenna system was experimentally demonstrated with a free-flight AR Drone at an altitude of 800 mm [99] (see Figures 19 and 20).

BEAM STEERING APPROACH FOR 5G MM-WAVE COMMUNICATION

To direct the radiated energy from the base station antenna array to the end user while overcoming increasing path losses, beam steering antennas will be required as 5G moves into higher frequencies (see Figure 21). Beam steering permits a signal to be concentrated in one direction instead of radiating over 120°, as it would do typically. Electronically steerable antennas (ESAs) control the signal, allowing for more precise propagation and a

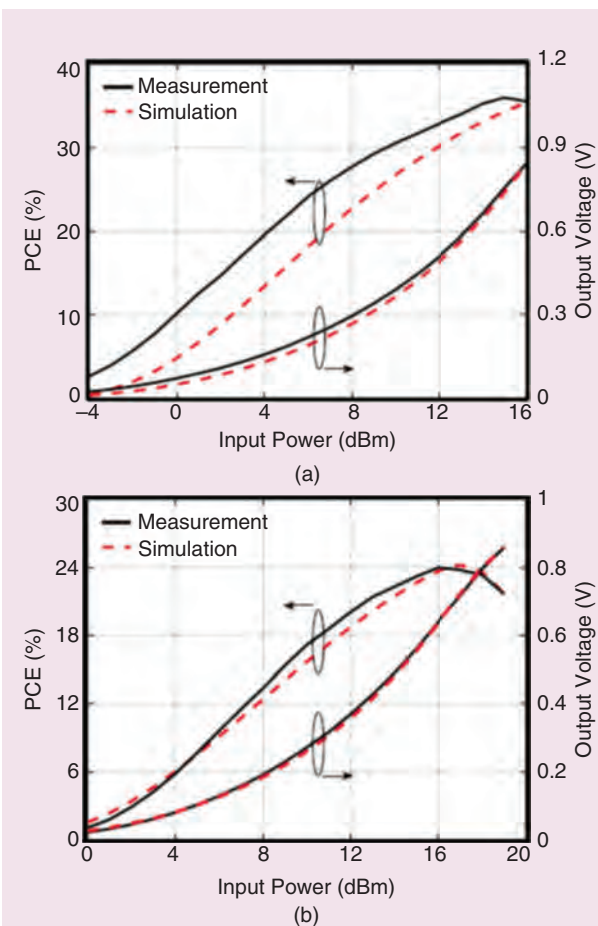


FIGURE 15. A performance comparison: (a) 35 GHz and (b) 94 GHz [72].

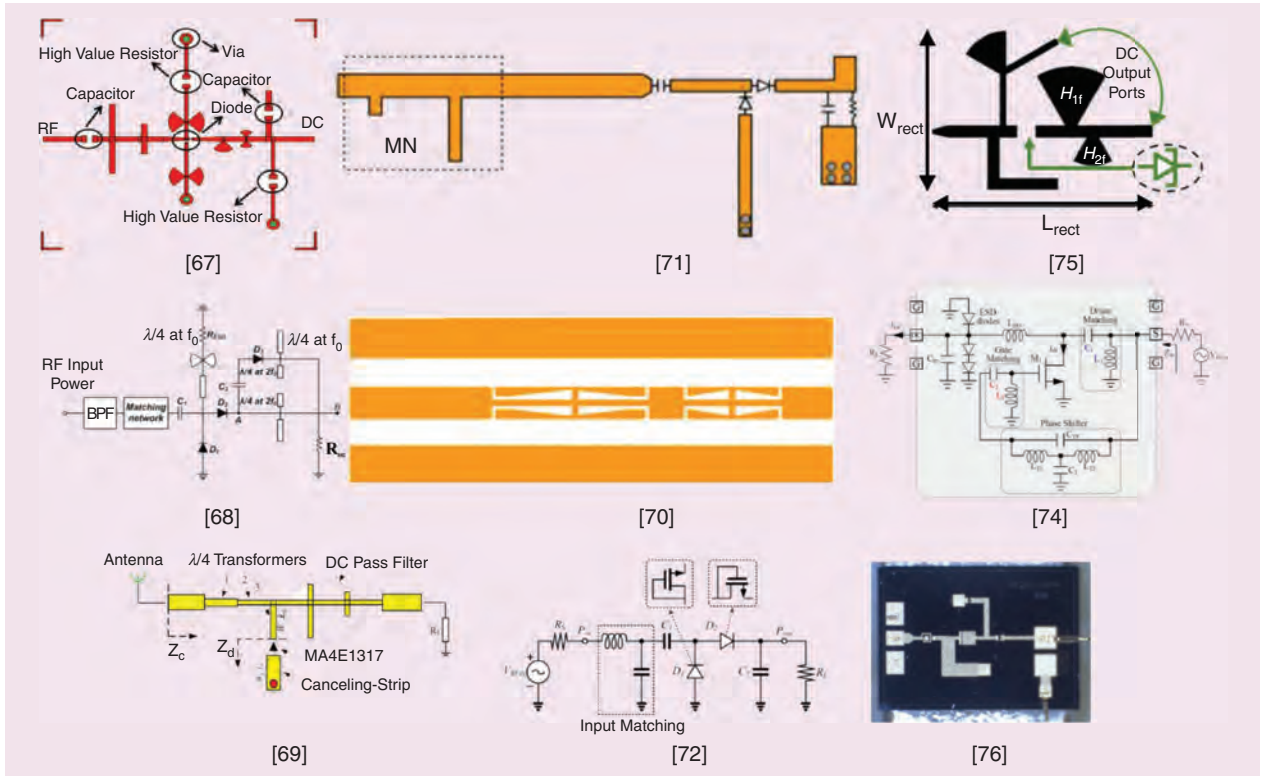


FIGURE 16. Rectifier topologies for mm-wave WPT applications. MN: matching network.

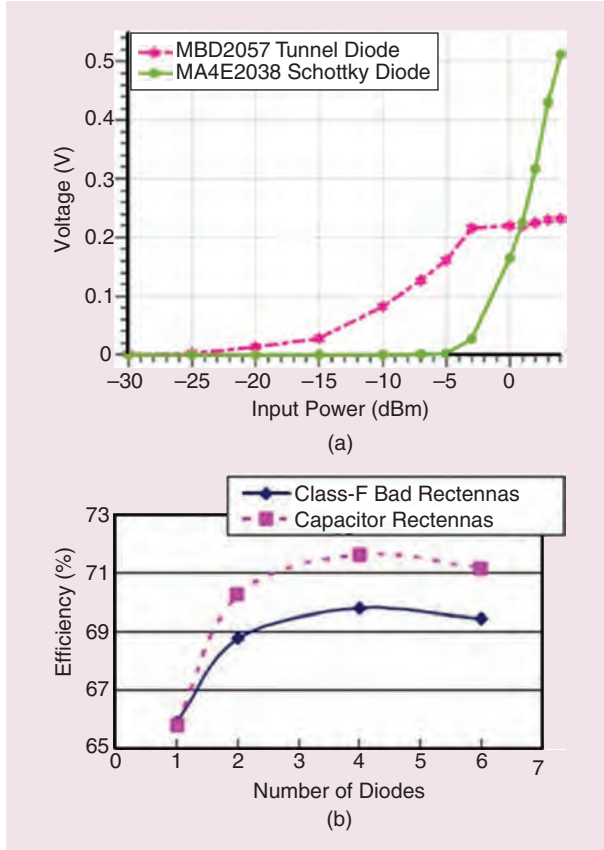


FIGURE 17. The rectenna performance: (a) V_{out} [75] and (b) PCE [82].

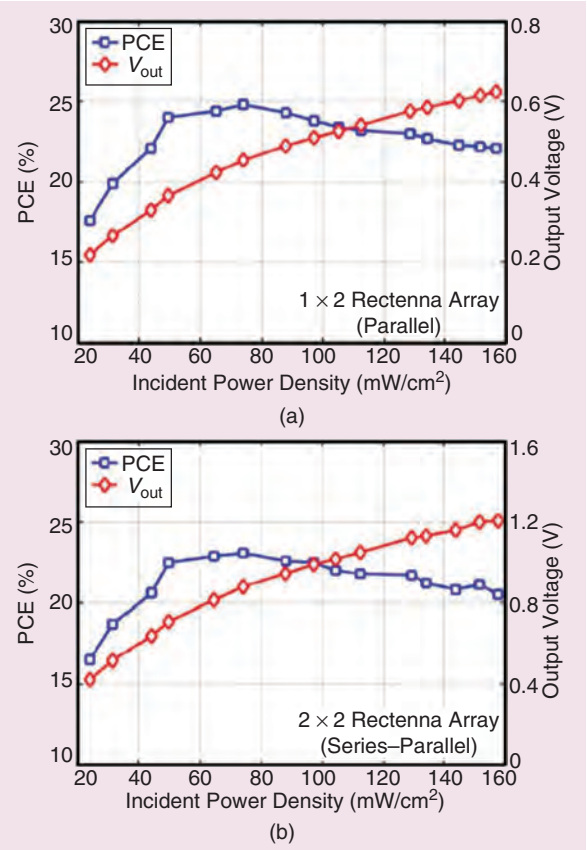


FIGURE 18. The rectenna array performance variation: (a) a 1×2 rectenna array and (b) a 2×2 rectenna array [95].

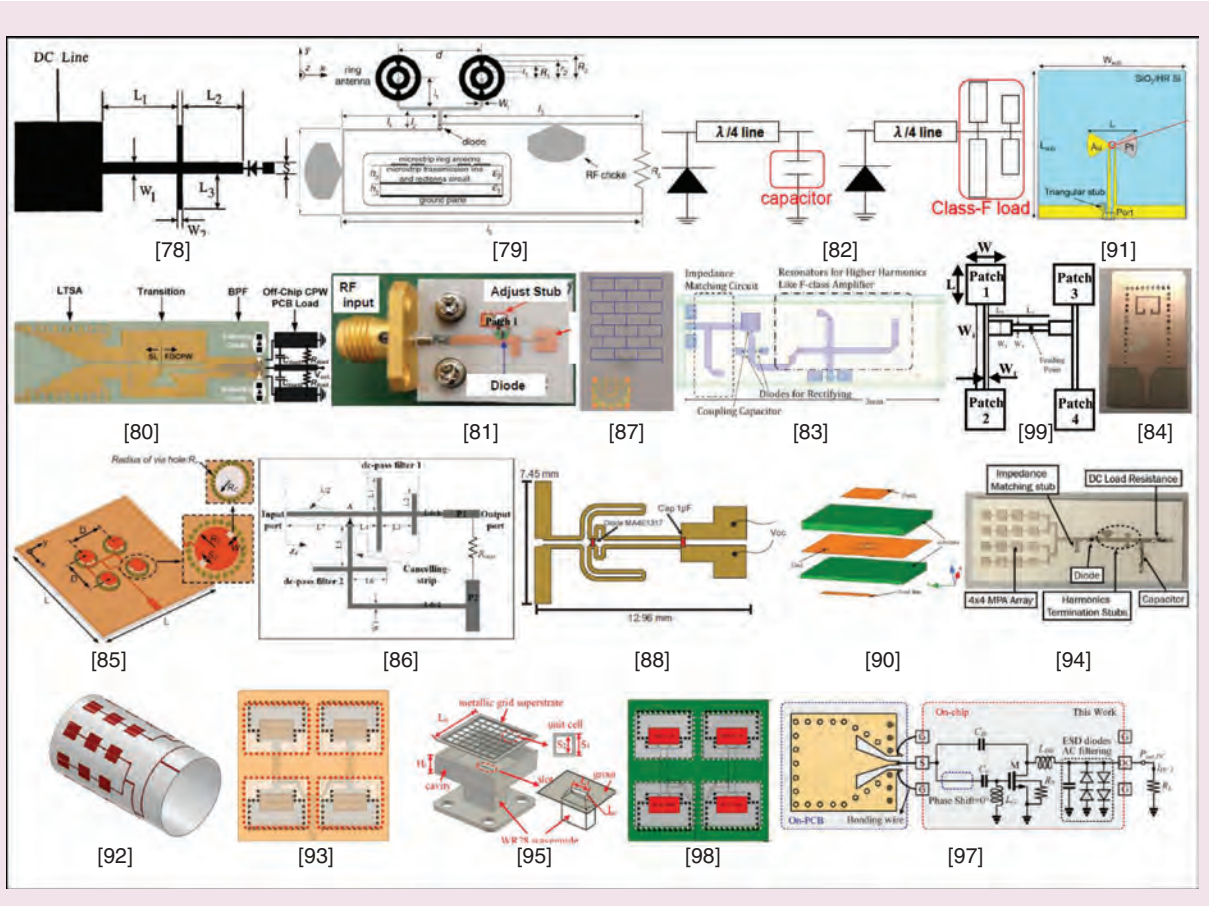


FIGURE 19. Antenna/rectifier configurations for mm-wave WPT applications.

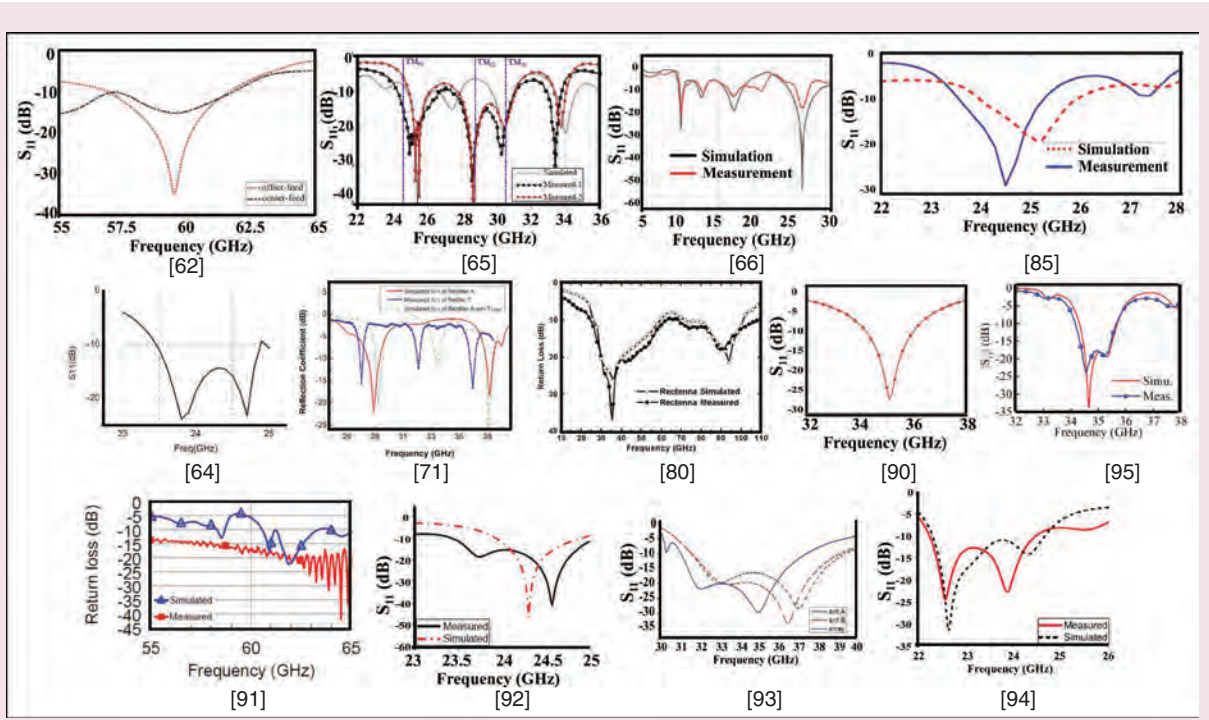


FIGURE 20. The $|S_{11}|$ characteristics of antenna/rectifier configurations for mm-wave WPT applications.

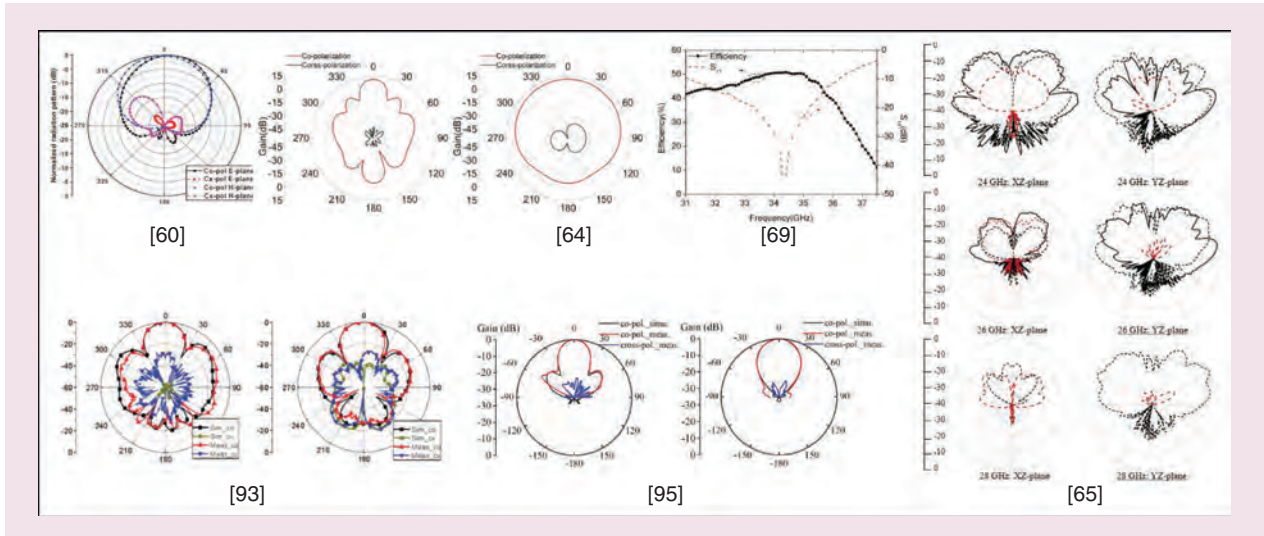


FIGURE 21. The radiational characteristics of some antenna configurations for mm-wave WPT applications.

faster more reliable connection than would be possible otherwise. This reduces the propagation loss and extends the range of

5G in mm-wave frequencies. The Rotman lens is a unique and economical way to do mm-wave beam steering.

Dense mm-wave networks may provide comparable coverage and data rates to traditional microwave networks [100]. Advanced beamforming techniques that allow multiuser transmission can be used to generate a large gain. A hybrid power combining approach that adapts a beamforming matrix was proposed for achieving both a large dc output and wide angular coverage [101]. A 4×4 Butler matrix has been investigated for beam scanning and power transmission applications [102]. Larger antenna arrays have been used at mm-wave frequencies to realize higher gain values [103]. A beamforming network was investigated for WPT applications to enhance the output power [104]. WPT with a scalable array-based passive beamforming system was investigated to support concurrent multidirectional full field of view power transfer [105]. Different combinations of RF power combining and dc power combining approaches were investigated [106].

The following conclusions are presented:

- 1) In the four beamforming with dc and RF combining approaches, the output dc power grows significantly as the number of antennas increases at the transmitter/receiver.
- 2) For dc combining, optimized beamforming achieves higher output dc power than beamforming based on singular value decomposition (SVD).
- 3) SVD-based general receive beamforming outperforms analog receive beamforming for RF combining.
- 4) When the number of receive antennas grows large enough, RF combining outperforms dc combining.

The commonly used dc combining technique does not raise the overall rectenna system's turn-on sensitivity. To overcome the tradeoff between angular coverage and sensitivity, the Rotman lens has been used between the antenna and rectifier [107], [108], [109], [110].

TABLE 2. A PERFORMANCE ANALYSIS OF 5G SUB-6-GHZ ANTENNAS FOR RFEH SYSTEMS.

Reference	Frequency (GHz)	Bandwidth (GHz)	Approach	Gain (dBi)
[16]	1.8/1.9/ 2.1/2.4/ 4.9/5.5	1.53–2.47/ 4.9–5.63	Irregular diamond-shaped quadrangles	—
[17]	3–7.8	3–7.8	Monopole with rectangular strips	1.8
[18]	2.6/3.5	2.62–2.69/ 3.3–3.8	Modified E patch	4.26/2.58
[19]	2.4/5.8	1.9–2.8/ 3.9–6	Planar sector patch	2.05/2.7
[20]	3.5	3.17–3.86	Modified bow tie approach	8.6
[21]	1.8/2.6/ 3.5	1.7–1.84/ 2.54–2.68/ 2.96–4.64	Notch-included slotted ground	6.41
[22]	—	2.36–12.69	Partial ground	3
[23]	2.1/2.4/ 3.5/5.8	2.03–4.08/ 5.73–6.08	Back-to-back patch	-0.42/0.19/ 0.91/2.4

dBi: decibels isotropic.

TABLE 3. A PERFORMANCE ANALYSIS OF 5G SUB-6-GHZ RECTIFIERS FOR RFEH APPLICATIONS.

Reference	Frequency (GHz)	Diode/Transistor	Rectifier Topology	P_{in} (dBm)	PCE (%)	V_{out} (V)
[24]	0.86–1.96	CMOS	—	-14	10	1
[25]	2.6/3.5	HSMS285x	Greinacher	6	56.1/7.9	—
[26]	—	HMPS-282x	HWR	27.8	59	—

HWR: half-wave rectifier.

TABLE 4. A PERFORMANCE ANALYSIS OF 5G SUB-6-GHZ RECTENNAS FOR RFEH SYSTEMS.

Reference	Frequency (GHz)	Dimension (mm ³)	Gain (dB)	Polarization	Rectifier			V_{out} (V)
					Topology	P_{in} (dBm)	PCE (%)	
[27]	0.85	—	—	LP	HWR	-17.6	57.4	—
[28]	0.85	295 × 295 × 1.6	4.96	LP	GRC	-10	—	1.26
[29]	3.5	35 × 30 × 0.77	3.5	LP	HWR	0	54.9	—
[30]	3.5	27.4 × 15.6 × 0.125	2.07	LP	VDR	0	43.5	0.93
[31]	3.5	24 × 24 × 0.1	1.51	LP	VDR	0	42	0.9
[32]	3.5/5.8	60 × 50 × 1.6	6.41/5.01	CP	HWR	5	54.5/41.2	1.31/1.16
[33]	2.45/3.8/5.8	56 × 43 × 1.6	1.26/0.37/3.32	LP	HWR	0	26.8/29.1/43.3	—
[34]	3.5/7	35 × 35 × 0.6	4/3.8	CP	HWR	—	—	—

GRC: Greinacher rectifier circuit; LP: left-hand polarization.

TABLE 5. A PERFORMANCE ANALYSIS OF 5G MM-WAVE ANTENNAS FOR MM-WAVE EH SYSTEMS.

Reference	Frequency (GHz)	Bandwidth (GHz)	Approach	Gain (dBi)
[36]	60	56–61	Yagi structure	10.8
[37]	24/40	20.5–25.5/38–45	Hybrid structure	-1/0
[38]	—	15.9–19.7/22.5–34	DGS approach	4.8/8.8
[39]	49.8/31.6/31.4/45.45	—	Y-shaped antenna	7.8/6.14/4.97/6.73
[40]	26/28	20–30	Asymmetric antipodal	6.2/7
[41]	26	25.5–28.1	EBG	6.13

DGS: defective ground structure.

TABLE 6. A PERFORMANCE ANALYSIS OF 5G MM-WAVE RECTIFIERS FOR MM-WAVE EH SYSTEMS.

Reference	Frequency (GHz)	Diode/Transistor	Rectifier Topology	P_{in} (dBm)	PCE (%)	V_{out} (V)
[42]	24/81	MA4E2038 MA4E1317	HWR	5	45	0.53
[43]	24/ 28/ 38	—	VDR	15.6	44.3/ 42.7/ 40.6	—

characteristics. A few rectifier circuits reported in the literature for the sub-6-GHz band are compared in Table 3. The HSMS-285x series diodes are found to be suitable for sub-6-GHz applications operating at moderate to high input power levels. Table 4 presents a performance comparison of different sub-6-GHz rectennas. From [29], [30], and [31], it is found that the dimensions of the rectenna also affect its gain value. We also observe that the half-wave rectifier (HWR) offers better PCE at low input power levels.

COMPARATIVE STUDY

RFEH/WPT SYSTEMS FOR SUB-6-GHZ BAND APPLICATIONS

A performance comparison of different sub-6-GHz antennas is presented in Table 2. It is understood that a bow tie shape offers better gain, and slotted and partial ground-based structures help to achieve multiresonance and broadband

RFEH SYSTEMS FOR MM-WAVE APPLICATIONS

Table 5 compares the performance of different rectenna designs. Hybrid and antipodal structures are designed for a wide impedance bandwidth of the antenna, but a hybrid system offers a comparatively low gain. Limited articles on

rectifier circuits for 5G mm-wave are provided in Table 6, which is self-explanatory. Table 7 reveals the performance of various rectenna systems designed for RFEH 5G mm-wave applications. It may be noted that at high frequencies, the HWR circuit is the most-adopted rectifier topology. Also, a GFET-based rectenna shows better PCE performance and output voltage.

WPT SYSTEMS FOR MM-WAVE APPLICATIONS

The performance of various antennas designed for 5G mm-wave WPT applications is given in Table 8, which is

self-explanatory. Table 9 reveals that a VDR using a DMK2790 diode exhibits better PCE over a VDR with other possible diodes of the rectifier circuit. Table 10 presents the performance of 5G mm-wave rectenna systems for WPT applications. It is noticed that there is a need to develop rectenna systems with polarization-insensitive characteristics. It is observed that, at the same input power level, the maximum possible conversion efficiency is observed with an HWR topology, and the maximum output voltage is achieved with the VDR topology [92], [94]. The mm-wave rectenna systems are found to operate efficiently

TABLE 7. A PERFORMANCE ANALYSIS OF 5G MM-WAVE RECTENNA FOR MM-WAVE EH SYSTEMS.

Reference	Frequency (GHz)	Dimension (mm ³)	Gain (dB)	Polarization	Rectifier Topology	P _{in} (dBm)	PCE (%)	V _{out} (V)
[46]	71	—	—	—	Multistage	5	8	—
[48]	35	21.7 × 22.6 × 1.6	19	LP	HWR	8.45	67	2.18
[49]	24	13 × 20 × 0.18	5	LP	HWR	18	—	2.5
[50]	61	18.3 × 7.8 × 0.12	13.3	LP	HWR	0	49.3	0.05
[51]	36	4.5 × 4.5 × 0.52	4	LP	—	—	—	—
[52]	36	3.2 × 3.2 × 1.6	8.12	LP	GFET	2	80.3	6.38
[53]	24.25	40 × 40 × 1.6	7.8	CP	GFET	5	83	6.8
[57]	24	33 × 16 × 0.5	7.41	LP	VDR	10	12	1.7

TABLE 8. A PERFORMANCE ANALYSIS OF 5G/MM-WAVE ANTENNAS FOR WPT APPLICATIONS.

Reference	Frequency (GHz)	Dimension (mm ³)	ε _r	Bandwidth (GHz)	Gain (dBi)
[58]	35	—	2.33	33–41	5
[59]	35	100.8 × 100.8 × NS	2.87	—	0.65
[60]	35	20 × 20 × 0.63	2.2	33.9–36.13	12.4
[62]	60	9 × 6 × 0.504	3.2	57–61.5	12.6
[63]	30	60 × 60 × 1.5	2.33	28–32	—
[64]	24	20 × 33.6 × 1.143	2.2	23.5–24.5	16.8
[65]	26	0.59 × 0.75 × 0.034	1.95	24.9–31.1	8.2

TABLE 9. A PERFORMANCE ANALYSIS OF 5G/MM-WAVE RECTIFIERS FOR WPT SYSTEMS.

Reference	Frequency (GHz)	Diode/Transistor	Topology	P _{in} (dBm)	PCE (%)	V _{out} (V)
[67]	24	HSMS 2862	VDR	40	45	—
		DMK 2790		9	42	—
		MA4E1317		20	68	—
[69]	35	MA4E1317	HWR	12.5	50	2.92
[71]	28/38	MA4E1317	VDR	15	46/42	—
[72]	35/94	CMOS	—	15	36.5/21	0.7/0.5
[75]	28	MBD2057-E28X	HWR	0	0.23	0.22
[76]	24	—	Dickson charge pump	15	51	8

TABLE 10. A PERFORMANCE ANALYSIS OF 5G/MM-WAVE RECTENNAS FOR WPT SYSTEMS.

Reference	Frequency (GHz)	Gain (dB)	Polarization	Diode	Rectifier Topology	P_{in} (dBm)	PCE (%)	V_{out} (V)
[79]	35	4.54	LP	MA4E1317	HWR	10	36	1.73
[80]	35/94	7.4/6.5	LP	CMOS	FWR	29.3	53/37	0.38/0.29
[81]	24	6.8	LP	MADS-001317	HWR	16	41	2
[82]	24/60	—	LP	MA4E1317	HWR	—	65.6	—
[83]	24	—	LP	—	VDR	23.2	47.9	—
[84]	25	—	LP	MA4E2502L	HWR	8	17	—
[85]	24	12.6	CP	MA4E1317	HWR	19.5	24	0.6
[86]	35	17	CP	MA4E1317	HWR	18.8	63.8	4.61
[88]	24	—	LP	MA4E1317	HWR	15	35.2	—
[89]	94	1.85	LP	MA4E1310	HWR	20.2	38	—
[90]	35	7.74	LP	MA4W1310	HWR	16	61.5	1.83
[92]	24	4.8	LP	MA4E2054A	HWR	14	35	—
				—	VDR	14	20	2.4
[93]	35	15	LP	SMA1317	HWR	13	21	—
[94]	24	13	LP	MA4E2054A	HWR	12.5	46	1.5
				—	VDR	—	36	1.9
				SMS7621	HWR	—	25	1.1
				—	VDR	—	20	1.4
[95]	35	15.2	LP	—	HWR	19	67	4
[96]	60	2.6	LP	HSMS 2850	Two-stage VDR	30	—	1.447
[98]	35	14.7	LP	MA4E1317	HWR	32	49.2	—
[99]	28	4	LP	MA4E1317	HWR	23.89	55.5	—

at high input power levels rather than low input power levels. From the analytical results, it can be concluded that large gain values are possible with mm-wave communication bands.

CONCLUSION

This article has presented a comprehensive review of the current literature on 5G/mm-wave rectenna systems for wireless power transfer and EH systems. A comparative assessment of the performance of various published rectenna systems has also been presented. The applications of 5G have been increasing due to the technology's increased energy density in the ambient environment; hence, 5G bands are highly preferred for RFEH at present. Among various 5G bands, 5G mm-wave bands overcome the spectrum scarcity issues that arise in the sub-6-GHz 5G band and also provide a high data rate and widespread coverage.

For WPT applications, a high-gain antenna and CP characteristics are preferred, and for RFEH applications, omnidirectional and all polarization characteristic antennas are highly preferred due to multisource harvesting. Applications at a 3.5-GHz frequency in the sub-6-GHz 5G band and

24/35-GHz frequencies in the mm-wave 5G band are found more than at other frequencies. At sub-6-GHz 5G band frequencies, HSMS-285x series diodes are found to be suitable for moderate to high input power levels. At mm-wave 5G frequencies, a Schottky diode with a low junction capacitance is found suitable; hence, the MA4E1317 Schottky diode is the most adopted for rectifier design. Low PCE and output voltage performances are observed at high RF frequencies over low RF frequencies.

The wide angular coverage of the rectenna helps to increase the harvesting power. The Rotman lens-based beamforming network is widely used for wide angular coverage in mm-wave EH applications. The writers have done their best to compile the most recent contributions from the global research community; nonetheless, if any significant article(s) is/are overlooked unintentionally, the authors humbly apologize.

ACKNOWLEDGMENT

This work was supported by the Science and Engineering Research Board, Government of India, under the Visiting Advanced Joint Research scheme (grant VJR/2019/000009).

AUTHOR INFORMATION

Daasari Surender (surender.daasari@gmail.com) is an assistant professor in the Department of Electronics and Communication Engineering, Vaageswari College of Engineering, Karimnagar 505527 India. His research interests include planar antennas, dielectric resonator antennas, and radio-frequency energy harvesting systems. He is a Member of IEEE.

Md. Ahsan Halimi (ahsanhalimi@gmail.com) is pursuing his Ph.D. degree in the Department of Electronics and Communication Engineering, National Institute of Technology Silchar, Silchar 788010 India. His research interests include radio-frequency energy harvesting, microwave rectifiers, and ultra-wideband and reconfigurable antennas. He is a Student Member of IEEE.

Taimoor Khan (ktaimoor@ieee.org) is an associate professor in the Department of Electronics and Communication Engineering, National Institute of Technology Silchar, Silchar 788010 India. His research interests include printed microwave circuits, dielectric resonator antennas, artificial intelligence paradigms, and radio-frequency energy harvesting systems. He is a Senior Member of IEEE.

Fazal A. Talukdar (fatalukdar@gmail.com) is a professor in the Department of Electronics and Communication Engineering, National Institute of Technology Silchar, Silchar 788010 India. His research interests include signal processing, communication, power electronics, and analog circuit design. He is a Senior Member of IEEE.

Nasimuddin (nasimuddin@i2r.a-star.edu.sg) is a scientist with the Institute for Infocomm Research, Agency for Science, Technology, and Research, Singapore 138632, Singapore. His research interests include multilayered microstrip-based structures, millimeter-wave antennas, ultrawideband antennas, and metamaterials-based microstrip antennas. He is a Senior Member of IEEE.

Sembiam R. Rengarajan (sembiam.rengarajan@csun.edu) is a professor in the Department of Electrical and Computer Engineering, California State University, Northridge, Northridge, CA 91330 USA. His research interests include applications of electromagnetics to antennas, scattering, and passive microwave components. He is a Life Fellow of IEEE.

REFERENCES

- [1] N. A. Muhammad et al., "Stochastic geometry analysis of electromagnetic field exposure in coexisting sub-6 GHz and millimeter wave networks," *IEEE Access*, vol. 9, pp. 112,780–112,791, Aug. 2021, doi: 10.1109/ACCESS.2021.3103969.
- [2] D. Wang et al., "A 24-44 GHz broadband transmit-receive front end in 0.13- μ m SiGe BiCMOS for multistandard 5G applications," *IEEE Trans. Microw. Theory Techn.*, vol. 69, no. 7, pp. 3463–3474, Jul. 2021, doi: 10.1109/TMTT.2021.3069858.
- [3] T. A. Khan et al., "Millimeter wave energy harvesting," *IEEE Trans. Wireless Commun.*, vol. 15, no. 9, pp. 6048–6062, Sep. 2016, doi: 10.1109/TWC.2016.2577582.
- [4] D. Surender et al., "2.45 GHz Wi-Fi band operated circularly polarized rectenna for RF energy harvesting in smart city applications," *J. Electromagn. Waves Appl.*, vol. 36, no. 3, pp. 407–423, Aug. 2021, doi: 10.1080/09205071.2021.1970030.
- [5] D. Surender et al., "Key components of rectenna system: A comprehensive survey," *IETE J. Res.*, vol. 20, pp. 1–28, May 2020, doi: 10.1080/03772063.2020.1761268.
- [6] W. Brown et al., "An experimental microwave-powered helicopter," in *IRE Int. Conv. Rec.*, New York, NY, USA, Mar. 1966, pp. 225–235, doi: 10.1109/IRECON.1965.1147518.
- [7] M. Wagih et al., "Millimeter-wave power harvesting: A review," *IEEE Open J. Antennas Propag.*, vol. 1, pp. 560–578, Oct. 2020, doi: 10.1109/OJAP.2020.3028220.
- [8] M. Wagih, A. S. Weddell, and S. Beeby, "Rectennas for radio-frequency energy harvesting and wireless power transfer: A review of antenna design [Antenna Applications Corner]," *IEEE Antennas Propag. Mag.*, vol. 62, no. 5, pp. 95–107, Oct. 2020, doi: 10.1109/MAP.2020.3012872.
- [9] S. K. Divakaran et al., "RF energy harvesting systems: An overview and design issues," *Int. J. RF Microw. Comput. Aided Eng.*, vol. 29, no. 1, p. e21633, 2019, doi: 10.1002/mmce.21633.
- [10] S. E. Hassani et al., "Overview on 5G radio frequency energy harvesting," *Adv. Sci. Technol. Eng. Syst. J.*, vol. 4, no. 4, pp. 328–346, 2019, doi: 10.25046/aj040442.
- [11] D. Surender et al., "Rectenna design and development strategies for wireless applications," *IEEE Antennas Propag. Mag.*, early access, Aug. 12, 2021, doi: 10.1109/MAP.2021.3099722.
- [12] A. Inoue, "Millimeter-wave GaN devices for 5G: Massive MIMO antenna arrays for sub-6-Ghz and mm-wave bandwidth," *IEEE Microw. Mag.*, vol. 22, no. 5, pp. 100–110, May 2021, doi: 10.1109/MMM.2021.3056936.
- [13] J. Lan, Z. Yu, J. Zhou, and W. Hong, "An aperture-sharing array for (3.5, 28) GHz terminals with steerable beam in millimeter-wave band," *IEEE Trans. Antennas Propag.*, vol. 68, no. 5, pp. 4114–4119, May 2020, doi: 10.1109/TAP.2019.2948706.
- [14] N. Shinohara, *Wireless Power Transfer: Theory, Technology, And Applications*. Six Hills Way, U.K.: Institution of Engineering and Technology, Michael Faraday House, 2018.
- [15] W. C. Brown, "The microwave powered helicopter," *J. Microw. Power*, vol. 1, no. 1, pp. 1–20, 1966, doi: 10.1080/00222739.1966.11688626.
- [16] Z. Wang et al., "A multiband rectenna for self-sustainable devices," in *Proc. Int. SoC Design Conf. (ISOCC)*, Nov. 12–15, 2018, pp. 178–179, doi: 10.1109/ISOCC.2018.8649903.
- [17] D. N. Elsheakh, "Frequency reconfigurable and radiation pattern steering of monopole antenna based on graphene pads," in *Proc. 2019 IEEE-APWC Topical Conf. Antennas Propag. Wireless Commun.*, Granada, Spain, pp. 436–440, doi: 10.1109/APWC.2019.8870446.
- [18] A.D. Boursianis et al., "Dual-band single-layered modified e-shaped patch antenna for RF energy harvesting systems," in *Proc. Eur. Conf. Circuit Theory Design (ECCTD)*, Bulgaria, Sep. 7–10, 2020, pp. 1–4, doi: 10.1109/ECCTD49232.2020.9218354.
- [19] T. G. Ali, X. Bai, and L. J. Xu, "Dual-band energy harvesting antenna based on PVDF piezoelectric material," in *Proc. 9th Asia-Pacific Conf. Antennas Propag. (APCAP)*, Xiamen, China, Aug. 4–7, 2020, pp. 1–2, doi: 10.1109/APCAP50217.2020.9245943.
- [20] A.D. Boursianis et al., "Modified printed bow-tie antenna for RF energy harvesting applications," in *Proc. IEEE Microw. Theory Techn. Wireless Commun.*, 2020, pp. 67–71, doi: 10.1109/MTTW51045.2020.9245049.
- [21] D. Surender, T. Khan, and F. A. Talukdar, "A triple-band hexagonal-shaped microstrip patch antenna for RF energy harvesting in smart city applications," in *Proc. IEEE Int. Conf. Comput., Power Commun. Technol. (GUCON)*, Oct. 2020, pp. 389–393, doi: 10.1109/GUCON48875.2020.9231228.
- [22] T. Gayatri, N. Anvesh Kumar, and V.K. Sharma, "A hexagon slotted circular monopole UWB antenna for cognitive radio applications," in *Proc. Int. Conf. Emerg. Trends Inf. Technol. Eng.*, Vellore, India, Feb. 24–25, 2020, pp. 1–5, doi: 10.1109/ic-ETITE47903.2020.447.
- [23] P. Zhang et al., "Back-to-back microstrip antenna design for broadband wide-angle RF energy harvesting and dedicated wireless power transfer," *IEEE Access*, vol. 8, pp. 126,868–126,875, Jul. 2020, doi: 10.1109/ACCESS.2020.3008551.
- [24] J. S. Gaggat and S. F. S. Vajrala, "An 860MHz - 1960MHz multi-band multi-stage rectifier for RF energy harvesting in 130nm CMOS," in *Proc. IEEE Int. Conf. Electron., Comput. Commun. Technol.*, Bangalore, India, Jul. 2–4, 2020, pp. 1–4, doi: 10.1109/CONECCT50063.2020.9198677.
- [25] M. S. Papadopoulos et al., "Dual-band rectifier design for ambient RF energy harvesting," in *Proc. 3rd World Symp. Commun. Eng.*, Thessaloniki, Greece, Oct. 9–11, 2020, pp. 7–11, doi: 10.1109/WSCE51339.2020.9275569.
- [26] R. Kashimura et al., "Rectifying circuit with high impedance microstrip line for wide dynamic range characteristics," in *Proc. IEEE Wireless Power Transfer Conf. (WPTC)*, Taipei, Taiwan, May 10–12, 2017, pp. 1–4, doi: 10.1109/WPT.2017.7953855.
- [27] S. D. Assimonis et al., "RF energy harvesting with dense rectenna-arrays using electrically small rectennas suitable for IoT 5G embedded sensor-nodes," in *Proc. IEEE MTT-S Int. Microw. Workshop Ser. 5G Hardware Syst. Technol.*, 2018, Ireland, pp. 1–3, doi: 10.1109/IMWS-5G.2018.8484384.

- [28] A. D. Boursianis et al., "Advancing rational exploitation of water irrigation using 5G-IoT capabilities: The AREThOU5A project," in *Proc. 29th Int. Symp. Power Timing Modeling, Optim. Simul.*, Greece, Jul. 1–3, 2019, pp. 127–132, doi: 10.1109/PATMOS.2019.8862146.
- [29] C. Bahhar, C. Baccouche, and H. Sakli, "A novel 5G rectenna for IoT applications," in *Proc. 20th Int. Conf. Sci. Techn. Autom. Control Comput. Eng.*, Tunisia, 2020, pp. 287–290, doi: 10.1109/STA50679.2020.9329349.
- [30] A. K. M. Z. Hossain et al., "A planar antenna on flexible substrate for future 5G energy harvesting in Malaysia," *Int. J. Adv. Comput. Sci. Appl.*, vol. 11, no. 10, pp. 151–155, 2020, doi: 10.14569/IJACSA.2020.0111020.
- [31] S. M. K. Azam et al., "Monopole antenna on transparent substrate and rectifier for energy harvesting applications in 5G," *Int. J. Adv. Comput. Sci. Appl.*, vol. 11, no. 8, pp. 84–89, 2020, doi: 10.14569/IJACSA.2020.0110812.
- [32] D. Surender et al., "Circularly polarized DR-rectenna for 5G and Wi-Fi bands RF energy harvesting in smart city applications," *IETE Tech. Rev.*, vol. 12, pp. 1–15, May 2021, doi: 10.1080/02564602.2021.1923079.
- [33] Y. Shinki et al., "Wireless power transmission circuit on a small planar wide-band antenna," in *Proc. Int. Conf. IEEE Region*, China, 2013, pp. 1–4, doi: 10.1109/TENCON.2013.6718459.
- [34] X. Gu et al., "Diplexer-based fully passive harmonic transponder for sub-6-GHz 5G-compatible IoT applications," *IEEE Trans. Microw. Theory Techn.*, vol. 67, no. 5, pp. 1675–1687, May 2019, doi: 10.1109/TMTT.2018.2883979.
- [35] R. H. Rasshofer, M. O. Thieme, and E. M. Biebl, "Circularly polarized millimeter-wave rectenna on silicon substrate," *IEEE Trans. Microw. Theory Techn.*, vol. 46, no. 5, pp. 715–718, May 1998, doi: 10.1109/22.668688.
- [36] K. Issa and H. Fathallah, "High performance 60 GHz antenna for electromagnetic energy harvesting," in *Proc. Int. Conf. Inf. Commun. Technol. Res.*, 2015, pp. 13–15, doi: 10.1109/ICTRC.2015.7156409.
- [37] P. Burasa et al., "On-chip dual-band rectangular slot antenna for single-chip millimeter-wave identification tag in standard CMOS technology," *IEEE Trans. Antennas Propag.*, vol. 65, no. 8, pp. 3858–3868, Aug. 2017, doi: 10.1109/TAP.2017.2710215.
- [38] M. T. Hafeez, S. F. Jilani, "Novel millimeter-wave flexible antenna for RF energy harvesting," in *Proc. IEEE Int. Symp. Antennas Propag. USNC/URSI Nat. Radio Sci. Meeting*, Jul. 9–14, 2017, pp. 2497–2498, doi: 10.1109/APUSN-CURSINRSM.2017.8073291.
- [39] W. A. Awan et al., "Frequency Reconfigurable patch antenna for millimeter wave applications," in *Proc. 2nd Int. Conf. Comput., Math. Eng. Technol.*, 2019, pp. 1–5, doi: 10.1109/ICOMET.2019.8673417.
- [40] M. Wagih, A. S. Weddell, and S. Beeby, "Millimeter-wave textile antenna for on-body RF energy harvesting in future 5G networks," in *Proc. IEEE Wireless Power Transfer Conf.*, 2019, pp. 245–248, doi: 10.1109/WPTC45513.2019.9055541.
- [41] E. M. Wissem et al., "A textile EBG-based antenna for future 5G-IoT millimeter-wave applications," *Electronics*, vol. 10, no. 2, pp. 1–12, 2021, doi: 10.3390/electronics10020154.
- [42] A. Eid et al., "Flexible W-band rectifiers for 5G-powered IoT autonomous modules," in *Proc. IEEE Int. Symp. Antennas Propag. USNC/URSI Radio Sci. Meeting*, 2019, pp. 1163–1164, doi: 10.1109/APUSN-CURSINRSM.2019.8888600.
- [43] A. Riaz et al., "A triband rectifier toward millimeter-wave frequencies for energy harvesting and wireless power-transfer applications," *IEEE Microw. Wireless Compon. Lett.*, vol. 31, no. 2, pp. 192–195, Feb. 2021, doi: 10.1109/LMWC.2020.3037137.
- [44] V. M. Shoknro and D. V. Gretskikh, "A model of receiving-rectifying elements of MM wave band rectennas," in *Proc. 5th Int. Conf. Antenna Theory Techn.*, Ukraine, May 24–27, 2005, pp. 248–250, doi: 10.1109/ICATT.2005.1496939.
- [45] S. Pellerano, J. Alvarado, and Y. Palaskas, "A mmWave power-harvesting RFID tag in 90 nm CMOS," *IEEE J. Solid-State Circuits*, vol. 45, no. 8, pp. 1627–1637, Aug. 2010, doi: 10.1109/JSSC.2010.2049916.
- [46] H. Gao et al., "A 71GHz RF energy harvesting tag with 8% efficiency for wireless temperature sensors in 65nm CMOS," in *Proc. IEEE Radio Frequency Integr. Circuits Symp.*, 2013, pp. 403–406, doi: 10.1109/RFIC.2013.6569616.
- [47] N. Weissman, S. Jameson, and E. Socher, "W-band CMOS on-chip energy harvester and rectenna," in *Proc. IEEE MTT-S Int. Microw. Symp. (IMS2014)*, Tampa, FL, USA, Jun. 1–6, 2014, pp. 1–3, doi: 10.1109/MWSYM.2014.6848243.
- [48] A. Mavaddat, S. H. M. Armaki, and A. R. Erfanian, "Millimeter-wave energy harvesting using 4×4 microstrip patch antenna array," *IEEE Antennas Wireless Propag. Lett.*, vol. 14, pp. 515–518, 2015, doi: 10.1109/LAWP.2014.2371013.
- [49] J. Bito et al., "Millimeter-wave ink-jet printed RF energy harvester for next generation flexible electronics," in *Proc. IEEE Wireless Power Transf. Conf. (WPTC)*, Taipei, Taiwan, May 10–12, 2017, pp. 1–4, doi: 10.1109/WPTC.2017.7953871.
- [50] C. Hannachi, S. Boumaiza, and S. O. Tatu, "A highly sensitive broadband rectenna for low power millimeter-wave energy harvesting applications," in *Proc. IEEE Wireless Power Transfer Conf. (WPTC)*, Jun. 3–7, 2018, doi: 10.1109/WPTC.2018.8639130.
- [51] M. Aldrigo et al., "Harvesting electromagnetic energy in the V-Band using a rectenna formed by a bow tie integrated with a 6-nm-thick Au/HfO₂/Pt metal-insulator-metal diode," *IEEE Trans. Electron Devices*, vol. 65, no. 7, pp. 2973–2980, Jul. 2018, doi: 10.1109/TED.2018.2835138.
- [52] N. Singh et al., "A compact and efficient graphene FET based RF energy harvester for green communication," *Int. J. Electron. Commun.*, vol. 115, p. 153,059, Feb. 2020, doi: 10.1016/j.aeue.2019.153059.
- [53] N. Singh et al., "A compact broadband GFET based rectenna for RF energy harvesting applications," *Microsyst. Technol.*, vol. 26, no. 6, pp. 1881–1888, 2020, doi: 10.1007/s00542-019-04737-0.
- [54] H. Rahmani and A. Babakhani, "A dual-mode RF power harvesting system with an on-chip coil in 180-nm SOI CMOS for millimeter-sized biomedical implants," *IEEE Trans. Microw. Theory Techn.*, vol. 67, no. 1, pp. 414–428, Jan. 2019, doi: 10.1109/TMTT.2018.2876239.
- [55] T. H. Lin et al., "Achieving fully autonomous system-on-package designs: An embedded-on-package 5G energy harvester within 3D printed multilayer flexible packaging structures," in *Proc. IEEE MTT-S Int. Microw. Symp. (IMS)*, Boston, MA, USA, Jun. 2–7, 2019, pp. 1375–1378, doi: 10.1109/MWSYM.2019.8700931.
- [56] M. Aldrigo et al., "Graphene diodes for 5G energy harvesting: Design, simulations and experiments," in *Proc. 49th Eur. Microw. Conf.*, Paris, France, Oct. 1–3, 2019, pp. 7–10, doi: 10.23919/EuMC.2019.8910802.
- [57] M. Wagih et al., "Broadband millimeter-wave textile-based flexible rectenna for wearable energy harvesting," *IEEE Trans. Microw. Theory Techn.*, vol. 68, no. 11, pp. 4960–4972, Nov. 2020, doi: 10.1109/TMTT.2020.3018735.
- [58] M. Aboulalaa et al., "Compact coplanar stripline-fed folded strip dipole antenna for millimeter energy combining," in *Proc. IEEE 17th Annu. Wireless Microw. Conf. (WAMICON)*, Clearwater, FL, USA, Apr. 11–13, 2016, pp. 1–3, doi: 10.1109/WAMICON.2016.7483820.
- [59] S. L. Liu et al., "A near field focused lens antenna for wireless power transmission systems," in *Proc. IEEE Asia-Pacific Conf. Antennas Propag. (APCAP)*, Auckland, New Zealand, Aug. 5–8, 2018, pp. 313–315, doi: 10.1109/APCAP.2018.8538187.
- [60] S. D. Joseph et al., "A novel dual-polarized millimeter-wave antenna array with harmonic rejection for wireless power transmission," in *Proc. 12th Eur. Conf. Antennas Propag. (EuCAP 2018)*, Apr. 9–13, 2018, pp. 1–3, doi: 10.1049/cp.2018.0693.
- [61] H. Flores-Garcia et al., "High gain wireless power transfer using 60GHz antenna array," in *Proc. SoutheastCon*, Huntsville, AL, USA, Apr. 11–14, 2019, pp. 1–2, doi: 10.1109/SoutheastCon42311.2019.9020471.
- [62] R. Gopika and C. Saha, "Millimeter wave grid array antenna for wireless power transmitter," in *Proc. IEEE Recent Adv. Geosci. Remote Sens., Technol., Standards Appl.*, Oct. 17–20, 2019, pp. 54–56, doi: 10.1109/TEN-GARSS48957.2019.8976061.
- [63] K. Lee et al., "Design of a metasurface superstate for improved reception of wireless power at Ka-band," in *Proc. IEEE Wireless Power Transfer Conf.*, Seoul, Korea, Nov. 15–19, 2020, pp. 112–114, doi: 10.1109/WPTC48563.2020.9295624.
- [64] F. Xiao et al., "High-efficiency millimeter-wave wide-angle scanning phased array using metasurface," in *Proc. IEEE MTT-S Int. Wireless Symp. (IWS)*, Nanjing, China, May 23–26, 2021, pp. 1–3, doi: 10.1109/IWS52775.2021.9499440.
- [65] M. Wagih et al., "Millimeter-wave power transmission for compact and large-area wearable IoT devices based on a higher-order mode wearable antenna," *IEEE Internet Things J.*, vol. 9, no. 7, pp. 5229–5239, Apr. 2022, doi: 10.1109/JIOT.2021.3107594.
- [66] D. H. Sadek, H. A. Shawkey, and A. A. Zekry, "Multiband triple L-arms patch antenna with diamond slot ground for 5G applications," *Appl. Comput. Electromagn. Soc. J.*, vol. 36, no. 3, pp. 302–307, Mar. 2021.
- [67] S. Ladan, S. Hemour, and K. Wu, "Towards millimeter-wave high-efficiency rectification for wireless energy harvesting," in *Proc. IEEE Int. Wireless Symp. (IWS)*, Beijing, China, Apr. 14–18, 2013, pp. 1–4, doi: 10.1109/IWE-IWS.2013.6616819.
- [68] S. Ladan, and K. Wu, "35 GHz harmonic harvesting rectifier for wireless power transmission," in *Proc. IEEE MTT-S Int. Microw. Symp.*, USA, Jun. 1–6, 2014, pp. 1–4, doi: 10.1109/MWSYM.2014.6848572.
- [69] G. N. Tan, X. X. Yang, and C. Tan, "Design of rectifying circuit for wireless power transmission in Ka band," in *Proc. IEEE Antennas Propag. Soc.*

- Int. Symp. (APSURSI)*, Memphis, TN, USA, Jul. 6–11, 2014, pp. 639–640, doi: 10.1109/APS.2014.6904650.
- [70] P. Zhu, Z. Ma, G. A. E. Vandebosch, and G. Gielen, “160 GHz harmonic-rejecting antenna with CMOS rectifier for millimeter-wave wireless power transmission,” in *Proc. 9th Eur. Conf. Antennas Propag.*, Portugal, Apr. 13–17, 2015, pp. 1–5.
- [71] A. Riaz, M. Awais, M.M. Farooq, W.T. Khan, “A single cell dual band rectifier at millimeter-wave frequencies for future 5G communications,” in *Proc. 49th Eur. Microw. Conf. (EuMC)*, Paris, France, Oct. 1–3, 2019, pp. 41–44, doi: 10.23919/EuMC.2019.8910897.
- [72] P. He and D. Zhao, “High-efficiency millimeter-wave CMOS switching rectifiers: Theory and implementation,” *IEEE Trans. Microw. Theory Techn.*, vol. 67, no. 12, pp. 5171–5180, Dec. 2019, doi: 10.1109/TMTT.2019.2936566.
- [73] S. Mizojiri and K. Shimamura, “Recent progress of wireless power transfer via sub-THz wave,” in *Proc. IEEE Asia-Pacific Microw. Conf. (APMC)*, Singapore, Dec. 10–13, 2019, pp. 705–707, doi: 10.1109/APMC46564.2019.9038353.
- [74] D. Zhao, P. He, and X. Wang, “Millimeter-wave rectenna and rectifying circuits for far-distance wireless power transfer,” in *Proc. 12th Global Symp. Millimeter Waves (GSMM)*, Sendai, Japan, May 22–24, 2019, pp. 90–92, doi: 10.1109/GSMM.2019.8797674.
- [75] A. Eid, J. Hester, and M. Tentzeris, “mm-Wave tunnel diode-based rectifier for perpetual IoT,” in *Proc. IEEE Int. Symp. Antennas Propag. North Amer. Radio Sci. Meeting*, Canada, Jul. 5–10, 2020, pp. 1495–1496, doi: 10.1109/IEEECONF35879.2020.9329745.
- [76] D. Matos, R. Correia, and N. B. Carvalho, “Millimeter-wave hybrid RF-DC converter based on a GaAs chip for IoT-WPT applications,” *IEEE Microw. Wireless Compon. Lett.*, vol. 31, no. 6, pp. 787–790, Jun. 2021, doi: 10.1109/LMWC.2021.3058542.
- [77] P. Koert and J. T. Cha, “Millimeter wave technology for space power beaming,” *IEEE Trans. Microw. Theory Techn.*, vol. 40, no. 6, pp. 1251–1258, Jun. 1992, doi: 10.1109/22.141358.
- [78] J. O. McSpadden et al., “Theoretical and experimental investigation of a rectenna element for microwave power transmission,” *IEEE Trans. Microw. Theory Techn.*, vol. 40, no. 12, pp. 2359–2366, Dec. 1992, doi: 10.1109/22.179902.
- [79] Y. J. Ren, M. Y. Li, and K. Chang, “35 GHz rectifying antenna for wireless power transmission,” *Electron. Lett.*, vol. 43, no. 11, pp. 1–2, May 2007, doi: 10.1049/el:20071061.
- [80] H. K. Chiou et al., “High-efficiency dual-band on-chip rectenna for 35- and 94-GHz wireless power transmission in 0.13-μm CMOS technology,” *IEEE Trans. Microw. Theory Techn.*, vol. 58, no. 12, pp. 3598–3607, Dec. 2010, doi: 10.1109/TMTT.2010.2086350.
- [81] N. Shinohara, K. Nishikawa, T. Seki, and K. Hiraga, “Development of 24 GHz rectennas for fixed wireless access,” in *Proc. 30th URSI General Assembly Scientific Symp.*, Istanbul, Aug. 13–20, 2011, pp. 1–4, doi: 10.1109/URSI-GASS.2011.6050505.
- [82] K. Hatano et al., “Development of class-F load rectennas,” in *Proc. IEEE MTT-S IMWS Innovative Wireless Power Transmission, Technol., Syst., Appl.*, Japan, May 12–13, 2011, pp. 251–254, doi: 10.1109/IMWS.2011.5877123.
- [83] K. Hatano, N. Shinohara, T. Seki, and M. Kawashima, “Development of MMIC rectenna at 24GHz,” in *Proc. IEEE Radio Wireless Symp.*, Austin, TX, USA, Jan. 20–23, 2013, pp. 199–201, doi: 10.1109/RWS.2013.6486687.
- [84] A. Collado and A. Georgiadis, “24 GHz substrate integrated waveguide (SIW) rectenna for energy harvesting and wireless power transmission,” in *Proc. IEEE MTT-S Int. Microw. Symp. Dig.*, Jun. 2–7, 2013, pp. 1–3, doi: 10.1109/MWSYM.2013.6697772.
- [85] S. Ladan, A. B. Guntupalli, and K. Wu, “A high-efficiency 24 GHz rectenna development towards millimeter-wave energy harvesting and wireless power transmission,” *IEEE Trans. Circuits Syst. I, Reg. Papers*, vol. 61, no. 12, pp. 3358–3367, Dec. 2014, doi: 10.1109/TCSI.2014.2338616.
- [86] H. Mei, X. Yang, B. Han, and G. Tan, “High-efficiency microstrip rectenna for microwave power transmission at Ka band with low cost,” *IET Microw. Antennas Propag.*, vol. 10, no. 15, pp. 1648–1655, 2016, doi: 10.1049/iet-map.2016.2055.
- [87] M. Nariman et al., “A compact 60-GHz wireless power transfer system,” *IEEE Trans. Microw. Theory Techn.*, vol. 64, no. 8, pp. 2664–2677, Aug. 2016, doi: 10.1109/TMTT.2016.2582168.
- [88] S. Daskalakis et al., “Inkjet printed 24 GHz rectenna on paper for millimeter wave identification and wireless power transfer applications,” in *Proc. IEEE MTT-S Int. Microw. Workshop Ser. Adv. Mater. Processes RF THz Appl.*, Italy, Sep. 20–22, 2017, pp. 1–3, doi: 10.1109/IMWS-AMP.2017.8247367.
- [89] K. Matsui et al., “Microstrip antenna and rectifier for wireless power transfar at 94GHz,” in *Proc. IEEE Wireless Power Transfer Conf.*, Taiwan, May 10–12, 2017, pp. 1–3, doi: 10.1109/WPT.2017.7953902.
- [90] P. Pang et al., “A high-efficiency 35GHz rectenna with compact structure for rectenna arrays,” in *Proc. IEEE Asia-Pacific Conf. Antennas Propag.*, Aug. 2018, pp. 303–305, doi: 10.1109/APCAP.2018.8538263.
- [91] M. Aldrigo et al., “Bow-tie antenna integrated with an HfO₂-based MIM diode for millimetre wave harvesting,” in *Proc. 48th Eur. Microw. Conf.*, Madrid, Spain, Sep. 25–27, 2018, pp. 769–772, doi: 10.23919/EuMC.2018.8541525.
- [92] B. T. Malik et al., “Flexible rectennas for wireless power transfer to wearable sensors at 24 GHz,” in *Proc. Research, Invention, Innovation Congr. (RI2C)*, Thailand, Dec. 11–13, 2019, pp. 1–5, doi: 10.1109/RI2C48728.2019.899964.
- [93] W. Huang et al., “A novel 35-GHz Slot-coupled patch rectenna array based on SIW cavity for WPT,” in *Proc. Int. Conf. Microw. Millimeter Wave Technol. (ICMMT)*, Guangzhou, China, May 19–22, 2019, pp. 1–3, doi: 10.1109/ICMMT45702.2019.8992128.
- [94] B. T. Malik et al., “Wireless power transfer system for battery-less sensor nodes,” *IEEE Access*, vol. 8, pp. 95,878–95,887, May 2020, doi: 10.1109/ACCESS.2020.2995783.
- [95] Q. Chen, Z. Liu, Y. Cui, H. Cai, and X. Chen, “A metallic waveguide-integrated 35-GHz rectenna with high conversion efficiency,” *IEEE Microw. Wireless Compon. Lett.*, vol. 30, no. 8, pp. 821–824, Aug. 2020, doi: 10.1109/LMWC.2020.3002163.
- [96] C. Bahar et al., “Optical RECTENNA for energy harvesting and RF transmission in connected vehicles,” in *Proc. 17th Int. Multi-Conf. Syst., Signals Devices (SSD)*, Tunisia, Jul. 20–23, 2020, pp. 262–266, doi: 10.1109/SSD49366.2020.9364243.
- [97] P. He et al., “A W-band 2×2 rectenna array with on-chip CMOS switching rectifier and On-PCB tapered slot antenna for wireless power transfer,” *IEEE Trans. Microw. Theory Techn.*, vol. 69, no. 1, pp. 969–979, Jan. 2021, doi: 10.1109/TMTT.2020.3032971.
- [98] Y. Wang, X. X. Yang, G. N. Tan, and S. Gao, “Study on millimeter-wave SIW rectenna and arrays with high conversion efficiency,” *IEEE Trans. Antennas Propag.*, vol. 69, no. 9, pp. 5503–5511, Sep. 2021, doi: 10.1109/TAP.2021.3060120.
- [99] R. Moro et al., “28 GHz microwave power beaming to a free-flight drone,” in *Proc. IEEE Wireless Power Transfer Conf.*, San Diego, CA, USA, Jun. 1–4, 2021, pp. 1–4, doi: 10.1109/WPTC51349.2021.9458030.
- [100] T. Bai et al., “Coverage and capacity of millimeter-wave cellular networks,” *IEEE Commun. Mag.*, vol. 52, no. 9, pp. 70–77, Sep. 2014, doi: 10.1109/MCOM.2014.6894455.
- [101] D. J. Lee et al., “Hybrid power combining rectenna array for wide incident angle coverage in RF energy transfer,” *IEEE Trans. Microw. Theory Techn.*, vol. 65, no. 9, pp. 3409–3418, Sep. 2017, doi: 10.1109/TMTT.2017.2678498.
- [102] J. J. Kuek et al., “A compact Butler matic for wireless power transfer to aid electromagnetic energy harvesting for sensors,” in *Proc. Asia Pacific Microw. Conf.*, 2017, pp. 334–336, doi: 10.1109/APMC.2017.8251447.
- [103] T. A. Khan et al., “Energy coverage in millimeter wave energy harvesting networks,” in *Proc. IEEE Globecom Workshops*, San Diego, CA, USA, Dec. 6–10, 2015, pp. 1–6, doi: 10.1109/GLOCOMW.2015.7414219.
- [104] P. W. Fink et al., “Beamforming rectennas, systems and methods for wireless power transfer,” U.S. Patent 10 243 412b1, 2019.
- [105] M. Y. Huang et al., “Concurrent multi-directional beam-forming receiving network for full-FoV high-efficiency wireless power transfer,” in *Proc. IEEE/MTT-S Int. Microw. Symp.*, 2019, pp. 1511–1514, doi: 10.1109/MWSYM.2019.8700746.
- [106] S. Shen and B. Clerckx, “Beamforming optimization for MIMO wireless power transfer with nonlinear energy harvesting: RF combining versus DC combining,” *IEEE Trans. Wireless Commun.*, vol. 20, no. 1, pp. 199–213, Jan. 2021, doi: 10.1109/TWC.2020.3024064.
- [107] B. Schweber, “Rotman-lens antenna system harvests 28-GHz 5G energy.” Electronic Design. Accessed: Jun. 11, 2021. [Online]. Available: <https://www.electronicdesign.com/industrial-automation/article/21164377/electronic-design-rotmanlens-antenna-system-harvests-28ghz-5g-energy>
- [108] A. Eid et al., “A scalable high-gain and large-beamwidth mmWave harvesting approach for 5G-powered IoT,” in *Proc. 2019 IEEE MTT-S Int. Microw. Symp. (IMS)*, Boston, MA, USA, pp. 1309–1312, doi: 10.1109/MWSYM.2019.8700758.
- [109] H. Y. Hong, H. S. Park, S. K. Hong, “Design of Rotman lens for far-field wireless power transfer at Ka-band,” in *Proc. IEEE Wireless Power Transfer Conf. (WPTC)*, Seoul, Korea, Nov. 15–19, 2020, pp. 109–111, doi: 10.1109/WPTC48563.2020.9295528.
- [110] A. Eid, J. G. D. Hester, and M. M. Tentzeris, “5G as a wireless power grid,” *Scientific Rep.*, vol. 11, no. 1, pp. 1–9, 2021, doi: 10.1038/s41598-020-79500-x.



Matthew W. Nichols^{ID}, Alfredo Gonzalez,
Elias A. Alwan^{ID}, and John L. Volakis^{ID}

An Accordion-Folding Series-Fed Patch Array With Finite Thickness

IMAGE LICENSED BY INGRAM PUBLISHING

A folding technique for CubeSat arrays.

Combining antenna arrays with physical reconfigurability (i.e., origami) allows for additional degrees of freedom in operation and enables larger structures to be folded into smaller volumes. The packaging ability of origami antennas is of great interest for CubeSat applications in particular. However, traditional origami is based on the manipulation of thin sheets, making physical reconfigurability with thick substrates very difficult. In this article, we present a foldable series-fed patch array designed on a strictly rigid printed circuit board (PCB). Notably, the array does not require any

external mechanical folding appendages (i.e., brackets, tapes, or offsets), and it can be manufactured using commercially available PCBs and equipment. The PCB itself is strategically cut to form lamina emergent torsion (LET) joints. When fully deployed, the array operates at 5.7 GHz. A significant shift is not seen in the operational frequency until the folding exceeds 60° (5.7–5.61 GHz). This shows that the array, even in a state of near extreme faulty deployment, will operate as intended. An 8 × 6 prototype array was fabricated using a Rogers DiClad 880. When fully deployed, the array is extended in a surface area of 280 × 198 × 1.524 mm and can be folded into a 35.5 × 198 × 12.5-mm compartment. The array held its integrity well after 100 cycles. (One cycle starts at a state of full deployment,

moves to a state of being fully packaged, and goes back to a state of full deployment.) Measurements show that the active reflection coefficients are in good agreement with the finite array simulations. The measured realized gains at 5.7 GHz for 0° and 30° folds were 22.4 and 21.4 dBi, respectively. At the 60° fold, a realized gain of 20.6 dBi was achieved at the frequency of 5.61 GHz.

INTRODUCTION

Satellite communications have recently shifted to a new paradigm with the adoption of CubeSats: using the trend of modern electronics, fully functioning satellites can be compressed into much smaller volumes [1]. Communication systems are no exception,

The packaging ability of origami antennas is of great interest for CubeSat applications in particular.

but sub-6-GHz antennas can be cumbersome for these compartments. In other words, the development of origami electromagnetic (EM) structures is still hindered by several challenges, among them 1) a lack of approaches for reconfigurable and multifunctional EM origami structures, 2) a lack of design algorithms for simultaneous EM physics and origami math analysis, and 3) a lack of materials and mechanisms for robust and repeatable actuation. Here, we focus on the lack of materials and mechanisms for robust and repeatable actuation. Notably, there is a strong recent interest in folding and packaging large apertures on rigid substrates into small footprints [2]. An example can be seen in parabolic antennas, formed

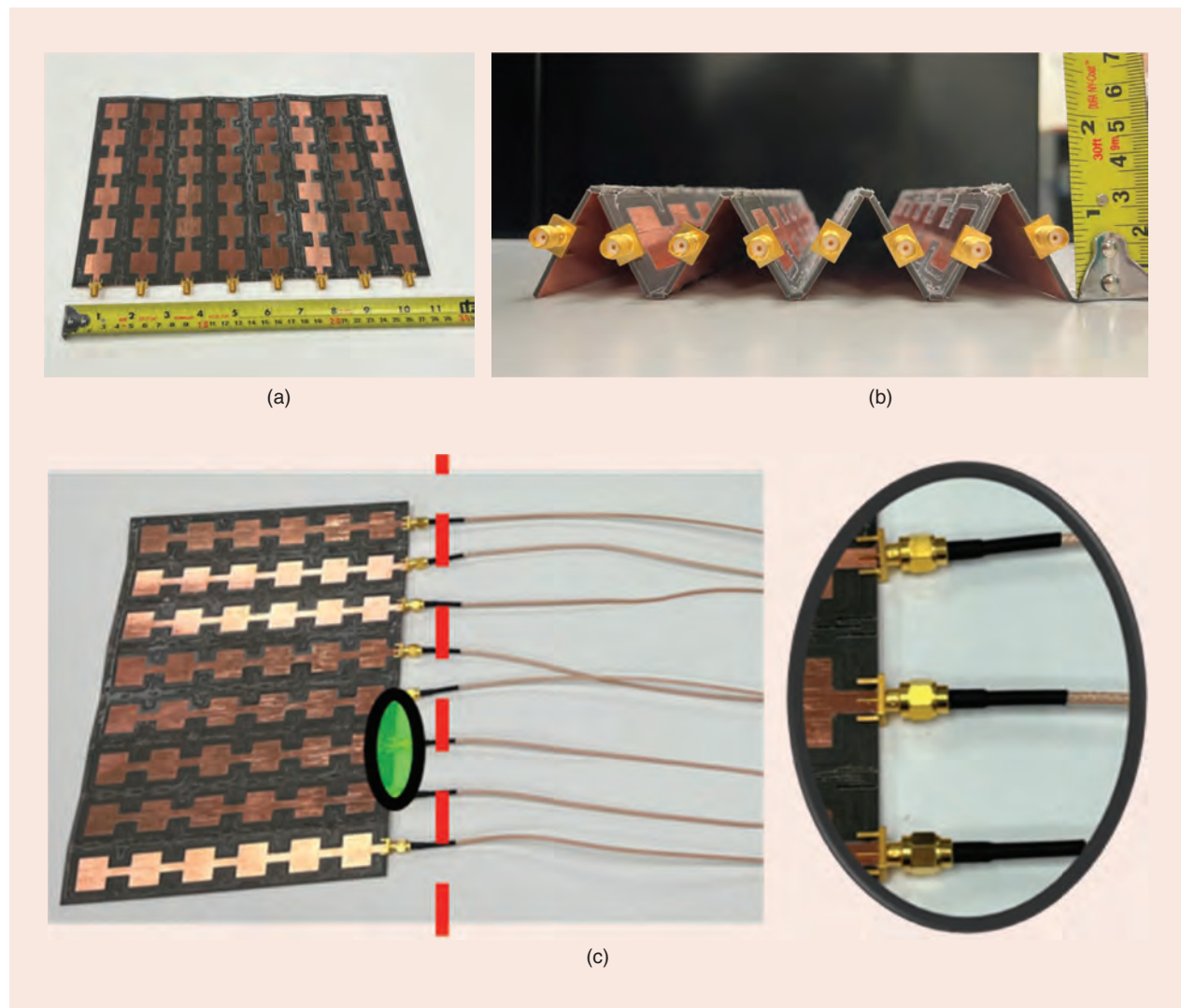


FIGURE 1. The fabricated prototype. (a) Case 1: a 0° fold. (b) Case 3: a 60° fold. (c) Case 1: a 0° fold showing the 50- Ω coax feeding.

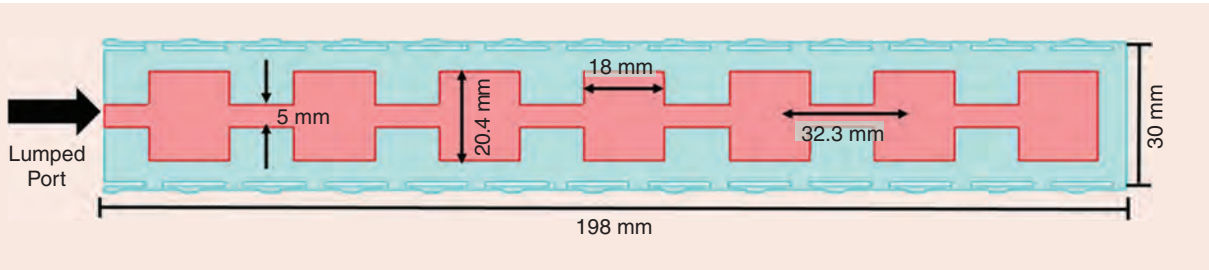


FIGURE 2. A simulation model of the accordion-fold series-fed patch array using LET joints: the dimensions of a single periodic element.

of wire meshes [3], [4]. To form the adaptability that mesh parabolics lack, further work has been conducted concerning reflectarrays [5], [6]. However, the challenge for materials and mechanisms for robust and repeatable actuation remains. Origami-folding techniques provide alternative approaches for these antenna arrays [7], [8], [9]. Attempts to realize origami-based structures using rigid PCB foldings have been reported in [10] and [11], but extensive testing in terms of radio-frequency (RF) performance is still limited. Notably, although flexible materials exist, their reliability is still an issue [7], [8], [9], [10], [11]. Specifically, when these substrates are exposed to harsh environments (extreme rain, wind, and temperature variations), they may be susceptible to damage.

In this article, we propose a foldable series-fed patch array, implemented on rigid homogeneous PCB, as depicted in Figure 1. Notably, the array achieves folding by strategically cutting LET joints in between the active antenna elements and requires no external folding appendages. Full-wave simulations are conducted (utilizing Ansys HFSS software) to analyze three states of deployment, namely, 1) case 1: a 0° fold where the array is fully deployed, 2) case 2: a 30° fold where the array is partially deployed, and 3) case 3: a 60° fold where the array is at a state of faulty deployment. A prototype is fabricated and measured to verify simulations.

ACCORDION FOLD USING A SERIES-FED PATCH ARRAY

A foldable series-fed patch array was designed on a 1.5-mm-thick Rogers DiClad 880 PCB, intended to operate at 5.7 GHz when fully deployed. The array comprises eight rows, each consisting of six individual series-fed patches. Each individual patch is 18×20.4 mm, as depicted in Figure 2. Each of the eight rows, as a whole, will be referred to as a *single element* and fed at one end. The spacing along the plane of feeding was initially set at half of a wavelength (at 5.7 GHz) and optimized to reduce coupling. The transmission line connecting the patches is matched to 50Ω . Also, the adjacent series-fed patch rows were placed approximately 0.52Ω away and then shifted further for the addition of the LET Joints [11]. These spacings were optimized with the goal of keeping the array's performance. The simulation model of the array can be seen in Figure 3.

LET JOINTS

LET joints are cut directly into the PCB, requiring no external hinges, connections, or substrate add-ons. Additionally, they do not require any extra assembly and are part of the PCB fabrication. Initial prototypes were fabricated using the Rogers 5880, Rogers DiClad 880, Rogers 3003, Rogers 4350, Rogers 3010, and FR4. It was found that the Rogers DiClad 880 proved to yield the highest range of motion, with the greatest durability over a set number of complete folds (shown in Figure 4). Using the Rogers DiClad 880, periodic notches were cut out between the elements of the antenna array in 1D measuring 2×10 mm, with 5-mm horizontal spacing and 2-mm vertical spacing. These are depicted in Figure 4. Furthermore, the joints are carefully positioned and optimized to not only avoid substrate splintering during folding but also to minimize performance variations. We note that the rectangular cutouts were made with dimensions significantly smaller than the operational wavelength to prevent effects from the perforated ground plane. It is remarked that the fabricated prototype endured well more than 100 cycles.

FINITE ARRAY SIMULATION

A finite 8×6 array was designed, modeled, and simulated. The finite array was evaluated under three different cases in deployment: 1) case 1: a 0° fold when fully deployed, 2) case 2:

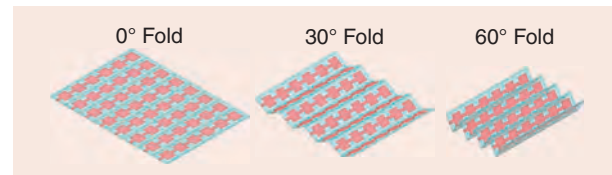


FIGURE 3. The setup of the finite array simulations at different fold angles.

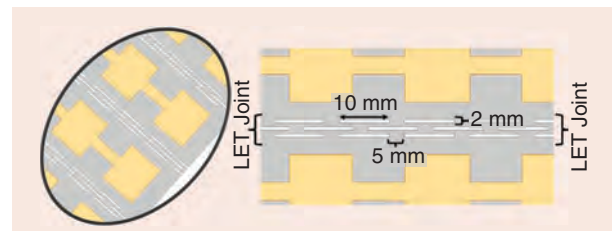


FIGURE 4. The placement and dimensions of the LET joint arrays in the simulation model.

a 30° fold when partially deployed, and 3) case 3: a 60° fold at a state of faulty deployment. These simulations were intended as a reference for measurements. Simulations for the three folding cases gave the following gain results:

- **Case 1:** With a 0° fold when fully deployed, the array achieved a peak gain of 23.73 dBi at 5.7 GHz (with a

directivity of 23.76 dBi). Additionally, as expected, the side-lobe level is approximately 13 dB less than the main lobe and is located 16° away from the boresight.

- **Case 2:** With a 30° fold when partially deployed, the array achieved a peak gain of 21.9 dBi at 5.7 GHz. As expected, the beam pattern shows a wider main lobe, with the

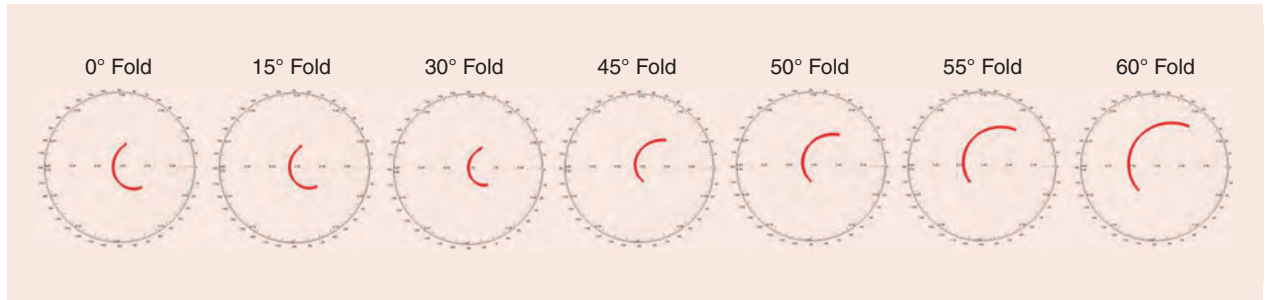


FIGURE 5. Simulations of a single center element impedance showing the growing mismatch as the array folds after the start of a 45° folding angle. This mismatch is due to the increased element-to-element coupling and is the cause of the frequency shift.

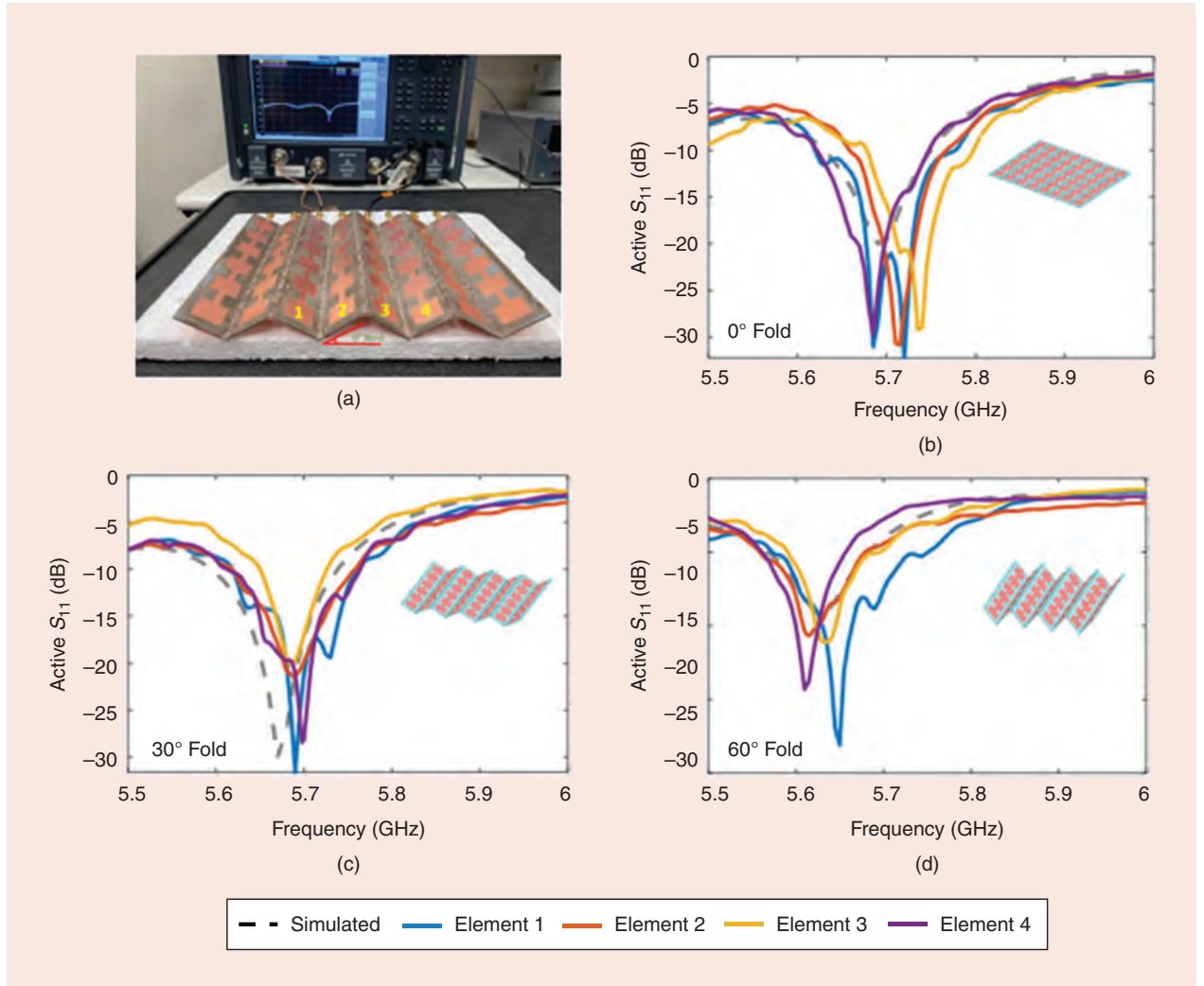


FIGURE 6. (a) The fabricated prototype, followed by (b)–(d) active matching measurements for the three analyzed states of deployment. Here, center elements 1–4 are fed, with the rest being terminated to 50 Ω.

sidelobes pushed farther away from the boresight. This is the result of reduced element spacing due to folding [10].

- **Case 3:** With a 60° fold, the array achieved a peak gain of 21.75 dBi at 5.61 GHz. This frequency shift of 90 MHz is due to the increase in mutual coupling. That is, the adjacent patch-to-patch faces begin to radiate directly onto each other, causing coupling. Notably, a frequency shift is seen at 45° , but the array retains operation at 5.7 GHz, as it is still within the operational bandwidth. A shift outside the operational bandwidth occurs when folding reaches 60° or greater.

This analysis can be seen in Figure 5.

FABRICATION AND MEASUREMENT

An 8×6 prototype of the accordion-fold series patch array was fabricated on Rogers DiClad 880 substrate. The active S-parameter measurements were conducted using the Keysight power network analyzer N5222B. The gain and voltage standing-wave ratio results are as follows:

- **Case 1:** For a 0° fold, both the active matching and beam pattern measurements align with simulations. A measured peak gain of 22.4 dBi was observed. This is 1.3 dBi lower than the ideal.
- **Case 2:** For a 30° fold, both the active matching and beam pattern measurements (an achieved gain of 21.4 dBi) align

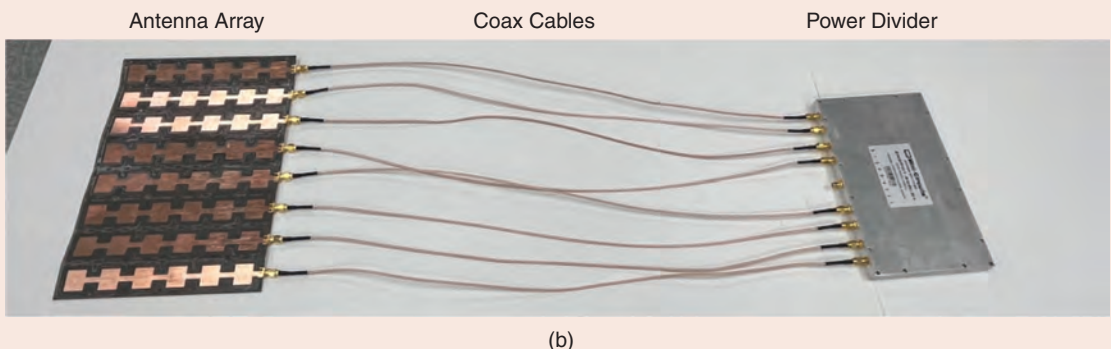
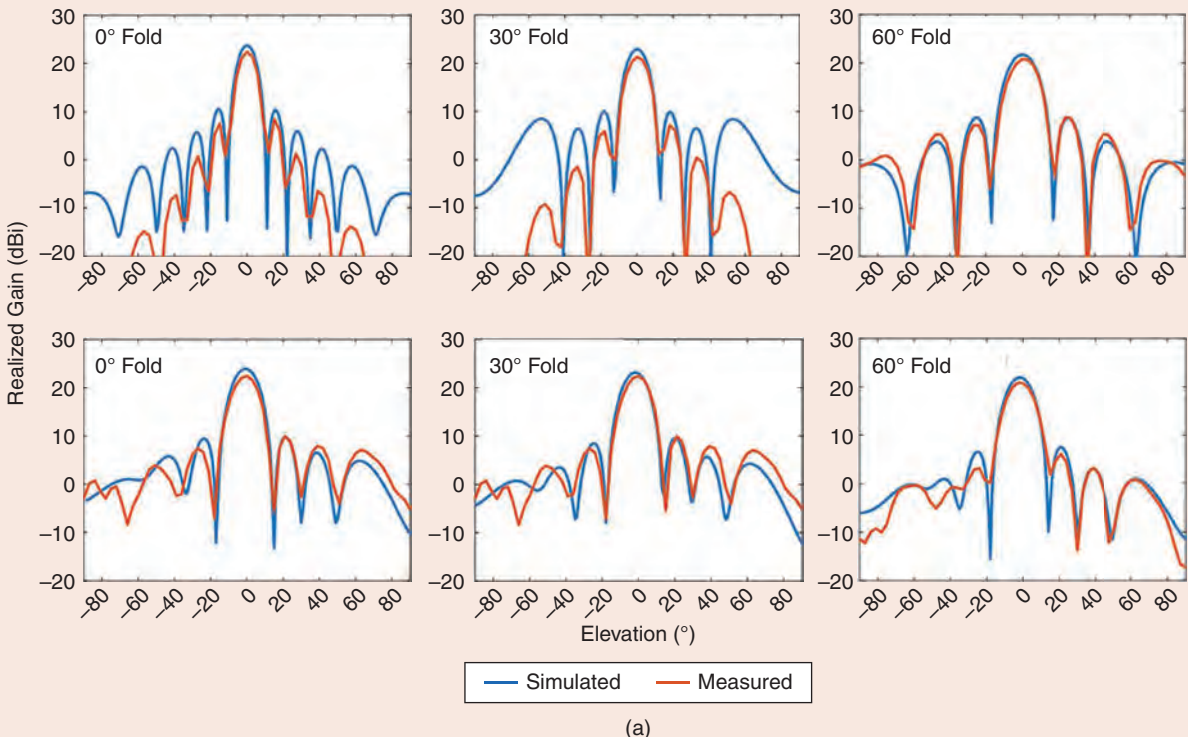


FIGURE 7. (a) The measured versus simulated beam pattern of the 8×6 fabricated antenna array prototype at the three states of deployment. The measured gain corresponds to the excitation of all array elements using a one-to-eight power divider. The top row shows the H-plane, with the bottom row showing the E-plane. (b) The antenna array, coax cables, and power divider. This power divider was de-embedded from the plotted patterns.

with simulations in the E-plane, with, again, some sidelobe differences seen mostly in the H-plane. This was expected, as folding is achieved along the H-plane axis.

- **Case 3:** For a 60° fold, a frequency shift of approximately 90 MHz is recorded, as in simulations. Also, the radiation patterns in the E- and H-planes are in excellent agreement. The main lobe achieves a peak gain of 20.6 dBi.

These details can be seen in Figures 6 and 7. It is noted that only the four center element results are displayed in Figure 6, but all elements were in agreement with simulations. Gain measurements were achieved with a one-to-eight power divider in an anechoic antenna chamber at Florida International University. The power divider was de-embedded prior to plotting the results seen in Figure 7.

A manual “move and hold” method was employed to achieve deployment and to keep the structure at certain fold angles. This method was chosen because the focus of this article is on LET joints and the folding approach. The mechanical actuation mechanisms have already been discussed elsewhere in [12], [13], and [14]. Notably, no appreciable performance degradation was seen after 100 folding cycles. (The array was folded and unfolded manually.) Furthermore, depending on the application, different feeding approaches can be used. For example, a microstrip-line power divider could be employed. In that case, the transmission lines could be placed over LET joints, as discussed in [10].

CONCLUSIONS

This article presented a folding technique for CubeSat arrays. It was demonstrated that both the array structure and its RF performance are maintained after repeated folding cycles. A proof-of-concept array was also fabricated to demonstrate performance showing an optimal gain at 5.7 GHz. Furthermore, the accordion-fold technique requires no additional appendages, thereby minimizing cost and assembly requirements. The designed LET joints have high levels of durability, with no signs of snapping or wear after 100 folding cycles. A change in the intended frequency operation is seen at a folding of 60° or greater.

ACKNOWLEDGMENT

This work was supported in part by the Air Force Office of Scientific Research Grant FA9550-19-0290 and by NASA Grant 80NSSC18K1736.

AUTHOR INFORMATION

Matthew W. Nichols (mnich036@fiu.edu) is currently pursuing his Ph.D. degree in electrical engineering with the RFCOM Lab, Florida International University, Miami, FL 33174 USA. He is a Student Member of IEEE.

Alfredo Gonzalez (agonz341@fiu.edu) is currently pursuing his M.S. degree in computer science at the Georgia Technical

Institute of Technology, Atlanta, GA 30332 USA. He received his M.S. degree in electrical engineering from Florida International University, Miami, FL 33174 USA. He is a Member of IEEE.

Elias A. Alwan (ealwan@fiu.edu) is an Eminent Scholar Chaired Assistant Professor with the Department of Electrical and Computer Engineering, Florida International University, Miami, FL 33174 USA. He is a Member of IEEE.

John L. Volakis (jvolakis@fiu.edu) is the dean of and a professor with the College of Engineering and Computing, Florida International University, Miami, FL 33174 USA. He is a Life Fellow of IEEE.

REFERENCES

- [1] S. Lee et al., “CubeSat design specification rev. 13,” CubeSat, 2014. [Online]. Available: www.cubesat.org
- [2] Y. Rahmat-Samii and A. C. Densmore, “Technology trends and challenges of antennas for satellite communication systems,” *IEEE Trans. Antennas Propag.*, vol. 63, no. 4, pp. 1191–1204, Apr. 2015, doi: 10.1109/TAP.2014.2366784.
- [3] Y. Rahmat-Samii, V. Manohar, J. M. Kovitz, R. E. Hodges, G. Freebury, and E. Peral, “Development of highly constrained 1m ka-band mesh deployable offset reflector antenna for next generation CubeSat radars,” *IEEE Trans. Antennas Propag.*, vol. 67, no. 10, pp. 6254–6266, Oct. 2019, doi: 10.1109/TAP.2019.2920223.
- [4] N. Chahat, E. Thiel, J. Sauder, M. Arya, and T. Cwik, “Deployable one-meter reflectarray for 6U-class CubeSats,” in *Proc. 13th Eur. Conf. Antennas Propag. (EuCAP)*, Krakow, Poland, 2019, pp. 1–4.
- [5] N. Chahat et al., “Advanced CubeSat antennas for deep space and earth science missions: A review,” *IEEE Antennas Propag. Mag.*, vol. 61, no. 5, pp. 37–46, Oct. 2019, doi: 10.1109/MAP.2019.2932608.
- [6] R. E. Hodges, D. J. Hoppe, M. J. Radway, and N. E. Chahat, “Novel deployable reflectarray antennas for CubeSat communications,” in *Proc. IEEE MTT-S Int. Microw. Symp.*, Phoenix, AZ, USA, 2015, pp. 1–4, doi: 10.1109/MWSYM.2015.7167153.
- [7] S. I. H. Shah, M. M. Tentzeris, and S. Lim, “A deployable quasi-yagi monopole antenna using three origami magic spiral cubes,” *IEEE Antennas Wireless Propag. Lett.*, vol. 18, no. 1, pp. 147–151, Jan. 2019, doi: 10.1109/LAWP.2018.2883380.
- [8] S. I. H. Shah, M. M. Tentzeris, and S. Lim, “Low-cost circularly polarized origami antenna,” *IEEE Antennas Wireless Propag. Lett.*, vol. 16, pp. 2026–2029, Apr. 2017, doi: 10.1109/LAWP.2017.2694138.
- [9] X. Liu, S. Yao, B. S. Cook, M. M. Tentzeris, and S. V. Georgakopoulos, “An origami reconfigurable axial-mode bifilar helical antenna,” *IEEE Trans. Antennas Propag.*, vol. 63, no. 12, pp. 5897–5903, Dec. 2015, doi: 10.1109/TAP.2015.2481922.
- [10] M. Hamza, C. L. Zekios, and S. V. Georgakopoulos, “A thick origami reconfigurable and packable patch array with enhanced beam steering,” *IEEE Trans. Antennas Propag.*, vol. 68, no. 5, pp. 3653–3663, May 2020, doi: 10.1109/TAP.2020.2963922.
- [11] J. O. Jacobsen, G. Chen, L. L. Howell, and S. P. Magleby, “Lamina emergent torsion (LET) joint,” *Mechanism Mach. Theory*, vol. 44, no. 11, pp. 2098–2109, 2009, doi: 10.1016/j.mechmachtheory.2009.05.015.
- [12] N. E. Russo, C. L. Zekios, and S. V. Georgakopoulos, “Capacity reconfigurable origami enabled MIMO antenna,” in *Proc. United States Nat. Committee URSI Nat. Radio Sci. Meeting (USNC-URSI NRSM)*, 2019, pp. 1–2, doi: 10.23919/USNC-URSI-NRSM.2019.8712870. [Online]. Available: <https://ieeexplore.ieee.org/document/8712870>
- [13] D. E. Williams, C. Dom, S. Pellegrino, and A. Hajimiri, “Origami-inspired shape-changing phased array,” in *Proc. 50th Eur. Microw. Conf. (EuMC)*, 2021, pp. 344–347, doi: 10.23919/EuMC48046.2021.9338189.
- [14] Y. Miyazaki, “Deployable techniques for small satellites,” *Proc. IEEE*, vol. 106, no. 3, pp. 471–483, Mar. 2018, doi: 10.1109/JPROC.2018.2799608. [Online]. Available: <https://ieeexplore.ieee.org/document/8293792>





Raymond P. Wasky

EDITOR'S NOTE

The worldwide coronavirus (COVID-19) pandemic may have resulted in the cancellation or delay of some of the meetings and symposia listed below. Please check all meeting websites for the latest information prior to making plans for registration or travel.

The number of submissions for meetings and symposia has fallen off drastically in the past 1–2 years. To help keep this column current, please e-mail any notices or calls for papers of upcoming conferences to raymond.wasky@jhuapl.edu.

2023 IEEE/MTT-S INTERNATIONAL MICROWAVE SYMPOSIUM (IMS 2023)

11–16 June 2023, San Diego, CA, USA. Contact: General information: e-mail: support@mtt.org. <http://www.ims-ieee.org>.

2023 IEEE INTERNATIONAL SYMPOSIUM ON ANTENNAS AND PROPAGATION & USNC-URSI RADIO SCIENCE MEETING

23–28 July 2023, Portland, OR, USA. Contacts: Jamesina J. Simpson, general cochair, e-mail: jamesina.simpson@utah.edu; Reyhan Baktur, general cochair, e-mail: reyhan.baktur@usu.edu. Magda El-Shenawee, student paper competition cochair, e-mail: magda@uark.edu; Ahmed Hassan, student paper competition cochair, e-mail: hassanam@umkc.edu. <https://2023.apsursi.org/>.

35TH URSI GENERAL ASSEMBLY AND SCIENTIFIC SYMPOSIUM (URSI GASS 2023)

19–26 August 2023, Sapporo, Hokkaido, Japan. Contacts: Kazuya Kobayashi, URSI GASS 2023 general chair, e-mail: kazuya@tamacc.chuo-u.ac.jp; Satoshi Yagitani, URSI GASS 2023 general co-chair, e-mail: yagitani@is.t.kanazawa-u.ac.jp; URSI GASS 2023 secretariat, e-mail: gass2023_secretariat@c-linkage.co.jp. <https://www.ursi-gass2023.jp>.



Raymond P. Wasky

EDITOR'S NOTE

The worldwide coronavirus (COVID-19) pandemic may have resulted in the cancellation or delay of some of the short courses listed below. Please check all course websites for the latest information prior to making plans for registration or travel. Please email notices of upcoming short courses to raymond.wasky@jhuapl.edu.

SHORT COURSES

RADAR CROSS SECTION REDUCTION

5–7 June 2023, Atlanta, GA, USA.

BASIC RADAR CONCEPTS

6–8 June 2023, Las Vegas, NV, USA.

RADAR SOFTWARE DEVELOPMENT

6–8 June 2023. ONLINE.

RADAR SYSTEMS ENGINEERING

6–8 June 2023. ONLINE.

BASIC RF ELECTROMAGNETIC WARFARE CONCEPTS

6–8 June 2023, Las Vegas, NV, USA.

TEST AND EVALUATION OF RF SYSTEMS

6–8 June 2023, Las Vegas, NV, USA. Georgia Institute of Technology, Professional Education, P.O. Box 93686, Atlanta, GA 30377-0686 USA. +1 404 385-3500, fax: +1 404 894-8925. <http://www.pe.gatech.edu>.

ANTENNA AND ARRAY FUNDAMENTALS

13–15 June 2023. ONLINE.

Digital Object Identifier 10.1109/MAP.2023.3262168
Date of current version: 5 June 2023

SONAR SIGNAL PROCESSING

27–29 June 2023. ONLINE.

ELECTRONIC PROTECTION AND ELECTRONIC ATTACK

27–29 June 2023. ONLINE. Applied Technology Institute, 349 Berkshire Drive, Riva, MD 21140-1433 USA. +1 410 956-8805 or +1 888 501-2100, fax: +1 410 956-5785, e-mail: ati@ATIcourses.com. <http://www.ATIcourses.com>.

MODERN ELECTRONIC AND DIGITAL SCANNED ARRAY ANTENNAS

26–30 June 2023, Las Vegas, NV, USA.

BASIC RF ELECTROMAGNETIC WARFARE CONCEPTS

27–29 June 2023, Las Vegas, NV, USA.

FUNDAMENTALS OF RADAR SIGNAL PROCESSING

27–30 June 2023, Las Vegas, NV, USA. Georgia Institute of Technology, Professional Education, P.O. Box 93686, Atlanta, GA 30377-0686 USA. +1 404 385-3500, fax: +1 404 894-8925. <http://www.pe.gatech.edu>.

PRINCIPLES OF MODERN RADAR

17–21 July 2023, Las Vegas, NV, USA.

SYNTHETIC APERTURE RADAR IMAGE FORMATION PROCESSING

18–21 July 2023, Las Vegas, NV, USA.

TRANSMIT/RECEIVE MODULES FOR PHASED-ARRAY RADAR: COMPONENTS, CONSTRUCTION AND COST

25–27 July 2023, Atlanta, GA, USA.

FUNDAMENTALS OF SYNTHETIC APERTURE RADAR SIGNAL PROCESSING

31 July–4 August 2023, Denver, CO, USA. Georgia Institute of Technology, Professional Education, P.O. Box 93686, Atlanta, GA 30377-0686 USA. +1 404 385-3500, fax: +1 404 894-8925. <http://www.pe.gatech.edu>.

AIRBORNE AESA RADAR

15–17 August 2023, Las Vegas, NV, USA.

BASIC ANTENNA CONCEPTS

15–17 August 2023, Las Vegas, NV, USA. Georgia Institute of Technology, Professional Education, P.O. Box 93686, Atlanta, GA 30377-0686 USA. +1 404 385-3500, fax: +1 404 894-8925. <http://www.pe.gatech.edu>.

SONAR PRINCIPLES AND ASW ANALYSIS

22–24 August 2023. ONLINE. Applied Technology Institute, 349 Berkshire Drive, Riva, MD 21140-1433 USA. +1 410 956-8805 or +1 888 501-2100, fax: +1 410 956-5785, e-mail: ati@ATIcourses.com. <http://www.ATIcourses.com>.

ELECTROMAGNETIC MATERIALS AND MEASUREMENTS:

RAM, RADOME AND RAS

19–21 September 2023, Atlanta, GA, USA.

BASIC ELECTROMAGNETIC WARFARE MODELING

19–22 September 2023. ONLINE.

FUNDAMENTALS OF RADAR SIGNAL PROCESSING

25–28 September 2023, Atlanta, GA, USA. Georgia Institute of Technology, Professional Education, P.O. Box 93686, Atlanta, GA 30377-0686 USA. +1 404 385-3500, fax: +1 404 894-8925. <http://www.pe.gatech.edu>.

BASIC ANTENNA CONCEPTS

3–5 October 2023, Lake Buena Vista, FL, USA.

MODELING AND SIMULATION OF PHASED-ARRAY ANTENNAS

17–19 October 2023. ONLINE.

PRINCIPLES OF MODERN RADAR

23–27 October 2023, Atlanta, GA, USA.

RADAR WARNING RECEIVER SYSTEM DESIGN

AND ANALYSIS

24–26 October 2023, Atlanta, GA, USA.

RADAR CROSS SECTION REDUCTION

30 October–1 November 2023, Atlanta, GA, USA.

MODELING AND SIMULATION OF ANTENNAS

30 October–2 November 2023, Atlanta, GA, USA. Georgia Institute of Technology, Professional Education, P.O. Box 93686, Atlanta, GA 30377-0686 USA. +1 404 385-3500, fax: +1 404 894-8925. <http://www.pe.gatech.edu>.

RADAR WAVEFORMS: PROPERTIES, ANALYSIS, DESIGN, AND APPLICATION

7–9 November 2023, Atlanta, GA, USA.

MODERN ELECTRONIC AND DIGITAL SCANNED ARRAY ANTENNAS

13–17 November 2023, Lake Buena Vista, FL, USA.

SIGNALS INTELLIGENCE (SIGINT) FUNDAMENTALS

14–15 November 2023, Lake Buena Vista, FL, USA.

BASIC RADAR CONCEPTS

14–16 November 2023, Lake Buena Vista, FL, USA.

TEST AND EVALUATION OF RF SYSTEMS

14–16 November 2023, Lake Buena Vista, FL, USA. Georgia Institute of Technology, Professional Education, P.O. Box 93686, Atlanta, GA 30377-0686 USA. +1 404 385-3500, fax: +1 404 894-8925. <http://www.pe.gatech.edu>.



IEEE Access®

Multidisciplinary : Rapid Review : Open Access Journal

Harness the
publishing
power of
IEEE Access®



- Receive high-quality, rigorous peer review in only 4 to 6 weeks
- Reach millions of global users through the IEEE Xplore® digital library by publishing open access
- Submit multidisciplinary articles that may not fit in narrowly focused journals

: Learn more at
ieeeaccess.ieee.org



A Survey of On-Body Antenna Arrays

Future improvements, new designs, and lessons learned.

Hanne Herssens , Wout Joseph , and Arno Thielens 

This manuscript presents a survey of the existing literature on on-body antenna arrays. They can be used to enable wireless communication to and from different on-body nodes in a wireless body area network (WBAN) and are also used in medical applications. The design process and the required characteristics of on-body antenna arrays are discussed. On-body antenna arrays should be small, lightweight, and low profile to ensure user comfort. The different types of on-body antenna arrays are discussed as well. On-body antenna arrays differ in the type of antenna element and in the geometric configuration of the array. The gain normalized to the area for the antenna arrays is compared, and it is found that, in the current state of the art, this quantity reduces with increasing frequency from 36 to 0.7 dBi. From our literature review, we draw important lessons that can be used to develop future on-body antenna arrays.

INTRODUCTION

On-body antenna arrays are collections of interconnected on-body antennas. Together, these antennas collectively transmit or receive radio-frequency electromagnetic fields (RF-EMFs) with the

EDITOR'S NOTE

This article for the “Bioelectromagnetics” column provides an extensive review of the literature on antenna arrays for placement upon the human body. The review discusses challenges associated with the design of such antennas, covers their design process and associated performance, and provides several examples with a focus on medical applications. The utmost goal is to provide the background necessary for developing future on-body antenna arrays with a performance that surpasses the state of the art.

This column welcomes articles on biomedical applications of electromagnetics, antennas, and propagation in terms of research, education, outreach, and more. If you are interested in contributing, please e-mail me at kiourt1.1@osu.edu.



Asimina Kiourt1

aim to communicate data wirelessly, perform microwave imaging, or achieve targeted dielectric heating. On-body antennas have different characteristics, depending on their application, and a wide variety of such antennas exists. They consist of different materials and operate at different frequencies, etc. Several reviews have been made about on-body antennas [1], [2], [3], focusing on different types of on-body antennas. The review in [1] focuses on wearable antennas at 60 GHz, the review in [2] focuses on ultrawideband wearable antennas, and the review in [3] focuses on EM bandgap integrated wearable antennas. None of these prior reviews focuses on on-body antenna arrays, so there is currently no

single source in the literature that can be used by antenna designers to obtain the specifications and properties of such arrays. This is the first time a review of on-body antenna arrays is presented, according to the authors' knowledge.

A typical application of on-body antenna arrays is in so-called WBANs. WBANs have received much attention because of their applications in health care, the military, and sports [4], [5]. These networks connect wireless on-body nodes and can be used, e.g., for continuously monitoring a patient's health remotely. Motion sensors can also be used to track movement in military and sports applications, e.g., for observing and improving the training of an

athlete. A key part of these WBANs is the on-body antennas that enable wireless communication between different on-body nodes.

Therefore, in this article, a systematic review of on-body antenna arrays is presented. The goal of this review is to provide an overview of the existing on-body antenna arrays for WBANs in the literature and discuss future improvements, new designs, and lessons learned. Additionally, some medical applications of on-body antenna arrays will be discussed. The novelty of this review lies in the fact that it focuses solely on on-body antenna arrays in comparison to preexisting reviews, which only focus on some specific on-body antenna types. The outline is as follows. The section “Design Requirements” describes general design requirements for on-body antenna arrays. The section “On-Body Antenna Arrays” presents the results of our review of on-body antenna arrays intended for RF communication. The section “RF-EMF Exposure” considers the RF-EMF exposure of the user by on-body antenna arrays. Section S.3 of the supplementary material discusses the design aspects of antenna arrays for medical applications like microwave imaging and hyperthermia treatment. The section “Lessons

The relatively high permittivity and conductivity of the human body can lead to a shift in resonance frequency and result in an impedance mismatch.

Learned and Future Research” provides an outlook on future research on this topic, and the final section contains the conclusions.

DESIGN REQUIREMENTS

This section will outline the main considerations that have to be made when designing an on-body antenna and how they translate into requirements for wearable antenna array design. This section focuses on the design requirements of arrays intended for wireless communication. On-body antenna array design requires optimizing or finding a tradeoff between a set of antenna (array) parameters. The most commonly used parameters are illustrated in Figure 1(a) and discussed in Section S.1 of the supplementary materials. In general, body-worn antennas should be

small, lightweight, and low profile [1], [2], [3]. However, the dimensions of an antenna are not freely chosen since they are related to the operating frequency. A higher operating frequency means smaller dimensions; therefore, most on-body antennas operate at microwave and millimeter-wave (mm-wave) frequencies, i.e., between 0.9 and 77 GHz [6], [7]. A lightweight antenna will ensure the user’s comfort. The human body will absorb part of the radiated EM energy by the on-body antenna. Ideally, an on-body antenna radiates while minimizing this exposure. Using an on-body antenna with a ground plane can reduce the backward radiation and consequently reduce the exposure [8].

When an antenna is placed close to or on a human body, the antenna parameters will change because of the coupling between the human body and the antenna [9], [10], [11]. The relatively high permittivity and conductivity of the human body [12] can lead to a shift in resonance frequency and result in an impedance mismatch. Therefore, it is necessary to retune the antenna after designing it in free space. For this reason, antennas

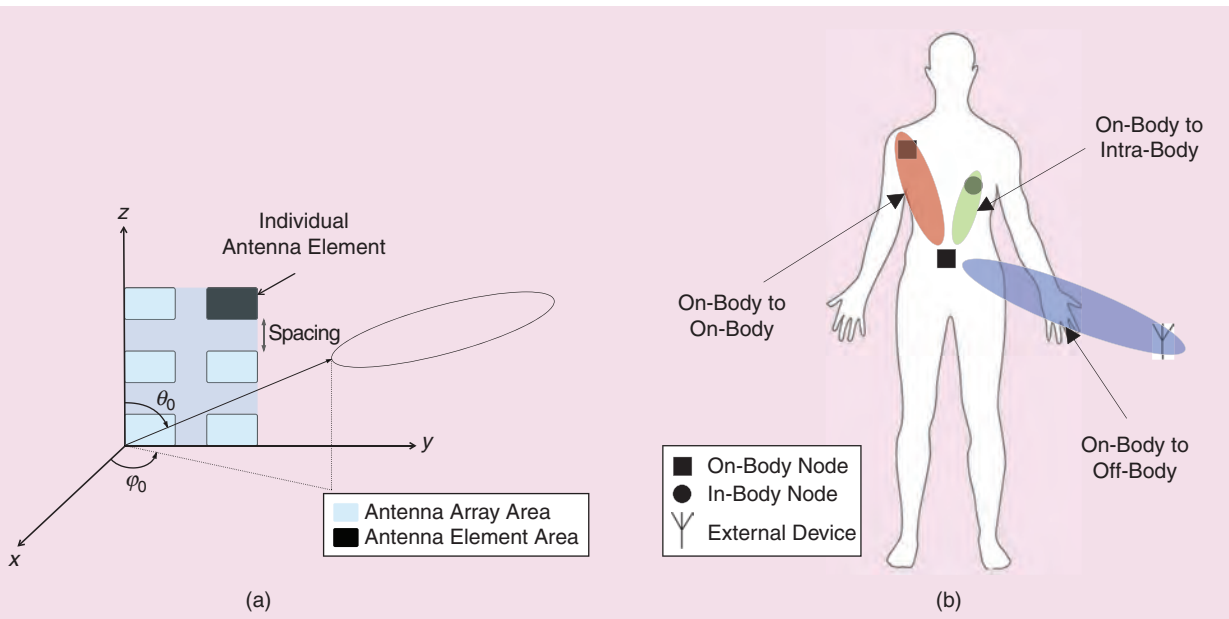


FIGURE 1. (a) Illustration of an antenna array in the yz-plane with the beam direction along θ_0 and ϕ_0 . The rectangles represent individual antenna elements. (b) Different communication links in a WBAN.

with wide bandwidths or very high isolations to surrounding dielectric materials are preferred. This isolation can be obtained by introducing a ground plane.

A body-worn antenna will be used to communicate with other antennas inside, on the body, or off the body through various wireless channels [13]. The lossy nature of the human body means that high propagation losses can occur in these channels [14]. To mitigate these losses, antennas with a high gain in these on-body channels can be used. An option to increase the channel gain is to use antenna arrays. An increasing number of antenna elements will lead to a higher antenna gain (see the section “Comparison of On-Body Antenna Array Parameters”) but also to a larger array caused by the physical area occupied by the individual antenna elements and the minimum separation distance between the elements, which is required to achieve decoupling between the elements. The minimum separation distance is related to the operating frequency. A higher frequency will result in a smaller separation distance. This increase in area decreases the wearability of the array. Therefore, a tradeoff needs to be made between the size and the gain of the antenna array. The separation distance of the antenna elements will affect the exposure of the user. Choosing an interelement spacing of $>0.5\lambda$ will result in grating lobes and will consequently increase the exposure [8].

Single on-body antennas are faced with two disadvantages that can be mitigated by using an array: 1) a single antenna has a fixed radiation pattern, and 2) single on-body antennas have limited gain. Antenna arrays provide a straightforward solution to both issues: 1) by steering multiple antenna elements, an array can have a dynamic radiation pattern, and 2) by combining multiple antenna elements, a higher gain can be obtained. The direction and amplitude of the radiation pattern of an on-body antenna depend on the amplitudes and the relative phases between the elements. Feeding of these elements requires a specific design of a feeding network, e.g., using (microstrip) transmission lines, phase shifters, splitters and

The high gains required for body-centric communication can be obtained by an antenna array consisting of multiple antenna elements.

combiners, and amplifiers. The design process of such an array consists thus of not only designing the antenna element and the feeding network, but also of designing the array system, i.e., the interelement spacing and orientation, such that radiation patterns can be formed in the desired direction(s).

The choice of fabrication technique and used materials will influence the design of the on-body antenna array. Conformal and flexible antennas on the one hand and rigid antennas on the other require different materials and fabrication techniques. Using textile materials, it is possible to make the antenna flexible and easy to integrate into clothes. This type of on-body antenna array is further discussed in the section “Textile Antenna Arrays.” On-body arrays can also be realized by inkjet printing [15], [16] and screen printing [7], [17] the radiating elements on a thin, flexible substrate. This results in very thin and flexible antenna arrays. A screen-printed layer will have a thickness between 10 and 20 μm , and an inkjet-printed layer will have a thickness of 0.5 μm [15]. They can be printed on plastic or paper substrates of 100–200- μm thickness to achieve a flexible stack. These thinner layers will result in fewer cracks in the metal layer when the antennas are bent.

The required radiation characteristics, i.e., the direction of maximum radiation, channel excitation, and polarization, depend on the application for which the antenna array is used.

WBAN LINKS

The three possible communication links in a WBAN are 1) on-body to on-body, 2) on-body to intrabody, and 3) on-body to off-body links. Each of these links uses a different channel [Figure 1(b)]. Therefore, they each have different requirements for the antenna. The antenna arrays used

for the on-body-to-intrabody link are out of scope in this review since we focus here on on-body antenna arrays for on- and off-body communication, and the requirements for these antennas differ a lot from the requirements of the antennas used in the other two links

[18]. Note that the on-body-to-intrabody link here refers to the wireless communication link and does not refer to the links used for medical applications (discussed in Section S.3 of the supplementary material).

ON-BODY COMMUNICATION

For on-body communication, different on-body devices will communicate with each other [Figure 1(b), in red]. The body surface is used as a communication channel, which can result in a higher attenuation than free space. The propagation during on-body communication is a combination of surface waves and space waves [19]. Surface waves propagate along the interface between air and the body, and space waves propagate in the air surrounding the body. The propagation loss or attenuation of free space waves does not depend on the polarization of the waves. However, surface waves do have a polarization dependency [19]. As an example of this polarization dependency, the lowest attenuation of surface waves for the 2.45-GHz Industry, Science, Medicine (ISM) band is found for a perpendicular polarization to the body surface [10], [20]. In practice, a perpendicular polarization will mean antennas with a high profile [10], [11], [20], [21], which are not comfortable for the user. Additionally, the maximum radiation needs to be along the body surface, and the radiation away and toward the body needs to be minimized.

OFF-BODY COMMUNICATION

For off-body communication, the on-body antennas communicate with off-body devices, e.g., via data sent to an external device. In this case, the antenna array will need to have its maximum radiation away from the user as opposed to along the body surface, which was the case in on-body communication.

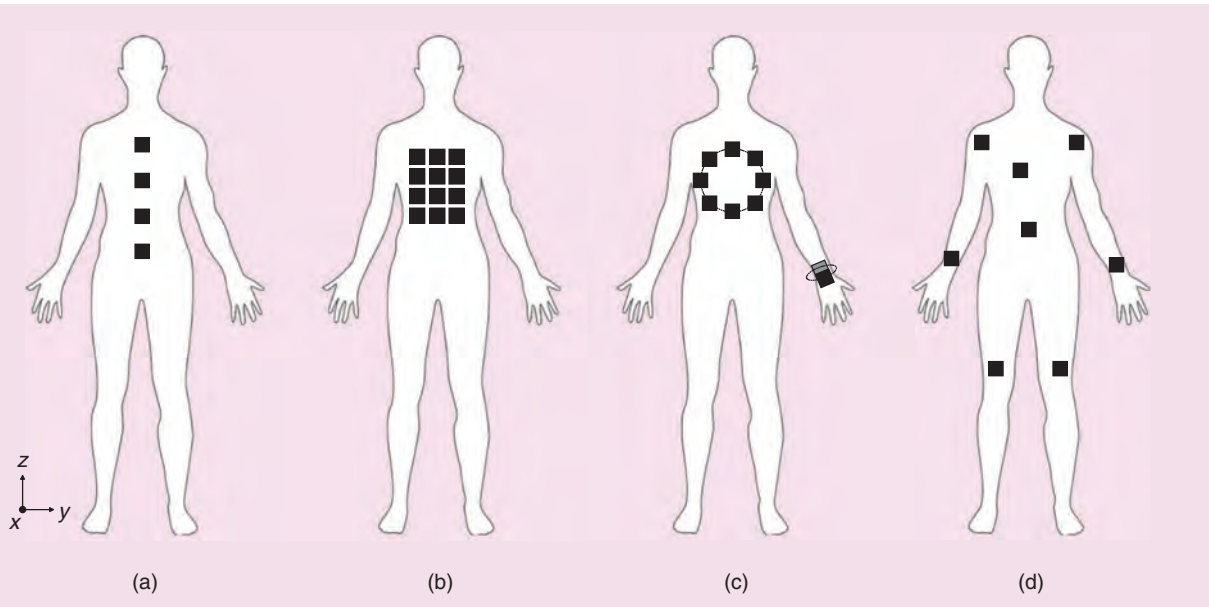


FIGURE 2. On-body antenna arrays. (a) Linear array. (b) Rectangular array. (c) Circular arrays. (d) Distributed array.

However, it should be noted that in the case of a colocated antenna array on one side of the body, the external antenna can be shielded by the body. In this case, the radiation still needs to go around the body surface.

ON-BODY ANTENNA ARRAYS

The high gains required for body-centric communication can be obtained by an antenna array consisting of multiple antenna elements [22]. Usually, the antenna elements are identical. The total field emitted by an array depends on the interelement spacing, the excitation amplitude and phase of the individual elements, and the geometrical configuration of the array. Figure 2 shows common types of antenna arrays: a uniform linear array, uniform rectangular array, uniform circular array, and a distributed antenna array, where the elements are distributed at convenient on-body locations. On-body antenna arrays can also be classified according to their on-body deployment, rather than their geometrical configuration. A (circular) array can be placed in different ways on a human body. The array can be placed in a plane parallel to the body on a specific part of the body (colocated), it can be wrapped around the body, e.g., around the waist or a limb (wrapped), or it can be spread over the entire body or torso (distributed).

ed). A linear array can be used to control the beam of the antenna in one dimension, e.g., at elevation angle θ_0 when the array is placed along the z -axis. A planar, wrapped, or distributed array can be used to control the beam in two dimensions, i.e., (θ_0, ϕ_0) [22].

Besides its geometrical configuration and its on-body deployment, an on-body array is also characterized by the type of antenna elements used in the array, the materials used to create the array, or the antenna parameter for which the array was optimized. Therefore, we have subdivided the literature on on-body antenna arrays into the following categories, which are discussed in this section: patch antenna arrays, textile antenna arrays, antenna arrays with improved isolation, parasitic arrays, circular arrays, on-body antenna arrays used for beam steering, and distributed antenna arrays. Section S.2 of the supplementary material discusses other interesting on-body antenna arrays that are not covered in the other categories. Table S.1 (supplementary material) lists these on-body antenna arrays, subdivided based on the targeted communication channels. The array configuration is given together with two important antenna parameters: array dimensions and gain. Note that on-body gain does not imply gain in the direction of the body but indicates the gain when

the antenna is placed on the body. The direction of maximal gain varies from one reference to the next.

PATCH ANTENNA ARRAYS

The patch antenna is the most common type of on-body antenna since this type of antenna has a low profile, which makes it suitable for wearable applications. It consists of a radiating patch placed above a ground plane with a dielectric substrate in between [22]. The ground plane shields the user from the radiation and consequently minimizes the RF-EMF exposure [8]. Additionally, it will make the antenna performance less sensitive to the presence of the human body [23], [24]. Figure 3(a) shows an example of a textile 2×1 patch antenna array designed in [25] operating at 2.45 GHz. The maximum radiation of the patch antenna is away from the body if the ground plane is worn touching the body's surface. This makes it ideal for off-body communication but less ideal for on-body communication. However, patch antennas were also used for on-body communication in [26] and [27].

The most popular patch shape is rectangular [8], [16], [23], [25], [27], [28], [29], [30], [31], [32], [33], [34], [35], [36], [37], [38], [39], [40], [41], [42], [43], [44], [45], [46], [47], [48], [49], [50], [51] since there exist approximate formulas [22] for

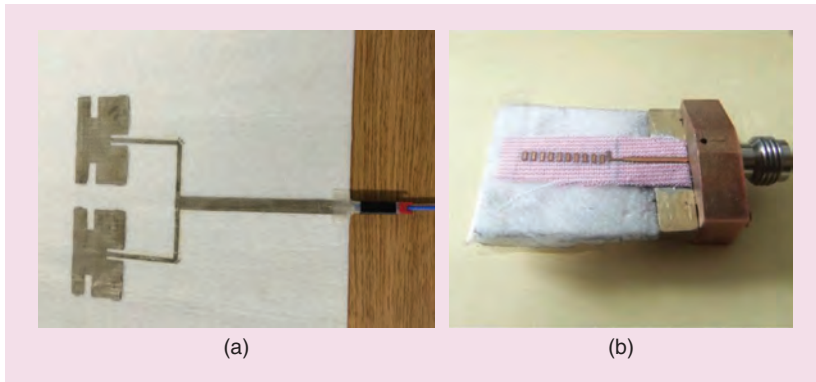


FIGURE 3. Textile antenna arrays. (a) A 2×1 patch antenna array operating at 2.45 GHz. (Source: [25].) (b) Yagi–Uda antenna operating at 60 GHz. (Source: [61].)

the dimensions of a rectangular patch antenna, which makes their design relatively easy. In [26], a dual polarization 2×2 array of circular patch antennas is designed for both on- and off-body communication in a WBAN at 28 GHz.

Besides rectangular and circular patches, there exist more complex patch shapes that are used for on-body antennas. Ring-shaped [52], T-shaped [15], and octagonal [53] patches are chosen to make the antenna element and, consequently, the array smaller. To make the antenna even more compact, slots can be introduced in the radiating elements, which is done in [15], [16], and [25].

In [24], a 4×1 antenna array operating at 2.45 GHz consisting of tip-truncated equilateral triangular patch antennas is designed to minimize the coupling between the different antenna elements. The antenna array system is fully integrated into a rescue-worker's vest. In [54], a circular conformal array con-

sisting of E-shaped patches resonating at 3.4 GHz is designed. The choice of patch shape results in a wider bandwidth in comparison to a rectangular patch. In [55], an 8×8 cross-shaped patch antenna array operating at 13.5 GHz is designed for a WBAN. The antenna elements can realize two orthogonal linear polarizations and a circular polarization by exciting different ports. In [56], a hexagonal patch with a slotted-ring antenna array is presented to obtain dual-band operation, i.e., at 2.45 GHz and 3.5 GHz.

TEXTILE ANTENNA ARRAYS

Textile antennas are often considered as on-body antennas because of their straightforward integration in clothes. At RFs (0.9–5.8 GHz), conductive textiles are used for the radiating elements and ground planes in combination with a textile substrate [6], [24], [25], [27], [31], [34], [39], [44], [46], [47], [54], [56], [57], [58], [59], [60]. This makes the antenna flexible, which makes it more comfortable for the user to wear. At mm-waves, the radiating elements of the antenna are much smaller, and a higher accuracy is needed to fabricate them. Therefore, a thin and flexible metallic foil was used instead in combination with a textile substrate to make a 2×2 patch antenna array [23] for short-range off-body communications and a Yagi–Uda antenna [61] for on-body high-data-rate communications at 60 GHz. The use of a textile substrate still makes the antenna flexible. Textile substrates often have low real and imaginary parts of the dielectric constant, which

reduces the losses and improves the impedance bandwidth [52].

When designing a textile antenna, flexibility needs to be considered. The textile can be twisted, folded, and bent. This deformation can affect the antenna performance. In [23], a 2×2 patch antenna array is studied under bending and crumpling conditions. It was shown that the antenna array remained matched in the 57–64-GHz band under bending in the H-plane. When the antenna array is bent in the H-plane, the radiating edges of the patches remain unbent. Therefore, the resonance frequency remains unchanged. The free space gain decreased from 9.0 to 7.9 dBi when the bending radius decreased from 15 to 5 mm. The array also remained matched under crumpling conditions, but the radiation pattern was strongly affected. The effect of the deformation on the antenna performance was also studied in [7], [24], [31], and [47]. From these studies, it can be concluded that the antenna performance under various bending conditions can remain unaffected when choosing appropriate materials. Therefore, in most cases, the antenna array can be designed in its planar form.

In [59], the flexibility of the textile is used for beam steering. A planar log-periodic dipole array (LPDA) consisting of 12 dipoles is designed for body-worn applications to operate between 0.9 and 3 GHz. Frequency-dependent beam steering is obtained by bending the dipole array at specific lengths.

ANTENNA ARRAYS WITH IMPROVED ISOLATION

For on-body antenna arrays, the dimensions of the array should be as small as possible. A small array area implies small spacing between the array elements and, consequently, a potentially increased coupling. Therefore, the articles listed in Table 1 have focused on improving the isolation such that a smaller spacing than $\lambda/2$ between the elements of the on-body antenna array can be taken. The isolation is improved by introducing C-shaped slots [36], an “8”-shaped stub [52], a parasitic structure [62], a shorted strip and two slits [63], and a line patch, rotating one patch by 90° [56]. In [48], a

TABLE 1. ON-BODY ANTENNA ARRAYS WITH IMPROVED ISOLATION.

Article	Spacing*	Isolation (dB)	
		Free Space	On-Body
[36]	0.1λ	-15	—
[52]	0.052λ	-26	—
[62]	0.008λ	-27	—
[63]	0.06λ	-32	-38
[56]	0.1λ	-30	—

*Edge to edge.

combination of a defected ground structure and split-ring resonators is used as an isolator to improve the isolation under bending of the array (Figure 4). The mutual coupling varies between -27.1 and -31.3 dB under different bending conditions with an isolator and between -17.9 and -23.2 dB without an isolator.

The obtained isolations and the used spacings for the previous articles are summarized in Table 1. In general, several prior investigations have demonstrated that high antenna isolation can be achieved with a spacing less than 0.5λ in wearable antenna arrays, and [63] suggests that these techniques could also be used on the human body. These results are promising for the development of future, compact on-body antenna arrays.

PARASITIC ARRAYS

A parasitic array consists of one or more driven antenna elements and several parasitic antenna elements [22]. The currents in these parasitic elements are induced by mutual coupling with the driven element not connected directly to the source or load. In most antenna arrays, this coupling is avoided since this will degrade the performance of the array. However, in parasitic arrays, mutual coupling is used to improve the directivity and gain of the antenna. These parasitic elements can also be used to direct the beam in a wanted direction. A parasitic array is sometimes not considered an antenna array since it consists of only one driven element. However, we did include a brief discussion of these arrays in our review because they can be important building blocks in certain WBAN applications.

BEAM STEERING PARASITIC ARRAY

A parasitic array can act as a reflector or as a director. A reflector radiates more power away from the antenna, and a director directs the power in its direction. When the parasitic elements are shorted to a ground plane, they act as a reflector, and when they are not shorted, they act as a director. This is used to beam switch in a (sector) top-loaded monopole antenna array [21] and a parasitic array of patch antennas [7]. Here, the reflectors and directors are fixed.

The reflectors and the directors can also be controlled. This is done for parasitic arrays consisting of dipoles using variable capacitors [6], [64] or p-i-n diodes [57], [65] and with patch antennas using p-i-n diodes [66]. In [6], the beam can be steered in three directions, i.e., 0° , 45° , and 315° . This is illustrated in Figure 5.

YAGI–UDA ANTENNA

In [61], a Yagi–Uda antenna is designed to operate at 60 GHz for on-body high-data-rate communications [Figure 3(b)]. A Yagi–Uda antenna has a maximum radiation parallel to the body surface when it is placed parallel to the body. This makes it suitable for directive on-body communication.

In [67] and [68], an antenna array of four printed parallel Yagi–Uda antennas and a substrate integrated waveguide (SIW) Yagi–Uda antenna are designed for 60-GHz on-body communication, respectively.

SURFACE WAVE PARASITIC ARRAY

In [20], a parasitic array is designed for on-body communication at 2.45 GHz for body-worn devices. The array consists of a printed monopole with parasitic elements placed parallel to the driven monopole. The parasitic elements are added to enhance the launching of the surface waves. The antenna has a low profile, which is often not the case with vertically polarized antennas, and is also capable of launching a sufficiently strong surface wave.

In general, the current literature on on-body parasitic arrays demonstrates that parasitic elements can be used to enable (on-body) beam steering and enhance the on-body channel gain. This approach can be beneficial in comparison to using multielement active arrays in terms of system complexity and energy consumption.



FIGURE 4. On-body antenna array with split-ring resonators and a defected ground plane to improve the isolation. (a) Front view. (b) Back view. (Source: [48].)

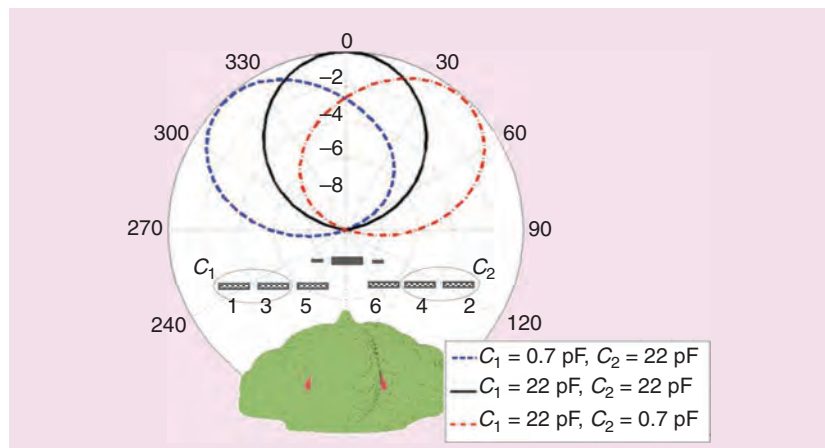


FIGURE 5. Simulated radiation pattern of the beam steering parasitic antenna array designed in [6]. (Source: [6].)

CIRCULAR ARRAYS

The human body will influence the radiation pattern of an antenna. A single antenna placed on the front of the body will have poor backward radiation because of the shielding of the human body. This can be mitigated by placing another antenna on the back of the body. This is investigated in [58]. A circular array can thus be used to achieve an omnidirectional radiation pattern, which is desirable for both on-body and off-body communication [27], [37], [44], [58], [69], [70].

In [37], a circular array consisting of patch antennas is designed to operate at 5 GHz for long-time health monitoring. The performance of the circular array is investigated with single, four, eight, and 16 patch antennas distributed uniformly across a cylinder that represents the human trunk. Again it is seen that the human body hinders the propagation of the EMFs. In [70], a cylindrical array of dipole antennas is designed to operate at



FIGURE 6. Circular antenna array operating at 5.8 GHz. (Source: [27].)

5 GHz. The beampattern is investigated as a function of circular arrays present in the cylindrical array.

In [27], a circular array consisting of patch antennas resonating at 5.8 GHz is designed (Figure 6). It is investigated how to achieve omnidirectionality and avoid radiation nulls with a circular array. This is also investigated in [44].

Only a few on-body circular antenna arrays are mentioned in the literature (six circular arrays versus 54 linear/rectangular arrays), despite their potential. We believe that circular arrays have a substantial potential since they can be used to achieve an omnidirectional radiation pattern, and they can be integrated into a belt or a wristband, which simplifies rooting between the antennas.

ON-BODY ANTENNA ARRAYS USED FOR BEAM STEERING

An antenna array can be used to steer a beam in a desired direction [22]. This is useful in both on-body and off-body communication. To obtain a beam in the desired direction, the fields of the separate elements need to interfere constructively in that direction and destructively in the other directions. Since a user is mobile, the direction in which on-body or external nodes will be found constantly changes. Therefore, it is useful that the direction of the beam can be adapted. This is commonly referred to as adaptive beamforming.

The direction of the beam depends on the phase difference between the

different antenna elements in the array. This phase difference can be fixed, e.g., by the length of the feed lines, or it can be changed by using one port per antenna element. This is not ideal for an on-body antenna since it will increase the size of the array. As mentioned earlier, parasitic elements can also be used to steer the beam depending on whether they act as a reflector or a director. This has the advantage of requiring only one port instead of multiple ones. The reflectors and directors can be fixed [7], [20], [21], [61], [67], [68] or controlled by using, e.g., varactor diodes [6], [57], [64], [65], [66], [71].

DISTRIBUTED ANTENNA ARRAYS

Distributed on-body antenna arrays are arrays in which the antennas are distributed over the body in convenient places, not in a particular geometric configuration [Figure 2(d)]. These antenna arrays are often not explicitly designed for improving the gain. Therefore, these on-body arrays are not considered in the analysis of the next section, “Comparison of On-Body Antenna Array Parameters.” The positioning of these antenna elements depends on the application of the antenna array, e.g., as a personal distributed exposimeter [72], [73], [74] and for investigating (dynamic) channel models [75], [76], [77], [78].

COMPARISON OF ON-BODY ANTENNA ARRAY PARAMETERS

Figure 7(a) shows an overview of the obtained maximum antenna gain in free

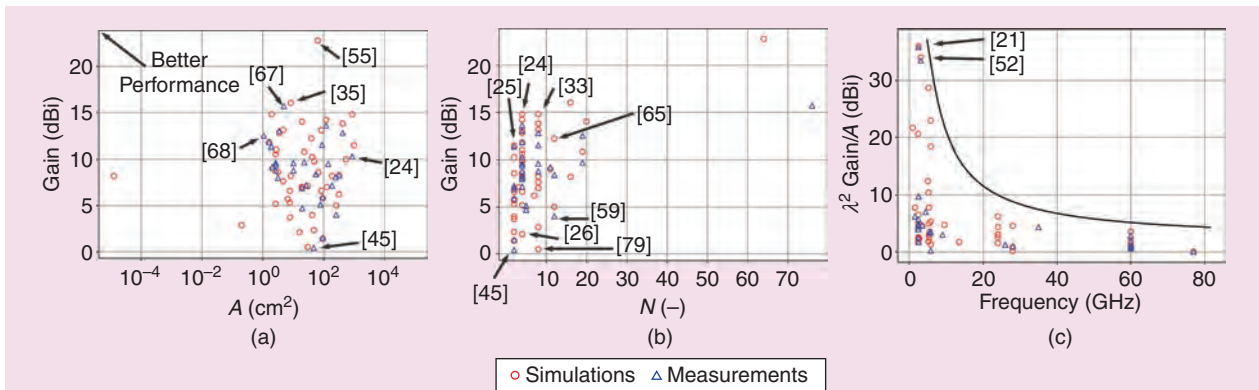


FIGURE 7. (a) Free space gain as a function of area. (b) Free space gain as a function of number of elements. (c) Normalized free space gain as a function of frequency. A: area; N: number of elements.

space as a function of the area of the antenna array for the different on-body antenna arrays. The distributed antenna arrays were not considered since the area for these would correspond to the human body area, and the array is usually not used to increase the gain. If only the dimensions of a single antenna element were given, a spacing between the antenna elements of 0.5λ was assumed, and approximate dimensions of the array were used based on the values given in the articles. It was also assumed that the gain values were given in decibels relative to isotrope. The smallest fabricated array (see the blue triangles) is the SIW Yagi–Uda antenna designed in [68], operating at 60 GHz with an area of 1.0672 cm^2 , and the largest is the 4×1 patch antenna array designed in [24], operating at 2.45 GHz with an area of 864 cm^2 . From Figure 7(a), we can conclude that the measured gains are situated between 0.42 dBi (a 2×1 patch antenna array [45]) and 15.7 dBi (the 4×1 printed Yagi–Uda antennas [67]) for the fabricated antenna arrays. Figure 7(a) also shows higher gains, i.e., 16.04 dBi (a 4×4 patch antenna array [35]) and 22.8 dBi (an 8×8 patch antenna array [55]), but these gains are only achieved with simulations and not verified with measurements.

When designing an on-body antenna array, there will be a tradeoff between the size of the array and the obtained gain. More elements will increase the gain but will also increase the size of the array. This can be seen in Figure 7(b). A good on-body antenna array will therefore be small in size with an acceptable gain. The antenna array consisting of 64 patches [55] shows the highest gain, i.e., 22.8 dBi. The lowest gain, i.e., 0.42 dBi, is found for the 2×1 patch antenna array presented in [45]. For two, four, eight, and 12 elements, the minimum obtained gain is 0.42 dBi (2×1 patches [45]), 2.1 dBi (2×2 patches [26]), 0.5 dBi (circular array of dipoles [79]), and 4 dBi (a planar LPDA [59]), respectively. For two, four, eight, and 12 elements, the maximum obtained gain is 11.45 dBi (2×1 patches [25]), 14.8 dBi (4×1 patches [24]), 14.8 dBi (4×2 patches [33]), and 12.2 dBi (a parasitic array of dipoles [65]), respectively.

As mentioned before, a good on-body antenna array has a high gain but is small in size. Therefore, a higher value of Gain/A will lead to a better on-body antenna array. However, it is difficult to compare the areas of arrays operating at different frequencies since a higher frequency will result in smaller antenna elements, and, consequently, more elements can be placed in the same area or a smaller antenna array is obtained using the same number of elements. A solution to this is to use the normalized area, i.e., $A_{\text{norm}} = A/\lambda^2$. A good on-body antenna array should be small relative to its wavelength and have a high gain. Figure 7(c) shows the normalized gain as a function of frequency, with $\text{Gain}_{\text{norm}} = \text{Gain}/A_{\text{norm}}$. Almost all measured normalized gains are less than 10 dBi. There are only two arrays with a measured normalized gain above 10 dBi. The first array is the patch antenna array designed in [52]. An “8”-shaped stub was placed between the antenna elements to improve the isolation. As a result, the elements could be placed closer together, which leads to a smaller area and a higher normalized gain. The second array is the parasitic array consisting of sector top-loaded monopoles presented in [21]. The sector top loading of the monopoles reduces the ground plane size, which results in a smaller area. However, this also increases the height of the array, which is not practical. The other normalized gains above 10 dBi are simulation results and therefore represent ideal cases. From Figure 7(c), we can conclude that the normalized gain reduces with increasing frequency from 36 to 0.7 dBi. This trend is shown by the black curve. There is a research opportunity to develop on-body arrays in mm-wave frequencies with a normalized gain comparable to that currently found at lower RF frequencies.

RF-EMF EXPOSURE

The human body will absorb part of the radiated EM energy by the on-body antenna array. The absorption depends on the antenna design and the frequency of the EM waves; e.g., a higher frequency generally results in a more localized absorption because

of the smaller penetration depth. The exposure can be quantified in terms of the specific absorption rate (SAR). Table 2 lists the peak SARs averaged over 1 and 10 g for the on-body antenna arrays studied in this review that have listed such values. These SAR values scale linearly with the input power into an antenna array and therefore put a limit on the maximal power that can be emitted by the arrays. The local SAR limit (averaged over 10 g) for the general public is 2 W/kg for frequencies below 6 GHz [80]. The on-body antenna arrays designed in [8], [30], and [33] operate at 60 GHz and will result in a more localized absorption. Therefore, the quantity used to describe the exposure in these articles is the peak power density averaged over 1 and 20 cm^2 . The exposure limits for the general public for these quantities are 200 W/m² and 10 W/m² for the power density averaged over 1 cm^2 and 20 cm^2 , respectively. Note that for frequencies above 6 GHz, exposure should be described in terms of the absorbed power density (S_{ab}) averaged over 4 cm^2 and additionally for frequencies above 30 GHz averaged over 1 cm^2 according to current exposure guidelines defined by the International Commission on Non-Ionizing Radiation Protection [80].

LESSONS LEARNED AND FUTURE RESEARCH

There exists a variety of on-body antenna arrays in the literature. These on-body antenna arrays can differ in the type of antenna element, e.g., patch antennas and slot antennas. They can also differ in the geometric configuration of the array, e.g., a linear array or rectangular array. These on-body antenna arrays have different characteristics, but there are general considerations that apply to all on-body antenna arrays. The antenna arrays need to be compact since they are body worn. The characteristics depend on the communication link in the WBAN, i.e., on-body communication or off-body communication. The on-body antenna arrays designed for off-body communication had their

maximum radiation away from the body to communicate with an external device. This differs from the on-body antenna arrays designed for on-body communication. On-body communication makes use of surface waves. Since it is known that a monopole effectively launches these surface waves in the 2.45 GHz ISM band, several articles have tried to obtain a monopole-like radiation with their antenna arrays since a monopole is not practical because of its high profile. One way to do this is to still use monopoles but to top-load them with a disk to reduce the height [21]. Another way to do this is to use dipoles in a colocated circular array [79], [82]. The most common on-body antenna array is a patch antenna array. Most of the patch antenna arrays are designed for off-body communication as the antennas have their maximum radiation away from the body.

A higher frequency resulted in a lower normalized gain for the antenna arrays found in the literature. Future research can include designing arrays at mm-waves with the comparable normalized gains that are found at lower frequencies.

An interesting on-body antenna array is a circular array wrapped around a limb or the waist. These are useful since the human body can shield different antenna elements from each other. The circular arrays can thus be used to achieve an omnidirectional radiation pattern. They are also practical since they can be integrated into a belt or a wristband. Only a few of these circular arrays are mentioned in the literature (six circular arrays versus 54 linear/rectangular arrays), despite their potential. This type of array could potentially be used to achieve uniform on-body coverage for situations where the on-body nodes in a WBAN are spread over the entire body. This requires further research.

CONCLUSIONS

An overview of the existing on-body antenna arrays, their performance, and their potential in the literature has been presented. This has not been done until now. These antenna arrays operate at frequencies between 0.9 and 77 GHz. The design process of the on-body antenna arrays is discussed as well as the required characteristics.

The performance of the on-body antenna arrays is discussed and compared. The antenna arrays have an area between 1.07 and 864 cm² for frequencies between 0.9 and 77 GHz. The measured gains are situated between 1.5 and 15.7 dBi. The highest obtained gain with simulations is 22.8 dBi, but this has not been verified with measurements. More antenna elements will lead to a higher gain but also to an increase in area of the array. An antenna array consisting of 64 patch antennas has the highest gain, i.e., 22.8 dBi. The lowest gain, 0.42 dBi, is found for a 2 × 1 patch antenna array. The normalized gain was also discussed since it is difficult to compare antenna array areas for different operating frequencies. It was found that the normalized gain reduces with increasing frequency. Additionally, it was found that almost all measured normalized gains are less than 10 dBi.

Two medical applications, i.e., microwave imaging and hyperthermia treatment, of on-body antenna arrays have been discussed. The general design requirements, i.e., compactness and a low profile, also apply since they are wearable. Additionally, a tradeoff needs to be made between the penetration depth of the EMFs and the resolution of the image (for microwave imaging) or the size of the focus spot (for hyperthermia treatment).

SUPPLEMENTARY INFORMATION

This article has supplementary downloadable material available at <https://doi.org/10.1109/MAP.2023.3262144>, provided by the authors.



ACKNOWLEDGMENT

Arno Thielens is a postdoctoral fellow of the Research Foundation Flanders under Grant agreement 1283921N.

TABLE 2. PEAK SAR AVERAGED OVER 1 AND 10 G AND PEAK POWER DENSITY AVERAGED OVER 1 AND 20 CM² OF THE ON-BODY ANTENNA ARRAYS.

Paper	Frequency (GHz)	Input Power (W)	SAR (W/kg)		Power Density (W/m ²)	
			1 g	10 g	1 cm ²	20 cm ²
[6]	0.9	1	3.5	2	—	—
[81]	4.5–6.5	—	0.59	—	—	—
[24]	2.45	2	—	0.0124	—	—
[27]	5.8	0.1	0.29/0.105*	—	—	—
[29]	5.8	—	—	0.313	—	—
[39]	2.38	0.1	—	0.02	—	—
[64]	2.45	0.25	1.35	0.85	—	—
[65]	5.2	2	3.33	1.34	—	—
[60]	5.2	0.5	—	0.0942	—	—
[63]	2.4	0.1	1.52	—	—	—
[8]	60	0.5	—	—	13.1/685.9/11.2**	4.6/39.7/1.8**
[30]	60	0.322	—	—	38	—
[33]	60	1.4	—	—	—	9.48

* Dual polarization.

** Three different feeding techniques.

AUTHOR INFORMATION

Hanne Herssens (hanne.herssens@ugent.be) is with the Department of Information Technology, Ghent University-IMEC, 9052 Ghent, Belgium. She is a Ph.D. student at the Waves Research Group, Ghent University. Her research interests include electromagnetic exposure, on-body antennas, and body-centric wireless communication.

Wout Joseph (wout.joseph@ugent.be) is with Ghent University-IMEC, 9052 Ghent, Belgium. He is a professor in experimental characterization of wireless communication systems and a principal investigator. His interests are electromagnetic field exposure assessment and propagation. He is a Senior Member of IEEE.

Arno Thielens (arno.thielens@ugent.be) is with the Department of Information Technology, Ghent University-IMEC, 9052 Ghent, Belgium. He is a professor at Ghent University and a senior postdoctoral fellow of the Research Foundation Flanders. His research focuses on bioelectromagnetics. He is a Member of IEEE.

REFERENCES

- [1] A. Pellegrini et al., "Antennas and propagation for body-centric wireless communications at millimeter-wave frequencies: A review [Wireless Corner]," *IEEE Antennas Propag. Mag.*, vol. 55, no. 4, pp. 262–287, Aug. 2013, doi: 10.1109/MAP.2013.6645205.
- [2] S. Yan et al., "Wearable ultrawideband technology—A review of ultrawideband antennas, propagation channels, and applications in wireless body area networks," *IEEE Access*, vol. 6, pp. 42,177–42,185, Jul. 2018, doi: 10.1109/ACCESS.2018.2861704.
- [3] A. Y. I. Ashyap et al., "An overview of electromagnetic band-gap integrated wearable antennas," *IEEE Access*, vol. 8, pp. 7641–7658, Jan. 2020, doi: 10.1109/ACCESS.2020.2963997.
- [4] M. Ghamari et al., "A survey on wireless body area networks for eHealthcare systems in residential environments," *Sensors*, vol. 16, no. 6, Jun. 2016, Art. no. 831, doi: 10.3390/s16060831.
- [5] Q. Liu et al., "Performance issues in wireless body area networks for the healthcare application: A survey and future prospects," *SN Appl. Sci.*, vol. 3, no. 2, pp. 1–19, Jan. 2021, doi: 10.1007/s42452-020-04058-2.
- [6] M. R. Islam et al., "A 900 MHz beam steering parasitic antenna array for wearable wireless applications," *IEEE Trans. Antennas Propag.*, vol. 61, no. 9, pp. 4520–4527, Sep. 2013, doi: 10.1109/TAP.2013.2269764.
- [7] A. Meredov et al., "Screen-printed, flexible, parasitic beam-switching millimeter-wave antenna array for wearable applications," *IEEE Open J. Antennas Propag.*, vol. 1, pp. 2–10, Nov. 2019, doi: 10.1109/OJAP.2019.2955507.
- [8] C. Leduc et al., "Impact of antenna topology and feeding technique on coupling with human body: Application to 60-GHz antenna arrays," *IEEE Trans. Antennas Propag.*, vol. 65, no. 12, pp. 6779–6787, Dec. 2017, doi: 10.1109/TAP.2017.2700879.
- [9] L. Roelens et al., "Characterization of scattering parameters near a flat phantom for wireless body area networks," *IEEE Trans. Electromagn. Compat.*, vol. 50, no. 1, pp. 185–193, Feb. 2008, doi: 10.1109/TEMC.2007.915280.
- [10] P. S. Hall et al., "Antennas and propagation for on-body communication systems," *IEEE Antennas Propag. Mag.*, vol. 49, no. 3, pp. 41–58, Jun. 2007, doi: 10.1109/MAP.2007.4293935.
- [11] G. Conway et al., "An antennas and propagation approach to improving physical layer performance in wireless body area networks," *IEEE J. Sel. Areas Commun.*, vol. 27, no. 1, pp. 27–36, Feb. 2009, doi: 10.1109/JSC.2009.090104.
- [12] C. Gabriel et al., "The dielectric properties of biological tissues: I. Literature survey," *Phys. Med. Biol.*, vol. 41, no. 11, pp. 2231–2249, Nov. 1996, doi: 10.1088/0031-9155/41/11/001.
- [13] K. Kwak et al., "An overview of IEEE 802.15.6 standard," in *Proc. 3rd Int. Symp. Appl. Sci. Biomed. Commun. Technol.*, Dec. 2010, pp. 1–6, doi: 10.1109/ISABEL.2010.5702867.
- [14] A. Thielens et al., "A comparative study of on-body radio-frequency links in the 420 MHz–2.4 GHz range," *Sensors*, vol. 18, no. 12, Nov. 2018, Art. no. 4165, doi: 10.3390/s18124165.
- [15] S. F. Jilani et al., "Low-profile flexible frequency-reconfigurable millimetre-wave antenna for 5G applications," *Flexible Printed Electron.*, vol. 3, no. 3, Aug. 2018, Art. no. 035003, doi: 10.1088/2058-8585/aad392.
- [16] S. F. Jilani et al., "Millimeter-wave liquid crystal polymer based conformal antenna array for 5G applications," *IEEE Antennas Wireless Propag. Lett.*, vol. 18, no. 1, pp. 84–88, Jan. 2019, doi: 10.1109/LAWP.2018.2881303.
- [17] A. Meredov et al., "77 GHz screen printed, flexible, beam-switching antenna array for wearable radar applications," in *Proc. IEEE Int. Symp. Antennas Propag. USNC-URSI Radio Sci. Meeting*, 2019, pp. 867–868, doi: 10.1109/APUSNCURSINRSM.2019.8889032.
- [18] A. K. Teshome et al., "A review of implant communication technology in WBAN: Progress and challenges," *IEEE Rev. Biomed. Eng.*, vol. 12, pp. 88–99, 2019, doi: 10.1109/RBME.2018.2848228.
- [19] J. Bae et al., "The signal transmission mechanism on the surface of human body for body channel communication," *IEEE Trans. Microw. Theory Techn.*, vol. 60, no. 3, pp. 582–593, Mar. 2012, doi: 10.1109/TMTT.2011.2178857.
- [20] L. Akhoondzadeh-Asl et al., "Parasitic array antenna with enhanced surface wave launching for on-body communications," *IEEE Trans. Antennas Propag.*, vol. 61, no. 4, pp. 1976–1985, Apr. 2013, doi: 10.1109/TAP.2012.2231918.
- [21] M. R. Kamarudin et al., "Switched beam antenna array with parasitic elements," *Prog. Electromagn. Res. B*, vol. 13, no. 13, pp. 187–201, Jan. 2009, doi: 10.2528/PIERB09011603.
- [22] C. A. Balanis, *Antenna Theory: Analysis and Design*. Hoboken, NJ, USA: Wiley, 2015.
- [23] N. Chahat et al., "60-GHz textile antenna array for body-centric communications," *IEEE Trans. Antennas Propag.*, vol. 61, no. 4, pp. 1816–1824, Apr. 2013, doi: 10.1109/TAP.2012.2232633.
- [24] M. L. Scarpello et al., "High-gain textile antenna array system for off-body communication," *Int. J. Antennas Propag.*, vol. 2012, no. 4, Jan. 2012, Art. no. 573438, doi: 10.1155/2012/573438.
- [25] E. Workman et al., "Flexible textile antenna array," in *Proc. IEEE Int. Conf. Electro/Inf. Technol.*, 2015, pp. 569–574, doi: 10.1109/EIT.2015.7293399.
- [26] X. Tong et al., "A dual-mode multi-polarization millimeter wave wearable antenna for WBAN applications," in *Proc. IEEE MTT-S Int. Microw. Biomed. Conf.*, 2019, vol. 1, pp. 1–3, doi: 10.1109/IMBIOC.2019.8777910.
- [27] C.-X. Mao et al., "Dual-polarized embroidered textile armband antenna array with omnidirectional radiation for on/off-body wearable applications," *IEEE Trans. Antennas Propag.*, vol. 68, no. 4, pp. 2575–2584, Apr. 2020, doi: 10.1109/TAP.2019.2951517.
- [28] A. S. M. Alqadami et al., "Assessment of PDMS technology in a MIMO antenna array," *IEEE Antennas Wireless Propag. Lett.*, vol. 15, pp. 1939–1942, 2016, doi: 10.1109/LAWP.2015.2513960.
- [29] A. S. Alqadami et al., "Efficacy of a wideband flexible antenna on a multilayer polymeric nanocomposites Fe3O4-PDMS substrate for wearable applications," *Current Appl. Phys.*, vol. 19, no. 11, pp. 1259–1265, Aug. 2019, doi: 10.1016/j.cap.2019.08.007.
- [30] N. Chahat et al., "Characterization of the interactions between a 60-GHz antenna and the human body in an off-body scenario," *IEEE Trans. Antennas Propag.*, vol. 60, no. 12, pp. 5958–5965, Dec. 2012, doi: 10.1109/TAP.2012.2211326.
- [31] K.-S. Chin et al., "Designs of textile antenna arrays for smart clothing applications," *Autex Res. J.*, vol. 18, no. 3, pp. 295–307, May 2018, doi: 10.1515/aut-2018-0002.
- [32] U. Farooq et al., "Design of a 1×4 CPW microstrip antenna array on PET substrate for biomedical applications," in *Proc. IEEE Int. Symp. Antennas Propag. USNC-URSI Radio Sci. Meeting*, 2019, pp. 1345–1346, doi: 10.1109/APUSNCURSINRSM.2019.8889355.
- [33] Y. Hong et al., "60 GHz patch antenna array with parasitic elements for smart glasses," *IEEE Antennas Wireless Propag. Lett.*, vol. 17, no. 7, pp. 1252–1256, Jul. 2018, doi: 10.1109/LAWP.2018.2841512.
- [34] T. F. Kennedy et al., "Body-worn E-textile antennas: The good, the low-mass, and the conformal," *IEEE Trans. Antennas Propag.*, vol. 57, no. 4, pp. 910–918, Apr. 2009, doi: 10.1109/TAP.2009.2014602.
- [35] V. Kumar, "24 GHz graphene patch antenna array," *Appl. Comput. Electromagn. Soc. J.*, vol. 34, no. 5, pp. 676–683, May 2019.
- [36] Y. Li et al., "A compact UWB MIMO antenna for 4.5G/5G wearable device applications," in *Proc. 6th Asia-Pacific Conf. Antennas Propag.*, 2017, pp. 1–3, doi: 10.1109/APCAP.2017.8420881.
- [37] Y. Li et al., "A study of a one-turn circular patch antenna array and the influence of the human body on the characteristics of the antenna," *Ad Hoc Netw.*, vol. 99, Mar. 2020, Art. no. 102059, doi: 10.1016/j.adhoc.2019.102059.
- [38] M. Mirzaee et al., "Low-profile wearable wideband antenna with high gain based on franklin array for future 5G wireless body area networks," in *Proc. IEEE Int. Symp. Antennas Propag. North Amer. Radio Sci. Meeting*, Jul. 2020, pp. 449–450, doi: 10.1109/IEEECONF35879.2020.9329727.
- [39] D. Rano et al., "Design and analysis of wearable patch antenna array for MBAN applications,"

- in Proc. 22nd Nat. Conf. Commun., 2016, pp. 1–6, doi: 10.1109/NCC.2016.7561201.
- [40] B. R. Sanjeeda Reddy et al., “Performance analysis of wearable antenna array for WLAN applications,” in Proc. IEEE Indian Conf. Antennas Propag., 2018, pp. 1–4, doi: 10.1109/INCAP.2018.8770832.
- [41] Q. Rubani et al., “A compact MIMO antenna for WBAN operating at Terahertz frequency,” *Optik*, vol. 207, Apr. 2020, Art. no. 164447, doi: 10.1016/j.ijleo.2020.164447.
- [42] D. G. Rucker et al., “Microstrip antenna arrays for implantable and wearable wireless applications,” in Proc. Int. Conf. Wireless Mobile Commun. Healthcare, Springer, 2010, pp. 135–143.
- [43] U. Ullah et al., “A series inclined slot-fed circularly polarized antenna for 5G 28 GHz applications,” *IEEE Antennas Wireless Propag. Lett.*, vol. 20, no. 3, pp. 351–355, Mar. 2021, doi: 10.1109/LAWP.2021.3049901.
- [44] H. Yang et al., “Design of broadband circularly polarized all-textile antenna and its conformal array for wearable devices,” *IEEE Trans. Antennas Propag.*, vol. 70, no. 1, pp. 209–220, Jan. 2022, doi: 10.1109/TAP.2021.3098542.
- [45] Y. G. Rabobason et al., “Design of flexible passive antenna array on Kapton substrate,” *Prog. Electromagn. Res. C*, vol. 63, pp. 105–117, Apr. 2016, doi: 10.2528/PIERC15120906.
- [46] P. J. Soh et al., “A smart wearable textile array system for biomedical telemetry applications,” *IEEE Trans. Microw. Theory Techn.*, vol. 61, no. 5, pp. 2253–2261, May 2013, doi: 10.1109/TMTT.2013.2247051.
- [47] Q. Bai et al., “Crumpling of microstrip antenna array,” *IEEE Trans. Antennas Propag.*, vol. 61, no. 9, pp. 4567–4576, Sep. 2013, doi: 10.1109/TAP.2013.2269133.
- [48] J. Zhang et al., “Mutual coupling suppression for on-body multiantenna systems,” *IEEE Trans. Electromagn. Compat.*, vol. 62, no. 4, pp. 1045–1054, Aug. 2020, doi: 10.1109/TEMC.2019.2936679.
- [49] M. Han et al., “Solution-processed Ti3C2Tx MXene antennas for radio-frequency communication,” *Adv. Mater.*, vol. 33, no. 1, Jan. 2021, Art. no. 2003225, doi: 10.1002/adma.202003225.
- [50] M. Bilal et al., “A miniaturized FSS-based eight-element MIMO antenna array for off/on-body WBAN telemetry applications,” *Electronics*, vol. 11, no. 4, Feb. 2022, Art. no. 522, doi: 10.3390/electronics11040522.
- [51] H. Qiu et al., “Compact, flexible, and transparent antennas based on embedded metallic mesh for wearable devices in 5G wireless network,” *IEEE Trans. Antennas Propag.*, vol. 69, no. 4, pp. 1864–1873, Apr. 2021, doi: 10.1109/TAP.2020.3035911.
- [52] A. K. Biswas et al., “Compact wearable MIMO antenna with improved port isolation for ultrawideband applications,” *IET Microw., Antennas Propag.*, vol. 13, no. 4, pp. 498–504, Mar. 2019, doi: 10.1049/iet-map.2018.5599.
- [53] S. Tripathi et al., “A compact UWB Koch fractal antenna for UWB antenna array applications,” *Wireless Pers. Commun.*, vol. 92, no. 4, pp. 1423–1442, Feb. 2017, doi: 10.1007/s11277-016-3613-1.
- [54] A. Y. Svezhentsev et al., “Omnidirectional wideband E-shaped cylindrical patch anten-
- nas,” *IEEE Trans. Antennas Propag.*, vol. 64, no. 2, pp. 796–800, Feb. 2016, doi: 10.1109/TAP.2015.2506735.
- [55] Z. Wang et al., “A broad beam-width microstrip cross antenna design for wide scan angle phased array,” in Proc. IEEE MTT-S Int. Microw. Workshop Series RF Wireless Technol. Biomed. Healthcare Appl., 2013, pp. 1–3, doi: 10.1109/IMWS-BIO.2013.6756220.
- [56] H. A. Mashagba et al., “A hybrid mutual coupling reduction technique in a dual-band MIMO textile antenna for WBAN and 5G applications,” *IEEE Access*, vol. 9, pp. 150,768–150,780, Nov. 2021, doi: 10.1109/ACCESS.2021.3125049.
- [57] P. Czeresko et al., “Fabric based beam steering wearable antenna array,” in Proc. 12th Eur. Conf. Antennas Propag., 2018, pp. 1–4, doi: 10.1049/cp.2018.0461.
- [58] L. Januszkiewicz, “The analysis of textile antenna array radiation pattern,” in Proc. 18th Int. Conf. Microw., Radar Wireless Commun., 2010, pp. 1–4.
- [59] A. D. Johnson et al., “Reconfigurable log-periodic dipole array on textile,” *IET Microw., Antennas Propag.*, vol. 14, no. 14, pp. 1791–1794, Nov. 2020, doi: 10.1049/iet-map.2019.0705.
- [60] J. Zhang et al., “Dual-band dual-polarized wearable button array with miniaturized radiator,” *IEEE Trans. Biomed. Circuits Syst.*, vol. 13, no. 6, pp. 1583–1592, Nov. 2019, doi: 10.1109/TBCAS.2019.2953989.
- [61] N. Chahat et al., “Wearable endfire textile antenna for on-body communications at 60 GHz,” *IEEE Antennas Wireless Propag. Lett.*, vol. 11, pp. 799–802, Jul. 2012, doi: 10.1109/LAWP.2012.2207698.
- [62] A. I. Abbosh et al., “Flexible CPW-IFA antenna array with reduced mutual coupling,” in Proc. IEEE Antennas Propag. Soc. Int. Symp. (URSI), 2014, pp. 1716–1717, doi: 10.1109/APS.2014.6905184.
- [63] D.-G. Kang et al., “MIMO antenna with high isolation for WBAN applications,” *Int. J. Antennas Propag.*, vol. 2015, pp. 1–7, Jul. 2015, doi: 10.1155/2015/370763.
- [64] M. R. Islam et al., “A novel wearable antenna array for 2.45 GHz WLAN application,” in Proc. IEEE Int. Symp. Antennas Propag. (APSURSI), 2011, pp. 2754–2757, doi: 10.1109/APS.2011.5997096.
- [65] M. R. Islam et al., “Body-wearable beam steering antenna array for 5.2 GHz WLAN applications,” in Proc. 7th Int. Conf. Elect. Comput. Eng., 2012, pp. 447–449, doi: 10.1109/ICECE.2012.6471583.
- [66] P. Lotfi et al., “Printed endfire beam-steerable pixel antenna,” *IEEE Trans. Antennas Propag.*, vol. 65, no. 8, pp. 3913–3923, Aug. 2017, doi: 10.1109/TAP.2017.2716399.
- [67] X. Wu et al., “Printed Yagi–Uda array for on-body communication channels at 60 GHz,” *Microw. Opt. Technol. Lett.*, vol. 53, no. 12, pp. 2728–2730, Sep. 2011, doi: 10.1002/mop.26443.
- [68] X. Wu et al., “Substrate integrated waveguide Yagi–Uda antenna,” *Electron. Lett.*, vol. 46, no. 23, pp. 1541–1542, Nov. 2010, doi: 10.1049/el.2010.2558.
- [69] M. Ali et al., “Design and analysis of a wearable antenna system for wireless safety applications,” in Proc. 9th Eur. Conf. Antennas Propag., 2015, pp. 1–4.
- [70] Y. Li and M. Zhang, “Study on a cylindrical sensor network for intelligent health monitoring and prognosis,” *IEEE Access*, vol. 6, pp. 69,195–69,202, Nov. 2018, doi: 10.1109/ACCESS.2018.2880209.
- [71] N. H. Chamok et al., “A high-gain beam steering fabric-based array for body-worn wireless applications,” in Proc. IEEE Int. Symp. Antennas Propag. USNC/URSI Nat. Radio Sci. Meeting, 2015, pp. 2221–2222, doi: 10.1109/APS.2015.7305499.
- [72] A. Thielens et al., “A personal, distributed exposimeter: Procedure for design, calibration, validation, and application,” *Sensors*, vol. 16, no. 2, Jan. 2016, Art. no. 180, doi: 10.3390/s16020180.
- [73] R. Aminzadeh et al., “A multi-band body-worn distributed radio-frequency exposure meter: Design, on-body calibration and study of body morphology,” *Sensors*, vol. 18, no. 1, Jan. 2018, Art. no. 272, doi: 10.3390/s18010272.
- [74] R. Aminzadeh et al., “A multi-band body-worn distributed exposure meter for personal radio-frequency dosimetry in diffuse indoor environments,” *IEEE Sensors J.*, vol. 19, no. 16, pp. 6927–6937, Aug. 2019, doi: 10.1109/JSEN.2019.2913309.
- [75] S. J. Ambroziak et al., “Radio channel measurements in body-to-body communications in different scenarios,” in Proc. URSI Asia Pacific-Radio Sci. Conf. (URSI AP-RASC), 2016, pp. 1376–1379, doi: 10.1109/URSIAP-RASC.2016.7601348.
- [76] C. Oliveira et al., “Perspectives for the use of MIMO in dynamic body area networks,” in Proc. 7th Eur. Conf. Antennas Propag., 2013, pp. 482–486.
- [77] S. van Roy et al., “Dynamic channel modeling for multi-sensor body area networks,” *IEEE Trans. Antennas Propag.*, vol. 61, no. 4, pp. 2200–2208, Apr. 2013, doi: 10.1109/TAP.2012.2231917.
- [78] M. Marinova et al., “Diversity performance of off-body MB-OFDM UWB-MIMO,” *IEEE Trans. Antennas Propag.*, vol. 63, no. 7, pp. 3187–3197, Jul. 2015, doi: 10.1109/TAP.2015.2422353.
- [79] J. Tak et al., “A low-profile dipole array antenna with monopole-like radiation for on-body communications,” *J. Electromagn. Eng. Sci.*, vol. 15, no. 4, pp. 245–249, Oct. 2015, doi: 10.5515/JKIEES.2015.15.4.245.
- [80] International Commission on Non-Ionizing Radiation Protection, “Guidelines for limiting exposure to electromagnetic fields (100 kHz to 300 GHz),” *Health Phys.*, vol. 118, no. 5, pp. 483–524, Mar. 2020.
- [81] H. Zu et al., “Wideband and high-gain wearable antenna array with specific absorption rate suppression,” *Electronics*, vol. 10, no. 17, Aug. 2021, Art. no. 2056, doi: 10.3390/electronics10172056.
- [82] S. Lee et al., “A 60-GHz Yagi-Uda circular array antenna with omni-directional pattern for millimeter-wave WBAN applications,” in Proc. IEEE Int. Symp. Antennas Propag. USNC/URSI Nat. Radio Sci. Meeting, 2018, pp. 1699–1700, doi: 10.1109/APUSNCURSINRSM.2018.8609346.





Rajeev Bansal

The Annual Quiz

As New Zealander geophysicist Gillian Turner's book *North Pole, South Pole: The Epic Quest to Solve the Great Mystery of Earth's Magnetism* [1] shows, our planet's magnetic properties have intrigued people since ancient times. This quiz offers a quick tour of the early history of geomagnetism. It is now time to grab a pen and test your own knowledge of this fascinating subject! Google and ChatGPT are *not* allowed. The answers appear on page 116 of this issue.

- 1) The solar wind (energetic charged particles from the sun) and cosmic rays are safely deflected by Earth's...
 - a) ozone layer
 - b) magnetosphere
 - c) ionosphere
 - d) none of the above.
- 2) The sun is strongly magnetic, and (in addition to Earth), so is/are the following planet(s)...
 - a) Venus, Mars, and Mercury
 - b) Pluto
 - c) Jupiter, Saturn, Neptune, and Uranus
 - d) none of the above.
- 3) The earliest ideas on the nature of magnetism are attributed to the Greek philosopher...
 - a) Aristotle
 - b) Pythagoras
 - c) Thales
 - d) none of the above.

- 4) The earliest recorded use of the compass was in the first century AD in ...
 - a) India
 - b) China
 - c) Egypt
 - d) None of the above
- 5) Englishman Alexander Neckam, writing in the late 12th century, reported the use of a magnetic compass for navigation by European sailors. This was _____ Marco Polo's visit to China.
 - a) before
 - b) after
 - c) much later than
 - d) none of the above.
- 6) The _____ Medal of the European Geosciences Union honors the 13th-century French scholar who discovered the difference between the north and south poles of a magnet and the polarity-based magnetic attraction/repulsion.
 - a) Petrus Peregrinus
 - b) William Gilbert
 - c) Andre-Marie Ampere
 - d) none of the above.
- 7) The inclination (the "dip" of a freely suspended magnetic needle, which depends on the latitude) was described in 1581 by the English hydrographer _____.
 - a) Georg Hartmann
 - b) Robert Norman
 - c) Francis Bacon
 - d) none of the above.
- 8) The American Geophysical Union held a special session at its Spring 2000 meeting to celebrate the 400th anniversary of the publication of *De Magnete (On the Magnet)* by _____.
 - a) Wilhelm Eduard Weber
 - b) Carl Friedrich Gauss
 - c) William Gilbert
 - d) none of the above.
- 9) In the final chapter of Book I of the multivolume treatise *De Magnete*, the author presents his famous conclusion that the Earth _____.
 - a) owes its magnetism to moving charges
 - b) has a lodestone core
 - c) is a great magnet
 - d) none of the above.
- 10) The author of *De Magnete* was aware of declination (the deviation of the compass needle from the geographical north). We know now that this declination _____.
 - a) is time invariant
 - b) is location independent
 - c) varies with both time and place
 - d) none of the above.

REFERENCES

- [1] G. Turner, *North Pole, South Pole: The Epic Quest to Solve the Great Mystery of Earth's Magnetism*. New York, NY, USA: The Experiment, 2011.
- [2] R. Bansal, *From ER to E.T.: How Electromagnetic Technologies are Changing our Lives*. New York, NY, USA: Wiley-IEEE Press, 2017.

(continued on page 116)

Game of Tenures

(*Not by George R.R. Martin*)

Sema Dumanlı 

INDEPENDENCE—BUT DO I HAVE WHAT IT TAKES?

Many of us are forced to relocate in the search of a place where we can grow into independent researchers. In my case, this relocation meant reuniting with my lovely family and with the winter sun. But then again, it also meant a major economic crisis, a crunch of the local currency, a pandemic, the president's intervention in my university's domestic affairs, and major earthquakes. This is the story of my relocation to Turkiye from the United Kingdom. I constantly receive the same question from people around me: "Sema, do you regret going back?" My answer is no, and here is why.

THE BIG DECISION

Cersei Lannister famously says to Ned Stark, "When you play the game of thrones, you win or you die. There is no middle ground." However, in the game of tenures, we have a middle ground. There actually is quite an attractive alternative: joining industry and making a lot of money (which, in the eyes of the academic community, equates to affording to stay in the conference hotel). After I graduated from the University of Bristol, I joined Toshiba Research Europe, turning down a postdoc offer. And yes,

EDITOR'S NOTE

The June "Women in Engineering" column contribution is authored by Assoc. Prof. Sema Dumanlı, Boğaziçi University, Istanbul, Turkey. She describes her career journey, moving from the industry world, at Toshiba Research Europe, to founding the antennas and propagation research and biohybrid systems laboratories at her university. Many key messages and much advice are to be found through her experience. Assoc. Prof. Dumanlı is the recipient of the 2022 IEEE Antennas and Propagation Society Donald G. Dudley Jr. Undergraduate Teaching Award and a three-time recipient of the Boğaziçi University Faculty of Engineering's Excellence in Teaching Award.



Francesca Vipiana



FIGURE 1. The author meets the late Queen Elizabeth II.

for six years, I enjoyed that glamorous life. Look at me shaking the hand of the late Queen Elizabeth (Figure 1), representing Toshiba. Posh old days.

Why did I leave? I often think being a scientist is like freely traveling in time and space. You might be an archaeologist

dwelling in the past or a physicist observing the natural course of events. We researchers in the field of engineering are into the future. We imagine how the world might look in the coming years, solve the problems that have not happened yet, and simply design the future.

The need for traveling further in time was the reason why I needed to leave Toshiba. Good as it may have been, I did feel like the research I was conducting there was short-term. Being in the safe arms of a technology giant, without the need to worry about funding, was convenient, to say the least. I knew the step I was taking meant that I needed to find my own funding. To put it more frankly, I needed to convince funding agencies to support my crazy futuristic and high-risk research. I knew it, and I decided that I could rise to the challenge. Oh my, little did I know!

THE RELOCATION

I might be a bit naive at times, but as soon as I arrived in Turkiye, I realized that most of academia was also conducting short-term research that required industrial support. Some professors advised me to collaborate with industry on topics that I thought were not even short-term—they were *now*. No, I did not want to go back to square one. In addition, before me, Boğaziçi University did not have any researchers working in the area of antennas and propagation; hence, most of my first year there was spent trying to establish my lab (Figure 2) (<https://bountenna.boun.edu.tr/>).

Believe me, in the summer of 2018, I learned quite a lot about interior design, but never mind that. During this time, I used a colleague's laboratory to continue my research. I know this is common knowledge, but I cannot not say it enough: having my colleagues' support at the beginning of my journey was ever so critical (Figure 3). I would have given up multiple times if it wasn't for their support. Getting help from people who know the drill is crucial.



FIGURE 2. The author's lab when she arrived at Boğaziçi University.

REGRETS AND MISTAKES

Funding-wise, I was trying really hard, with few to no returns in my first years. First, I applied to Marie Skłodowska-Curie Actions. Let me set the scene for my non-European colleagues. In Europe, Marie Skłodowska-Curie Actions, offered by the European Commission, provide you with the smoothest relocation. I applied to the Marie Skłodowska-Curie Individual Fellowship program and got a score of 86.4%. Unfortunately, that year, the total funding was insufficient to support me. However, this actually was a good result for the first try. But here, I made my first mistake: I moved before I secured funding. I could not apply again because there was a limitation on the time spent in the host country, a requirement that slipped from my attention. My advice for young researchers: make sure you understand all the details of the funding opportunities that you intend to apply for while planning your relocation.

Learn every little detail and all the requirements about the funding programs. Know your game!

Then, I started applying for local funding in Turkiye. I got rejected for two consecutive terms. I cried and cried. Did it help? Of course, it did. I now have a “coping with rejection procedure.” I strongly urge you to create one. For me, it involves a variety of carbs, some tears, and bingeing comedy shows (all right, maybe a bit of period drama, as well) for a day or two. Then, start over. The trouble was that I didn't know what the local funding agency was after in a proposal. And the way to write a successful proposal was clearer to me once I managed a project. Now, this might seem like an infinite loop. But do not worry. Because the funding agencies are aware of this loop. That is why there are programs created only for young researchers.

Try targeted calls for proposals. Maximize your chances.



FIGURE 3. The author poses with colleagues. From left: Assistant Prof. Faik Başkaya, the author (in a Bristolian gown that cost a fortune), Prof. Günhan Dündar, and Prof. Arda Deniz Yalçınkaya.

Use them! That was my second big mistake. I jumped into the cold, cold ocean (multiple times) before practicing in a warm swimming pool.

My last, but not least, mistake was to fight fights that did not matter. I faced unfair situations, where I felt helpless. Nonetheless, I spent my energy and time on them, although the other party was offering me nothing but what the Turkish-Dutch singer Karsu was offering in one of her songs:

Let's play a game that only I can win.

And yet, I still played their game with their rules. Mistake! Now, I have my own rule: I fight only if my fight is going to have an impact on the lives of other researchers after me, too.

IT'S NOT ALL DOOM AND GLOOM

The best thing that I did since I returned to Turkiye was to apply for a European Research Council (ERC) grant. The ERC is a program by the European Commission for researchers

who have great scientific track records and excellent research proposals. The funding is intended for high-risk and high-gain projects. This was what I longed for before I left for academia. Remember, I wanted to travel far into the future. I did not get the ERC grant, but, with a similar proposal, I got the local equivalent of the ERC, which opened a great many doors for me. I am really glad that during my first years, I did not fall into the trap of losing hope.

Always remember why you are here. Stick to the plans of that kid who dreamed of being a curious scientist!

I have always considered my years in industry as a great eye-opener. I have not only learned to be an engineer but also to approach daily life from a different perspective. Patenting was one of those habits that I got from industry. Therefore, when I came up with the idea that was also behind my

ERC proposal, the first thing I did was patent it. To my surprise, a couple of years later, some unpleasant things happened, and my patent application came in handy. This had never happened to me before, and chances are it won't happen to you either, but hey, better safe than sorry.

Don't forget to patent your ideas!

Another amazing thing in my life is the IEEE Antennas and Propagation Society (AP-S). I have always felt included in the AP-S. I am now chairing the IEEE AP-S/Microwave Theory and Technology Society/Electromagnetic Compatibility Society/Electron Devices Society Turkey Joint Chapter, and I am thoroughly enjoying it. Last year, I had the honor to receive one of the AP-S field awards, the Donald G. Dudley Jr. Undergraduate Teaching Award (Figure 4). Apparently, this is the reason why I was invited to write this piece. Thanks, Prof. Francesca Vipiana, for the invitation. I received my award by sharing the stage with scientists whom I greatly respect. But behind the scenes, there were two people. First, I was encouraged to apply by a fellow AP-S scientist, Prof. Qammer Abbasi, with whom I became friends over the years at antenna conferences. I always treasure my conference mates! When I asked my lifelong mentor, Prof. Özlem Aydin Çivi, for her opinion, she proposed to nominate me. I am ever so lucky to have had her by my side all these years. She is thoroughly inspirational.

Enjoy being part of a community and getting support from fellow scientists.

Finally, you have to be prepared to face local problems. Especially if you are relocating to a new country, you are bound to be surprised (let's hope it will happen in a positive way). For me, the biggest surprise was the constant decline of the currency. When I secure a certain amount of funding in local currency, by the time the sum is transferred to the university accounts, it's halved in terms of its real value. This seemed like a huge problem at



FIGURE 4. The author poses with the Donald G. Dudley Jr. Undergraduate Teaching Award.



FIGURE 5. The author and her team at Boğaziçi University.

first. Then I thought, there are people who have been there and who have done that, right? I started asking around and learned little hacks. For example, although we are obliged to propose our budgets in the local currency, we can submit proforma in euros and dollars and then demand the difference from the research council when the

time comes. How would I know? Whenever I panic, I remind myself:

People have been there and done that; I am not alone.

Five years have passed, and now I am an associate professor with a great



FIGURE 6. The author poses in her anechoic chamber.

team (Figure 5), a laboratory with all the equipment I need (Figure 6), loads of funding, and great collaborators, like Prof. Urartu Şafak Şeker, whose wisdom is invaluable to me. Have I settled down? Yes. Should I settle down? I am not sure. As I was saying, I often think being a scientist is like freely traveling in time and space. I can't give up my space travel. Don't you think?

AUTHOR INFORMATION

Sema Dumanlı (sema.dumanli@boun.edu.tr) is an associate professor at Boğaziçi University, Istanbul 34342 Turkey, where she founded and directs the BOUNtenna Antennas and Propagation Research Laboratory and AntennAlive Biohybrid Systems Laboratory.



MEETINGS & SYMPOSIA

(continued from page 83)

2024 USNC-URSI NATIONAL RADIO SCIENCE MEETING (NRSM 2024)

9–13 January 2024, Boulder, CO, USA. (Papers and abstracts including papers for Student Paper Competition: 27 September 2023). Contacts: Technical Program: Sembiam R. Rengarajan, Department of Electrical and Computer Engineering, California State University, Northridge, CA 91330-8346 USA. +1 818 677 3571, e-mail: srengarajan@csun.edu. Michael H. Newkirk, Johns Hopkins University Applied Physics Laboratory, Laurel, MD 20723 USA. +1 240 228 6976, e-mail: michael.newkirk@jhuapl.edu. Conference Logistics: Christina

Patarino, CCEP, CU Conference Services, University of Colorado Boulder, 454 UCB, Boulder, CO 80309, USA. +1 303 492 5151, fax: +1 303 492 5959, e-mail: christina.patarino@colorado.edu. <http://www.nrsmboulder.org>.

IEEE RADIO AND WIRELESS WEEK 2024 (RWW 2024)

21–24 January 2024, San Antonio, TX, USA. (Papers: 25 July 2023). Elsie Vega, IEEE MCE, 445 Hoes Lane, Piscataway, NJ 08854 USA. +1 732 981 3428, e-mail: elsie.vega@ieee.org. <http://radiowirelessweek.org>.



Innovation, a Skewed Balance Between Old and New—Lessons From My Journey to Compressive Antenna Arrays

Heinrich Edgar Arnold Laue 

Participating in local science fairs was a highlight of my school years, teaching me about scientific investigation and discovery from a young age. A design-focused project greatly influenced my decision to pursue a career in engineering, and I only recently started appreciating the link between my experience at science fairs and my present passion for research, writing, and public speaking.

My biggest challenge during science fairs was coming up with an idea for a project. I always wanted to come up with my own idea and refused to simply repeat an existing experiment. I mostly had no idea where to start and would spend not only days and weeks but months trying to come up with a topic. The problem, I suspect, was that I was trying to pull new ideas out of thin air. I should probably have spent more time reading scientific literature than scouring the depths of my own mind.

When conducting research, you are faced with a similar challenge of coming up with new hypotheses and making new discoveries. More generally, innovation—coming up with an idea for a



EDITOR'S NOTE

In this issue of *IEEE Antennas and Propagation Magazine*, Dr. Heinrich Edgar Arnold Laue contributes an interesting article on the topic of innovation as a balance between novelty and conventionality. Dr. Laue is one of the 2022 IEEE Antennas and Propagation Society (AP-S) Young Professional Ambassadors as well as serving as the Students and Young Professionals Coordinator for the IEEE South Africa AP/MTT/EMC Joint Chapter. This article looks into a practical approach for introducing new ideas into a conventional domain, leading to innovation. It is a must-read for all young researchers on how to innovate and make an impact.

We have many more exciting articles planned for this column in future issues. Anyone who would like to contribute to the "Young Professionals" column or has any suggestions on topics of interest may contact me at cjreddy@ieee.org. Follow us on LinkedIn, at <https://www.linkedin.com/company/ieee-aps-yp>, for the latest updates and events that are of interest to AP-S Young Professionals.



C.J. Reddy

business or a product, for example—requires some form of novelty.

But how are new ideas generated? Theories of creativity, the study of how innovation works, indicate that innovation happens when existing ideas are combined in new ways [1], [2], [3]. New ideas grow not simply from existing ones but from existing ideas brought together in new ways. If I knew this earlier, I would probably have approached my search for science fair topics differently.

Economist Martin Weitzman [3] likens innovation to the cultivation of new botanical varieties from old ones. We often talk of the cross-pollination of ideas, which turns out to be a perfect analogy—existing ideas coming together to breed new ones.

However, Weitzman points out that with the vast amounts of knowledge available today, the challenge lies not primarily in finding new ways of combining ideas but rather in identifying those combinations that are

actually useful. He quotes the famous mathematician, physicist, and philosopher Henri Poincaré [3], who said the following in the context of mathematical creativity:

To create consists precisely in not making useless combinations and in making those which are useful and which are only a small minority. Invention is discernment, choice. ... Among chosen combinations the most fertile will often be those formed of elements drawn from domains which are far apart. Not that I mean as sufficing for invention the bringing together of objects as disparate as possible. Most combinations so formed would be entirely sterile. But certain among them, very rare, are the most fruitful of all. ... The true work of the inventor consists in choosing among these combinations so as to eliminate the useless ones or rather to avoid the trouble of making them, and the rules which must guide this choice are extremely fine and delicate.

What are these delicate guiding principles that Poincaré speaks of that can maximize our chances of finding useful combinations of ideas? One possible guiding principle is to understand the balance between novelty and conventionality that is required for innovation. Novel combinations can be defined as ideas “drawn from domains which are far apart,” whereas conventional combinations stick to closely related domains as per the established convention. Having only novel combinations of ideas will clearly not suffice as you will end up with a mixed bag of mostly “sterile” combinations. On the other hand, sticking only to ideas that are conventionally considered closely related will prevent you from discovering the “most fertile” combinations.

The most useful ideas will often proceed from a careful balance between novelty and conventionality, from exploring foreign lands yet staying close to home. Getting this balance just right greatly increases your

chances of making not only discoveries but impactful ones.

BALANCING NOVELTY AND CONVENTIONALITY

In 2013, a sociologist, an economist, and two data scientists, Uzzi et al. [1], came together to investigate how conventionality and novelty must be balanced to generate high-impact, i.e., highly cited, scientific research.

They found that high-impact articles are highly conventional yet with a dash of completely unexpected novelty. In other words, articles that tend to be cited often are firmly rooted in convention with a hint of something completely new and unexpected.

To determine this, they considered the pairwise combinations of all of the references in a particular article. They would take two references and determine how often their respective journals appear together in the wider literature. Journals that are cited together often are considered a conventional pairing. Think, for example, of the closely related *IEEE Transactions on Antennas and Propagation* (TAP) [4] and *IEEE Transactions on Microwave Theory and Techniques* [5]. Journals that are not cited together often (e.g., TAP and *Life Sciences*) are considered a novel pairing. In this way, the combination of sources in an article was used as a proxy for the combination of ideas that informed the findings of the article.

The highest impact articles had overwhelmingly conventional combinations of sources and yet a few highly unconventional combinations. Such articles had almost twice the probability of being highly cited or high-impact articles [1].

In line with Poincaré’s observations, balancing novelty and conventionality in practice turns out to be quite challenging. Instead of novelty and conventionality bearing equal weight, the optimal balance is heavily skewed toward conventionality. Imagine not simply an acrobat walking a tightrope but a tightrope walker with an exceedingly heavy load on one end of his balance pole.

In the remainder of the article, we will consider a practical approach to achieving this balance for high-impact innovation. We will then briefly consider the novel field of compressive antenna arrays as an example. Finally, we will consider some more personal applications and see how being both a specialist and a generalist can benefit your career.

AN APPROACH FOR HIGH-IMPACT INNOVATION

Figure 1 presents an approach to balancing novelty and conventionality to maximize your chances of discovering useful new ideas. Let us consider each of these points in more detail.

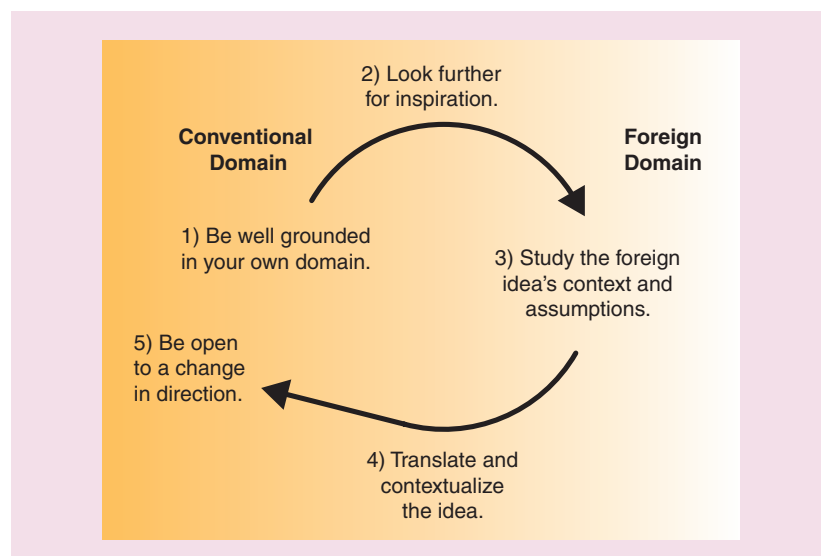


FIGURE 1. The proposed methodology for high-impact innovation.

BE WELL GROUNDED IN YOUR OWN DOMAIN

As the adage goes, you need to learn the rules before you can break them. Before you can start taking inspiration from other domains, you need to be well grounded in your own.

The obvious scenario is where you are making contributions in your own specialty. Clearly, you need to master the fundamentals of your own discipline before making any kind of novel contribution. The less obvious scenario is the converse, where you wish to apply an idea from your domain to a foreign domain, especially if you are not an expert in that other domain. In that case, you will need to first spend a significant amount of time mastering the fundamentals of the foreign domain. Alternatively, you can collaborate with an expert in that field. Remember the skewed balance toward conventionality—it is much easier to apply a foreign idea to your own domain than to apply an idea from your domain to someone else's.

For example, making contributions to the field of antennas requires a solid understanding of the conventional properties of antennas, such as gain, directivity, return loss, sidelobe level (SLL), etc. You can easily take inspiration from the most obscure source, for example, something you see in nature, and still design a new antenna that is measurably better in conventional terms. But imagine a biologist trying to design an antenna without extensive training in electromagnetics—that is a different story.

LOOK FURTHER FOR INSPIRATION

As you bury yourself deeply in your own domain, don't forget to look up! Be curious about other domains and look further for inspiration. Do you see how difficult this balance is, how novelty and conventionality want to pull you in seemingly opposite directions?

I believe that the best way to look further is to develop a general curiosity. In practical terms, this could mean reading more widely—not necessarily just journal articles but even high-quality journalism can broaden your horizons. (This is how I discovered several of the sources in this article!) Going even

further, you could find inspiration in nature or the arts. Biomimicry is an obvious example here. Even more profoundly, first-hand accounts tell of Einstein finding inspiration in music not only as a distraction but possibly even as an integral part of his intuition into physics [2].

In terms of your social and professional networks, do not restrict yourself to your own specialization but have a wide range of acquaintances from different specialties, and you might pick up something interesting.

Again, there is no restriction in terms of where you find inspiration. Clearly, there is no guarantee that you will find inspiration for antenna design while reading a book on politics, but do not make that the point. Simply develop a general curiosity for things both technical and nontechnical, and you will be well positioned to catch inspiration when it passes you by.

STUDY THE FOREIGN IDEA'S CONTEXT AND ASSUMPTIONS

When you find an idea in a foreign domain that you want to apply in your own domain, study its context and assumptions. The level to which you will need to master that topic will differ, but the key is to have a deep enough knowledge to identify the assumptions that might not hold in your own domain. The challenge is that such assumptions may be regarded as almost self-evident in the foreign domain, and you might have to delve quite deeply to uncover them. An example of such a scenario is discussed in the case study on compressive antenna arrays to follow.

TRANSLATE AND CONTEXTUALIZE THE IDEA

Once you have identified a foreign idea to apply to your domain, properly taking its context and assumptions into account, the next step is to translate that idea to your domain.

Recognize that there may be differences in terminology. Perhaps this idea has already been tried in your domain, only under a different name. Or perhaps something better already exists!

One of the most important steps is to contextualize the idea in your domain. Contextualization in this case means

linking your idea to the existing body of knowledge—helping your idea find a home. If it feels like there is nothing else to compare your idea to, you have likely not developed the idea enough yet. Ultimately, you will have to find something to compare to in order to demonstrate why your idea is superior. In particular, you need to make use of the conventional performance measures you identified in step one because they might differ from those of the foreign domain.

BE OPEN TO A CHANGE IN DIRECTION

When you have studied the foreign idea with its context and assumptions, translated it to your domain, contextualized it, and established any differences in performance measures, then you can finally apply the new idea to the old domain.

Initially, you may have all sorts of lofty ideas, but they may not all turn out as expected. The real insight and the real contribution might be something completely different from what you had expected, and it might turn out that your idea from the other domain was nothing more than a fresh perspective that led to a new insight. If this happens, don't hold on too strongly to your initial ideas, but be open to a change in direction. An incremental but real contribution is much more useful than a big but naive idea.

The key to balancing novelty and conventionality is to apply the correct weight to each. While you need to be rigorous with your conventionality, you need to be flexible with your novelty. Hold conventionality firmly in your left hand and novelty loosely in your right. Maintain the discipline and rigor of conventionality and the childlike curiosity of novelty. They are not mutually exclusive but complimentary.

A JOURNEY TO COMPRESSIVE ANTENNA ARRAYS

I learned many of these lessons from my journey to the field of compressive antenna arrays. When I first started looking at the topic, the field was little more than the suggestion to apply the sub-Nyquist sampling scheme called *compressive sensing (CS)* from signal processing to antenna arrays. While there are many other applications of CS

in electromagnetics, compressive arrays specifically look at reducing the number of samples/signals in an antenna array. Figure 2 shows a recent example of a prototype compressive array with four antenna elements and two outputs or subarrays [6].

Following the aforementioned outline, I first had to be well grounded in my own domain and understand antenna arrays in conventional terms. I had to understand that antenna arrays are traditionally designed based on measures like gain, beamwidth, SLL, and steering range before even considering the performance measures of a particular application, like direction finding, for example.

Second, I looked further to the foreign idea of CS for inspiration. I was lucky because the idea of applying CS to antenna arrays had already been proposed.

Third, I studied the context and assumptions behind CS. I needed to develop a working knowledge of CS [7]. Delving into the derivations of CS, I discovered that some of the fundamental theorems rely on the assumption of a large number of samples, which clearly did not apply to antenna arrays, which often have small numbers of elements [8]. This meant that the standard random sampling scheme, where you weigh and combine samples with random Gaussian compression weights, would not work for moderately sized antenna arrays.

Fourth, I had to translate and contextualize the idea of a compressive sampling process to antenna arrays.

By carefully comparing CS and antenna arrays, I realized that, under the right conditions, the concept of coherence in CS translates to SLL in antenna arrays. This allowed me to adapt a coherence-optimization algorithm to minimize SLL in compressive arrays [9]. I could now design compressive arrays with my newly developed SLL-minimization algorithm.

To contextualize the idea, I searched extensively for conventional antenna arrays to compare my new designs to. I ended up realizing that a compressive array is, in fact, a type of subarray

system where an overlapped feed network is used to weigh and combine antenna-element signals [10]. Suddenly, I had a host of conventional techniques to compare to!

Finally, I had to be open to a change in direction. When the process of translation had been completed, very few of my original CS ideas remained, but what did remain was a disruption to the conventional way of thinking. Traditionally, subarrays are designed based on particular feed-network layouts, where the approach is essentially to start with the hardware and see what performance you can get. But the lack of hardware constraints in CS, which allows random and therefore arbitrary compression weights, inspired me to remove all hardware constraints when minimizing SLL and consider hardware implementation only at the very end. This led to a new overlapped feed-network architecture with increased design freedom that opened the door to novel array designs while still allowing fair comparisons to be made to existing techniques [6], [11].

DISCUSSION AND CONCLUSION

The broader question when it comes to your career is whether you should be a specialist with a deep focus or a generalist with a broad outlook. The findings of Uzzi et al. [1] hint toward the fact that the

answer is not either/or but rather a careful balance of both. They note that there may be “advantages to being within the mainstream of a research trajectory, ... while being distinctive in one’s creativity”.

Some of the most influential people in history have had multiple interests. These jacks-of-all-trades have always been around with names varying across history. Author Michael Simmons [12] gives an insightful overview of this concept of polymathy, noting how, in generations past, we have had:

- philosopher kings such as Aristotle
- Renaissance men such as Leonardo da Vinci
- gentleman scholars such as Benjamin Franklin
- polymaths such as Isaac Newton
- modern polymaths such as Steve Jobs.

In terms of modern polymaths, think of the founders of some of the world’s largest companies. Simmons notes that Bill Gates, Steve Jobs, Warren Buffett, Larry Page, and Jeff Bezos have all been described as polymaths.

He offers a view of modern polymathy as being T-shaped. In other words, you specialize deeply in one domain and yet have a working knowledge across a broad range of disciplines. He draws on a powerful aid, the Pareto principle—a rule of thumb that states that 80% of something’s output is typically a result of only 20% of the input. For example, it

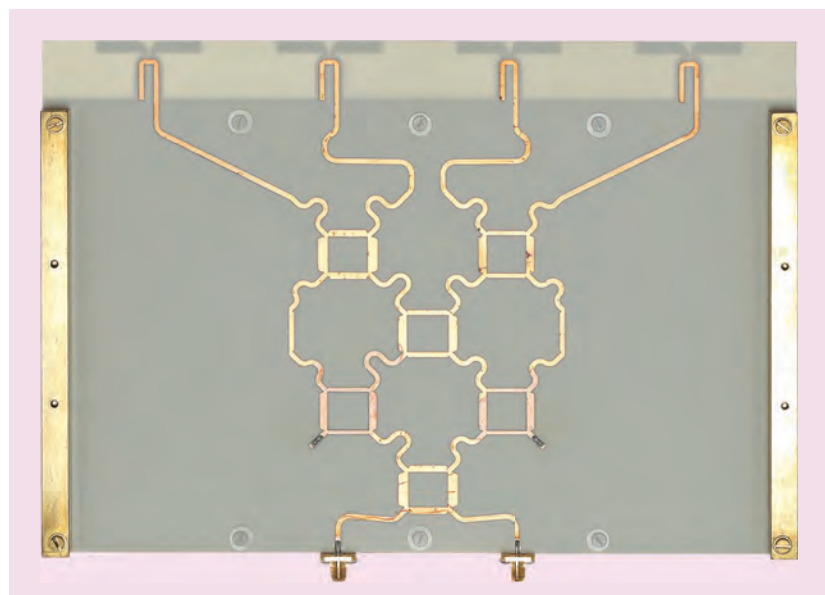


FIGURE 2. A prototype compressive array. (Source: Taken from [6].)

will take you a lifetime to become a master in a topic, but within a week, you can have a better working knowledge of that topic than most people.

One can see how such a T-shaped polymathy fits within the conclusions of Uzzi et al. [1]. Deep specialization in one field with a dash of inspiration from a completely different one assumes that you have some working knowledge of the foreign domain you are getting inspiration from.

Ironically, Benjamin Jones [13], one of the coauthors of Uzzi et al. [1], spoke of “the burden of knowledge and the death of the Renaissance man,” referring to the idea that as the store of human knowledge increases, an increasingly large burden of education falls on each successive generation, necessitating ever greater specialization. And yet, with Uzzi, he showed that both breadth and depth is required for innovation.

It turns out that the idea of modern polymathy is somewhat controversial, with some arguing that the burden of knowledge will eventually make it virtually impossible to become an expert in multiple domains [2]. However, making significant contributions to multiple disciplines, as Renaissance men like

Leonardo da Vinci and polymaths like Henri Poincaré did, is not the only form of polymathy. This T-shaped model of polymathy, for example, where you are an expert in one domain and an amateur in multiple others, is not inconsistent with the trend in increasing specialization [2]. Another form of polymathy is sequential polymathy, where you dedicate different periods in your life to different disciplines. These broader views of polymathy include many gifted individuals from history as examples [2].

My challenge to you is to cultivate a general curiosity and to realize that everything has the potential to be interesting even if it is outside of your current specialization. If you find yourself in a place of deep specialization and are frustrated with the lack of diversity, don't despair. Being a specialist does not mean that you cannot also be a generalist. Keep specializing, but also, keep exploring elsewhere—read widely, have obscure hobbies, and make diverse friends. Having a broad range of interests, even as a specialist, may just lead to your greatest breakthroughs.

AUTHOR INFORMATION

Heinrich Edgar Arnold Laue (hlaue@ieee.org) is a communications engineer

with the Namibia Water Corporation Ltd, Windhoek, Namibia. He is the Students and Young Professionals Coordinator for the IEEE South Africa AP/MTT/EMC Joint Chapter and served as a 2022 IEEE Antennas and Propagation Society Young Professional Ambassador. He is a Member of IEEE.

REFERENCES

- [1] B. Uzzi, S. Mukherjee, M. Stringer, and B. Jones, “Atypical combinations and scientific impact,” *Science*, vol. 342, no. 6157, pp. 468–472, Oct. 2013, doi: 10.1126/science.1240474.
- [2] R. Root-Bernstein, “Multiple giftedness in adults: The case of polymaths,” in *International Handbook on Giftedness*, L. V. Shavinina, Ed. New York, NY, USA: Springer, 2009, ch. 42, pp. 853–870.
- [3] M. L. Weitzman, “Recombinant growth,” *Quart. J. Econ.*, vol. 113, no. 2, pp. 331–360, May 1998, doi: 10.1162/00355398555595.
- [4] *IEEE Trans. Antennas Propag.* [Online]. Available: <https://ieeexplore.ieee.org/xpl/RecentIssue.jsp?punumber=8>
- [5] *IEEE Trans. Microw. Theory Techn.* [Online]. Available: <https://ieeexplore.ieee.org/xpl/RecentIssue.jsp?punumber=22>
- [6] H. E. A. Laue and W. P. du Plessis, “Design and analysis of a proof-of-concept checkerboard-network compressive array,” *IEEE Trans. Antennas Propag.*, vol. 70, no. 9, pp. 7546–7555, Sep. 2022, doi: 10.1109/TAP.2022.3188531.
- [7] H. E. A. Laue, “Demystifying compressive sensing [Lecture Notes],” *IEEE Signal Process. Mag.*, vol. 34, no. 4, pp. 171–176, Jul. 2017, doi: 10.1109/MSP.2017.2693649.
- [8] H. E. A. Laue and W. P. du Plessis, “Compressive direction-finding antenna array,” in *Proc. IEEE-APS Topical Conf. Antennas Propag. Wireless Commun. (APWC)*, Cairns, QLD, Australia, Sep. 19–23, 2016, pp. 158–161, doi: 10.1109/APWC.2016.7738145.
- [9] H. E. A. Laue and W. P. du Plessis, “A coherence-based algorithm for optimizing rank-1 Grassmannian codebooks,” *IEEE Signal Process. Lett.*, vol. 24, no. 6, pp. 823–827, Jun. 2017, doi: 10.1109/LSP.2017.2690466.
- [10] H. E. A. Laue and W. P. du Plessis, “Numerical optimization of compressive array feed networks,” *IEEE Trans. Antennas Propag.*, vol. 66, no. 7, pp. 3432–3440, Jul. 2018, doi: 10.1109/TAP.2018.2829834.
- [11] H. E. A. Laue and W. P. du Plessis, “A checkerboard network for implementing arbitrary overlapped feed networks,” *IEEE Trans. Microw. Theory Techn.*, vol. 67, no. 11, pp. 4632–4640, Nov. 2019, doi: 10.1109/TMTT.2019.2940223.
- [12] M. Simmons, “People who have ‘too many interests’ are more likely to be successful according to research,” Observer Media, New York, NY, USA, Apr. 2018. [Online]. Available: <https://observer.com/2018/05/people-with-too-many-interests-more-likely-successful-polymath-entrepreneurship-antifragile/>
- [13] B. F. Jones, “The burden of knowledge and the death of the Renaissance man: Is innovation getting harder?” *Rev. Econ. Stud.*, vol. 76, no. 1, pp. 283–317, Jan. 2009, doi: 10.1111/j.1467-937X.2008.00531.x.

Are You Moving?

Don't miss an issue of this magazine—update your contact information now!

Update your information by:

E-MAIL: address-change@ieee.org
PHONE: +1 800 678 4333 in the United States
or +1 732 981 0060 outside
the United States

If you require additional assistance regarding your IEEE mailings, visit the IEEE Support Center at supportcenter.ieee.org.

IEEE publication labels are printed six to eight weeks in advance of the shipment date, so please allow sufficient time for your publications to arrive at your new address.



IEEE Antenna Measurements Committee Events

ANTENNA MEASUREMENTS COMMITTEE

Committee Co-Chair: Debatosh Guha^{ID}

IEEE ANTENNA MEASUREMENTS COMMITTEE EVENTS IN ASSOCIATION WITH IEEE MAPCON 2022, THE LEELA BHARTIYA CITY, BANGALORE, INDIA, 12–15 DECEMBER 2022

The IEEE Technical Committee on Antenna Measurements, jointly with the IEEE Microwave, Antennas, and Propagation Conference (MAP-Con) 2022, organized two technical events with two specific objectives. The activities of 12 December were dedicated to preconference workshops in the conference venue. A full-day “Workshop on Fundamentals of Antenna Measurement” was held at the Varuna Hall from 8.30 a.m. to 5.30 p.m. It created enormous interest among the young scientists, researchers, and students. Although it was initially planned to cater to a maximum of 20 IEEE Antennas and Propagation Society (AP-S) members and student members, eventually, it turned out to include around 58, nearly three times our target (Figure 1). Most of the participants were IEEE AP-S members. Indeed, the workshop covered antenna measurement principles, laboratory



FIGURE 1. Group photo: workshop participants with the technical instructors.



FIGURE 2. Workshop participants, volunteers, and delegates with IEEE President-Elect Prof. Saifur Rahman (sitting: second from the left) and IEEE AP-S President-Elect Prof. Stefano Maci (standing: seventh from the left).

setup, and associated instrumentations in three consecutive sessions, each of a 2-h duration. Senior engineers from Anritsu India Pvt. Ltd. took the major

roles as instructors. All participants were served a buffet lunch and sufficient refreshments over the whole day. Out-of-town AP-S student members

were provided free accommodations, and a selected group of them was supported to and from travel by train or bus. The event was coordinated by Puneet Mishra, the general chair of MAPCon, and Debi Dutta, an IEEE AP-S volunteer. IEEE AP-S President-Elect Prof. Stefano Maci and Antenna Measurements Committee Chair Prof. Debashish Guha were present during the event (Figure 2).

A special session exclusively on antenna measurement facilities and modern requirements was organized on 14 December, the third day of the conference. Prof. Sungtek Kahng, Incheon National University, Republic of Korea, gave the keynote address, titled "Development and Antenna Measurement of Millimeter-Wave

Metamaterials for 5G Mobile and Satellite Communication Systems," which was followed by four technical presentations by Dor Yahalom of MVG Sadanand Bhatt of Anritsu; Caner Özdemir of Diamond Microwave Chambers, USA; and Marwin Coutinho of Rohde & Schwarz. Some short presentations on state-of-the-art measurement techniques were delivered by industry experts from JV Micronics, SABIK, Albatross, Altair, and Airbus. The session started at 8.30 a.m. and continued for 2 h, and it was attended by nearly 70 participants. Each talk was followed by inquisitive and thoughtful discussions. This session was conducted by IEEE AP-S Antenna Measurements Committee Co-Chair Prof. Debashish Guha.



Please click the link for contact details for the AP-S Measurements Committee chair.

ACKNOWLEDGMENT

This article has supplementary downloadable material available at <https://doi.org/10.1109/MAP.2023.3262102>, provided by the authors.



TAP. CONNECT. NETWORK. SHARE.



Connect to IEEE—no matter where you are—with the IEEE App.



Stay up-to-date
with the latest news



Schedule, manage, or
join meetups virtually



Get geo and interest-based
recommendations



Read and download
your IEEE magazines



Create a personalized
experience



Locate IEEE members by location,
interests, and affiliations

Download Today!



Remembering Ross Stone

With great sorrow and a profound sense of loss, we have learned of the passing of Ross Stone, the founding editor of our magazine.

With more than 45 years of experience in the field, Ross was a pillar and a model for many of us. Over his long professional life he impacted industry, consulting, and research in antennas, propagation, and related technologies. He served this journal for over 30 years as the magazine founding editor-in-chief. A generous volunteer, he was very active in several scientific and technical societies, and for over 20 years he was the editor of the *Radio Science Bulletin* of the International Union of Radio Science (URSI). Ross was also very sensitive to the needs of young scientists and was committed to serve and educate the next generation of students and engineers, and he was always happy to help them and share his words of wisdom.

Ross Stone was born on 26 August 1947 in San Diego, California, USA. He graduated in 1963 at age 16 with academic distinction from Crawford High School in San Diego. In the same year, he received “Received Honors at Entrance” to San Diego State University, and two years later he entered the University of California, San Diego (UCSD). In 1967, Ross received a BA in geophysics at age 19; he was one of seven to graduate in the first UCSD graduating class. After leaving his studies for three years, during which he was a physicist



Ross Stone (26 August 1947–29 March 2023).

at Gulf Energy and Environmental Systems, La Jolla, California, he earned an M.Sc. in applied physics in 1973 and, during his activity as senior scientist at Megatek Corporation in San Diego, he earned his Ph.D. in applied physics in 1978 with a thesis entitled “The Concept, Design, and Operation of a Demonstration Holographic Radio Camera.”

From 1976 to today, Ross was the president of his company, Stoneware Limited, engaged in consulting and contract management, research, analysis, engineering, development, and testing for government agencies and industry. Ross managed to run his company since he was 28 years old, together with other professional activities. From 1969 to 1970 and from 1970 to 1972 he was physicist and senior physicist, respectively, in the Radiation Technology Division, Gulf Energy and Environmental Systems, La Jolla. He did research in

the theory of field generation and propagation in plasmas and other dispersive media, antennas, field generation by charge transport, space-charge limiting, coupling to complex transmission lines, and radiation effects on materials. From June 1972 to August 1973 he was with the Engineering Division, Gulf General Atomic, La Jolla, California, with activity in assessment, specification, design, coding, and implementation of three major computer management information systems, for forecasting, budgeting, manufacturing, engineering, and personnel information, for a division of 435 employees. From August 1973 to May 1980 he was senior scientist at Megatek Corporation, San Diego. There, he was a program manager for Megavision, a Megatek entity that provided true 3D stereoscopic viewing of computer graphics and video displays. From May 1980 to November 1987 he was research advisor at the IRT Corporation, San Diego, with the activity of senior scientific advisor, consultant, and “information broker.” From September 1989 to July 1990 Ross was chief scientist of McDonnell Douglas Technologies Inc., a 440-employee subsidiary of McDonnell Douglas Corp. There, he directed technical work of over 250 scientists and engineers and was in charge of a US\$7 million internal R&D program, with full budgetary authority and responsibility, with over 17 principal investigators. From October 1990 to April 1992 he was a chief scientist at Expersoft Corporation, a company providing leading-edge products and services utilizing new

knowledge-engineering and reasoning techniques in the defense, agricultural, publishing, and training fields. He was part of corporate senior management and responsible for providing technical leadership in all business areas.

From May 1992 to January 1998 he was executive director of the Fund for International Scientific Interchange, a private benevolent fund primarily offering scholarships to people working in telecommunications in other countries to study in United States universities and, upon returning to their home countries, to improve telecommunications there. He organized and directed all aspects of the fund and scholarships provided by it, including complete financial responsibility and management of business operations, international relations, legal aspects, relationships with over 15 universities, and coordination of educational programs for over 35 foreign scholars. He represented the fund to leaders in telecommunications in over 40 countries, at all levels, from technicians to directors general of operating companies and deputy ministers of telecommunications. He organized and led 14 international workshops on telecommunications, with over 35 invited foreign technical experts from over 24 countries (topics covered all aspects of telecommunications, including switching, networks, outside plant, cellular and wireless, data communications, and satellite systems).

Ross was the inventor of the holographic radio camera: at the Prague General Assembly of URSI, which was the first opportunity the Russians working in this area had to really meet their Western counterparts, they told him that it was his dissertation on the holographic radio camera (which they obtained through University Microfilms) that led them to do all of the ionospheric tomography research. He had substantial research interests in electromagnetic compatibility (EMC) and electromagnetic pulse (EMP) measurements on loops and wire antennas, as well as in computational electromagnetics. He carried out analysis and modeling to assess EMP vulnerability and survivability of several army, air force, and navy strategic and

This newsletter was the precursor of *IEEE Antennas and Propagation Magazine* that he founded in 1990, becoming its first and founding editor-in-chief, and which he served continuously for over 30 years.

tactical systems. Ross developed comprehensive models for predicting probability of detection and carried out system design for vehicles employing active and passive observables control. He carried out studies on contour determination of parabolic antennas, design of an experiment and analysis of the resulting data to measure coherence of laser propagation through clouds, and analysis of a very low frequency/extremely low frequency surface-wave radar for targets submerged in sea water. He did extensive systems analysis work; research in optical and electromagnetic propagation; and system design, development, documentation, and experimental verification of an optical heterodyne communications system, employing reciprocal pointing and tracking. He developed computer models of optical propagation and of an optical communication system involving an over-the-horizon scatter channel, and employed these models to interpret experimental results. His research activity has been published in more than 100 papers in scientific journals.

Ross was editor of several books. In 1982 he edited *New Methods for Optical, Quasi-Optical, Acoustic, and Electromagnetic Synthesis* (Proceedings Society of PhotoOptical Instrumentation Engineers 294, Bellingham, WA, Society of PhotoOptical Instrumentation Engineers; in 1989, he edited *Radar Cross Sections of Complex Objects* (Piscataway, NJ, IEEE Press). From 1990 to 2002, he edited four books entitled *The Review of Radio Science* (1990–1992 and 1993–1996, published by Oxford University Press, in 1993 and 1996, respectively; 1996–1999 and 1999–2002, published by New York, Wiley/IEEE, in 1999 and 2002, respectively).

From 2001 to the time of his passing, he was editor of the *Radio Science Bulletin*, a peer-reviewed archival publication of URSI. From 1984 to 1990 he was editor of the *IEEE Antennas and Propagation Society Newsletter*, publishing 60 to 80 pages every two months to an international readership of 8,000; this newsletter was the pre-

cursor of *IEEE Antennas and Propagation Magazine* that he founded in 1990, becoming its first and founding editor-in-chief, and which he served continuously for over 30 years.

Ross was an IEEE Fellow for “Contributions to the fields of inverse problems and computational electromagnetics,” a fellow of the Chinese Institute of Electronics (one of fewer than a dozen foreign fellows at the time of election), and a fellow of the Electromagnetics Academy. He was a recipient of the IEEE Third Millennium Medal and one of the few Distinguished Service Award recipients from the IEEE Antennas and Propagation Society (AP-S). He was an Honorary Life Member of the AP-S Administrative Committee (AdCom). He was a recipient of an award for supporting the International Symposium on Antennas and Propagation, and a recipient of the Society for Technical Communication Award of Distinguished Technical Communication as editor-in-chief of *IEEE Antennas and Propagation Magazine*. He has been an adjunct professor of Beijing Jiaotong University, Beijing, China. In 2015, he was recipient of the European Association on Antennas and Propagation (EurAAP) Award “for outstanding achievements in the field of antennas and for establishing and improving the relationships among Europe and USA in antennas and propagation.”

In recent news, he won the 2023 IEEE Richard M. Emberson Award, for distinguished service advancing the technical objectives of IEEE. The citation “For sustained contributions to and impactful leadership in the IEEE Technical Activities publication enterprise” well synthesizes his service.

He probably didn't have the pleasure to know about this award.

For his extraordinary capability in promoting new initiatives, Ross was a key person in the international communities for establishing and structuring large international societies and networks. He was extremely active in IEEE, URSI, and EurAAP. Concerning IEEE, he was a board member from 2005 to 2011 of the IEEE Publications Services and Products Board (PSPB), setting policy for and overseeing all IEEE publications; he was chair from 2007 to 2009 of the IEEE Technical Activities Board (TAB) Newsletters Committee, and a member of the IEEE Periodicals Committee and Periodicals Review Committee. From 2005 to 2007 he was a member of the IEEE TAB/PSPB Products and Services Committee, setting policy for and overseeing business aspects of all IEEE publications. He was a member and recently chair of the IEEE Press Liaison Committee of AP-S. Due to his outstanding service in AP-S, he was nominated as an honorary life member of AP-S AdCom.

Concerning URSI, he was a member of United States National Committee (USNC)-URSI, where he served as publication coordinator, and a delegate of commissions A, B, E, F, and G from the National Academy of Sciences from the XIX to the XXIX General Assemblies of URSI. He was a member of USNC-URSI Commissions A, B, E, F, and G. For 30 years, starting from 1993, he was chair of the URSI Standing Committee on Publications. He was also chair of the Committee for Revision of the URSI Statutes and a member of the URSI Long-Range Planning Committee. From 2001 to present he was assistant secretary general for publications of URSI.

Concerning EurAAP, he was since 2008 the AP-S representative in the Delegate Assembly of EurAAP, and since 2008 on the Board of the European School of Antennas and Propagation (ESoA). In this role, he promoted several initiatives in ESoA, playing a key role in establishing the ESoA courses in China. In the last six years of his life he was a member of the Board of Directors of EurAAP.

Ross was also a senior member of the Society for Technical Communications,

For his extraordinary capability in promoting new initiatives, Ross was a key person in the international communities for establishing and structuring large international societies and networks.

a life member of the Society of Exploration Geophysicists, and a member of the Society of Professional Journalists, the Association of Computing Machinery, the Optical Society of America, the Acoustical Society of America, the Society of Industrial and Applied Mathematics, the Society of PhotoOptical Instrumentation Engineers, the Applied Computational Electromagnetics Society, and the American Society for Non-destructive Testing.

Ross spent his life traveling all over the world for conferences and meetings. Unfortunately, since a few years ago, his mobility became limited, but this did not prevent him from continuing to travel. In the last two years Ross' health substantially worsened, but nonetheless his commitment to AP-S and other societies was always strong until his last days. His last AP-S AdCom meeting was on 25 February 2023. The meeting was in Dubai in a time zone prohibitive for anybody in California. Despite this and his health conditions, he participated in the meeting from midnight to nine in the morning, interacting with all of the meeting members and giving, as always, sage advice.

Ross Stone passed away on 29 March 2023. Although it is hard to express how much we will miss him, the magazine, together with his colleagues and friends, would like to honor him with this in memoriam and remember the important role he had in our antennas and propagation community.

—Francesco Andriulli 

Editor in Chief of *IEEE Antennas and Propagation Magazine*

—Stefano Maci 

2023 President of the IEEE Antennas and Propagation Society (AP-S)

PERSONAL STATEMENTS AND MEMORIES BY FRIENDS AND COLLEAGUES

Mahta Moghaddam, 2020 IEEE Antennas and Propagation Society president, 2015–2019 *IEEE Antennas and Propagation Magazine* editor-in-chief:

Ross was and is the quintessential ambassador of the AP-S. His knowledge of how the society and the IEEE worked were boundless, his generosity with this time immeasurable, and the sincerity of his actions unquestionable. I observed all of these throughout the three-and-a-half decades that I had known him. This started with the time when I first met him in 1988 in Syracuse, New York, the first time that as a graduate student I attended the AP-S/URSI annual flagship conference. Ross came to my talk, and afterward he engaged in a most interesting and insightful technical discussion, providing the kind encouragement that is immensely inspiring to any graduate student. I had the honor of working closely with Ross on *IEEE Antennas and Propagation Magazine* in 2015, when he passed the baton to me as the editor-in-chief. He worked with me and Christina as we went through the process of transitioning the magazine to a new format. He spent countless hours assembling information about the magazine from his 30+ years at its helm. I experienced first-hand his collaborativeness and true care for the magazine and for the AP-S. He continued to be generous with his time during my time as *IEEE Antennas and Propagation Magazine* editor-in-chief, when he continued writing his "From the Screen of Stone" column and answering many questions I had for him about various editorial processes. He was also a pleasure to work with during the AdCom meetings, none of which he had missed in decades. We could always count on Ross to have the most accurate, contextual, and up-to-date information relevant to conducting AP-S business.

Ross, we will miss you, your kindness, and your insights. You will always be with us.

David R. Jackson:

Dear Ross,

Thank you so much for all of the wonderful service that you gave to all of us, including AP-S, EurAAP, USNC-URSI, and URSI. You set a standard for service that will always be remembered by us. Your leadership in selflessly serving the scientific communities that you were associated with was truly inspiring, and much appreciated by those communities. On a personal note, I'll miss getting those e-mails from you that always ended with "best wishes." Our best wishes to you now as you embark on your next journey. We will miss you.

Bertram Arbesser-Rastburg:

I first met Ross at an URSI General Assembly and I was impressed by his wealth of knowledge but equally attracted by his pleasant character.

When we started the EurAAP organization, Ross came and helped us in many ways. In particular, when it came to signing a memorandum of understanding with URSI, IEEE, the Antenna Measurement Techniques Association, and the International Symposium on Antennas and Propagation (ISAP), he gave invaluable advice. Ross was the only non-European member of the EurAAP Steering Committee and it was always a pleasure to have him in our midst with his friendly smile. He always helped us to find good solutions to all the problems we encountered and he never complained about anything. He was a friend and a true gentleman. We will all miss him.

Rest in peace, dear Ross!

Rick Ziolkowski:

I knew Ross for nearly 40 years. We first met during an AP-S/URSI conference in the early 1980s and we had interacted at that annual meeting every year since then, as well as at many European Conference on Antennas and Propagation (EuCAP), ISAP, and URSI events.

Ross was a consummate volunteer in the international antennas and propagation and URSI communities. His knowledge and advice on publications was unparalleled. They were invaluable to me when I was an AP-S AdCom

He had a warm smile every week in our regular video meetings, and consistently entertained us with stories from his many travels and experiences.

member, particularly when I was the AP-S president.

I will sorely miss a special friend, as will many in the antennas and propagation/URSI communities. My heart and special condolences go out to his wife, Sue, for her significant loss.

Laura Creighton, director of Society Programs and Audience Engagement at IEEE:

My heart is truly saddened by Ross' passing. He's become a great friend who provided plenty of hearty laughs and sage advice through the decades as we've both poured our care and efforts into IEEE. He had a warm smile every week in our regular video meetings, and consistently entertained us with stories from his many travels and experiences. I'll be thinking of Ross each time I reach for my ham radio (he was a real encourager) and each time I look at the stunning bay photograph he took and had stretched onto canvas for my wall. I hope his family can find solace in the many, many good memories people will be sharing about Ross. I'm sending prayers for your peace, Ross, and know you are still smiling on us all.

Karl Warnick:

Early in my career, Ross sought me out at a conference and suggested that I write an article for *IEEE Antennas and Propagation Magazine* on the research I was working on at the time. Being new to a community as large as the AP-S, it was meaningful to me to have someone with a kind and personal touch recognize the value of my work. In the years since that time, Ross became a friend and colleague to me as well as to many others in our society. Thank you, Ross, for what you have meant to all of us.

Constantine A. Balanis:

I was saddened to hear of Ross' passing. For all the years that I attended the IEEE Antennas and Propagation Society International Symposium, which spanned a few decades, Ross was there and always greeted us with a smile. His life was devoted to IEEE, especially the AP-S

and URSI. He contributed significantly at all levels, especially being the founder and editor-in-chief of *IEEE Antennas and Propagation Magazine*, which he served with honor for 30 years. He will be missed dearly, and I extend my condolences to his wife Sue and loved ones. May his memory be eternal.

Gianluca Lazzi, 2022 past president of the IEEE Antennas and Propagation Society:

I have known Ross for nearly 30 years. He was a pillar of the AP-S. Those who knew him well will attest to the fact that he was a visionary leader, broadly appreciated by many, including AP-S members, AP-S leadership, and IEEE at large. Ross was unique, bringing experience, insights, wit, and humor to the many meetings I have participated in with him. He will be greatly missed.

Cynthia Furse:

Ross was so welcoming and supportive when I first came to the IEEE Antennas and Propagation Society International Symposium as a young graduate student, over 25 years ago. His quick smile and genuine care for me and all of our young AP-S members made me feel a part of the society. As the editor of *IEEE Antennas and Propagation Magazine*, Ross loved that magazine. He cared so much, grew many new initiatives, such as the "Education" column, inclusion of patents, and feature articles of all kinds. As I grew and eventually became a member of AdCom, Ross was the rock that everyone turned to for details on how IEEE runs, how IEEE publications worked, and how we could collectively work together to move our society forward. AP-S has grown so very much in that

time, and Ross has been a solid foundation, consistently helping AP-S with care and determination.

George Uslenghi, president of the International Union of Radio Science, 2001 past president of the IEEE Antennas and Propagation Society:

Ross Stone and I had been friends for decades. I knew that his health was declining, but his death on March 29 still came as a shock to me. I remember when he injured his leg by falling at an URSI meeting in Ghent, Belgium several years ago. He never completely recovered from that injury, which eventually led to an antibiotic-resistant infection spreading to his kidneys. Through years of pain and hospital stays, Ross fought hard to regain his health, never lost hope, never wavered in his commitments, and never relinquished any of the many chores, which he had taken on to benefit professional societies. His contributions to IEEE, URSI, EuCAP, and Microwave, Antenna, Propagation and EMC Technologies for Wireless Communications (MAPE) have left a permanent, beneficial imprint on those organizations. His outstanding work as editor-in-chief of *IEEE Antennas and Propagation Magazine* and the *Radio Science Bulletin* is especially noteworthy. I remember his multiyear efforts to maintain and strengthen the connection between AP-S and USNC-URSI, resulting, in particular, in a renewed memorandum of understanding that he worked out with Roberto Graglia and me at the 2019 AP-S AdCom Meeting in Granada, Spain. Ross and I coauthored the USNC chapter in the book *100 Years of the International Union of Radio Science* three years ago. That was our last intimate collaboration, although we continued working together at meetings of the URSI board until a few months ago.

I have so many personal and social memories of Ross! He used to visit Chicago in winters when his daughter Michele was a student in criminal justice at the University of Illinois, Chicago, and later complain to me about the brutal cold and his inability to move against the howling wind on campus.

Ross was the rock that everyone turned to for details on how IEEE runs, how IEEE publications worked, and how we could collectively work together to move our society forward.

Ross' wife Sue and my wife Shelly met often at conferences and became friends. At the 2019 International Symposium on Electromagnetic Theory in San Diego, California, Sue drove us to a memorable visit to Safari Park. The four of us met for the last time for dinner at a restaurant in Denver, Colorado during the AP-S/URSI symposium in July 2022. Ross was obviously ill and in pain, but he managed to sound optimistic. His passing has left a big void among his many friends and colleagues. Shelly's and my deepest condolences go to his wife Sue, his daughter Michele, and their family.

Yahya Rahmat-Samii, Ross' friend and colleague, 1995 IEEE Antennas and Propagation Society president, 2008–2011 United States National Committee/International Union of Radio Science chair:

Dear colleagues and admirers of Ross,

There are certain people in one's life that you always rely on and admire. Ross was for sure one of them. His knowledge of so many diverse topics and his unbounded dedication to stay engaged and contribute was beyond any one's expectation. He was for sure the encyclopedia of our AP-S and URSI organizations.

I knew Ross at the very beginning of my career, going back to the 1980s, and he and his lovely wife were always very generous toward me. We exchanged holiday best wishes cards for the longest time. Yes, cards! He was always willing to write super strong recommendation letters for me and he was for sure one of the reasons I got some of my awards. Forever I will cherish my time spent talking to Ross, learning from him, and appreciating his willingness to help.

There will be no replacement of Ross in our careers and for sure we will all miss his presence in our future AP-S AdCom, USNC, and URSI meetings. The power of his pen elevated the production of our publications. He so uniquely served on so many of our major publications for the longest time. During his editorship of *IEEE Antennas and Propagation Magazine*, I interacted with him on many occasions as a reviewer, special issue editor, and contributor of many articles with cover page publications. Once he told me that he read every page of every issue of the magazine before going into the final production! I strongly believe that he was for sure the only one who could do that.

I can go forever talking about him, as he was so involved in my professional career when I served as 1995 president of AP-S and 2009–2011 chair of USNC-URSI. His depth of operating knowledge and remembering the history of these organizations were tremendous assets to all leaders of these organizations. He always willingly and enthusiastically helped all of us and made our technical organizations more progressive and stronger.

I already miss his presence and I wish his lovely wife, Sue, and his family patience in these difficult days. He is going to be admired and remembered for the longest time.

Juan R. Mosig, European Association on Antennas and Propagation founder, IEEE Life Fellow:

I will always remember Ross Stone as a towering figure in our community. Since our first exchanges, more than 20 years ago, motivated by my attempt at publishing an unusual paper in *IEEE Antennas and Propagation Magazine*, I found I was facing a most unusual person. He was an experienced editor, but also a great researcher, a strong team leader, and an excellent manager and organizer. And with him, the whole was much more than the sum of its parts.

From that time on, our acquaintance became a true friendship and he was

an essential actor in the success of our EurAAP and of its EuCAP conference. Things would have been much more difficult, not to say impossible, without his unconditional help.

Ross was a very generous person, fully dedicated to the service of our community. I will miss his reassuring presence and I will never forget him.

Cyril Mangenot, European Association on Antennas and Propagation past president:

I will always keep in mind my relations with Ross. He was a unique person, talented in so many respects and at the same time so humble. Ross' smile and politeness, even when he had to mark his disapproval for what you just said, is memorable. The way Ross expressed himself was always so well formulated and so well argued that you quickly were convinced what he said was the right path.

Ross has been instrumental for EurAAP, always positively thinking and acting for the benefit of the worldwide AP-S, irrespective of which association/organization entered into the play.

Not only was Ross a strong actor at the technical level but also a very friendly colleague, first as member of the EuCAP Steering Committee and later on elected as director within the EurAAP Board of Directors I was chairing at the time. During this time period it was always such a pleasure to meet Ross and Sue at each EuCAP edition until the illness forced him not to travel.

My message is for you, Sue and Michele, for the memory of Ross.

Stefania Monni, European Association on Antennas and Propagation president:

Dear Ross, dear friend,

The first time I received a message from you, as a freshly elected member of the EurAAP Board of Directors, I was pleasantly surprised by such a kind epithet.

But this is how you started all your messages, to all of us. Very soon I learned that the meaning and weight of this word was far beyond referring

Ross was a very generous person, fully dedicated to the service of our community.

to an existing relationship. It expressed an attitude [toward] your fellows, a profound sense of shared intentions and objectives, a complete abnegation, which led you to put yourself at the total service of the community, your great benevolence for others, your patience, your kindness, the ability to smooth out the tones and postpone the offenses, in the name of the common interest.

Your continuous support and positivity has been key to the growth and consolidation of our association.

We will greatly miss you, Ross, but your memory will always remain in our hearts and your legacy will continue inspiring our work.

Oscar Quevedo Teruel, *Reviews of Electromagnetics* editor-in-chief, European Association on Antennas and Propagation vice-president:

Dear Ross,

It is with great sadness that we say farewell to you, but we take comfort in the memories of the time we spent working alongside you. You were a true asset to our team, always eager to lend your vast expertise on publication policies and offer a helping hand to anyone in need.

As a fellow member of the Board of Directors of EurAAP, I had the honor of serving alongside you, and your contributions were invaluable. We will always be grateful for the instrumental role you played in establishing EurAAP's first journal, *Reviews of Electromagnetics*.

Your legacy will continue to live on in the many lives you touched and the countless contributions you made to our community. You will be dearly missed, but never forgotten.

Thank you, Ross, for everything you did for us. You will always hold a special place in our hearts.

Manuel Sierra Castañer, former European Association on Antennas

and Propagation vice-president:

Dear Ross,

Thank you so much for all of the wonderful service you gave to the antenna and propagation community. Your service to IEEE, URSI, and EurAAP was inspiring for all of the community. Thanks a lot for your years at the EurAAP board. There, I had the opportunity to know your professional and work capacity.

We will miss you.

Thomas Kürner, former European Association on Antennas and Propagation Board of Directors member:

When I first met Ross at the AP-S and USRI Symposium at London, Ontario, Canada in 1991, I was a young Ph.D. student and could not imagine that many years later I would have the privilege and pleasure to work with him very closely. From 2018 to 2021 we were both members of the EurAAP Board of Directors. This period includes the pandemic and we had to answer many difficult questions and solve complicated situations. In these situations, I always appreciated Ross' calm way of providing valuable advice, always showing us good ways out, frequently with a smile.

Thank you Ross for the great collaboration. We all will miss you.

Jennifer T. Bernhard, 2008 IEEE Antennas and Propagation Society president:

Ross Stone was a dear and trusted friend, mentor, and colleague. His dedication to our profession and our society was unmatched. His positive contributions to both will endure as part of his legacy. His passing leaves a hole in the fabric of my professional life that I find difficult to describe because it touches upon so many years and so many aspects of our work together. I know that we will continue to be reminded of his contributions and impact for years to come. He will be greatly missed.

Branislav M. Notaros, president elect of the IEEE Antennas and Propagation Society, former chair of

the IEEE Antennas and Propagation Society Meetings Committee, and Joint Meetings Committee chair of USNC-URSI Commission B:

I knew Ross for decades and worked very closely with him the last several years on our conferences and meetings. He was a living library and archive, and a go-to colleague and friend. He was a resource not only to his fellow AP-S and URSI volunteers but also to IEEE staff and officials, which I witnessed on several occasions. “Let’s ask Ross” was a last resort when the other sources of information failed. His responsiveness, promptness, and resourcefulness were unmatched, indeed. I am very glad and thankful that he was able to help us with the AP-S/URSI Conference in Denver, Colorado, that I chaired last July, as the only electromagnetic community event he attended in person during the last three-and-a-half years of his incredibly fruitful life and career. He was obviously not doing well physically, but was vividly excited and happy to reunite and interact face to face with so many colleagues and friends after three long years of pandemic separation. Recent messages from his beloved wife Sue were indicating the heart-breaking outcome, but when the final news came it was so hard to believe and understand that we will not be working and communicating with Ross any longer. It is comforting to know that he had Sue’s unparalleled love, care, and support to the last moment. Our professional community, most notably AP-S and URSI, was his extended family, truly and literally. He not only worked but lived for this family for many decades, every day, until the last one. As an “everyday” example of an immediate impact of his absence, we are already struggling to make up for things that he was so routinely and swiftly doing for AP-S, URSI, EurAAP, and others in the organization of our conferences and meetings. Ross will be deeply and dearly missed, as a colleague, visionary, and friend.

Anja Skrjervik, past European Association on Antennas and Propagation treasurer:

Ross Stone was a pillar of our community. His contributions to research, editorial work, and his leadership represented a beacon for the antenna and propagation community over many decades. But we will mostly miss his friendship, kindness, and immense human values.

May he rest in peace.

Koichi Ito, 2019 past president of the IEEE Antennas and Propagation Society:

In my eyes, so many memorable pictures with Ross came and went. Ross and Sue invited me to a dinner on the occasions of international conferences and meetings, such as AP-S/URSI annual symposia and IEEE organization unit meetings. Ross carefully chose a good restaurant and sent me a menu of the restaurant. I really enjoyed the dinner as well as chatting with Ross and Sue, and learned a lot from them.

Ross was a great supporter and promoter of antennas and propagation-related international conferences in Asia, as well including MAPE and ISAP. As for ISAP, Ross tremendously supported and attended the conferences for many years. When I served as general chair of ISAP 2012 in Japan, we negotiated with IEEE for inclusion of papers in the IEEE *Xplore* for the first time. We couldn’t have succeeded without Ross. Thank you, Ross, for everything.

Raj Mittra, long-time friend of Ross and Sue Stone:

I was in the process of making my flight reservations for the trip to Portland, Oregon, when I received an e-mail from Pres. Stefano Maci in which he asked me to say a few words about Ross Stone, who passed away recently. I was totally stunned when I went through the e-mail, and it took me awhile to accept the fact that Ross won’t be in Portland this July for the upcoming antennas and propagation meeting. I have been a regular at the AP-S/URSI meetings for the last—I don’t know how many—years, and I have always seen Ross’ cheerful face at these meetings. But, alas, Ross won’t be there anymore and we will all miss him terribly.

Much has already been said by other distinguished members of AP-S about

our friend Ross Stone, who was indisputably one of the “giants” in our field. So, I’m only going to make a few brief comments about Ross, but put in a bit of personal touch to them. I believe that I can claim to have known Ross for the longest time, perhaps longer than anyone else in the AP-S, and it has been a very pleasant journey together. More importantly, Ross has been a mentor to me for most of my academic life and has endorsed me for several awards, both AP-S and URSI. Strong endorsements from him undoubtedly played a very significant role in my winning many of these awards in just one try. Finally, I published a bunch of articles in *IEEE Antennas and Propagation Magazine*—several of them travelogues—when Ross was the editor, and he would always help me in many ways by polishing the manuscripts and sorting out the copyright issues, etc. I thank Ross from the bottom of my heart for all he has done for me, and my life would never be the same without him being around as a mentor. Ross, I will miss you terribly my friend, and I do hope that you have found other people to help up there, wherever you may be.

Ahmed A. Kishk, 2017 IEEE Antennas and Propagation Society president:

I started working with Ross in the late 1980s as an associate editor for the feature article of the newsletters and continued with him on *IEEE Antennas and Propagation Magazine* as a feature article editor until 2015. I was always amazed while working with him by his contribution to each issue as he edited every word of the magazine. This was beyond any expectation. He liked his work and never denied any excellent idea to establish a new column proposed by members of the society. When I joined AdCom, he was an Honorary Life Member of the IEEE AP-S AdCom. He never missed a meeting and always contributed his long experience and knowledge to all new members. He was also accommodating in helping me with the new journal proposal that changed later before starting with *IEEE Open*

Journal of Antennas and Propagation. I am so grateful to Ross for all of his help; he was always available to discuss any matter over the phone. Not enough words describe the sadness of missing him, knowing I will not see him in the next meeting with his smile and nice welcoming words. My deep sympathy to Sue and his family members, and we all know that he is in a better place; that is the destiny of all.

Michael Jensen, 2016 past president of Antennas and Propagation Society:

I am grateful to Ross for all of his service to AP-S and IEEE, and I have been amazed at the breadth of his experience and knowledge. But what I will remember most about Ross is his kindness and professionalism. I spent my career observing him in many capacities, and in every case he demonstrated respect for his colleagues, even during difficult times. To me personally, he was a mentor and friend, and I will miss him.

Michael Newkirk, chair of United States National Committee-International Union of Radio Science:

Dear colleagues,

There are no words to express my sadness upon learning of Ross' passing. While I was aware of his health issues, I had hoped that he would recover and continue to support the organizations that he was so devoted to: AP-S, USNC-URSI, and URSI itself. The last time I spoke to him he sounded quite positive and upbeat, which I thought was a promising sign. I was looking forward to the possibility of seeing him in Portland, Oregon this summer. This is truly sad news and my thoughts and prayers are with Sue and their family and friends.

There is no question that Ross is irreplaceable, both to his family and our organizations. I have known Ross since my first attendance at a National Radio Science Meeting in Boulder, Colorado when I was a graduate student. I was amazed that he seemed to know everyone and everything about URSI. Who knew that all these years later I would be working alongside him for the benefit of our organizations. I will miss not only his deep historical knowledge of AP-S and URSI, but also his keen sense of humor and most of all his friendship and kindness. Ross

worked tirelessly for both organizations, so I am glad to help recognize his unique contributions. We mourn his loss and are comforted that he can now rest in peace.

With a heavy heart.

Weng Cho Chew, 2018 IEEE Antennas and Propagation Society president:

Ross has been an important resource to our society. His indefatigable energy is most admirable. He is like a walking encyclopedia. Deepest condolences to Sue.

Sue Stone:

Ross spent his time on the things he loved: family, IEEE, URSI, EurAAP, MAPE. He never considered his volunteer hours *work*; it brought him great satisfaction. He looked forward to the conferences where he could interact in person with his colleagues. I am thankful I could accompany him and be a part of what was so important to him. The friendships we made enriched our lives and I appreciate the outpouring of support from so many. He is missed.



TURNSTILE (continued from page 97)

ANSWERS TO THE ANNUAL QUIZ

All the answers are derived from [1] and [2].

- 1) b) Magnetosphere (the region around Earth dominated by our planet's magnetic field).
- 2) c) Jupiter, Saturn, Neptune, and Uranus.
- 3) c) Thales (circa 624–546 BC) was a contemporary of Pythagoras. His own writings do not survive, but his hypothesis ("magnet has a soul because it moves the iron") was reported later by Aristotle (384–322 BC).
- 4) b) China. (It was apparently also used in the ancient art of feng shui.)
- 5) a) Before. (Marco Polo did not visit China until 1275, almost a century after Neckam's descriptions of the magnetic compass for navigation.)
- 6) a) Petrus Peregrinus.
- 7) b) Robert Norman.
- 8) c) William Gilbert.
- 9) c) Is a great magnet. (The original Latin was "Magnus magnes ipse est globus terrestris.")
- 10) c) Varies with both time and place.



Preliminary Call for papers

2023 IEEE Conference on Antenna Measurements & Applications

2023 IEEE CAMA

15–17 November 2023 – Genoa, Italy

Sponsor: IEEE Antennas and Propagation Society (<https://ieeepaps.org>)

Technical Co-Sponsor: URSI (<https://ursi.org>)

The scope of 2023 IEEE CAMA includes but is not limited to

- Antenna Measurements in Controlled and Non-Controlled Environments
- Electromagnetic Measurement Methods and Techniques
- Scattering and Diffraction Measurements
- Near-Field and Far-Field Measurements
- Radar and RCS Measurements, Processing, Quantum Radar
- Microwave, Millimeter-Wave, and THz Systems
- Sensors, Quantum Sensing
- Modeling, Simulations, and Predictions of Measurements in Realistic Environments
- Inverse & Imaging Methods and Techniques
- Applications: Electromagnetic Metrology and Compatibility, Radar, Terrestrial and Spaced-Based Communications including Wireless Communications, Sensing, Electronic Warfare, UAVs, UAS and Drones, Remote Sensing, Non-Destructive and Evaluation Testing, Industry, Medicine, and E-Health, etc.

Abstract (1 page) Submission Deadline: 30 June 2023

Notification of Acceptance: 15 July 2023

Final Paper (2-6 pages) Submission Deadline: 15 September 2023

2023 IEEE Antennas and Propagation Industrial Engineering Paper Award

2023 IEEE Antennas and Propagation Ulrich L. Rohde Innovative Conference Paper Awards



More information at
<https://2023ieecama.org>

General Chairs

Christian Pichot, Université Côte d'Azur, CNRS, France (christian.pichot@univ-cotedazur.fr)

Matteo Pastorino, University of Genoa, Italy (matteo.pastorino@unige.it)

Andrea Randazzo, University of Genoa, Italy (andrea.randazzo@unige.it)

Technical Program Committee Chairs

Giuliano Manara, University of Pisa, Italy (giuliano.manara@unipi.it)

Claire Migliaccio, Université Côte d'Azur, CNRS, France (claire.migliaccio@univ-cotedazur.fr)

Information for Authors

Authors of original work in the technical areas of interest are encouraged to submit one-page abstract and after acceptance to upload a two to six page-final paper of their work. All papers must be presented by one of the authors.



IEEE



Università
di Genova



Fred E. Gardiol

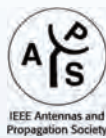
Cross out, in the grid, all the words that appear in the list below—they may appear horizontally, vertically, or diagonally. The seven remaining letters refer to a robotic and human moon exploration program by NASA.

I	T	A	E	G	A	R	O	T	S	T	N	E	V	E
N	U	P	D	R	N	N	O	I	L	I	C	E	X	E
N	O	C	O	D	E	I	R	L	I	N	M	C	X	R
O	L	T	I	D	R	H	T	L	A	C	I	P	O	T
V	C	A	R	N	A	C	U	T	T	T	A	O	L	N
A	A	I	T	O	O	N	S	P	E	N	S	R	T	E
T	V	R	E	I	M	I	A	R	D	G	C	E	L	L
E	E	I	I	T	D	V	L	U	N	A	T	I	V	E
T	R	M	A	A	E	S	E	U	G	I	T	R	A	M
A	N	T	A	R	N	G	R	A	N	I	T	E	I	E
G	R	A	Y	I	Y	N	T	A	S	E	I	T	N	N
I	N	L	L	P	E	I	G	T	T	F	L	I	R	T
V	L	A	S	S	E	R	R	N	A	A	S	B	O	A
A	S	Y	B	N	O	A	A	G	O	Y	E	R	A	R
N	O	I	T	I	D	D	A	O	L	N	W	O	D	Y

Actor	Cell	Entree	Iguana	Native	Topical
Addition	Clout	Events	Ilion	Navigate	Triode
Adopt	Code	Exciter	Inch	Next	Type
Alert	Dante	Expand	Innovate	OneDrive	Update
Ally	Dart	Flirt	Inroad	Orbiter	Varian
Antar	Daring	Getting	Inspiration	Organ	Vestal
Arena	Details	Granite	Ionic	Pore	Wyatt
Avery	Distance	Gray	Lysine	Rare	Yoga
Aviary	Download	Gypsy	Martigues	Simple	
Carnac	Elementary	IBAN	Mitla	Slant	
Cavern	Elitist	Ibsen	Morton	Storage	



IEEE AP-S International Workshop on
**CURRENT AND FUTURE CHALLENGES IN ELECTROMAGNETICS
AND ANTENNA ENGINEERING**



Bahçeşehir University
Sep 17-20, 2023



VIGNESH RAJAMANI
EXPONENT Consulting, US
IEEE EMC-S President



YAHIA M. ANTAR
Royal Military College, CA
Workshop Co-Chair



LEVENT SEVGİ
ATLAS University, TR
Workshop Co-Chair



BRANISLAV NOTAROS
Colorado State University, US
IEEE AP-S President-Elect



JAWAD SIDDIQUI
University of Calcutta, IN



REYHAN BAKTUR
Utah State University, US



ÖZLEM ÖZGÜN
Hacettepe University, TR
YANG HAO
Queen Mary University, UK



SEMA DUMANLI
BOĞAZİÇİ University, TR



ALEXANDRE PIANTINI
University of Sao Paulo, BR



MOHAMMAD SHARAWI
Polytechnic Montreal, CA



ALKIM AKYURTCLU
UMASS LOWELL, US

ADVERTISING & SALES

The Advertisers Index contained in this issue is compiled as a service to our readers and advertisers: the publisher is not liable for errors or omissions although every effort is made to ensure its accuracy. Be sure to let our advertisers know you found them through *IEEE Antennas & Propagation Magazine*.

COMPANY	PAGE NUMBER	WEBSITE	PHONE
AR/RF	7	www.arworld.us/sunarrfmotion	+1 215 723 8181
Comsol	3	comsol.com/feature/rf-innovation	
EMCoS	9	www.emcos.com	
Remcom	Cover 4	www.remcom.com/wireless-insite	+1 888 7 REMCOM
WIPL-D	5	www.wipl-d.com	

445 Hoes Lane, Piscataway, NJ 08854

IEEE ANTENNAS & PROPAGATION MAGAZINE REPRESENTATIVE

Mike Sroka
Media Consultant
Naylor Association Solutions
Phone: +1 352 333 3378
msroka@naylor.com

Digital Object Identifier 10.1109/MAP.2023.3273077

SOCIETY OFFICERS & ADMINISTRATIVE COMMITTEE

OFFICERS

Stefano Maci—President
Department of Information Engineering
and Mathematics
Via Roma, 56, 53100 Siena, Italy
Email: macis@dii.unisi.it

Branislav M. Notaros—President-Elect
Department of Electrical and Computer Engineering
Colorado State University
Fort Collins, CO, 80523
Email: notaros@colostate.edu

Michael Shields—Treasurer
MIT Lincoln Laboratory
Lexington, Massachusetts
USA

Felix Vega—Secretary

National University of Colombia, Bogota, Colombia
Electrical and Electronic Engineering Department
Edificio 411 off 210
Ciudad Universitaria, Bogota, Colombia
Email: jfvegas@unal.edu.co

2025

Sima Noghanian
C.J. Reddy
Camila Albuquerque
Zhi Ning Chen

HONORARY LIFE MEMBER

W. Ross Stone

PAST PRESIDENTS

Gianluca Lazzi, 2022
Yahia M.M. Antar, 2021
Mahta Moghaddam, 2020
Koichi Ito, 2019



ADMINISTRATIVE COMMITTEE

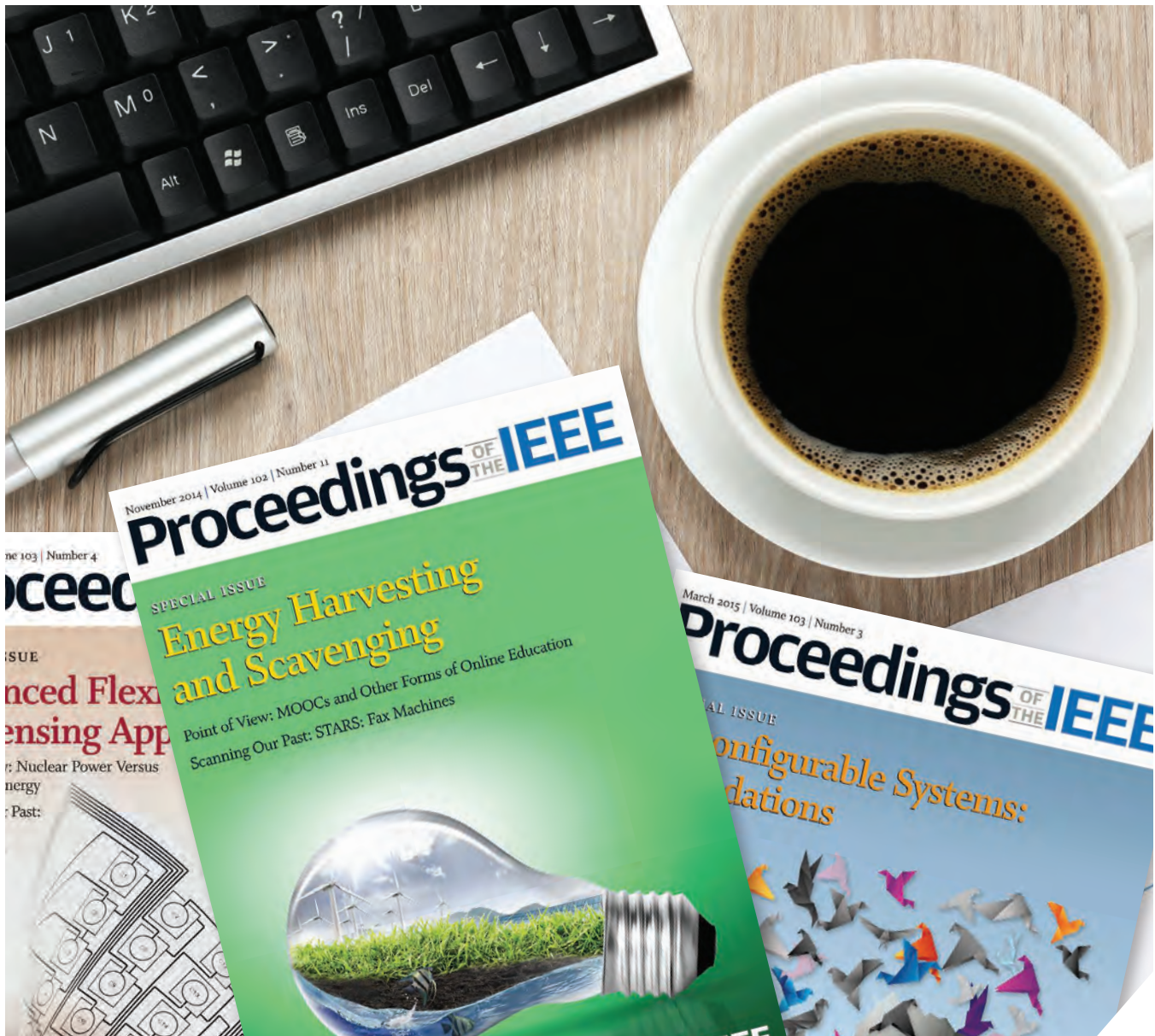
2023

Magda El-Shanawee
Branislav M. Notaros
Kamal Sarabandi
Kwai Man Luk

2024

Anisha M. Apte
Reyhan Baktur
Ashwin K. Iyer
Jiro Hirokawa

Digital Object Identifier 10.1109/MAP.2023.3273079
Date of current version: 5 June 2023



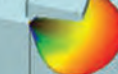
One of the most influential reference resources for engineers around the world.

For over 100 years, *Proceedings of the IEEE* has been the leading journal for engineers looking for in-depth tutorial, survey, and review coverage of the technical developments that shape our world. Offering practical, fully referenced articles, *Proceedings of the IEEE* serves as a bridge to help readers understand important technologies in the areas of electrical engineering and computer science.



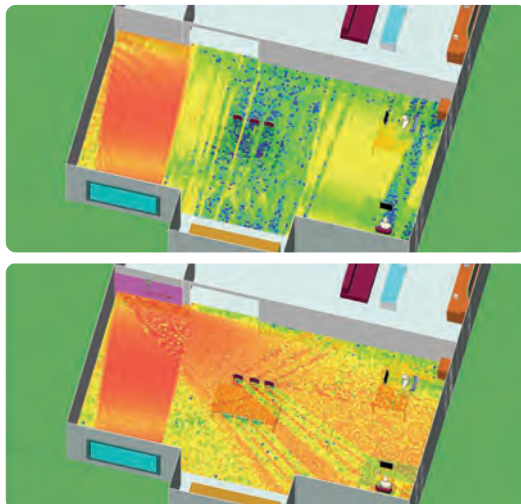
To learn more and start your subscription today, visit
ieee.org/proceedings-subscribe





Optimize Wireless Communication Coverage with Wireless InSite®

Now with Engineered Electromagnetic Surface Modeling



Wireless InSite simulates propagation in a scene with sub-optimal signal coverage (top) and reveals the improvement with the addition of an EES (bottom).

Model passive metasurfaces designed to optimize wireless communication coverage by manipulating how signals propagate through a scene.

Evaluate how the EES modifies the propagation environment to improve connectivity.



Learn more and request a demonstration at
www.remcom.com/wireless-insite

REMCOM®

+1.888.7.REMCOM (US/CAN) | +1.814.861.1299 | www.remcom.com

Improve the design process | Reduce development costs | Deliver superior results